THE INFLUENCE OF PARTIAL PEENING ON FATIGUE CRACK GROWTH

A Thesis submitted for the Degree of Doctor of Philosophy of Cranfield University

by

ALI SABAH AL-TURAIHI

May 2017

Offshore Renewable Energy Engineering Centre, Cranfield Energy and Power

Supervisors: Dr Ali Mehmanparast & Professor Feargal Brennan

ABSTRACT

Fatigue crack growth rate is an important factor for the life assessment of engineering components and structures. Various surface treatment techniques have previously been developed and employed in industrial applications to extend the fatigue life of engineering structures by implementing compressive residual stresses on material surfaces. Residual stresses can decelerate or accelerate fatigue crack growth in engineering structures, depending on their distribution profiles (i.e. tension or compression). In this thesis, the influence of partial surface peening on the fatigue crack growth of a high strength steel (HSS) material has been investigated by performing laboratory tests.

The effects of partial peening on the fatigue crack growth behaviour of *Optim*700*QL* ferritic HSS have been experimentally investigated. Dog-bone shaped specimens were tested under tension-tension fatigue load and specimens with semi-circular notches were tested under 4-point bending conditions. An initial notch was machined in the middle-width of all specimens to create a starter crack for fracture mechanics studies. Three distinct extents of partial shot peening and cavitation shotless peening, with respect to the crack tip and specimen symmetry line, were applied on the specimen geometry. The finite element modelling (FEM) was used to first calculate the shape function, and then the stress intensity factor (SIF), to develop a new model for 4-point bend specimen geometry with the dimensions considered in this project, the solutions of which are not available in the literature. Moreover, FEM was used to predict the stress concentration factor (SCF) for a dog-bone specimen to avoid reaching plasticity at the crack tip in load calculations for tension-tension tests. The fatigue crack growth results from the partially peened specimens have been compared with those obtained from similar specimen geometry but with no peening. The results show that the residual stress fields formed ahead of the initial notch tip due to the peening process play a significant role in the fatigue crack growth behaviour of the material, indicating that partial surface peening can be used as an effective method to decrease the fatigue crack growth rate under pure bending fatigue loading conditions, but is harmful under tension-tension loading conditions.

Keywords: Fatigue, Shot peening, Cavitation shotless peening, High strength steel, Surface defect, Residual stress

ACKNOWLEDGEMENTS

First and foremost I would like to thank God the Almighty for blessing me and guiding me through my studies. Then I would like to thank the Iraqi Ministry of Higher Education and Scientific Research, Iraqi Cultural Attaché in London, and the University of Babylon where I work, for providing me with the opportunity and support to complete my PhD.

I would like to express my greatest gratitude, respect, and admiration to my supervisor Prof Feargal Brennan for his richness in knowledge, experience and commitment, which he was always prepared to share, always had time to listen and was always open to discussion. A great appreciation also goes to my supervisor Dr Ali Mehmanparast who has always given me his precious time for technical support, writing, discussion, motivation and advice.

I must thank all my colleagues at Cranfield University and my friends for supporting me in this endeavour; you have all been great people to be associated with.

I would like to thank Mr Antony Charnley, Mrs Nicola Nally, Mrs Sam Skears and Miss Mel Lucas for their support and advice during different stages of the project. Also, I would like to thank Jarryd Braithwaite, Barry Walker and Ian Hancock for their support and assistance

I would also like to thank Prof. Hitoshi Soyama, Department of Nanomechanics, School of Engineering Tohoku University, Japan for his assistance to provide cavitation shotless peening for the specimen tests.

Special thanks to my Father and Mother; words cannot express how grateful I am to you. Your prayers for me were what sustained me this far. I am very thankful to my brothers, sisters and other family members, as I am sure that without their encouragement, patience and support, this work would not have achieved these results.

TABLE OF CONTENTS

ABSTRACT i
ACKNOWLEDGEMENTS ii
LIST OF FIGURES vii
LIST OF TABLES xiv
LIST OF EQUATIONS xv
LIST OF ABBREVIATIONS xvii
1 INTRODUCTION 1
1.1 Motivation 2
1.2 Hypothesis 2
1.3 Aim and objectives 3
1.4 Thesis methodology 4
2 LITERATURE REVIEW AND BACKGROUND 5
2.1 Linear Elastic Fracture Mechanics (LEFM) 5
2.2 The SIF (Stress Intensity Factor) 6
2.3 Growth Behaviour in Fatigue Crack 7
2.4 The Effects of Material Properties and Microstructure 9
2.4.1 Non-Metallic Inclusion Effects 10
2.4.2 Grain Size Effect 11
2.4.3 Environmental Effects 11
2.5 Residual Stresses 12
2.5.1 Residual Stresses Scale 13
2.5.2 Residual Stress Origins 13
2.5.3 Intentional Creation of Residual Stress in Enhancing Component Performance 14
2.5.4 Precautions against Residual Stresses 24
2.5.5 Stress Relief through Heat Treatment 24
2.5.6 Mechanical Precautions against Residual Stress 25
2.6 Residual Stress Measurement Methods 26
2.6.1 Destructive methods 27
2.6.2 Diffraction Methods: 29
2.6.3 Ultrasonic Residual Stress Measurement 34
2.6.4 Hole Drilling 36
2.7 Residual Stress Effect on Fatigue Crack Growth 37
2.7.1 Stress Intensity Factors Concerning Residual Stress 38
2.7.2 Crack shape evolution 39
2.7.3 Residual Stress Redistribution in Crack Propagation 41
2.7.4 Fatigue Crack Growth through Tensile Residual Stress Fields 41
2.8 High strength steel 42
2.9 Summary 44

3 Calculation of shape function and stress concentration factor using finite element modelling 47
3.1 Introduction 47
3.2 Crack modelling procedure: 48
3.2.1 Partitioning crack: 48
3.2.2 Generating a seam: 48
3.2.3 Defining the crack: 48
3.2.4 Crack tip/line and crack front: 49
3.2.5 Direction of crack extension: 49
3.2.6 Symmetry: 49
3.2.7 Prescribing a singularity: 49
3.2.8 Mesh: 49
3.2.9 Mesh seeding: 50
3.2.10 Requesting output: 50
3.2.11 Defining the rest of the simulation: 50
3.3 Methodology 50
3.3.1 Stress Intensity Factor for 2-Dimensional Plate with Notch 50
3.3.2 Semi-Elliptical Crack in a 3-Dimensional Surface Crack Tension Specimen 52
3.3.3 Shape function investigation for Four-point bending specimen 54
3.4 Results 57
3.4.1 Mesh Convergence 57
3.4.2 Width Convergence of 3-Dimensional Solid Plate 58
3.4.3 Intensity Factor for 2-Dimension Plate with Notch 59
3.4.4 Semi-Elliptical crack in 3-Dimensional SCT specimen 61
3.4.5 Numerical prediction of the stress concentration factor for a dog-bone specimen 62
3.4.6 Four-point bending load for the specimen 65
3.5 Summary 66
4 RESIDUAL STRESS MEASUREMENT IN PEENED SPECIMENS 67
4.1 Introduction 67
4.2 The Residual Stress Measurement 68
4.3 Hole Drilling Technique 68
4.3.1 Methodology 69
4.4 Results 80
4.4.1 Results of Residual Stress Distribution on 4-point Bending Specimen 80
4.4.2 Result of Residual Stress Distribution on dog-bone M(T) Specimen: 91
4.5 Comparison of residual stresses 96
4.6 Summary 97
5 The Influence of Partial Surface Shot Peening On Fatigue Crack Growth 101
5.1 Introduction 101
5.2 Experimental details 102

5.2.1 Material and specimen design 102
5.2.2 Partial surface shot peening details 104
5.2.3 Fatigue crack growth testing 105
5.2.4 Crack growth monitoring and fatigue crack growth rate calculations 106
5.3 Experimental results from fatigue crack growth tests 111
5.3.1 Fatigue test results for the A10 specimen 111
5.3.2 Fatigue test results for the A20 specimen 112
5.3.3 Fatigue test results for A30 specimen 112
5.3.4 Fatigue test results for the A60 specimen 114
5.4 Fractography 115
5.5 Discussion 117
5.6 Summary 120
6 The Influence of Partial Surface Cavitation Shotless Peening on Crack Shape Evolution and Fatigue Crack Growth 121
6.1 Introduction 121
6.2 Experimental details 122
6.2.1 Material and specimen design 122
6.2.2 Fatigue test set-up 124
6.2.3 Crack inspection and monitoring 126
6.2.4 Fatigue crack growth test method 128
6.2.5 Fatigue crack growth analysis 129
6.3 Experimental results from fatigue crack growth tests 129
6.3.1 Crack length measurements 129
6.3.2 Crack shape evolution results 135
6.3.3 Fatigue crack growth rate results 141
6.4 Fractography 145
6.5 Discussion 147
6.6 Summary 152
7 Conclusions and Future Work 154
7.1 Summary of thesis 154
7.2 Achievement and conclusions 156
7.3 Limitations of this work 159
7.4 Recommendations for Future Work 159
REFERENCES 161
APPENDICES A-1
Appendix A Four-point Bend rig design A-1
Appendix B Matlab Code for calculating residual stress for hole drilling B-1
Appendix C Tension-Tension Fatigue test C-1
Appendix D Material Microstructure D-1
Appendix E Material Certificate E-1
Appendix F Fatigue crack growth rate and Stress Intensity Factor calculation for surface fatigue crack under 4-point bending test F-1

Appendix G Fatigue crack growth under 4-point bend fatigue load using single wave matrix G-1
Appendix H Crack modelling in Finite Element Modelling H-4

LIST OF FIGURES

Figure 1-1: Schematic diagram of the task of research work methodology 4

Figure 2-1: Crack opening modes, Mode I, Mode II and Mode III 6

Figure 2-2: A commonly derived sigmoidal profile pertaining to the growth data of a crack when the growth rate (da/dN) is plotted against stress intensity amplitude (ΔK)[10] 9

Figure 2-3: Schematic diagram of the cross-section of a sheet showing how residual stresses can exist in the absence of an external load [45] 12

Figure 2-4: Some examples of sources of residual stress [45] 14

Figure 2-5: Shot peening process illustration 16

Figure 2-6: Laser Shock peening principle [85] 21

Figure 2-7: Schematic diagram of cavitation bubble [102] 23

Figure 2-8: Measurement penetration vs. spatial resolution for various residual stress measurement methods [117] 27

Figure 2-9: A schematic overview of the contour method and its principle [118] 28

Figure 2-10: Various types of d in comparison with sin2□ plots for a) a state of ideal biaxial stress, b) alongside the presence of shear stress, and c) a textured structure material [126] 32

Figure 2-11: A schematic overview of synchrotron measurement geometries, where a) displays 2Θ scanning, b) low-angle transmission, and c) the dispersion of white beam energy [129] 34

Figure 2-12: Schematic diagram of the ultrasonic system [138] 35

Figure 2-13: The effects of a) residual stress on total stress, and b) stress intensity factor within a combined cycle [142] 38

Figure 2-14 Prediction of Crack Shape Evolution under tension [148] 40

Figure 2-15: Prediction of Crack Shape Evolution under bending [148] 40

Figure 3-1: Global mesh for semi-infinite plate containing a semi-circular notch and crack 51

Figure 3-2: The boundary conditions of semi-infinite plate containing a semi-circular notch and crack 52

Figure 3-3: Geometry of semi-elliptical crack 53

Figure 3-4: Surface crack tension specimen dimensions 53

Figure 3-5: Structured mesh for surface crack specimen 54

Figure 3-6: The boundary conditions of SCT containing a semi-elliptical crack 54

Figure 3-7: Geometry of Four-point bending specimen with semi-circular notch containing semi-elliptical notch 55

Figure 3-8: Geometry of crack implemented in 4-point bend specimens 56

Figure 3-9: Structured mesh of 4-point bending specimen 56

Figure 3-10: The boundary conditions of 4-point bend specimen..... 56

Figure 3-11: Mesh convergence for modelling 57

Figure 3-12: Three-Dimensional modelling of plate with U-Notch Stress 58

Figure 3-13: Width convergence for plate with a U-Notch..... 59

Figure 3-14: Normalized Stress Intensity Factor for a crack from a semi-circular notch in a plate under uniform tension 60

Figure 3-15: Example of finite element model for a plate containing a semi-circular notch and crack 60

Figure 3-16: Normalized stress intensity factor for a plate with a semi-elliptical surface crack 61

Figure 3-17: Example of a finite element model for a 3-D plate containing a semi-elliptical surface crack 62

Figure 3-18: Dog-bone specimen partitions 63

Figure 3-19: The mesh in the finite element simulations for the dog-bone specimen ... 64

Figure 3-20: Stress concentration factor variation against the normalized hole diameter for the dog-bone specimen..... 64

Figure 3-21: Non-dimensional stress intensity factor for plates under 4-Point bending test 65

Figure 4-1: The sand grit with neutralizer..... 70

Figure 4-2: Rosette strain gauge types [172]..... 71

Figure 4-3: Strain gauge wiring..... 71

Figure 4-4: Strain gauge recorder..... 73

Figure 4-5: The hole drilling machine Micro-measurements RS-200 (Vishay Precision Group) 74

Figure 4-6: Residual stress variation with depth used by the Integral Method [172] 76

Figure 4-7: Physical interpretation of coefficient $\underline{\bar{a}_{ij}}$ [172] 79

Figure 4-8: Schematic graph of residual stress measurement points on four-point bending specimen geometry..... 80

Figure 4-9: Strain gauge reading versus depth at point 1 81
Figure 4-10: Residual stress distribution versus depth at point 1 82
Figure 4-11: Strain reading versus depth at point 2 83
Figure 4-12: Residual stress distribution versus depth at point 2 83
Figure 4-13: Strain reading versus depth at point 3 84
Figure 4-14: Residual stress distribution versus depth at point 3 85
Figure 4-15: Strain reading versus depth at point 4 86
Figure 4-16: Residual stress distribution versus depth at point 4 86
Figure 4-17: Strain reading versus depth at point 5 87
Figure 4-18: Residual stress distribution versus depth at point 5 88
Figure 4-19: Strain reading versus depth at point 6 89
Figure 4-20: Residual stress distribution versus depth at point 6 89
Figure 4-21: Strain reading versus depth at point 7 90
Figure 4-22: Residual stress distribution versus depth at point 7 90
Figure 4-23 Schematic diagram of Surface Crack Tension Specimen 92
Figure 4-24 Strain reading versus depth at point 1 93
Figure 4-25 Residual stress distribution versus depth at point 1 93
Figure 4-26 Strain reading versus depth at point 2 94
Figure 4-27 Residual stress distribution versus depth at point 2 94
Figure 4-28 Strain reading versus depth at point 3 95
Figure 4-29 Residual stress distribution versus depth at point 3 95
Figure 4-30: Comparison of residual stresses 96
Figure 4-31: 3-D illustration of longitudinal residual stress distribution in 4-point bending specimen 98
Figure 4-32: 3-D illustration of transverse residual stress distribution in 4-point bending specimen 98
Figure 4-33: 3-D illustration of longitudinal residual stress distribution in tension specimen 99
Figure 4-34: 3-D illustration of transverse residual stress distribution in tension specimen 99
Figure 5-1: Test specimen and notch details 104

Figure 5-2: Demonstration of the test method implemented in the wave matrix 106
Figure 5-3: Illustration of initial notch regarding peening area 107
Figure 5-4: Crack growth monitoring during fatigue tests 108
Figure 5-5: Fatigue crack growth data for A10 108
Figure 5-6: Fatigue crack growth data for A20 109
Figure 5-7: Fatigue crack growth data for A30-1 109
Figure 5-8: Fatigue crack growth data for A30-2 110
Figure 5-9: Fatigue crack growth data for A60 110
Figure 5-10: Fatigue crack growth retarded in the peened area 111
Figure 5-11: Fatigue crack growth results for A10 112
Figure 5-12: Fatigue crack growth results for A20 113
Figure 5-13: Fatigue crack growth results for A30 113
Figure 5-14: Fatigue crack growth rate for A60 114
Figure 5-15: Fracture surface for A10 specimen 116
Figure 5-16: Fracture surface for A30 specimen 116
Figure 5-17: Comparison between different fatigue crack growth trends 118
Figure 5-18: Illustrative diagram demonstrating the effect of partial peening on FCGR 119
Figure 5-19: Schematic diagram for a cross section of the dog-bone specimen 119
Figure 6-1: Geometry of 4-point bend test specimen 122
Figure 6-2: Surface finish of cavitation shotless peening and shot peening 124
Figure 6-3: Experimental set-up of four-point bend fatigue test 125
Figure 6-4: Schematic diagram for 4-point bend test set-up 125
Figure 6-5: Schematic diagram of the ACPD technique-surface crack [193] 126
Figure 6-6: Map of spot welded pins distribution along the width of the specimen 127
Figure 6-7: ACPD wires connected to spot welded pins on the specimen 127
Figure 6-8: Schematic diagram of the loop wave matrix 128
Figure 6-9: Map of spot welded pins distribution along the width of the A10 specimen 130
Figure 6-10: Fatigue crack growth data versus number of cycles for A10-1 specimen 131

Figure 6-11: Map of spot welded pins distribution along the width of the A20 specimen 131
Figure 6-12: Fatigue crack growth data versus number of cycles for A20-1 specimen 132
Figure 6-13: Map of spot welded pins distribution along the width of the A30 specimen 132
Figure 6-14: Fatigue crack growth data versus number of cycles for A30-1 specimen 133
Figure 6-15: Fatigue crack growth data versus number of cycles for A60-1 specimen 133
Figure 6-16: Fatigue crack growth data versus number of cycles for A10-2 specimen 134
Figure 6-17: Fatigue crack growth data versus number of cycles for A20-2 specimen 134
Figure 6-18: Fatigue crack growth data versus number of cycles for A30-2 specimen 135
Figure 6-19: Geometry of semi-elliptical crack 136
Figure 6-20: Crack Shape evolution for A10-1 specimen 137
Figure 6-21: Crack Shape evolution for A20-1 specimen 137
Figure 6-22 : Crack Shape evolution for A30-1 specimen 138
Figure 6-23: Crack Shape evolution for A60-1 specimen 138
Figure 6-24: Crack Shape evolution for A10-1 specimen 139
Figure 6-25: Crack Shape evolution for A20-2 specimen 139
Figure 6-26: Crack Shape evolution for A30-2 specimen 140
Figure 6-27: Aspect ratio of fatigue crack shape evolution for test specimens 140
Figure 6-28: Fatigue crack growth results for A10-1 specimen 142
Figure 6-29: Fatigue crack growth results for A20-1 specimen 142
Figure 6-30: Fatigue crack growth results for A30-1 specimen 143
Figure 6-31: Fatigue crack growth results for A60-1 specimen 143
Figure 6-32: Fatigue crack growth results for A10-2 144
Figure 6-33: Fatigue crack growth results for A20-2 144
Figure 6-34: Fatigue crack growth results for A30-2 145
Figure 6-35: Fracture surface for A10-1 specimen 146
Figure 6-36: Fracture surface for A30-1 specimen 147
Figure 6-37: Comparison of fatigue crack growth trends in different specimens under 70kN pure bend fatigue load 150

Figure 6-38: Comparison of fatigue crack growth trends in different specimens under 60kN pure bend fatigue load 150

Figure 6-39: Comparison of fatigue crack growth trends in different specimens 151

Figure 6-40: Schematic diagram for a cross section of the dog-bone specimen 151

Figure 1-1: create seam procedure H-4

Figure 1-2: crack defines steps H-4

Figure 1-3: crack singularity setup H-5

Figure 1-4 Mesh control for the area around the crack tip H-5

Figure 1-5: SIF calculation by ABAQUS H-6

Figure A-1 Four-point bend rig design A-1

Figure C-1: Fatigue crack growth test A60 specimen C-1

Figure C-2: Fatigue crack growth rate for A60 ..... C-2

Figure_Apx C-3: Fatigue crack growth for A20 specimen C-3

Figure C-4: Fatigue crack growth for A20 specimen C-3

Figure C-5: Fatigue crack growth rate for A60 ..... C-4

Figure C-6: Fatigue crack growth A10 ..... C-4

Figure C-7: Fatigue crack growth rate for A10 ..... C-5

Figure C-8: Experimental set-up C-5

Figure D-1: Sample extracted from the plate D-1

Figure D-2: The sample mounted epoxy D-2

Figure D-3: Micro-structure orientation in longitudinal direction D-2

Figure D-4: Micro-structure orientation in transverse direction D-3

Figure D-5: Four-point bend specimen D-3

Figure E-1: Mechanical properties of material 1 ..... E-1

Figure E-2: Mechanical properties of material 2 ..... E-2

Figure F-1: Flow chart of Newman & Raju model F-3

Figure G-1: Schematic diagram of single wave matrix G-1

Figure G-2: Demonstration of the test method implemented in the wave matrix G-2

Figure G-3: Fatigue crack growth data versus number of cycles for A60 specimen ... G-2

Figure G-4: Crack Shape evolution for A60 specimen G-3
Figure G-5: Fatigue crack growth results for A60 ..... G-3

LIST OF TABLES

Table 4-1: Rosette Gauge Factors type (A) 72

Table 5-1: Chemical composition and Mechanical properties of Optim700QL [179]. 102

Table 5-2: Test matrix 103

Table 5-3: Shot peening process details 105

Table 6-1: Fatigue crack growth test matrix for 4-point bend specimens 123

LIST OF EQUATIONS

Equation 2-1 6
Equation 2-2 6
Equation 2-3 7
Equation 2-4 7
Equation 2-5 7
Equation 2-6 7
Equation 2-7 8
Equation 2-8 8
Equation 2-9 8
Equation 2-10 8
Equation 2-11 30
Equation 2-12 30
Equation 2-13 31
Equation 2-14 31
Equation 2-15 33
Equation 2-16 38
Equation 3-1 50
Equation 3-2 51
Equation 3-3 63
Equation 3-4 63
Equation 4-1 75
Equation 4-2 75
Equation 4-3 75
Equation 4-4 75
Equation 4-5 75
Equation 4-6 75
Equation 4-7 75
Equation 4-8 75

Equation 4-9 75
Equation 4-10 75
Equation 4-11 77
Equation 4-12 77
Equation 4-13 77
Equation 4-14 78
Equation 4-15 78
Equation 5-1 106
Equation 5-2 106
Equation 5-3 107
Equation 5-4 107
Equation 5-5 107
Equation 5-6 107
Equation 6-1 126
Equation 6-2 129

LIST OF ABBREVIATIONS

σ_{max}	Maximum applied stress
σ_{min}	Minimum applied stress
σ_u	Ultimate strength
σ_y	Yield strength
a	Crack length
c	Material constant
E	Modulus of Elasticity
K	Stress intensity factor
K_{eff}	Effective stress intensity factor
K_{IC}	Fracture Toughness
K_{res}	Residual stress intensity factor
ΔK_{th}	Threshold stress intensity factor
m	Material constant
R	Load ratio
R_s	Residual stress
Y	Shape Function
$\Delta\sigma$	Stress range
σ	Applied Stress
υ	Poisson's ratio
ϵ	Strain
AC	Alternative Current
ACPD	Alternating Current Potential Difference
BB	Ball Burnishing

C(T)	Compact Tension
CMM	Coordinate Measuring Machine
CSP	Conventional Shot Peening
EDM	Electrical discharge machining
FCG	Fatigue crack growth
FCGR	Fatigue crack growth rate
FEM	Finite element method
FOD	Foreign Object Damage
HAZ	Heat Affected Zone
HCF	High cycle fatigue
HD	Hole drilling
HSS	High strength steel
ICHD	Incremental Centre Hole Drilling
LCF	Low cycle fatigue
LEFM	Linear Elastic Fracture Mechanics
LSP	Laser shock peening
M(T)	Middle Tension
ND	Neutron Diffraction
S11	Crack opening stresses
SCF	Stress Concentration Factor
SCT	Surface Crack Tension
SIF	Stress Intensity Factor
SP	Shot peening
USP	Ultrasonic shot peening

1 INTRODUCTION

A material's surface plays a significant role in the fatigue behaviour of engineering components. Surfaces are commonly made to experience a number of different surface treatment processes in order to achieve particular qualities otherwise unavailable from the main manufacturing processes. The approach is implemented for a number of different reasons, including enhanced materials performance, a change in physical properties, altering dimensions, and varying appearance. A number of different chemical, mechanical and thermal treatments have been developed to improve surface characteristics. Furthermore, different treatment processes have been applied for a number of different materials, ranging from semi-conductors to metal, bio, ceramics, and nanomaterials [1]. The fatigue behaviour of the material may be seen to be directly linked to the surface integrity created as a result of different surface treatment processes. Importantly, surface integrity may be seen to encompass a number of different aspects, including mechanical properties, metallurgical states, topography and other associated property variations in the work material throughout the procedure or surface processing [2]. Accordingly, surface integrity changes, particularly in regard to mechanical-related applications, which are seen to have a key influence both on engineering components' overall lifetime and on their fatigue strength.

A number of different mechanical treatment processes may be implemented for improving an engineering component's surface characteristics. Such treatments make use of physical processes in an effort to establish the condition of the subsequent surface. It is common for compressive stresses to be mechanically induced into ductile metals, usually through localised plastic deformation, which is seen to take place inside the outer surface. Moreover, it is common for those processes of mechanical surface treatment available in the modern-day industry to be roughly broken down into cutting and non-cutting methods [3]. Nonetheless, in cutting methods, key emphasis is placed on the creation of a final product shape; on the other hand, achieving the very best surface layer state is considered to be a secondary objective. However, non-cutting methods are recognised as primarily focused on improving the surface layer, such as peening. The peening process introduces a compressive residual stress on the material surface which can lead to improving the fatigue life of the engineering component.

1.1 Motivation

The fatigue crack growth behaviour and residual stress existence in engineering components are important for the fatigue life assessment of structures. The initiation and propagation behaviour of fatigue cracks in metallic materials have been the focus of much study, with fatigue and fracture mechanics analysis recognised as having facilitated engineers in devising accurate fatigue life assessments and prediction frameworks. Incorporating newly developed measurement approaches with theoretical frameworks has enabled residual stresses, as caused by fabrication and manufacturing processes, such as shot peening and welding, to be determined and investigated. Moreover, combining residual stresses with fatigue and fracture mechanics analysis is fundamental, and subsequently will result in more realistic life assessment frameworks. Despite the fact that residual stress measurement in different elements has been a common area of study for research, nonetheless, there remains a lack of data as to how residual stress, induced by partial surface peening, affects behaviour in terms of the fatigue crack growth rate of high strength ferritic steel.

Partial peening has advantages over entire surface peening as it is:

1. cost-effective,
2. a less time-consuming method, and
3. minimizes the negative effects of the peening process (i.e. erosion).

In the present work, the effect of a partial peening area on fatigue crack growth rate in structural components is investigated under tension-tension and pure bending fatigue loads.

1.2 Hypothesis

Most fatigue failures in engineering components occur due to surface cracks/defects and the remaining lifetime strongly depends on the material's resistance to surface crack growth. Therefore, surface treatment prior to operation can potentially play a significant role in the life extension and fatigue resistance of structural components. Knowing that, the surface peening treatment effects on fatigue crack initiation and growth were investigated by applying this surface treatment technique on the entire surface of the engineering components. However, the influence of partial peening on subsequent

fatigue crack growth behaviour is yet to be investigated and compared with similar specimen with no peening. *Applying partial peening can be used to enhance the fatigue performance of engineering structures at the construction stage or later as part of a repair and maintenance strategy. By implementing partial surface peening ahead of fatigue crack might lead to effectively retard the fatigue crack growth and improve the fatigue life of engineering components.* In the present study, partial peening areas were introduced in high strength steel (HSS) specimens. High strength steels provide advantages over conventional steels where the strength to weight ratio is important. High strength steels with yield strength ranging from 500 to 700MPa are being increasingly used in a wide range of applications from offshore and aerospace to the power generation industry, involving production jack-ups with demanding requirements.

1.3 Aim and objectives

The main aim of this work is to evaluate the effect of residual stresses induced by partial surface peening on fatigue crack growth rates.

The main objectives of this work are outlined as follows:

1. To design a partially peened specimen by using shot peening and cavitation shotless peening on which to conduct experimental fatigue tests under different loading configurations (i.e. tension and bending fatigue load).
2. To characterise the residual stress distribution in the peening and surrounding area.
3. To study the effect of partial shot peening on fatigue crack growth behaviour under tension-tension fatigue load and compare the results with similar specimens without peening under similar loading conditions.
4. To study the fatigue crack growth behaviour and fatigue crack evolution in specimens that were partially peened by cavitation shotless peening under a 4-point bending fatigue load and compare the results with similar specimens without peening under similar conditions.

5. To calculate and understand the stress concentration factor (SCF) and shape function (Y) using finite element simulations for the employed geometry for which a general solution is not available in standards and text books.

1.4 Thesis methodology

In order to achieve the main aim of this work, by designing specimens to conduct experimental fatigue test under different load conditions (i.e. tension and pure bend) of fatigue load. Introduce a partial peening zone on the surface ahead of the crack tip on different distances and mapping the through-thickness residual stress field created by cavitation shotless peening and shot peening on HSS specimens. Monitor the fatigue crack growth rates on similar specimens, it will be possible to separate the effects of residual stress from any changes in mechanical properties induced by the peening process, as shown in Figure 1-1.

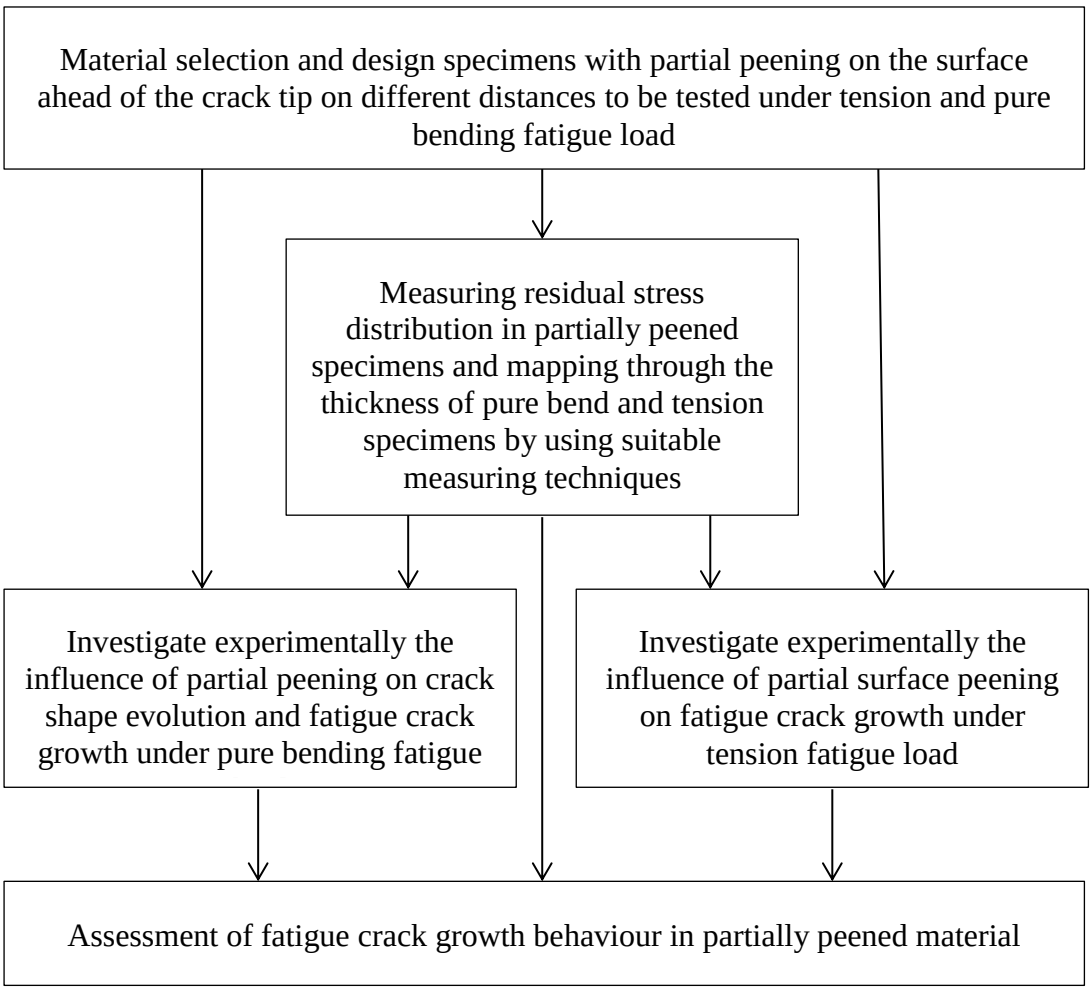

Figure 1-1: Schematic diagram of the task of research work methodology

2 LITERATURE REVIEW AND BACKGROUND

2.1 Linear Elastic Fracture Mechanics (LEFM)

The LEFM approach is regarded as a flexible technique when seeking to assess and determine the strength of a component or structure when facing flaw or crack presence. In this method, the stress distribution located near to the tip of the crack is recognised with regard to various parameters, including crack geometry, load, and material property [4], with crack behaviour recognised as being affected by crack tip stress fields. The application of the LEFM method in line with the growth of fatigue crack encompasses the crack growth process, spanning the range from an identifiable crack through to a final fracture. Accordingly, LEFM may be summarised as an approach centred on identifying the growth of cracks in materials in line with the assumption that material conditions are, in the main, linear elastic throughout the fatigue process, as implied by the approach name. In the adoption of a more conventional design method, when seeking to establish the material's overall structural integrity, the anticipated design stress and that of the material subjected are highlighted. In contrast, the LEFM method is centred on three key factors, namely flaw size, fracture toughness or material yield strength, and design stress [5].

In LEFM, the most important of the crack surface displacement modes, through which there may be the extension of a crack, may be grouped into three different modes as shown in Figure 2-1.

- Mode I is the opening mode, and is recognised as the most common, especially in the fatigue failure (the applied load perpendicular to the crack plane).
- Mode II is referred to as the sliding mode or in-plane shearing mode (the applied load perpendicular to the crack front).
- Mode III is the anti-plane shear mode or the tearing mode (the applied load parallel to the crack front).

The first of these is the most commonly occurring crack extension as a result of the normal growth of the crack with regard to the maximum principal stress.

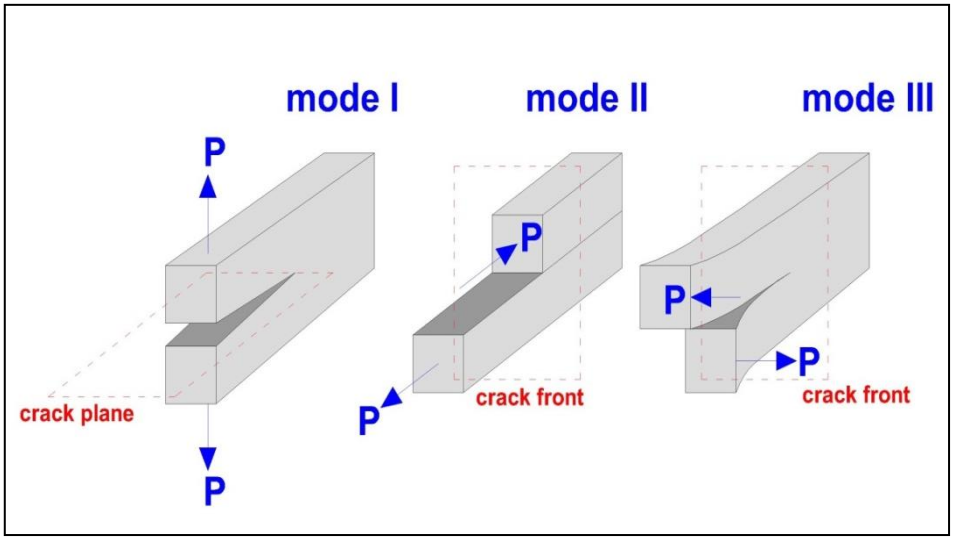

Figure 2-1: Crack opening modes, Mode I, Mode II and Mode III

2.2 The SIF (Stress Intensity Factor)

When examining fracture mechanics, insight into the stress/strain factor in regard to a crack tip is fundamental owing to the fact that crack behaviour is recognised as governing the crack tip stress field. Importantly, in linear elastic materials, the crack tip stresses are recognised as proportional to the remotely applied loading, with the only length dimension recognised across all cracked geometries being that of the crack size parameter, *a*. The link determined between SIF, *K* and the global conditions may be noted as follows [4]:

$$K = f(\sigma, \sqrt{a}) \qquad \textbf{Equation 2-1}$$

This link in the stress field makes the assumption that no crack tip plasticity is apparent or that the plasticity region is only minor when contrasted with the crack's overall dimensions and body. In the case of normal engineering applications, the SIF range is commonly communicated as follows:

$$\Delta K = Y \Delta\sigma \sqrt{a} \qquad \textbf{Equation 2-2}$$

where: ΔK is the intensity factor range for the corresponding applied stress range, Y represents the geometry correction factor, Δσ is the nominal applied stress range, *a* represents the crack depth.

Notably, the SIF range is a function of the size of the crack, its shape and the applied load, as can be seen in Equation 2-2. The geometry correction factor, which is also referred to as the non-dimensional SIF or normalized SIF, *Y*, is dependent on the component's individual geometry, the crack geometry and the loading conditions. Notably, as detailed in Equation 2-2, the applied stress and SIF are expressed in ranges owing to the fact that, in the crack growth mechanism, growth occurs as a result of cyclic stressing. The SIF has been recognised as having a key effect on the overall growth of the fatigue crack [5], and that, when ΔK is constant, the growth rate of the fatigue crack is continuous in a homogeneous material.

2.3 Growth Behaviour in Fatigue Crack

The stance of the LEFM approach is that, when a cyclic stress is applied to a material with a particular *R* ratio, then, for the length of a crack, *a*, the factor for stress intensity for Mode I crack growth may be provided with the following:

$$K_{\max} = Y\sigma_{\max}\sqrt{\pi a} \qquad \textbf{Equation 2-3}$$

$$K_{\min} = Y\sigma_{\min}\sqrt{\pi a} \qquad \textbf{Equation 2-4}$$

where *Y* represents the dimensionless parameter that depends on the crack geometry and the specimen. Accordingly, the applied SIF range may be detailed as follows:

$$\Delta K = \Delta K_{\max} - \Delta K_{\min} = Y\sigma_{\max}\sqrt{\pi a} - Y\sigma_{\min}\sqrt{\pi a} = Y\Delta\sigma\sqrt{\pi a} \qquad \textbf{Equation 2-5}$$

The growth rate of fatigue crack in a specific material may be explained through the commonly utilised Paris Law, where the rate of fatigue crack growth (FCG) is proportional to the SIF range. Therefore, Paris law will be

$$\frac{da}{dN} = C(Y\Delta\sigma\sqrt{\pi a})^m \qquad \textbf{Equation 2-6}$$

By rearranging Equation 2-6 to calculate the structure fatigue life (N)

$$dN = \frac{da}{C(\Delta K)^m}$$ **Equation 2-7**

For the case Δσ and Y are constant and by integrating Equation 2-7 will obtain

$$N_f = \int_0^{nf} dn = \int_{a_0}^{a_c} \frac{da}{C(\Delta K)^m}$$ **Equation 2-8**

By substituting (ΔK) will obtain

$$N_f = \int_{a_0}^{a_c} \frac{da}{C(Y\Delta\sigma\sqrt{\pi a})^m} = \frac{1}{C\pi^{\frac{m}{2}}(\Delta\sigma)^m} \int_{a_0}^{a_c} \frac{da}{Y^m a^{\frac{m}{2}}}$$ **Equation 2-9**

Figure 2-2 provides a schematic depiction of FCG behaviour, where the first region communicates the stress intensity range below which there will be no appearance of crack propagation. In Region II, there is the linear growth of the crack with the applied SIF range; once this reaches the critical SIF of the material, there is the occurrence of crack propagation; this is quick and can be seen depicted in Region III [6][7].

The work of Paris & Erdogan [8] focused on the application of fracture mechanics in relation to fatigue crack in a structure. This is the most widely implemented approach, and is seen to draw a link between crack growth rate $\left(\frac{da}{dN}\right)$ and stress intensity range (ΔK). For a crack with a length of *a*, for example, the equation may be expressed as follows:

$$\frac{da}{dN} = C(\Delta K)^m$$ **Equation 2-10**

Notably, m and C are seen to be material-specific constants, where *m* typically equals 3 for high strength ductile material, while for brittle material it varies (2~10). The conclusion was drawn by Ritchie & Knott [9] that the exponent m was reliant on fracture toughness, i.e. where lower fracture toughness (K_{IC}) values are seen to induce higher m values.

Importantly, the Paris equation is recognised as the most widely implemented when seeking to provide a representation of growth data in relation to cracks. This is owing to the fact that plotting a graph to display crack growth rate against stress intensity amplitude commonly creates a sigmoidal-like response, with an almost linear section expanding over a large proportion of the ΔK range of interest (as can be seen in Figure 2-2). Furthermore, the equation is recognised as easy to apply.

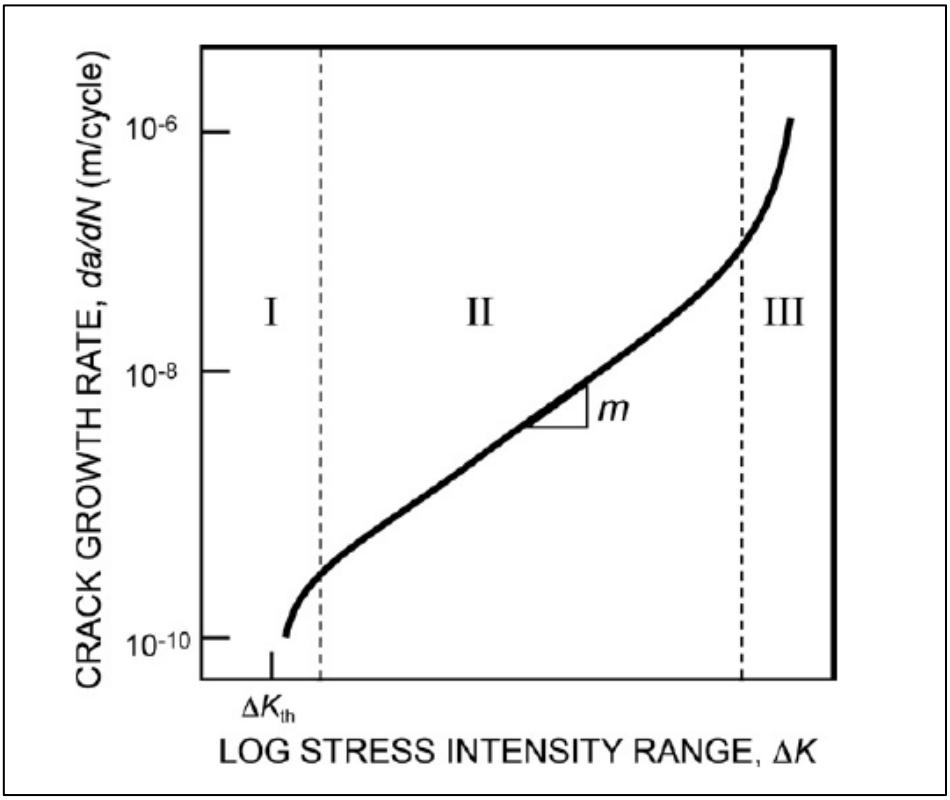

Figure 2-2: A commonly derived sigmoidal profile pertaining to the growth data of a crack when the growth rate (da/dN) is plotted against stress intensity amplitude (ΔK)[10]

2.4 The Effects of Material Properties and Microstructure

Material properties and microstructural characteristics, and the influence of such on fatigue crack propagation, are recognised as a complicated issue, and therefore have been afforded much academic attention over the years [11,12, 13, 14, 15]. However, a comprehensive treatment regarding this subject area is beyond the scope of this work.

The propagation of fatigue crack is governed mainly by an elastic modulus, with various other factors adopting a secondary role, to some extent. In this regard, it was shown by Speidel [16] that, at intermediate ΔK ranges, da/dN may be normalized for those materials with significantly differing moduli, notably by plotting against ΔK/E (where E is Young's Modulus). Various works have established an increase in the value of ΔK_{th} (where the crack growth is smaller than one atomic spacing per cycle, which is considered as dormant) when there has been an increase in the value of yield stress σ_y or ultimate stress σ_u [17,18]. Nonetheless, the majority of steels show a declining value of ΔK_{th} with an increase in the value of σ_u [19], with the most significant effect shown as greater at higher mean stresses (R ratios). Accordingly, the somewhat provisional conclusion is drawn [20] suggesting that, provided the alloy experiences cyclic hardening or otherwise is viewed as cyclically stable, the value of da/dN will decline with a greater yield stress.

2.4.1 Non-Metallic Inclusion Effects

Although there is evidence regarding the effect of non-metallic inclusions on the fatigue cracks' growth rate, much of this is conflicting. Inclusions have been recognised as having only a somewhat minor influence at near threshold growth rates [16], with no influence on ΔK_{th} in the case of medium-strength pearlitic steels [21] within a particular range. One rationalisation provided in this regard has been provided, suggesting that the inclusion spacing is more minor than the plastic zone size [18]. In this regard, it has also been noted by Broek [21] that, at higher propagation rates, such particles have been seen to induce small amounts of ductile fracture, with the scholar further emphasising that, '…in the absence of inclusions, the true fatigue crack propagation rate would be much lower'. Furthermore, Wilson [22] states that MnS and Al_2O_3 inclusions removal from a pressure-vessel steel would cause the propagation rate of fatigue crack to reduce further.

2.4.2 Grain Size Effect

A number of reviewers have drawn attention to the effect of grain size in relation to propagation in fatigue crack [23, 24, 25, 26, 27, 28]. There is much consensus with regard to the belief that, at intermediate crack growth rates, there is only a negligible effect; near to threshold rates, however, it is held that a finer grain size is able to delay the growth of the crack. In this regard, a theory centred on explaining the effect of grain size on ΔK has been put forward by Kitsunai [29]. This has shown that the variation in prior austenite grain size had little effect on the fatigue crack growth rate (FCGR) of high strength steel at the mid-range of ΔK. At low (ΔK <30 $kgmm^{-3/2}$) and high (ΔK >30 $kgmm^{-3/2}$) ΔK regions, however, the FCGR was increased as the grain size became fine.

2.4.3 Environmental Effects

Engineering structures and components are commonly exposed to environments that are far more abrasive than air, as well as facing those stresses and strains recognised in their design. It is believed that these could facilitate the initiation and subsequent propagation of crack instance. The most feasible attention is directed towards aqueous environments, with the crack process in metallic materials assisted by the environment with regard to corrosion fatigue and stress corrosion cracking. In the specific aqueous environment, the process is governed and controlled by the rates of tip dissolution or hydrogen embrittlement of the metal lattice ahead of the advancing crack [30, 31].

Crack processes that are notably affected by corrosion are a time-influenced phenomenon governed by the relevant chemical reactions and the rates of such. This generates an intermediate issue in garnering materials-related data for the validation of the design life of the structure. In a practical measurement pertaining to the contribution of corrosion to fatigue, any tests need to be completed at the frequency anticipated in service, rather than at an accelerated rate, as is commonly permissible in a relatively inert environment, as in air [32]. Furthermore, a notable effect will also be seen in the case of cyclic wave shape, which governs the period of crack opening and crack tip exposure in relation to the environment. The influence of the corrosion on the growth

rate of the crack will clearly demonstrate decline with the increased rate of growth in the crack. Essentially, this is owing to the time-dependence of the corrosion process, as well as whether or not the rate of penetration is slower or quicker than the growth rate of the crack [33, 34, 35, 36, 37, 38].

2.5 Residual Stresses

Residual stresses may be defined is follows: stress exists in a component in the absence of any external load. Should a structural component be strained to the point it exceeds its yield point, the removal of the load would result in a residual strain remaining. Such a component would be incompatible with neighbouring elements, and will demonstrate elastic deformation with its neighbours until the point at which compatibility is secured. This necessitates residual stresses to be self-equilibrating; in other words, that the body's forces and moments balance such that their sum is zero [39]. For example, Figure 2-3 illustrates that the residual stress distribution through the thickness of a sheet can exist without an external load. The tensile stresses in the central region balance the compressive stresses at the surfaces.

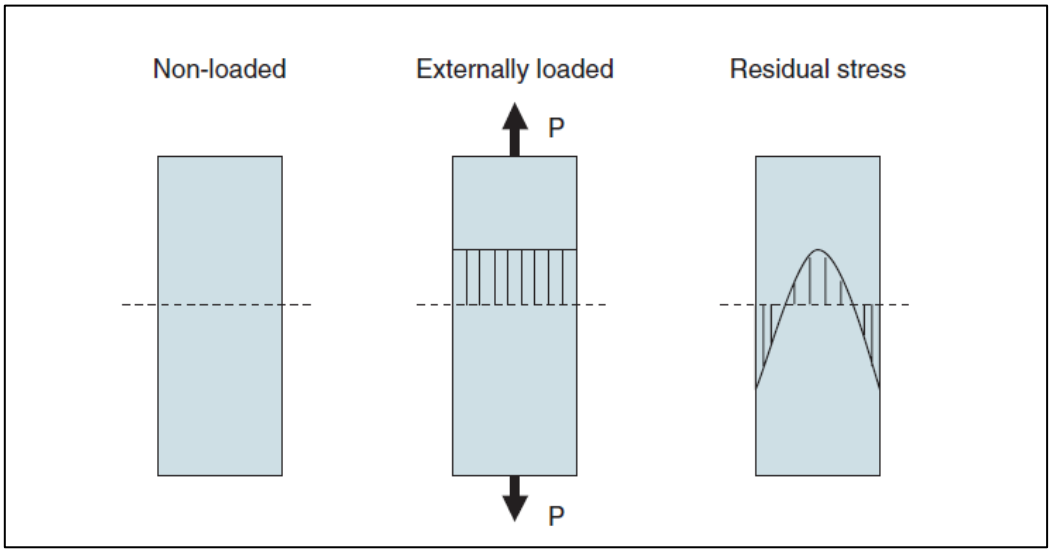

Figure 2-3: Schematic diagram of the cross-section of a sheet showing how residual stresses can exist in the absence of an external load [45]

2.5.1 Residual Stresses Scale

Residual stresses have been defined in various works [40, 41, 42] as encompassing three-dimensional (3-D) orders, as shown below:

$\sigma_y = \sigma^I + \sigma_{xy}^{II} + \sigma_{xy}^{III}$

where:

$\sigma^I = \int \sigma dA / \int dA$ overall several grains (millimetres)

$\sigma^{II} = \int \sigma dA / (\int dA - \sigma^I)$ over a microstructure unit (tens of micrometres)

$\sigma^{III} = \sigma - \sigma^I - \sigma^{II}$ over a distance of a few atoms' spacing

First-order residual stresses are commonly referred to as macrostresses, whereas second- and third-order residual stresses are recognised as microstresses.

2.5.2 Residual Stress Origins

It is recognised that residual stresses become apparent in engineering processes throughout most stages of processing, such as when there is joining, machining and heat treatment, for example. Moreover, it is commonly assumed that such stresses have been eradicated when there is further processing. The issue is far more complex when taking into account macrostresses, which may develop differently in one region when compared to another in the same component. Microstresses may occur on a microscopic scale, i.e. grain to grain, such as that which is recognised between ferrite and carbide phases in steels. Such residual stresses and their magnitude may be a notable fraction of the material's overall tensile strength. In a heat treatment process—notably one not encompassing a crystal structural change, in which material experiences a significant cooling cycle—the component's interior and surface will contract at varying rates, particularly across thicker aspects. This effect, when combined with a lower yield strength linked with high temperatures, might be seen to induce permanent yielding or, in other words, plastic flow. As a result of the significant rate of cooling, the surface demonstrates rapid contraction, which is extended by the interior and vice versa. When left to cool to room temperature, an extension in the surface regions will be identifiable, relative to the interior, and, as a result, will be in compression. Figure 2-4 provides a

graphical explanation of this, with a residual compressive stress recognised as needing to be overcome if cracks are to be initiated [43, 44].

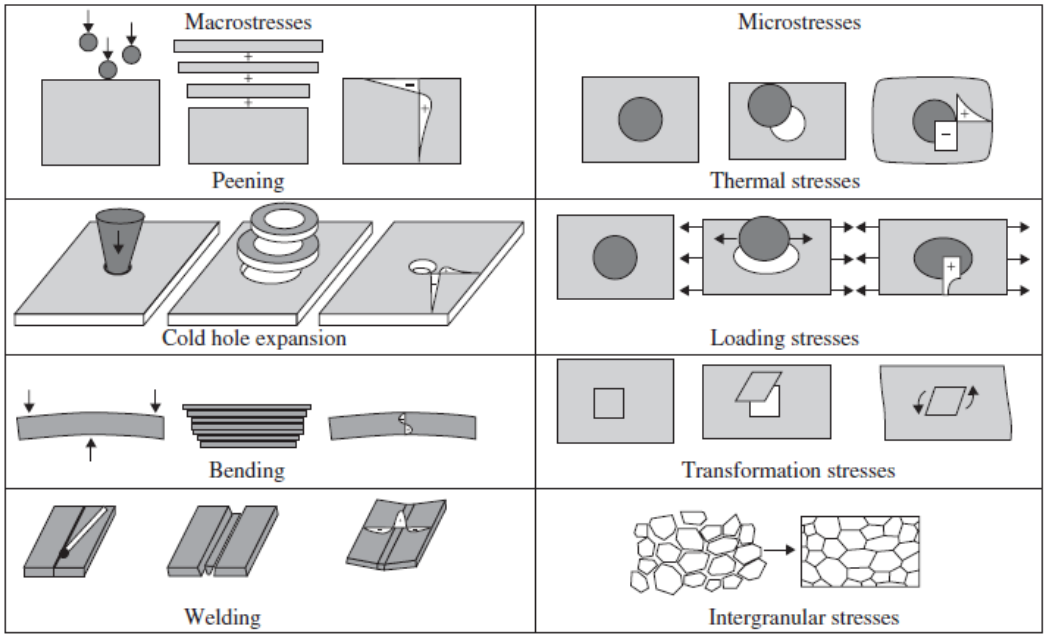

Figure 2-4: Some examples of sources of residual stress [45]

2.5.3 Intentional Creation of Residual Stress in Enhancing Component Performance

The use of residual stresses for fatigue performance enhancing can be directed towards components and structures. The intentional creation of compressive residual stresses in fatigue-prominent areas is a widely acknowledged approach to improving fatigue life. Moreover, it is recognised that such an approach is advantageous in the sense of increasing hardness, which could account for a notable improvement in fatigue life. There are various techniques that may be applied in order to generate such beneficial residual stresses.

Surface treatments, including ion-implantation, peening, nitriding rolling, and carburising can all induce compressive surface residual stresses. All of these have been recognised as effective in delaying fatigue crack initiation, with heat treatment also used in a comparable way [46, 47, 48].

A more significant and extreme approach to generating residual stresses, bearing in mind the enhancing of fatigue performance, is through intentional autofrettaging and overstressing [49]. Importantly, this is seen to be a prevalent practice in the production of large pressure vessels and gun barrels, for example. Another approach for regular use is subjecting fastener holes in thin sheets to cold expansion [50, 51, 52, 53, 54, 55], particularly for aircraft. In this work, the effect of partial surface peening on FCGR is investigated. There are different types of peening technique that are used in different industrial applications to enhance the fatigue performance of engineering components such as:

2.5.3.1 Shot peening process

Shot peening may be described as a cold working process creating compressive residual stress through placing significant plastic strain onto metals' surfaces. This particular method has commonly been applied in order to create a significant degree of surface hardness, combined with a greater level of resistance to fatigue failure in the case of in-service metal parts [56]. Shot peening is most widely implemented as a method concerned with mechanical surface treatment, and most commonly in the aerospace and automotive industries [57]. In this approach, the surface of the metal is made to take 'shots' in the form of balls made from tough materials, such as ceramic, glass or steel, which can be seen illustrated in Figure 2-5. Following the completion of this process, an effort is made by the elastically stressed area to recover to the unloaded state; importantly, however, permanent deformation can be seen in the case of the plastically deformed region. Owing to such inhomogeneous elasto-plastic deformations, the material demonstrates regions of compressive residual stress [58].

Many studies were carried out in the past to investigate the effect of shot peening on crack initiation, propagation and fatigue strength in different materials. For example Donzella et al. have studied the effect of shot peening on mechanical properties, material micro-structure and residual stress profile in sintered steel plates [59]. In another independent study, Yang et al. created a nanostructured surface layer in H13 steel by shot peening and noticed that the high temperature wear resistance was improved as a result of peening, and enhanced fatigue crack initiation and propagation

behaviour was observed in the nanostructured layer due to compressive residual stresses [60].

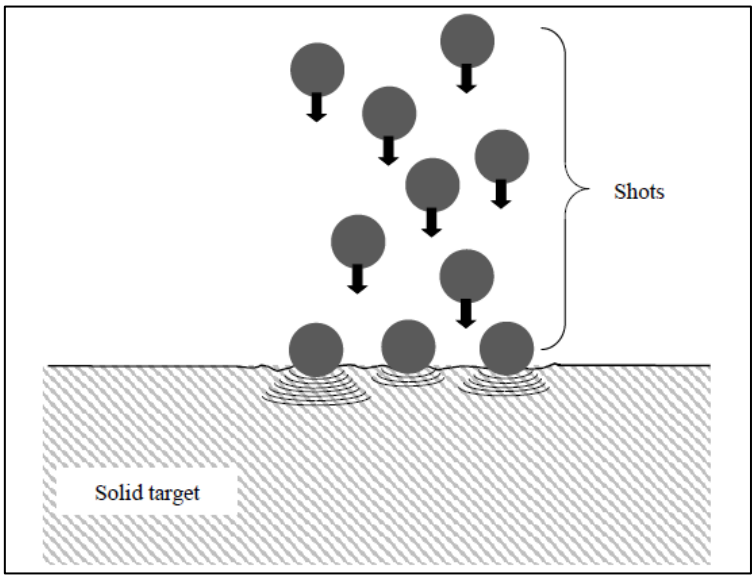

Figure 2-5: Shot peening process illustration

Gan et al. have investigated the effect of shot peening on a T-welded structure made of Q345D steel [61] and found that the suitable peening intensity could improve fatigue life compared with an unpeened structure. Pyttel et al. and Giannakis and Savaidis have calculated analytically fatigue strength based on the "Fracture Mechanics Proof of Strength for Engineering Components" (FKM) guidelines for stress shot peened high strength leaf spring samples under a three-point bending fatigue test [62] [63] and found that the fatigue life was improved as a result of peening. Mahmoudi et al. studied the effect of initial compressive residual stress on subsequent compressive residual stress induced by shot peening, and found that the initial residual stress was wiped out by shot peening up to the maximum compressive residual stress point [64]. Yang et al. used finite element simulations to study the effect of the initial surface finish of the target on shot peening effectiveness and found that the initial rough surface leads to a major reduction in the effectiveness of shot peening [65]. Takahashi et al. investigated the effect of shot peening on the torsional fatigue limit in specimens containing artificial defects in HSS specimens and found that the defect with specific dimensions could be rendered harmless by shot peening [66]. Moreover, Klocke et al. proposed a feasible method for assessing the homogeneity of residual stress distribution on shot peened

steel [67]. Torres and Voorwald [68] evaluated the fatigue life of AISI 4340 steel, used for aircraft landing gears, under four different peening intensities. They found that at the highest stress there was no change in the number of cycles until failure except in the specimen treated with the lowest peening intensity. However, there was an increase in the fatigue life for medium and high cycles. Also, they found that the best fatigue life conditions were found in the intermediate peening intensities. Perhaps, a lower fatigue life at the highest intensity was due to an effect of overpeening. The surface experiences some defects in the form of microcracks which may act as crack initiation in the fatigue test. Lee at al. [69] investigated the influence of shot peening process on the microstructure and corrosion resistance of AISI 304 stainless steel. They found the formation of nano-sized grains, multi-directional mechanical twins and strain-induced martensite based on microstructures at the surface. Also, the plastically deformed region with multi-directional mechanical twins and slip bands on the surface layer was formed to a depth of 200–250μm. The hardness was increased by about 40% with respect to the as-received specimen up to a depth of 300μm. However, the surface roughness was increased significantly after the shot peening treatment which leads to a lower corrosion resistance mainly because the practical area for corrosion per unit area also increases with increasing surface roughness. As other examples, Závodská et al. studied the effect of shot peening on fatigue strength in a low alloy steel and realised that there is an increasing positive effect on fatigue strength for crack initiation and growth as a result of shot peening [70]. A study was completed by Lee et al. which examined the impacts of the cementite phase on carbon steel's surface-hardening propensity, considering three varying carbon contents, spanning 0.1% C, 0.45% C and 0.8% C, when enduring shot peening[69]. Notably, varying peening durations (tp) were experienced by all specimens with the application of RCW (rounded cut wire) hardened steel shorts; notably, these had an average diameter equal to 250μm. When examining the findings, it can be seen that, with an increase in carbon content in the steel, the surface hardness similarly demonstrates an increase. Subsequently, the conclusion was drawn that the carbon steels' surface hardening throughout the shot peening process was achieved through the carbon dissolution and grain refinement, notably as a direct result of the cementite phase's spheroidisation. It was further acknowledged that, in the ferrite in the steels with higher carbon content, a greater amount of dissolved cementite could be seen,

alongside a greater degree of grain refinement. This renders the ferrite to be supersaturated with carbon, which subsequently causes a significant increase in surface hardening [58]. The effects of shot peening in the case of a duplex stainless steel, notably AISI 2205, were examined in the work of Sanjurjo et al. [56]. Importantly, the material was treated with the use of the shot peening process, ensuring controlled conditions with the development of a greater degree of intensity in peening. There was also the use of cast steel S-230 shots. When reviewing the results, a comparison was drawn with the same material following treatment with an industrial shot peening process, but which was seen to demonstrate a lower degree of intensity peening. As was predicted, a greater efficiency in the induction of a higher compressive residual stress, notably up to 631 MPa, was seen in the case of the controlled shot peening when contrasted alongside the industrial peening with 367MPa. Furthermore, the compressive layer induced as a result of the controlled peening treatment showed a total thickness that exceeded that generated by the industrial peening, with the former showing a greater depth of more than 350μm. Moreover, the effects of various shot peening media were examined in the study by Zhang et al. [71], with consideration towards Zirblast B30, Ce-ZrO2 and glass beads in relation to high strength wrought magnesium alloy AZ80 fatigue performance. It was established that, when peening with Ce-ZrO2 shots, a low number of surface defects could be seen, alongside low levels of roughness, high levels of maximum compressive residual stress, and a significant improvement in terms of fatigue strength. The various responses witnessed in regard to surface integrity, in the case of the peened magnesium alloy, could potentially be owing to the various peening medias' differing properties. Owing to the fact that Ce-ZrO2 is acknowledged as having a greater density and size when contrasted alongside Zirblast B30 and glass beads, it is clear that a lower travel speed is needed in order to ensure a similar peening intensity is achieved. As a result, through a lower kinetic energy of Ce-ZeO2 shots, less surface damage was caused.

A review of the past studies has revealed that shot peening effects on fatigue crack initiation and growth were examined by applying this surface treatment technique to the entire surface of the steel samples. However, the influence of partial peening on subsequent FCG behaviour is yet to be investigated and compared with full surface treatment.

2.5.3.2 Ultrasonic shot peening (USP)

Ultrasonic Shot Peening (USP) is an approach comparable to Conventional Shot Peening (CSP) in the sense that it is a cold working surface treatment. Both of these methods use media in order to effect a mechanical component's surface, thus causing a residual stress layer and accordingly enhancing the mechanical properties of the material. Both resistance to stress and fatigue life are seen to be enhanced through stress corrosion cracking. In this regard, USP differs from more CSP methods in terms of how kinetic energy is delivered to the shot. Rather than using a constant air flow, high-speed or gravity rotation of a turbine, the acceleration of a vibrating surface, known as a sonotrode, is implemented by USP. Vibration frequency is seen to be within the ultrasonic wave range (20kHz), which goes some way to providing a reasoning behind the technique's name [72, 73].

A sinusoidal electric signal exciting a piezo-electric transducer is delivered by a generator, in order to convert this energy into mechanical displacement. Owing to the fact that the vibration provided by the emitter is minor, there is a need for the vibration to undergo amplification through a number of boosters so as to transmit enough kinetic energy to the sonotrode; this has to be in direct contact with the peening media. Between the specific region to be peened and the sonotrode, a particular enclosure is designed. Accordingly, there is the hermetical containment of the media in a controlled volume. The sonotrode surface's longitudinal vibrations are seen to randomly disperse media into the treatment volume in the form of molecules into gas. Such movement results in all surfaces of the part undergoing treatment receiving homogeneous treatment. Where there is the necessity for deep compressive stresses and when there is a need to minimise surface roughness, such as in critical applications, USP may be a practical and valuable alternative to more traditional shot peening approaches [74, 75].

Due to the treatment's hermeticity, there is a reduction in media quantity to several grams, with USP thus able to be performed through high-quality media, including through bearing-balls with a high degree of sphericity, which means the component surface is not abraded. Those media with a greater diameter may be seen to achieve a greater intensity, lower surface roughness and deep compressive stresses [76]. A number of works have been completed in order to examine the effects of USP on

material structure integrity. As an example, Rodopoulos et al. completed an analysis focused on the impacts of LSP, CSP and USP on aluminium allow fatigue behaviour, based on extracting data in relation to particular products of treatments and their individual influence of fatigue damage. Accordingly, it was established that the various peening approaches to enhance materials' fatigue behaviour when the LSP covers the areas of safe-life and damage tolerance. Importantly, control shot peening is only able to derive advantages in the short crack growth, whereas both short and long crack growth may be seen to benefit from UIT [77]. Furthermore, Pile et al. adopted USP in order to enhance the overall fatigue life of TiAl alloys. It was established by the scholars that the USP has the potential to achieve significant stress levels (≈1000MPa) beneath the surface—notably far greater than that of the tensile yield stress of the material, which is seen to be within the range 350 to 600MPa [78]. Moreover, the study of Tao et al. took USP in mind of fabricating a nanocrystalline on pure Fe plate. Subsequently, it was determined that, following USSP treatments, the surface layer's initial coarse-grained structure was refined into equiaxed ultrafine grains (approximately 10nm) with random crystallographic orientations [79]. Another comparable study was completed by Liu et al. in order of creating nanocrystalline on 316L stainless steel [80].

2.5.3.3 Laser shock peening (LSP) process

Theoretically, LSP is comparable to other peening treatments in that it has the objective to improve engineering components' fatigue life. The LSP technique has been used for surface treatment for over 30 years in aerospace engineering [81]. In the completion of the process, a laser beam is directed towards a metal component's surface, which is coated with an ablative layer, such as tape or paint, and accordingly covered with a thin layer of transparent material, as depicted in Figure 2-6; this may be water. This causes a high-energy plasma which creates pressure shock waves and accordingly causes compressive stress to be propagated through the material [81]. When subjected to this, an extensive plastic deformation will be witnessed when the shock wave is seen to surpass its strength of dynamic yield. Following the shock wave flow, there is a tendency for the elastically stressed subsurface layer to recover and revert to its original condition; however, the material's continuity in the plastic and elastic regions means this cannot happen. As such, a compressive residual stress is induced at the surface,

which, in turn, creates yield strength and laser peened material hardness improvement [82, 83, 84].

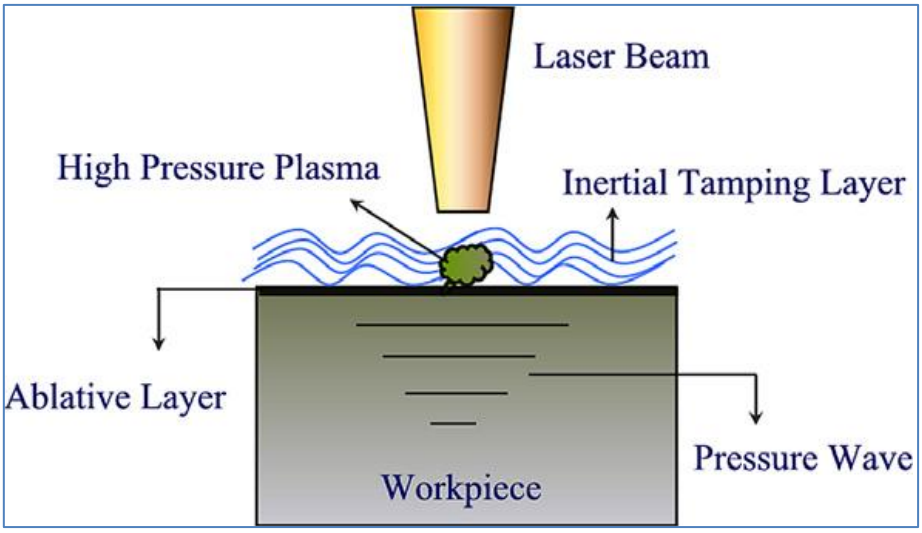

Figure 2-6: Laser Shock peening principle [85]

When a laser beam strikes the opaque material surface this leads to evaporation of the thin layer of opaque material. The vapour will absorb the incoming energy from the laser beam and expand and heat against the workpiece surface. This expanding and heating generates high pressure on the workpiece surface leading to deform plastically. The stress propagates in the material thickness, but the magnitude of stress decreases through the thickness and the material deformation continues until the magnitude of the stress falls below the material yield strength. The plastic deformation leads to generate residual stress and strain hardening in the workpiece [86, 84]. Compared to other techniques, such as shot peening (SP), ball-burnishing (BB) and USP, LSP is reported to produce the lowest work hardening close to the surface [87]. With a protective environment and good surface strengthening, laser peening is suitable for the fatigue life improvement of fastening holes. The LSP has also improved the crack growth resistance post foreign object damage (FOD) with delayed crack initiation [88], which is valuable for aircraft gas turbine engine compressors and fan blades [89]. It can also be used for rigid spinal implant Ti rods, which are improved in flexibility by LSP for a given fatigue strength [90]. For Ti alloys suitable for high-speed motor rotors used in

centrifugal compressors, LSP decreases the FCGR [91]. A number of process variables, including laser shock intensity (energy/power density), spot size, multiple laser shots, overlapping of laser spots, etc., are available to control the depth of residual stress, surface roughness and distortion. The intensity of LSP is mainly controlled by the power density (power per unit area) applied to the laser treated region and is proportional to the magnitude and depth of the compressive residual stress. The depth of compression can also be increased at the same energy by applying multiple impacts [92].

Peyre et al. studied the LSP effect on the fatigue properties of aluminium alloys under high cycle fatigue (HCF) and compared the results with samples fully treated by shot peening. They found that the LSP leads to higher surface hardening and residual stress but with very detrimental roughening not noticeable after LSP, and that the fatigue performance improvements with LSP mainly occurred during the crack initiation stage [93]. Rubio-González et al. investigated the effect of LSP on FCG and the fracture mechanics of 6061-T6 aluminium alloy. They found that the LSP increases fracture toughness and decreases the FCG of the aluminium compared with unpeened specimens [94]. Hatamleh investigated the various surface treatment techniques on the FCG behaviour of friction stir welded 2195 aluminium alloy, and also investigated the distribution of surface residual stress and through thickness in various regions of welds. It has been found that the tensile residual stress introduced by the welding process becomes compressive residual stress by LSP and it makes a significant improvement in fatigue crack retardation compared with shot peening and native specimens[82]. Voothaluru et al. studied the residual stress distribution areas from LSP in two different materials, which are hardened 52100 AISA and annealed 1053 steels. They found that there were large variations in residual stress distribution between annealed and hardened steels, and tensile residual stress present in the area surrounding the LSP area [95]. Ganesh et al. studied the effect of LSP treatment on extending the fatigue life of spring steel specimens after enduring 50% of their mean fatigue life. They found that the fatigue life of partly fatigue damaged specimens extended around 15 times due to compressive residual stress [96]. Correa et al. investigated the influence of LSP on the fatigue life of stainless steel samples for nuclear and biomedical applications and found that the fatigue life increased from 166% to 471% by optimizing the pulse sequence

[97]. Černý and Sis studied the effect of LSP on fatigue resistance and initiation mechanisms of 42CrMo steel under 3-point fatigue tests for quite small specimens of 8*8mm. They found that the compressive residual stress generated from LSP caused retardation or arrest of short fatigue cracks emanating from microstructure defects [98]. Chahardehi et al. investigated experimentally the effect of LSP on the FCG of steel under tensile fatigue load. They found that the tensile residual stress generated in the core affected the fatigue cracks' growth more than the compressive residual stress generated on the surface due to LSP [99].

2.5.3.4 Cavitation Shotless peening

Soyoma et al. introduced a new method for surface modification by using cavitation jet process, which is controlled by parameters such as upstream pressure and nozzle size [100, 101]. The method is to induce a compressive residual stress field in the treated surface, which is referred to as "cavitation shotless peening". The reason why this process is called shotless is because no shots are required and peening is done by cavitating jet (see Figure 2-7 (a). Cavitation is a phenomenon of phase change from liquid-phase into gas-phase. It is done by decreasing the static pressure of the liquid until saturated vapour pressure is reached due to increased flow velocity, and collapsed cavitation bubble when increasing static pressure by decreasing the flow velocity. When the cavitation bubble collapses, some part of the bubble is deformed and produces a micro-jet, as shown in Figure 2-7 (b). The speed of the micro-jet is about 1500m/s. This speed can result in plastic deformation on the metal surface.

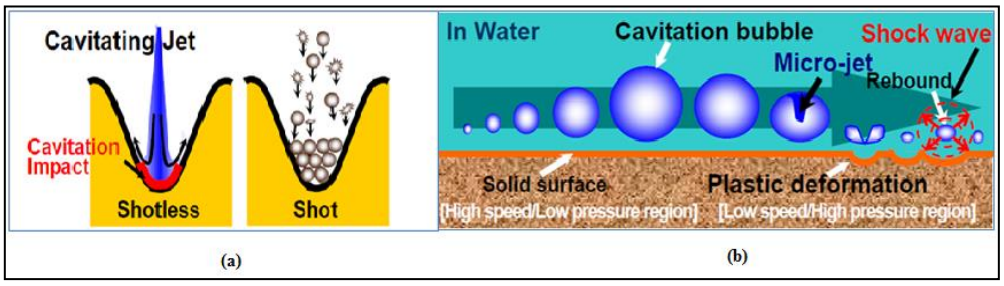

Figure 2-7: Schematic diagram of cavitation bubble [102]

Soyoma et al. investigated the effect of cavitation shotless peening on different materials such as Titanium [101], Carbonized steel [100], Stainless steel [103], and

Aluminium [104] and found that shotless peening improves the fatigue strength of the material [105, 101]. Also, they found that cavitation shotless peening could relieve micro-strains by introducing macro-strain in a polycrystalline metal surface [106]. They also noticed that plastic deformation areas beneath the surface are formed as a result of cavitation impact in the carbon steel specimens [107].

Although some limited studies have been performed in the past to examine the influence of cavitation shotless peening on the structural integrity of metallic materials, its influence on the FCG behaviour of HSSs has received little attention so far in order to expand the application of this surface treatment technique to wider industries such as offshore oil & gas and offshore wind.

2.5.4 Precautions against Residual Stresses

Heat treatments at moderate temperatures aimed at achieving stress relief might facilitate local yielding and accordingly eradicate or at least minimise residual stresses. Vibrational conditioning in the case of castings and weldments has been recognised as favourable when contrasted with thermal treatments. Nonetheless, neither of these approaches can be recognised as achieving improvements through the eradication of undesirable residual stresses [52, 108, 109].

Various surface treatments, such as shot peening, could be utilised in place of residual tensile stresses, instead of opting for compressive ones, and accordingly facilitating retardation in the initiation of fatigue cracks. However, surface treatments are not always beneficial for fatigue life [110] and instead might cause deleterious stresses, particularly should the fatigue history be predominantly tensile.

Large regions will experience loss in residual stress should they be broken down into smaller components. In the case of large welded structures, residual stresses are commonly seen to be the cause behind significant failure [111, 112].

2.5.5 Stress Relief through Heat Treatment

The relief of stress through thermal approaches involves taking the component or specimen and subjecting it to heat at a temperature at which the yield stress of the material has declined, thereby enabling creep to be effective. Significant residual

stresses are no longer supported and, should temperatures be great enough, the distribution of the stress will be regarded as more consistent. This heat treatment could result in ageing effects or tempering, subsequently causing the microstructure to demonstrate change. The degree of the latter would ultimately rest on the material in question; more specifically with regard to C/Mn steels, for example, stress-relieving heat treatment could prove advantageous in enhancing the fracture toughness of the heat affected zone (HAZ) associated with welds, thus facilitating service at a lower temperature. Nonetheless, low alloy steels are generally provided in a heat-treated state. Should stress-relieving heat treatment be deemed a requirement, it then needs to be implemented without making any significant change to the parent material's properties [113].

The structure scale to which the thermal stress relief process is to be applied is recognised as a critical consideration. In the case of more large-scale components, it might be feasible to successfully adopt such approaches to critical areas, or otherwise *in situ*, with the use of an electrical resistance method or one of induction. In this regard, there is a rule governing the butting of welds in a plate structure [114], which emphasises that, when seeking to successfully relieve residual stress, uniform heat input is necessary over a bandwidth equivalent to approximately double the weld length.

2.5.6 Mechanical Precautions against Residual Stress

In instances where it would be undesirable to implement thermal stress relief, predominantly in relation to metallurgical effects, mechanical means of stress relief might provide a valuable alternative. This approach could be delivered through a single overload, or alternatively by vibrational stress relaxation. The latter is not as well recognised, nor is knowledge on it particularly in-depth.

A single overloading exceeding the yield stress point could generally cause a decline in the impact of any pre-existing residual stresses in line with service performance. Such applications and their overload could result in the creation of compressive residual stresses surrounding present defects, with beneficial outcomes in relation to fatigue performance [115].

2.6 Residual Stress Measurement Methods

There are a number of different residual stress measurement methods includes destructive and non-destructive method that may be valuable to highlight in the context of this study. The destructive methods are viewed as being the least complex and as needing equipment that is cost-effective. Such methods are centred on the principle of material relaxation as a result of the readjustment of residual stresses following the boring of holes, the removal of surface layers, or cutting. While, the non-destructive methods such as ultrasonic technique is focused on changes in ultrasound velocity in the distance between atom plans in the crystal lattice, induced as a result of stress functioning on a crystal. Notably, this would affect incident radiation diffraction, thereby facilitating what is essentially viewed as a very precise internal strain gauge. In line with the relative intricacy and scale of the equipment deemed necessary, this approach is a little more difficult to adopt. X-ray and neutron diffraction methods for residual stress management are recognised as benefiting from being non-destructive, as is also the case with other approaches, such as Barkhausen noise, eddy-current and ultrasonic methods [45, 116]. Figure 2-8 provides a summarised overview of various different approaches with regard to their propensity to make residual stress measurements within a specimen and their spatial resolution. It is clear that a number of different aspects need to be considered in depth and accordingly offset so as to ensure the most appropriate selection of residual stress measurement for any given application. It may be seen that the most appropriate methods for measuring residual stresses, as generated by the peening process, are x-ray and the hole drilling (ICHD) approach; these have been at the core of the present work.

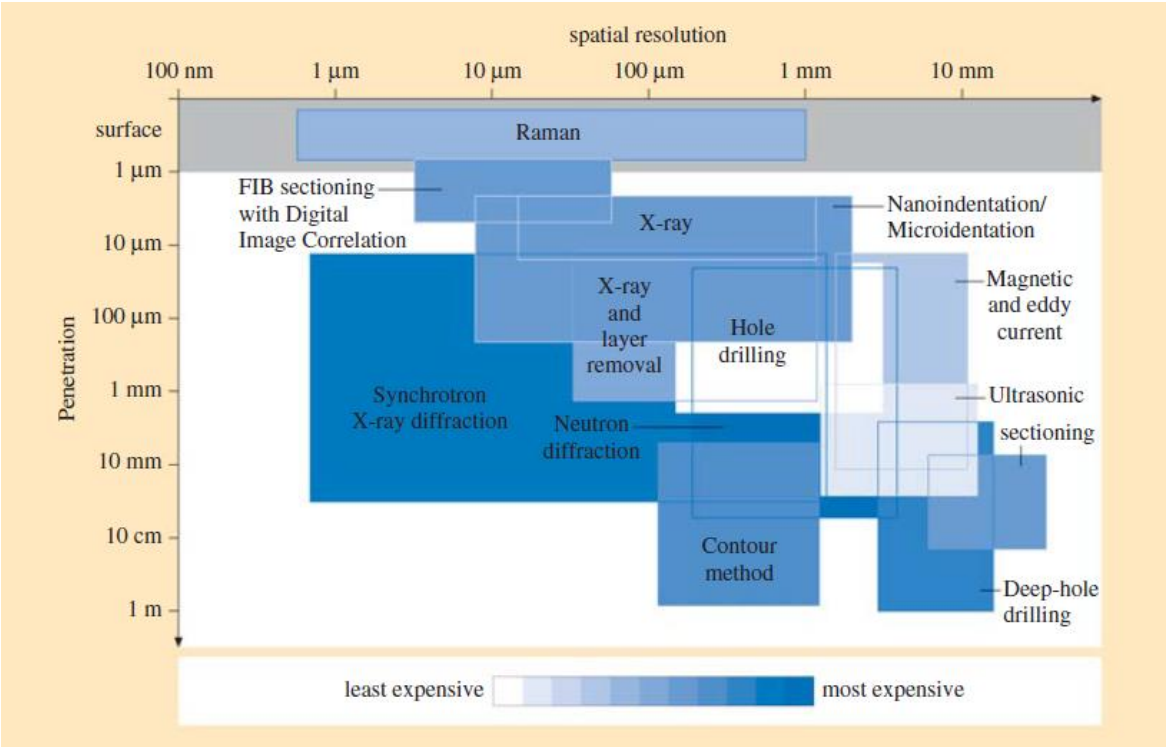

Figure 2-8: Measurement penetration vs. spatial resolution for various residual stress measurement methods [117]

2.6.1 Destructive methods

When measuring residual stress in materials, destructive experimental approaches include the curvature method, Hole Drilling (HD), compliance, slotting, and an innovative contour approach. These methods involve distortion measurement, which stems from cutting the material in a particular way, and provides fundamental relief of the residual stress perpendicular to the newly established surface. The creation of the original stress field is born from the distortion originating as a result of the inherent residual stress relaxation that is seen to arise. Although such approaches are commonly utilised in stress measurement, nonetheless, they remain have some limitation in terms of measuring the macrostress.

2.6.1.1 The Contour method

This particular approach to measuring residual stress is centred on the variation of the Bueckner's elastic superposition principle, as provided in Figure 2-9 [118].

2.6.1.1.1 Cutting:

Through the cutting approach, the specimen to be measured is commonly divided into two halves with the use of a wire electrical discharge machining (EDM). Such an approach offers benefits when compared with other cutting approaches, such as in the fact that it is able to create a straight cut without the need to remove any surplus materials from the surface. Moreover, there is no plastic deformation. Furthermore, in such an instance, a negligible machining stress is apparent. Nonetheless, this EDM cutting is restricted only to those materials that are electrically conducive [119].

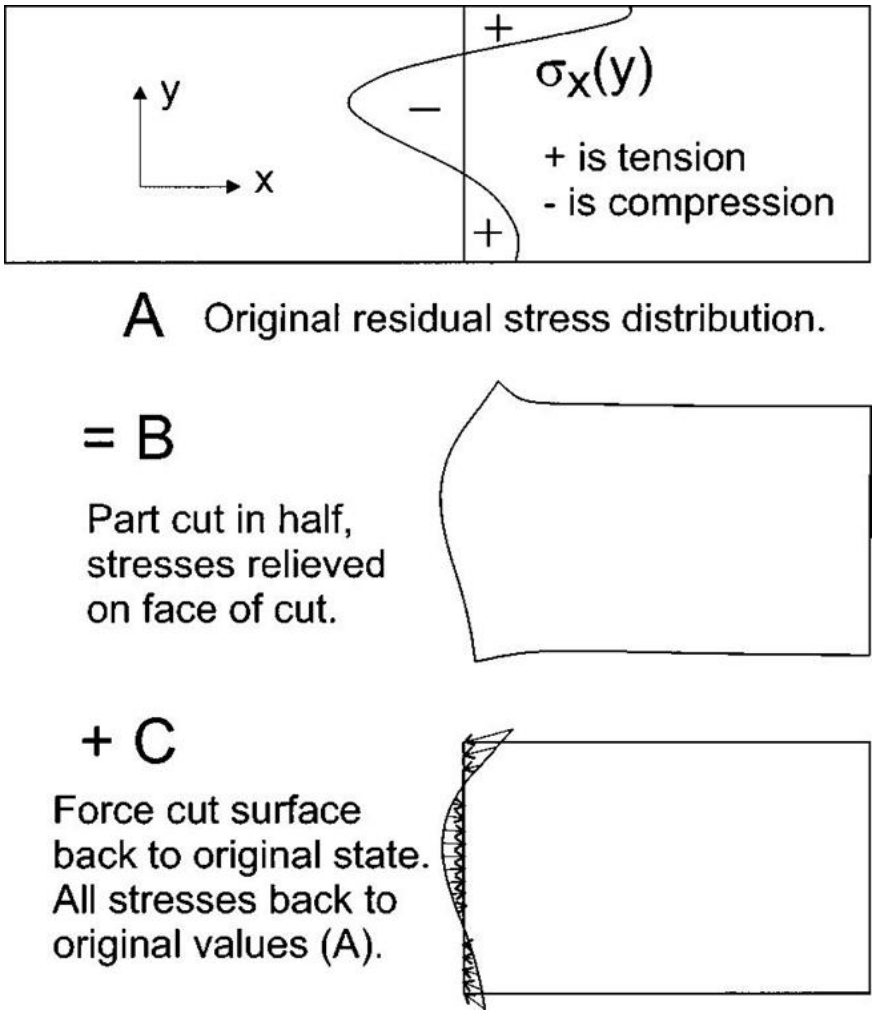

Figure 2-9: A schematic overview of the contour method and its principle [118]

2.6.1.1.2 Contour Measurement:

The newly created surface contour shifts from planarity owing to the intrinsic residual stresses experiencing elastic relaxation. The emphasis that only out of plane deformations are measured then takes place through the utilisation of a laser probe or touch probe on a commercial Coordinate Measuring Machine (CMM) [120, 121]. It should be recognised here that the best possible resolution able to be attained from the very best touch probe is a few microns; therefore, in an effort to minimise such issues, a more precise and speed-efficient laser-based approach has been devised [122] and applied to the measurement of residual stress [123].

2.6.1.1.3 Stress Calculation:

Lastly, the measured out of plane displacement data are then processed, reversed in sign and applied as surface boundary condition on the FE model of the cut part. There is the application of boundary conditions only to the direction that is normal to the cross-section; other directions do not face any limitations. A more than a single constraint is further deemed necessary in order to assist in preventing rigid body motion. The results of this approach are post-processed with the aim of achieving a two-dimentional (2-D) stress profile perpendicular to the cut surface [117].

Accordingly, it is possible to achieve the direct residual stresses through the measured surface contour; it is not necessary to complete inverse modelling approaches or to have prior assumptions in regard to the stress field. The contour method has limitations as it requires very accurate cutting and is not good for a near-surface residual stresses.

2.6.2 Diffraction Methods:

Across the various non-destructive methods, diffraction is regarded as being the most commonly applied and accurate approach when seeking to quantify residual stress fields with specific consideration of crystalline materials. When measuring the atomic lattice spacing, the primary radiation sources are electron, neutron and x-ray photon. It is noteworthy to highlight that the penetration depth, spatial resolution and overall accuracy are the fundamental and essential criteria when making a choice as to the diffraction approach for recognising residual stress. The diffraction technique principle is similar for each radiation source and will be discussed in details:

2.6.2.1 Bragg's Law:

An incident neutron or x-ray beam may be diffracted by crystalline materials with periodic lattice structure, in line with Bragg's equation, as provided below:

$$d_{hkl} = \frac{\lambda}{2\sin\theta} \qquad \textbf{Equation 2-11}$$

Where: d_{hkl} is recognised as the lattice spacing for a set of lattice hkl planes, λ is the incident beam wavelength, θ is the diffraction angle linked with this particular hkl plane set.

Importantly, any shift away from the strain-free lattice spacing or d-zero (d^0_{hkl}) may be seen to be associated with elastic strain, which becomes clear as an angular shift (Δθ) in the diffraction peak position. It may be expressed as shown in Equation 2-12:

$$\varepsilon_{hkl} = \frac{d_{hkl} - d^0_{hkl}}{d_{hkl}} = -\cot\theta\Delta\theta \qquad \textbf{Equation 2-12}$$

Such an elastic strain then can be directly converted into stress by using suitable elastic constant. The stress can be calculated by different method such as $Sin^2\psi$ method and two-Tilt method. Any plastic element inherent in the strain does not considerably affect the lattice to any notable degree; however, it does have a second order effect in relation to the Type II and Type III stresses. Nonetheless, besides stress, a number of other elements, including geometrical effects, local compositional change or local change in temperature may cause measured strain variation [124]. Accordingly, there is a need to pay attention for these other probable sources of apparent strain throughout residual stress measurement and analysis, with corrections made where these are deemed necessary.

2.6.2.2 Radiation Absorption:

When any radiation is incident to a material surface, there is then the chance for it to be absorbed, depending on the properties of the material. Accordingly, the incoming radiation intensity lessens, which therefore impacts on penetration depth. Should I_o be the initial intensity of an incident beam and I be the lesser intensity after travelling a

distance *x* along the material, they then may be linked in line with the following equation [125]:

$$I = I_0 \exp(\mu x)$$ **Equation 2-13**

2.6.2.3 Sin^{2}ψ Method:

This method's history with regard to the measurement of residual stress is many decades old [127]. Through the adoption of this approach, measurements are completed across a range of inclination angles (ϕ), with a high scattering angle applied (2Θ). By making the assumption of a biaxial stress state within in-plane stress conditions, the lattice spacing (d$\phi\psi$) in a specific direction $\phi\psi$ may be linked to the principal stress. This can be done by applying the following equation, as discussed in the works of [125, 126 and 128]:

$$\frac{d_{\phi\psi} - d_o}{d_o} = \varepsilon_{\phi\psi} = \left[\left(\frac{1+\nu}{E}\right)_{hkl} \sigma_\phi \sin^2\psi\right] - \left[\left(\frac{\upsilon}{E}\right)_{hkl} (\sigma_{11} + \sigma_{22})\right]$$ **Equation 2-14**

As per the aforementioned equation, d$\phi\psi$ is plotted against sin$^2\phi$, with the slope associated with the clearly linear curve providing a measure of the in-plane stress without any adoption of the strain-free lattice parameter, d_0, which is problematic in direct measurement.

It is essential at this stage to recognise that the linearity, as displayed in Figure 2-10, of the d in contrast to the sin$^2\phi$ curve could shift as a result of the presence of shear stress, the ϕ angle of the misaligned diffractometer throughout measurement, the preferred grain orientation, and the steep stress gradients, owing to the fact that increasing the ϕ angle lessens the depth of penetration [126].

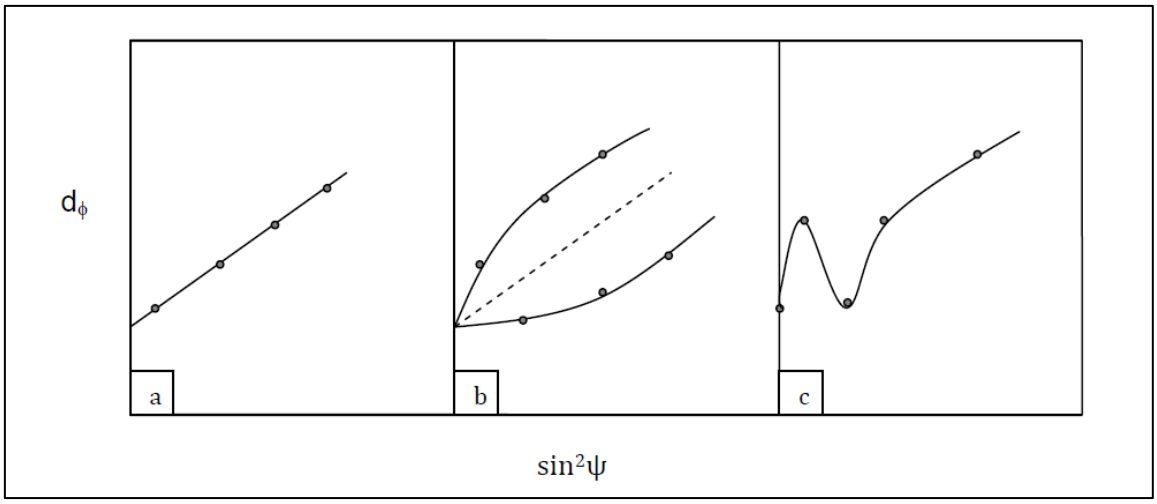

Figure 2-10: Various types of d in comparison with $\sin^2\phi$ plots for a) a state of ideal biaxial stress, b) alongside the presence of shear stress, and c) a textured structure material [126]

2.6.2.4 High Energy Synchroton X-ray Diffraction:

A synchroton source can produce x-rays that are able to provide a notably high spatial resolution in resolving microstresses and more in-depth penetration when contrasted alongside x-ray sources that are laboratory-based. Such x-ray sources are able to create photons that encompass energies equal to or in excess of 100keV, which permits a greater penetration depth when measuring subsurface residual stress in the range of just a few millimetres, depending on the sample's atomic number. In the case of titanium, one further advantage associated with the application of synchroton x-ray diffraction when compared with neutron diffraction, is a stronger diffracted beam.

Two different techniques are available when seeking to measure residual strain with the use of high-energy synchroton x-ray radiation. The first approach requires that a single diffraction peak be garnered through the application of monochromatic radiation, achieved by measuring the intensity of the diffracted beam as a diffraction angle functionality. The incidence of a white x-ray beam on a double-bounce monochromator or otherwise with the use of a Laue monochromator, subsequently diffracted by satisfying Bragg's Law, will facilitate the creation of a monochromatic beam. Owing to the incomplete diffraction and aborption in the monochromator aspects, a monochrome x-ray beam is seen to be less strong when contrasted with the incident white beam [126]. Nonetheless, such an approach facilitates the best diffraction peak resolution, in addition to the opportunity to include the use of an analyser crystal prior to

identification by the detector; this would eradicate any error sources stemming from an imperfectly positioned or thick sample.

The second approach requires that entire diffraction profiles at fixed angles be acquired through the use of a polychromatic white mean. In this instance, there is the identification of the diffracted mean through the utilisation of a multi-channel analyser crystal identifier, which has the ability to identify a number of different photon energies. Such an approach is regarded as appropriate and suited to dynamic *in situ* residual stress management measurement, as in the case of shape memory-related transitions, as shown in Figure 2-11. Furthermore, this particular approach may be adopted in an effort to measure residual strain in textured material, where a single diffraction peak's intensity could demonstrate unacceptable variation, or on the other hand may be unrepresentative of the bulk material overall. The diffracted beam's radiation λ is seen to be associated with the energy (keV), in line with the following equation:

$$Energy = \frac{12.3975}{\lambda}$$ **Equation 2-15**

When coupling equations 2-1 and 2-5, it becomes apparent that photon energy that is higher may be linked with diffraction from smaller d-spacings and at a smaller scattering angle. Subsequently, the smaller angle induces an elongated diamond-shaped gauge volume, which is seen to comprise a greater spatial resolution across the direction of the strain measurement, although the beam propagation direction offers a lower resolution. The method has limitations with variations in grain structure and surface texture.

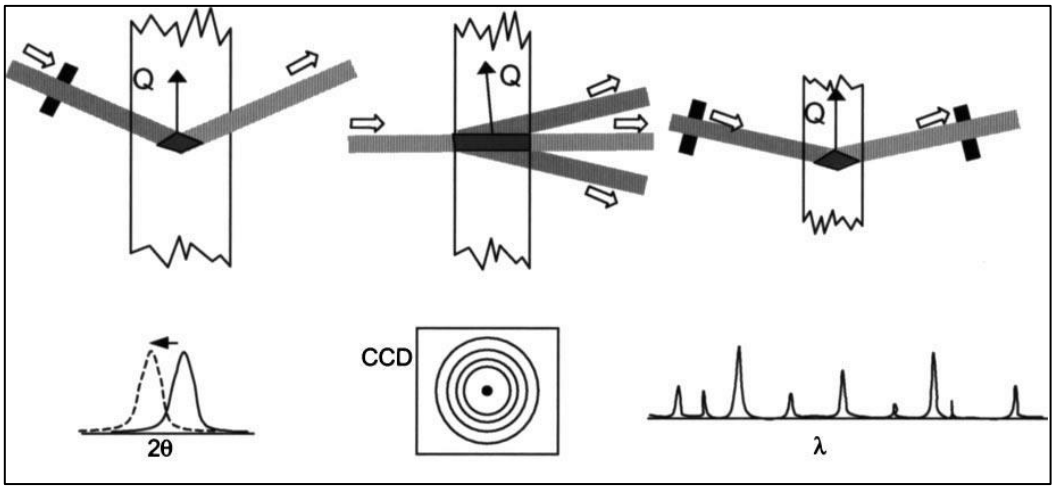

Figure 2-11: A schematic overview of synchrotron measurement geometries, where a) displays 2Θ scanning, b) low-angle transmission, and c) the dispersion of white beam energy [129]

2.6.3 Ultrasonic Residual Stress Measurement

In various works [130, 131, 132, 133, 134, 135], the measurement of residual stress through the application of ultrasonic methods has become a subject worth exploring. The main principle underpinning the measurement of such stress and elastic strain through these methods can be seen in the approximately linear change in ultrasound velocity following the application of stress. It has been recognised that it is possible to measure residual stress through the use of this phenomenon. The ultrasonic system usually contains three parts the ultrasonic generation (Nd:YAG laser) ultrasonic detection (laser Doppler vibrometer) and acoustoelastic constant measurement (pre-stress loading device) [138], as shown in Figure 2-12.

Importantly, ultrasound provides a number of wide-ranging practical applications, particularly in relation to 3-D stress fields. Stress is recognised as being measured through the induction of an ultrasound wave, which is incorporated into the element, with the flight time or other velocity-associated parameter then being measured. In general, the ultrasonic measurement technique can measure the residual stress in both cases: averaged through thickness or in surface layers.

Unfortunately, however, there are a number of limitations in its use:

- The ultrasound velocity in metals might be affected by other phenomena, such as texture and microstructure, and therefore warrants quantitative understanding.
- There is a need to take into account all characteristics with vectorial quantities, as in the case of acoustic propagation, meaning any mathematical link needs to consider such interrelations.
- The coupling witnessed between specimen and transducer needs to be repeatable.
- There is a lack of appropriate reference samples geared towards the calibration of instruments.

Such issues cannot be overcome, and digital signal processing and analysis improvements, combined with the ever-decreasing costs and ever-increasing compact nature of circuitry means ultrasonic methods are viewed as being a far more preferable approach, particularly when considering accuracy and viability in establishing residual stresses [136, 137]. One of the key restrictions can be seen in the fact that the component shape warranting examination might necessitate a special probe configuration. The method has a depth penetration from 1–20mm and requires material-specific calibration.

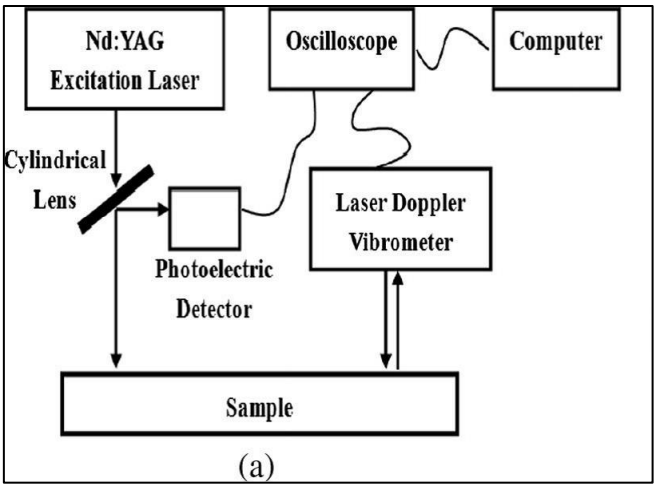

Figure 2-12: Schematic diagram of the ultrasonic system [138]

2.6.4 Hole Drilling

This approach is most likely to be viewed as being the most preferable and well-developed when seeking to measure surface residual stresses. Through the measurement of the expansion or contraction of a hole drilled at the component's surface, residual stresses may be measured. In the case of large specimens, it may be recognised as non-destructive; in small test pieces, however, the hole could be deemed damaged to an unacceptable degree. Accordingly, there is the affixing of a special three-element strain gauge rosette to the component at the point of interest; a small hole is then made through the centre. The strains relieved as a result of the hole production are measured and related back to the original surface stress [45, 139].

It is essential that the most suitable HD technique is chosen in line with the material under examination. Example of such techniques are between Incremental centre hole drilling (ICHD) and Orbiting Incremental hole drilling (O-IHD). The ICHD and O-IHD are technique used to measure residual stress in longitudinal and transverse direction from the surface to 1 mm and 2mm depth, respectively. In order for the technique to be deemed accurate and credible, the approach applied in the production of the hole, along with its geometry, must be repeatable, predictable, and should not incur any instance of machining stress; should this not be the case, inaccurate values would be incurred.

This approach is considered in the work of many researchers [140], where suitable data analysis techniques are applied. Aside from the damage caused to the specimen under examination, the method of HD has a number of different limitations; these are noted as follows:

Regions experiencing high-stress gradients should be circumvented owing to the fact that the stress gradient needs to be viewed as constant across the hole.

- Those regions recognised as encompassing greater levels of stress equal to more than one-third of the yield strength are most likely to induce erroneous results owing to the strain of the local plastic during the process of metal removal.
- The specimen's overall thickness needs to be at least four times the diameter of the hole.
- Holes need to be spaced at a distance of at least eight times their diameter.

- There needs to be accessibility for the coring/drilling device, which is frequently bulky.

The ICHD method is considered most suitable for near-surface measurement in the case of an in-plane stress profile when depth through thickness is up to 1mm. Importantly, measurement precision may be seen to be between 5% and 20%. So, Hole drilling has been decided to be used in this study.

2.7 Residual Stress Effect on Fatigue Crack Growth

Residual stresses have been recognised as having notable impacts in terms of the behaviour of materials in relation to fatigue. Importantly, ensuring the control and governance of harmful, whilst overseeing the adoption of beneficial, residual stresses has received much attention in the research, with these aspects acknowledged as critical to the fatigue performance of components and structures. Moreover, overall, tensile residual stresses are acknowledged as incurring a negative effect in relation to fatigue behaviour, whereas beneficial stresses tend to be those with a compressive residual nature. It is recognised that the effects associated with residual stresses on the growth of fatigue crack tend to be notably related; however, the majority of the work published in this area seems to consider these phenomena distinctively. The aim of this work is, however, investigating experimentally the residual stresses created by partial peening, which is producing compressive and tensile residual stress on FCGR and crack shape evolution.

FCG may be influenced by residual stresses through the crack initiation and growth either accelerating or slowing down, depending on its nature. It is common for residual stresses to be recognised as superimposed onto the applied stress such that an effective SIF is provided. Figure 2-13 provides a schematic overview of this; where Profile II is seen to represent the applied load cycle, the structure does not have any residual stresses. Upon the superimposition of a tensile residual stress field onto an applied stress, the effective SIF increases (Profile III). In contrast, however, the applied load is reduced by compressive residual stresses, meaning there is a lower SIF (Profile III). Owing to the fact that the negative SIFs are not physically present, only the positive element of the cycle is considered [141, 142].

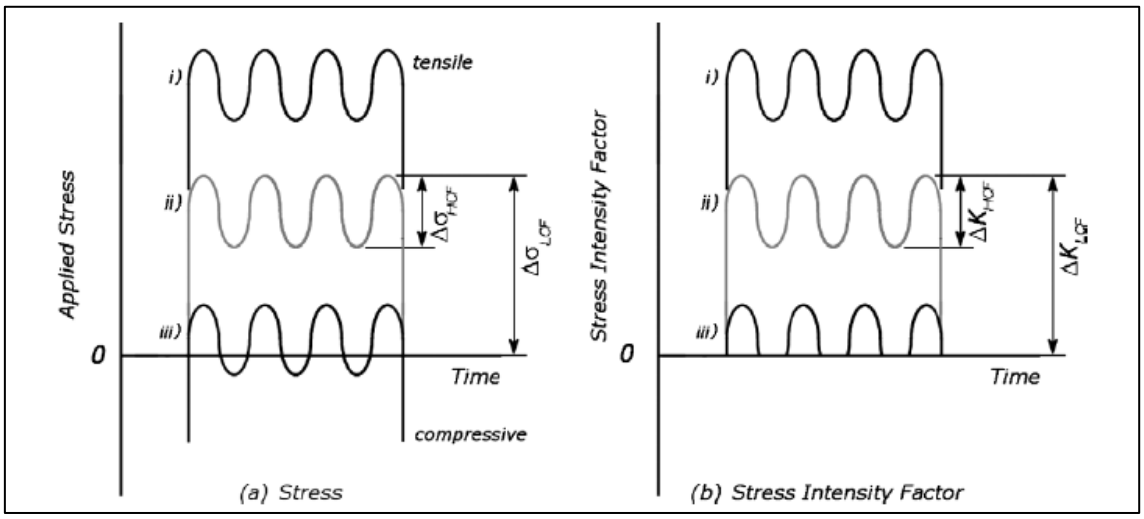

Figure 2-13: The effects of a) residual stress on total stress, and b) stress intensity factor within a combined cycle [142]

2.7.1 Stress Intensity Factors Concerning Residual Stress

In an effort to garner understanding of and insight into the effects of residual stresses on the propagation of fatigue crack, it is essential to ensure an approach to explaining the effects on the overall intensity of crack tip stress. The effective stress intensity, referred to as K_{eff}, when in the presence of residual stress, is achieved through the following:

$$K_{eff} = K_L + K_{res}$$ **Equation 2-16**

When seeking to calculate K for residual stress, or alternatively K_{res}, the process is more complex than for those loads applied externally, as in K_L. For external loads, one of a number of standard solutions may be applied in an effort to establish first-order estimates of K. Estimated SIFs may be identified for a number of different issues; this can be done by compounding recognised solutions [143]. When there is a lack of significant residual stresses, such K estimates are commonly sufficient in providing the foundation underpinning valuable LEFM frameworks.

2.7.2 Crack shape evolution

In the case of thick plate and tubular sections, the majority of fatigue cracks tend to be 2-D surface cracks, which are known to have propagation lives prior to reaching a critical state. The evolution of fatigue crack shape is a fundamental consideration across a number of sectors, whether power generation or offshore, meaning repair, inspection and maintenance approaches may be modified [144]. A number of different research efforts have been directed towards examining the evolution of fatigue crack shapes in different materials when faced with varying load conditions. As an example, the behaviour of surface crack in the case of austenitic pipes when faced with tensile fatigue load was examined by Kim and Hwang through taking into consideration the evolution of crack shape throughout the process of crack growth. They established that aspect ratio evolution in surface crack, notably throughout the fatigue cycle, causes an increase in the calculated life cycle of the conduit material, notably equal to more than a factor of two within the initial aspect ratio of 0.2, when applied to the central solenoid magnet design for the International Thermonuclear Experimental [145]. In this regard, Branco and Antunes performed a 3D finite element analysis in order to establish the development of fatigue crack in a Middle Cracked Tension specimen; they established that there is a link between fatigue crack evolution and SIF along the crack front [146]. Ngiam and Brennan investigated the effect of compressive residual stresses resultant from stitch rolling on the crack shape evolution of mild steel plate and found that the crack shape evolution was affected significantly by stitch rolling [147]. Brennan et al. investigated the fatigue crack shape evolution in steel specimens under fatigue load. They found that under pure bending and tension fatigue loads, the fatigue crack tends to grow to an optimum ratio regardless of the initial crack shape[148] as shown in Figure 2-14 and Figure 2-15. Further observed and reported in their study is that the crack shape evolution is dependent on material anisotropy and loading modes, but is independent of the applied stress magnitude.

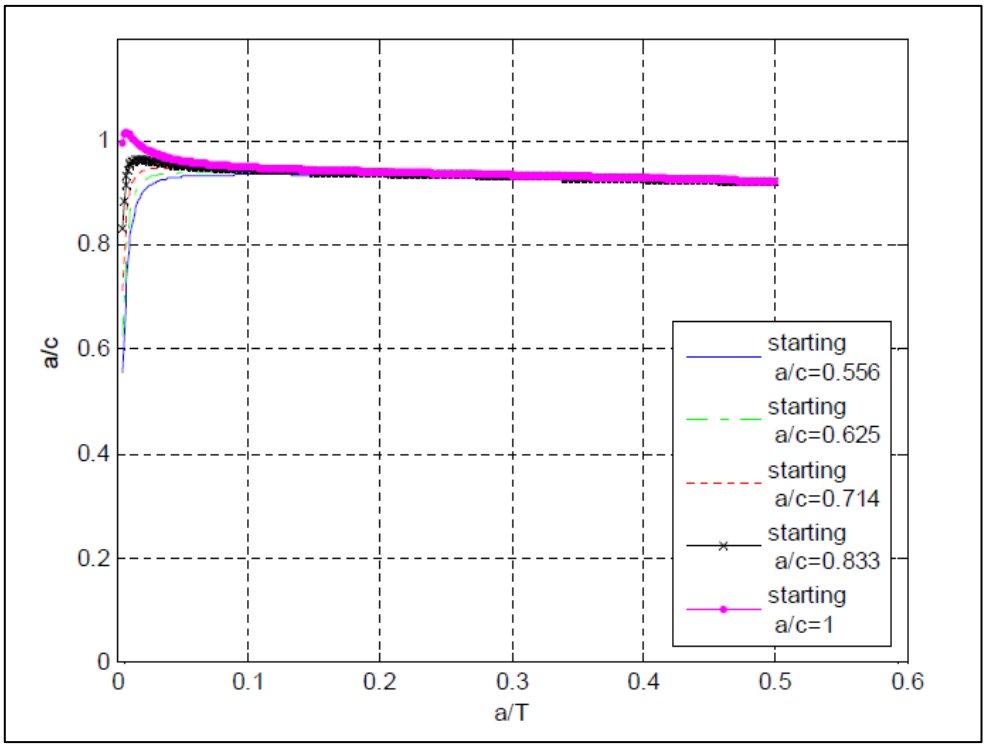

Figure 2-14 Prediction of Crack Shape Evolution under tension [148]

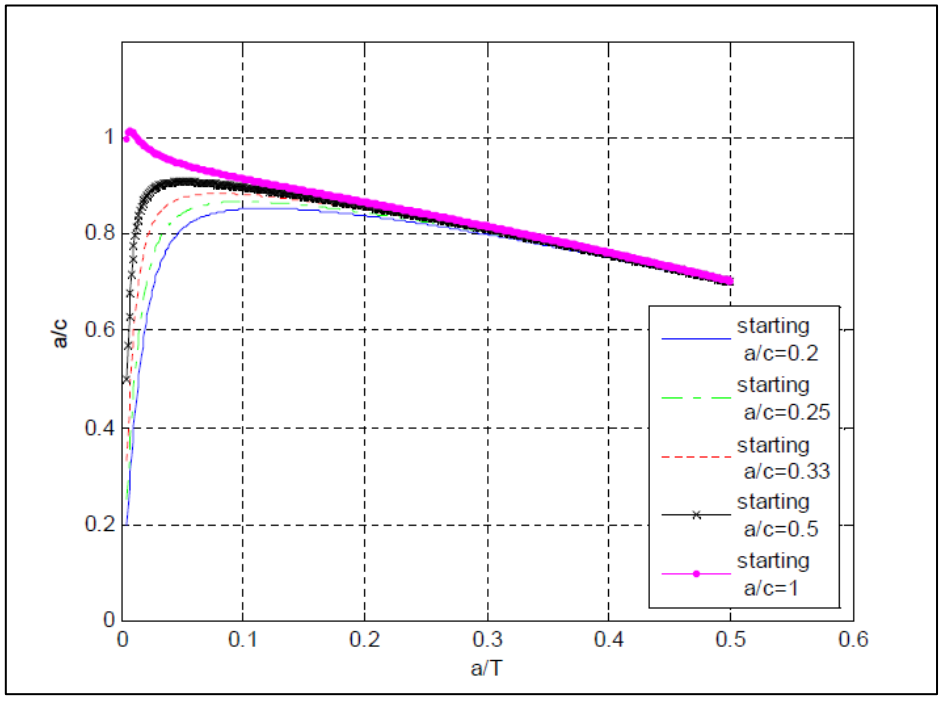

Figure 2-15: Prediction of Crack Shape Evolution under bending [148]

2.7.3 Residual Stress Redistribution in Crack Propagation

The residual stresses and their moments always need to be zero in the case of any plane. With the propagation of the crack, to some degree, the residual stress is established through the system's geometry, and relieved at the surface of the crack. There needs to be the redistribution of the residual stresses if a balance is to be maintained. The field of residual stress witnesses much continuous change with the propagation of the crack; this means that, at the crack tip, the residual stress is not the same as that recognised at the same position prior to the crack. Such changes need to be considered when SIFs for residual stresses are calculated. This is supported by the work carried out by Almer et al. who studied the effect of tensile residual macrostresses and residual microstresses on fatigue crack propagation of high-carbon steel. They found that the microstresses had little effect on FCGR, while tensile macrostresses increased the crack propagation rates in a manner that depends systematically on ΔK [149]. Lam and Lian investigated the effect of residual stresses and their redistribution on FCGR. They found that the residual stress redistribution has an effect on fatigue life and ignoring it can lead to non-conservative life predication [150].

2.7.4 Fatigue Crack Growth through Tensile Residual Stress Fields

A commonly acknowledged approach to describing the effect of tensile residual stress fields is through the effective increase of the R ratio. Such a method is seen to be aligned with the crack closure theories devised by Elber [151], where a tensile residual stress will ultimately decrease the fatigue threshold. In this regard, when completing an investigation into FCG under compressive loading, Fleck et al. [152] assumed that the crack opens when K_L and K_{res} sum at zero.

Cracks may demonstrate propagation when loaded in cyclic compressions, where the tensile residual stress and compressive stress attributable to an external load will demonstrate the effect of crack opening. This has been witnessed and detailed in the work by Suresh [153] as a fast-paced approach to acquiring data, decreasing uncertainties encompassed in other approaches. Fitzpatrick and Edwards [154] completed a review of the interaction between fatigue crack and residual stresses, and ultimately drew the conclusion that, despite crack closure monitoring being able to

provide a qualitative reflection as to the effects of a residual stress field on a growing crack, nonetheless, it was not helpful in estimating fatigue life. This was recognised as owing to the crack opening behaviour and the inherent complexity in such.

2.8 High strength steel

The fabrication of offshore structures with the use of moderate-strength steels that have a yield strength of up to 350MPa has been traditional in recent times, with the normalizing route being that commonly used for production. Nonetheless, in the last two decades, there has been much growth in the use of HSSs in the offshore engineering arena, which has been primarily driven by the need and motivation to save both cost and weight.

One of the main benefits to be derived from the use of such structural materials can be seen in their greater strength–weight ratio, as well as the corresponding savings in construction schedules and material costs as a result of the less pressing need for welding. The most fundamental increases have been seen to arise in the topside areas of jacket structures, where weight saving has not only created material savings but also permitted notable cost savings. A survey carried out in Billingham et al. [155] suggests that the proportion of HSS (which is defined in line with >350MPa yield strength) used in offshore structures has increased by less than 10% to now more than 40% in less than ten years also in automotive industries [156], bridge design [157] and construction [158].

The main application of HSSs in the offshore context has been witnessed in jack-up production. Those steels seen to have a nominal yield strength, commonly in the range of 500-800MPa, tend to be used when creating legs, rack and pinions, and spud cans. Such productions, which, in the main, are fabricated for the purpose of drilling, provide satisfactory use experience for a number of years, and are able to function at a number of different water depths, but are commonly brought into a dry environment for inspection on a 5-yearly basis. It is during these inspections that any repairs or instances of cracking can be identified and rectified.

In the construction of offshore structural applications, such as production jack-ups, which are faced with an ever-increasing number of requirements and criteria, HSSs (notably those with a yield strength >500MPa to around 700MPa) are most commonly used. Importantly, these provide various benefits when contrasted alongside more conventional steels, especially when weight is recognised as a consideration.

In the case of more recent applications, particularly with regard to lighter, more small-scale structures, such steels have been used in the jacket members themselves; however, there continue to be restrictions in their use in nodal areas owing to fatigue performance-associated concerns. Accordingly, it is expected that such materials and their use will continue to witness growth and greater popularity, with steel becoming more widely available. Furthermore, construction yards are now more experienced and knowledgeable than ever before when it comes to fabrication methods. At the present time, the majority of steels are restricted to 450 grades; however, development and research initiatives have highlighted the view that steel grades of up to 550MPa may be produced; these are readily weldable and are seen to encompass a significant degree of fracture toughness. Such steels are expected to be used more and more as their availability becomes more pronounced [155].

2.9 Summary

A number of works have stated that a various of different peening processes can be implemented in order to change the surface of materials through the introduction of compressive residual stresses, which subsequently improve the level of material fatigue life. Overall, the treated surfaces have demonstrated varying levels of strengthening and hardening through the various peening processes. The hardening layers and their respective depths can be seen to increase by as much as several hundred micron meters. Moreover, varying degrees of erosion can be seen in material surfaces. A review of the past studies has revealed that peening effects on fatigue crack initiation and growth have been examined by applying this surface treatment technique to the entire surface of the steel samples in a wide range of applications, from offshore and aerospace to power generation.

The material properties affect the fatigue life of the material, such as non-metallic inclusion, grain size and environment. The non-metallic inclusion has a significant influence on FCGR due to inducing small amounts of ductile fracture. The finer grain size causes higher FCGR in the intermediate stages of FCG due to less distance between grain boundaries needing a fatigue crack to follow. A corrosive environment leads to accelerating the fatigue crack rates. Also, a review of different peening techniques has been done and revealed that all the peening leads to generating compressive or beneficial residual stress on the surface and tensile residual stress through the thickness due to the self-equilibrating characteristics of residual stress.

The HSSs provide advantages over conventional steels where the strength to weight ratio is important. HSSs with yield strength ranging from 500 to 700MPa are being increasingly used in the offshore engineering industry, involving production jack-ups with demanding requirements.

However, some of the needs and gaps in the literature need to investigated such as:

1. Applying partial surface peening is cost-effective and less time consuming that full peening as well as minimize the area of peened surface that subjected to erosion to extend the fatigue life of engineering components

2. The influence of partial peening on subsequent FCG behaviour of HSS is yet to be investigated under tension fatigue load.
3. The influence of partial peening on FCG behaviour is yet to be investigated under pure bending fatigue load.
4. The influence of cavitation shotless peening on the FCG behaviour of HSSs has received little attention so far to expand the application of this surface treatment technique to wider industries such as offshore oil & gas and offshore wind.
5. Comparing the surface finish of the material treated by different peening techniques.

Therefore, the chapters of this thesis are organised as follows

Chapter 3 presents the finite element simulation to find the shape function to calculate the SIF for pure bend specimens, as well as prediction of the SCF for a dog-bone specimen to calculate the applied tension-tension fatigue load.

In Chapter 4 the methodology and results of the measurement residual stress distribution for bending and tension specimens are presented and the results are plotted in a 3-D figure for a better understanding of residual stress distribution.

In Chapter 5, an experimental investigation of the effect of partial shot peening on FCGR under tension-tension fatigue load is presented. The methodology and results of the experimental work are discussed in detail. The results are represented by FCGR versus SIF range.

In Chapter 6, an experimental investigation of the influence of the partially peened area by cavitation shotless peening under four-point bending fatigue load is presented. The methodology and results of the experimental work are discussed thoroughly. The results are represented by fatigue crack evolution and FCGR against the SIF range.

Chapter 7 presents the conclusions and findings of the present research work and offers suggestions for future work.

3 Calculation of shape function and stress concentration factor using finite element modelling

3.1 Introduction

The finite element method (FEM) has been widely used for engineering applications over the past few decades. FEM is a numerical method for solving an integral or differential equation to predict stress and strain distributions in engineering components and structures. FEM uses continuous functions by discretizing the object into small parts called elements. The elements are continuous over the object by connecting points called nodes. The purpose of continuous elements is to make the element functions accurate to global function. The accuracy of the simulation depends on the element number. The global equation system contains element functions as well as geometrical and material data. Finite element analysis can be achieved by a range of commercial softwares such as ABAQUS, ANSYS, etc.; these softwares give various analysis options to solve simple and complex problems [159].

ABAQUS is a useful software to simulate cracks and fracture mechanics factors' calculation; it has been used widely to investigate different problems in different materials. For instance, Teh. calculated the SCF and shape function for different engineering components [160]. Leitner et al. studied the numerical effects on notch fatigue strength assessment of welded and non-welded components. It has been found that the number of element should be at least twelve to minimize the numerical impact [161]. Huang and Hu have investigated fracture mechanics theory for pre-cracked specimen under 3-point bending load [162]. Yang and Vormwald investigated the three dimensional FCG of plate under cyclic non-proportional mixed mode load [163]. Liu et al. investigated the fatigue life U-notched polymethyl methacrylate (PMMA) for aerospace industries by using a local stress approach [164]. Arun et al. studied the extension of a ductile crack of steel under a combination of residual stress and primary load in a four point bend specimen contains circumferential surface crack through the thickness crack [165].

In this work, the finite element software package ABAQUS/6.13 version has been used for modelling different parts containing an artificial crack to calculate the SCF for a

dog-bone specimen and shape function (Y) for plate with a semi-circular notch that contains a semi-elliptical crack. The SCF solutions for the geometry used in the experimental part of this study are not available in the literature. The importance of SCF is to calculate the applied load for a tension specimen and avoid plasticity at the crack tip. Therefore a finite element model was developed to work out the SCF solutions for the specimen design employed in this project. Also, the SIF solution for plate with a semi-circular notch that contains a semi-elliptical crack under pure bending fatigue load is not available in the literature. The available solutions are the Newman & Raju model for plate that contains a semi-elliptical crack on the outer surface of the plate [166]. Therefore, finite element simulations were used develop the Newman & Raju model to calculate SIF for the specimen that was used in the experimental part of this study. The results were compared with data from the literature and good agreements have been found. The elastic properties used in the numerical analyses are provided from the material supply company for experimental work (Appendix E). The elastic properties are elasticity modulus E equal to $200GPa$, Poisson's ratio ν equal to 0.3, and yield strength is 690MPa.

3.2 Crack modelling procedure:

3.2.1 Partitioning crack:

First of all, the crack itself needs to be simulated. A partition is made representing the crack shape and dimension. In this case, the face is partitioned, and the Partition Cell: Extrude/Sweep Edges tool is used to extrude the partition on the face.

3.2.2 Generating a seam:

When creating a partition to represent the crack, the elements on both sides will share the same nodes. For crack modelling, sharing the same nodes is not required. By choosing independent instances mesh and generating seam, separate nodes on elements on each side of the crack.

3.2.3 Defining the crack:

A crack needs to be defined to be able to request crack-related output. This can be done by the Interaction module, using Special => Crack => Create, or by double clicking on

'Cracks' in the model tree, under 'Assembly', 'Engineering Features'. In the 'Create Crack' dialog box that appears the type 'Contour Integral' is selected, as shown in Appendix H.

3.2.4 Crack tip/line and crack front:

After the crack front is selected, the contour integral will be calculated for the layer of elements around the crack face. The edge of sharp crack represents the crack tip. While for the blunt cracks, the crack front needs to be defined as the crack tip or crack line.

3.2.5 Direction of crack extension:

The crack extension direction must be specified after defining the crack. The crack extension can be defined either as a q-vector or as normal to the crack plane. The direction of the crack extension can be specified by only one-direction. The crack extension direction is the same for all nodes along the crack line.

3.2.6 Symmetry:

When defining the q-vector and the "edit crack" window that opens, there is an option to specify that the crack is on a symmetry plane. When "no symmetry" is chosen, that means no symmetry boundary conditions are applied where the crack is defined, allowing it to open.

3.2.7 Prescribing a singularity:

The strain and stress field can be defined at the crack tip. A singularity can be included in the geometry mesh. Midside nodes can be moved towards the crack tip and hexahedral elements can be collapsed to wedges with multiple nodes at each location at the crack tip. At the crack tip, the nodes at the same location can either be compelled to move together as a single node, or they pursue as duplicate similar nodes, as shown in Appendix H. The relationship between strain (ε) and distance to the singularity (r) depends on these settings. For linear elasticity, $\epsilon \propto 1/\sqrt{r}$.

3.2.8 Mesh:

Extra partitions are required around the crack tip to generate a circle around the crack tip. This partition is beneficial to calculate the contour integral for the layer of elements

around the crack tip. A hex-dominated swept mesh technique is allocated in the newly partitioned cell.

3.2.9 Mesh seeding:

A local refined mesh is generated by specifying the number of elements along the crack and along the circular edge. The number of elements has to be specified according to mesh convergence study.

3.2.10 Requesting output:

Output can be requested after defining the crack and creating refine mesh around the crack tip. History output for the crack can be requested by selecting the crack as domain. The contour numbers which are represented by the number of layers around the crack front for contour integrals are shown in Appendix H.

3.2.11 Defining the rest of the simulation:

Material properties, loads and boundary conditions have to be defined and applied depending on the interested geometry. In this study, linear elastic steel is used and the different plates with different crack geometries were modelled under different load and boundary conditions.

3.3 Methodology

3.3.1 Stress Intensity Factor for 2-Dimensional Plate with Notch

Finite element models have been used to calculate the SIF for a 2-dimensional (2-D) plate. The finite element simulation has been carried out for a plate with a semi-circular notch and crack to calculate the SIF and calculate the normalized SIF by using equation (3-1).

$$Y = \frac{K_I}{\sigma_o \sqrt{\pi a}}$$ **Equation 3-1**

Where:

K_I : Stress Intensity factor, σ : Applied stress (MPa), and a : Crack length (m)

The investigation has been carried out on a 2-D notched plate, with plate width and notch radius at 4cm and 0.5cm, respectively. The plate under tension stress is $1\times10^5 Pa$. The crack length varies from 0.25-2cm. The 2-D plate was partitioned to obtain a finer mesh at the crack zone, as shown in Figure 3-1. A standard element and plane stress family type have been used for modelling. Owing to symmetry, half of the cracked plate depicted in Figure 3-1, was modelled by applying adequate symmetry boundary conditions, as shown in Figure 3-2. In order to be less time-consuming, the complete model consisted of an intensely-meshed region near to the crack tip and coarsely-meshed part for the rest of the plate. The SCF was calculated using :

$$SCF = \frac{\sigma_{local}}{\sigma_{global}}$$ **Equation 3-2**

where, σ_(local) is the maximum stress around the hole, σ_global is the global stress applied on the geometry

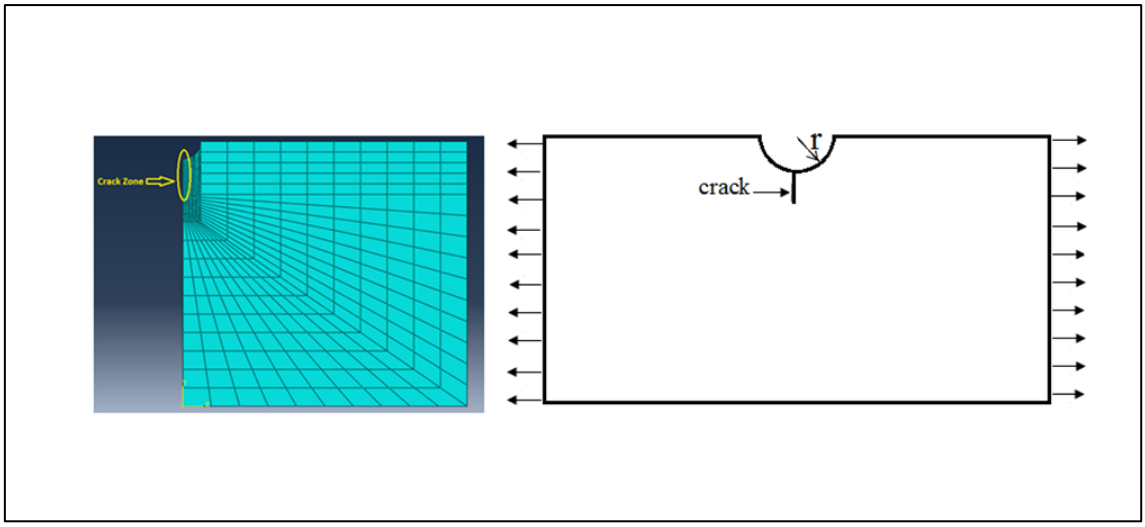

Figure 3-1: Global mesh for semi-infinite plate containing a semi-circular notch and crack

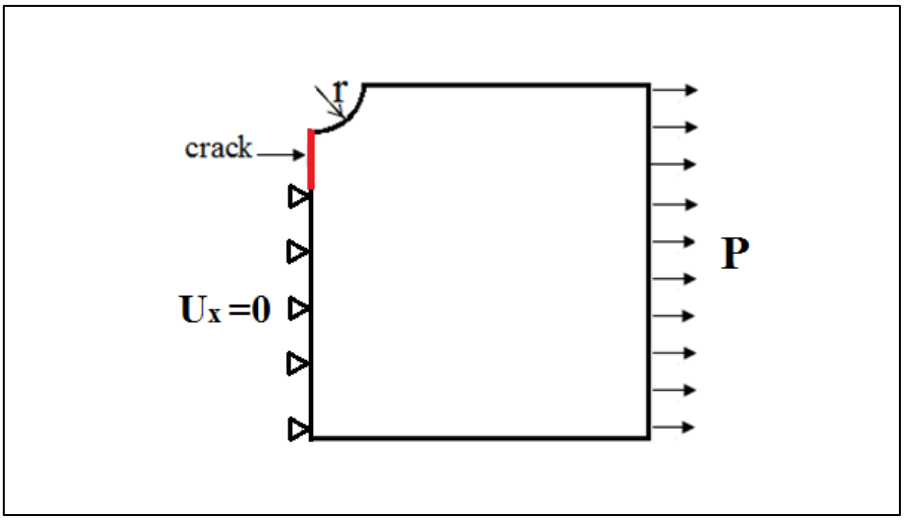

Figure 3-2: The boundary conditions of semi-infinite plate containing a semi-circular notch and crack

3.3.2 Semi-Elliptical Crack in a 3-Dimensional Surface Crack Tension Specimen

In order to validate the values of three dimensions of SIF, the effects of crack length on the magnitude of normalized SIF in a 3-D surface crack tension (SCT) specimen with semi-elliptical crack (see Figure 3-3) have been investigated in this work. The SCT specimen has been designed based on the ASTM-E740 [167] standard, as shown in Figure 3-4. The maximum width and length are 80mm and 320mm respectively, while the thickness and radius of curvature are 15mm and 40mm respectively. A full-scale model has been constructed with a semi-elliptical surface crack on the middle length of the specimen. The semi-elliptical crack has been implemented in the model with a/2c ratio equal (0.1), as shown in Figure 3-3. A structured mesh has been used; the mesh is more refined around the crack region to ensure reducing the time of simulation and mesh convergence for accurate results. A standard element type has also been used with a 3-D 8-node brick solid element C3D8R and three degrees of freedom per node (see Figure 3-5). The specimen under tension stress is $1\times10^{5}\,Pa$ as can be seen in Figure 3-6. Five different crack lengths were used in this study, which are 0.5, 1, 2, 3, 4mm. The result obtained has been compared with data from the literature (Newman & Raju) [166] and a good agreement has been found. The SIFs were calculated using the finite element model of a cracked geometry to calculate shape function by using Equation 3-1. The

result shows that there is a direct effect between crack length and normalized SIF due to a decrease in the cross-sectional area of the part and an increase in the magnitude of stress distribution at the crack tip.

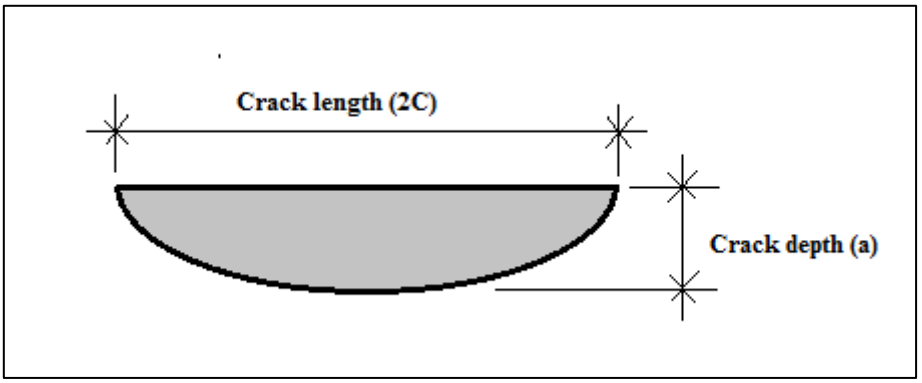

Figure 3-3: Geometry of semi-elliptical crack

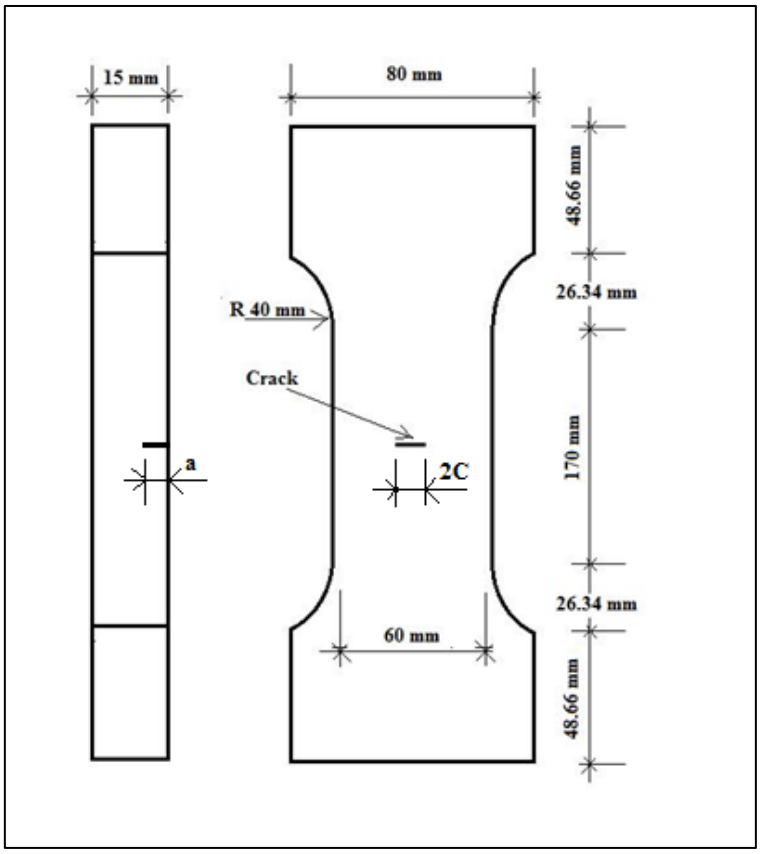

Figure 3-4: Surface crack tension specimen dimensions

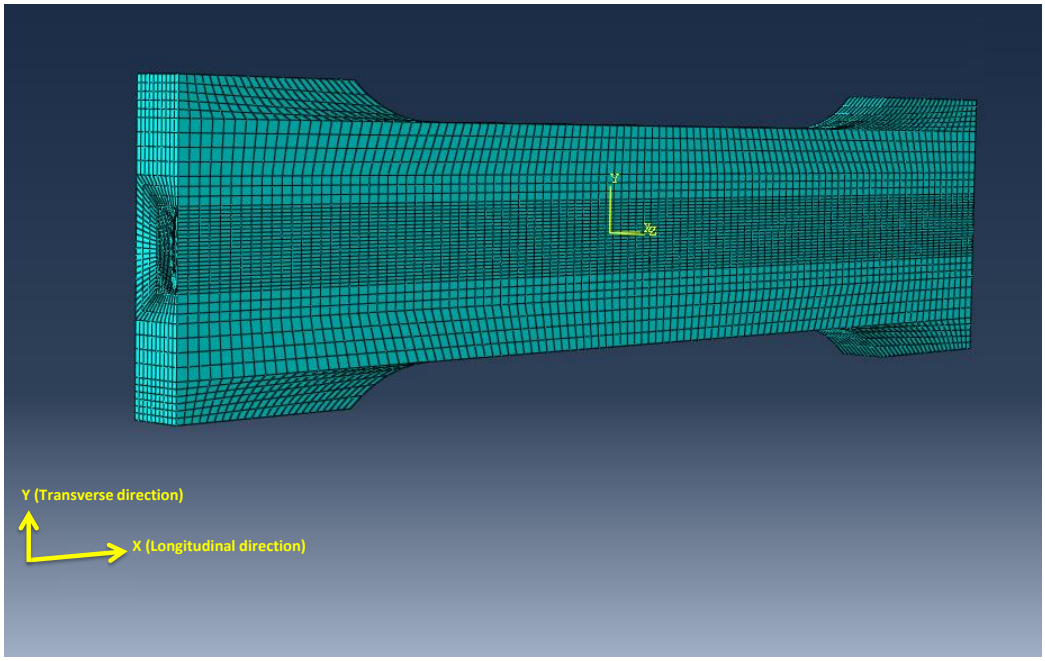

Figure 3-5: Structured mesh for surface crack specimen

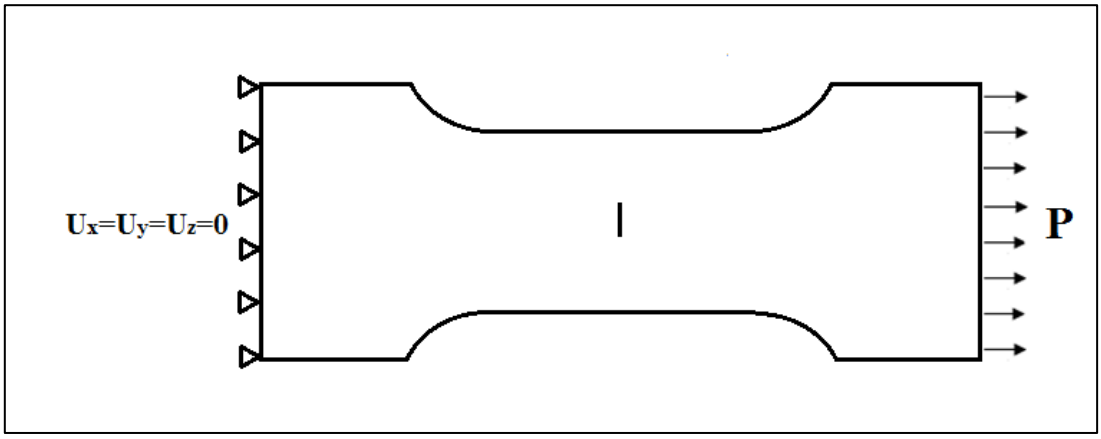

Figure 3-6: The boundary conditions of SCT containing a semi-elliptical crack

3.3.3 Shape function investigation for Four-point bending specimen

In order to calculate the shape function for the experimental work specimen, finite element simulations have been conducted. The shape function calculation is important for modifying the Newman & Raju model to calculate the SIF of experimental work. The effects of crack length on the magnitude of normalized SIF in a 3-D plate with a notch and semi-elliptical crack under a 4-point bending test have been investigated in this work. Also, a plate without a notch but with a semi-elliptical crack has been investigated. A finite element model of a cracked geometry was used for modelling

different crack depths of 0.5, 1, 2, 3, 4, 5mm, as can be seen in Figure 3-8. The plate with a semi-circular notch has been investigated, as shown in Figure 3-7. A full-scale model of the experimental specimen was constructed in the investigation with maximum width and length of 100mm and 330mm respectively, while the thickness and notch radius are 25mm and 5mm respectively. A full-scale model has been constructed with a semi-elliptical surface crack on the middle root channel of the specimen. The semi-elliptical crack has been implemented in the model with a/2c ratio equal (0.1). A structured mesh has been used, which is more refined around the crack region and the channel to ensure a reduced time of simulation and mesh convergence for accurate results. A mesh convergence has been conducted that resulted in each 1mm of crack front being discretized into seven solid elements. A standard element type has been used with a 3-D 8-node brick solid element C3D8R and three degrees of freedom per node Figure 3-9. The applied stress equal to 1MPa and boundary conditions are shown in Figure 3-10. The result obtained has been compared with data from the literature (Newman & Raju) [166] and good agreement has been found. For the plate with a notch, the notch radius was added to the crack length to calculate normalized SIF and, again, good agreement has been found.

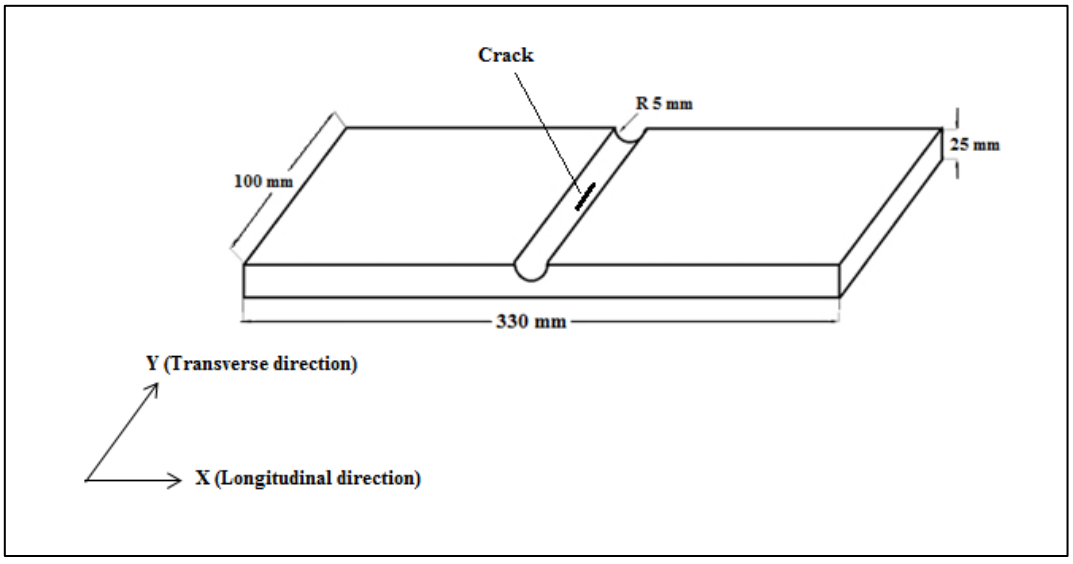

Figure 3-7: Geometry of Four-point bending specimen with semi-circular notch containing semi-elliptical notch

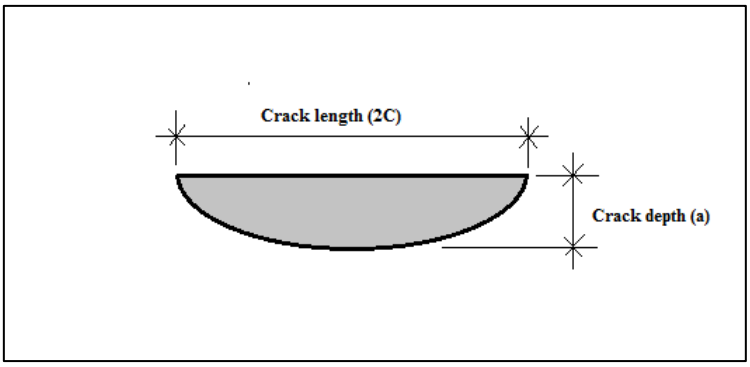

Figure 3-8: Geometry of crack implemented in 4-point bend specimens

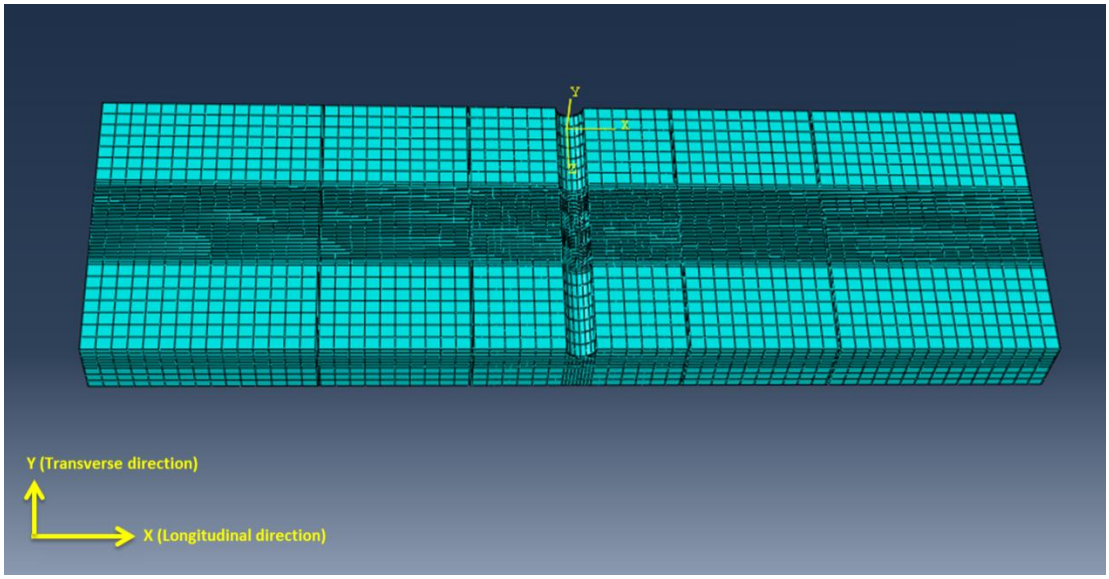

Figure 3-9: Structured mesh of 4-point bending specimen

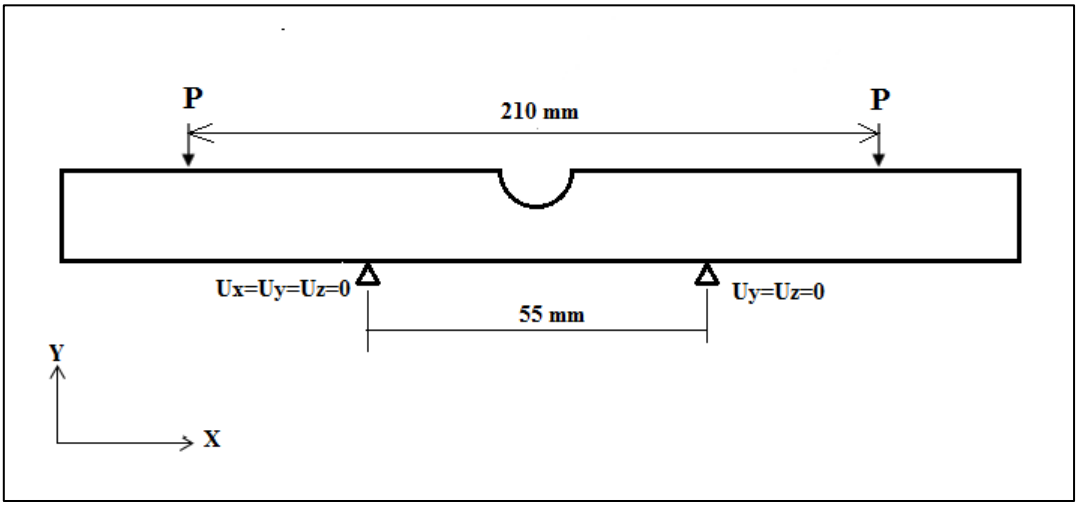

Figure 3-10: The boundary conditions of 4-point bend specimen

3.4 Results

3.4.1 Mesh Convergence

In order to obtain an accurate result for the finite element simulation, mesh convergence has been done. The modelling has been carried out for a 2-D notched plate width and notch radius which are 2.5cm and 0.5cm, respectively. The plate under tension stress is 1MPa, as shown in Figure 3-11. It can be observed that the optimum element number of modelling is around 8 elements/mm. The number of elements were calculated for the local area around the crack. So, in order to obtain an accurate result, the mesh should be around this number and reducing simulation time. The mesh convergence study was carried out by the following steps:

1. Create a mesh using a reasonable number of elements and calculate the SCF by using Equation 3-2 .
2. Recreate the mesh with a denser element distribution, re-calculate the SCF and compare the results to those of the previous mesh.
3. Increase the mesh density and re-calculate until the SCF result converges satisfactorily, as shown in Figure 3-11.

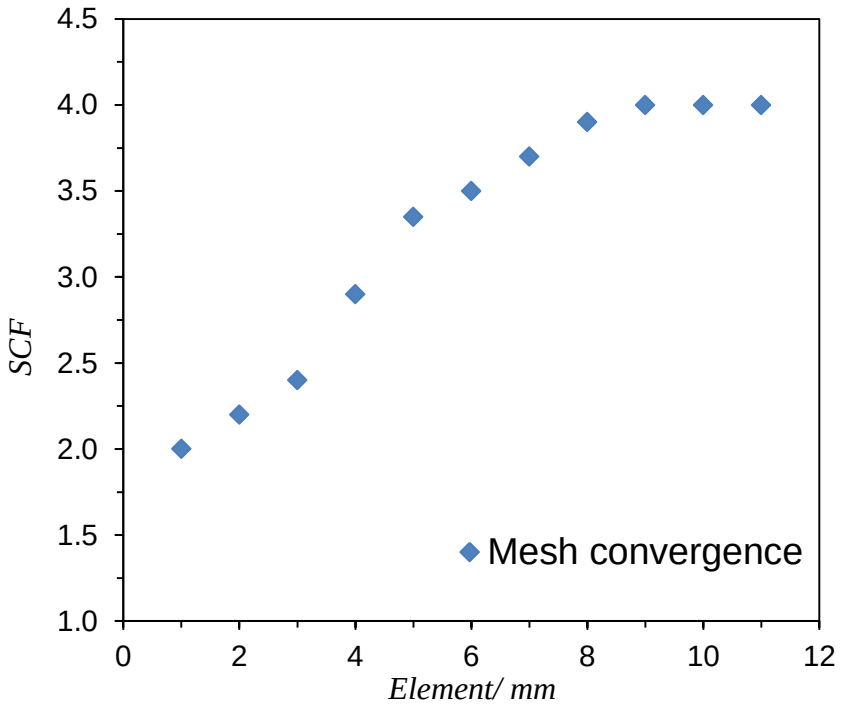

Figure 3-11: Mesh convergence for modelling

3.4.2 Width Convergence of 3-Dimensional Solid Plate

The width convergence of a 3-D solid plate with a U-notch in order to know the approximate width of an infinite plate width has been done. The width convergence is important for further simulation and to eliminate the effect of the specimen length from the simulation result. The geometry studied is a 3-D plate with a U-Notch, as shown in Figure 3-12. The plate length and thickness are equal to 6cm and 0.5cm, respectively. The plate width varies from 4cm to 13cm. Figure 3-13 shows the SCF with plate width. The boundary conditions used were similar to those for the 2-D plate with semi-circular notch as shown in Figure 3-2. It can be observed that the magnitude of the SCF becomes approximately constant at a plate width more than 6cm. So, it is essential to use a plate width in modelling that is more than 6cm wide in order to satisfy the condition of infinite plate width with a U-Notch.

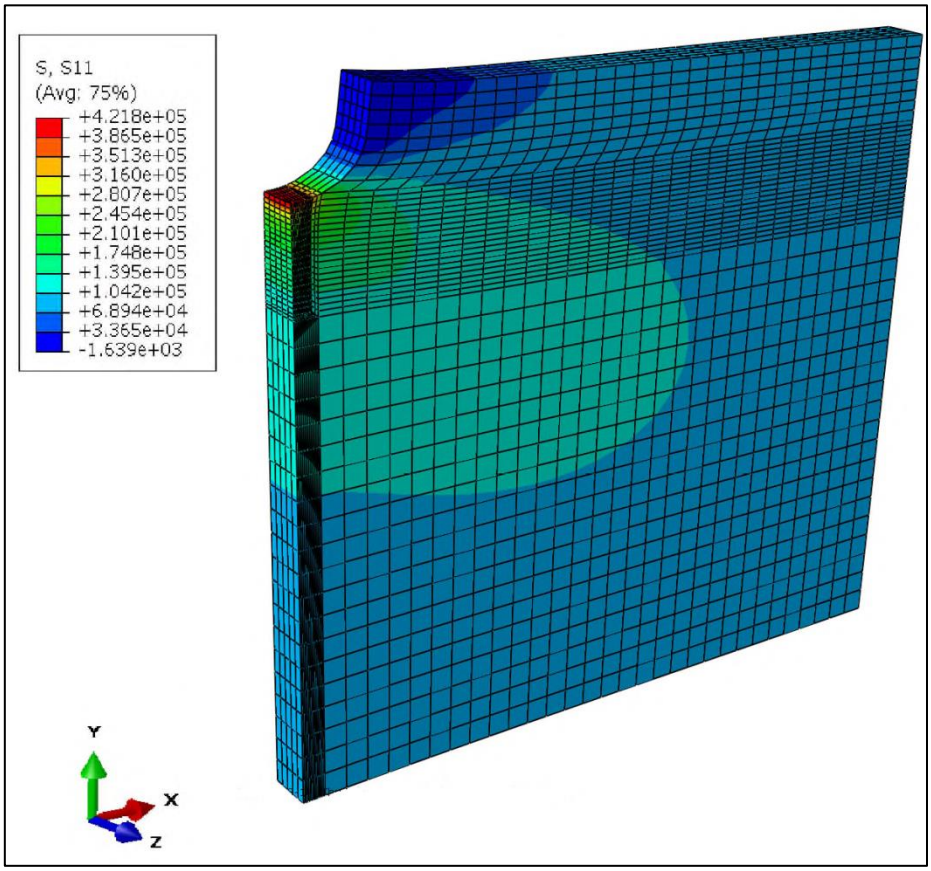

Figure 3-12: Three-Dimensional modelling of plate with U-Notch Stress

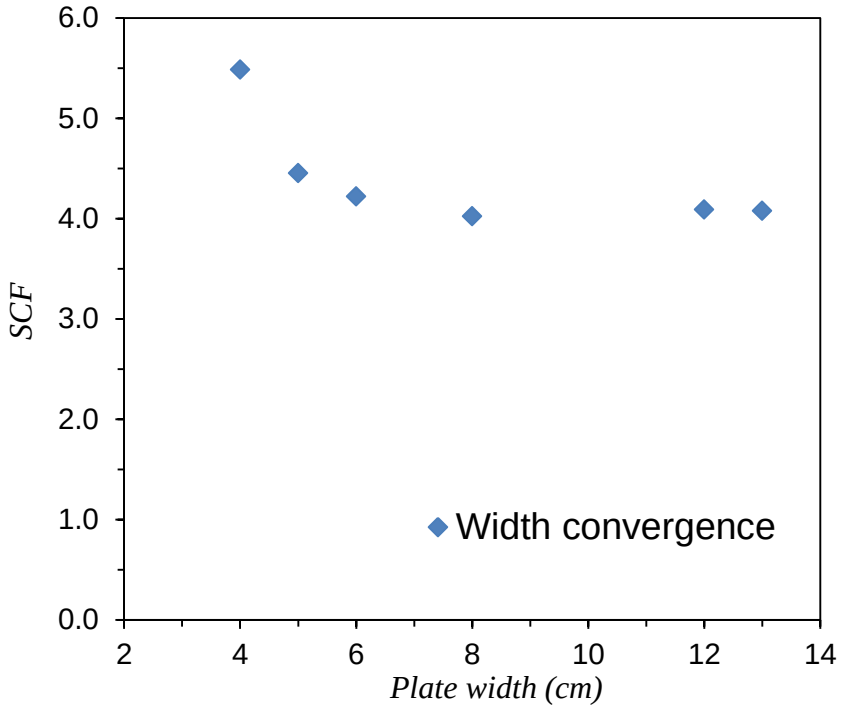

Figure 3-13: Width convergence for plate with a U-Notch

3.4.3 Intensity Factor for 2-Dimension Plate with Notch

Figure 3-14 shows the relationship between normalized SIF and normalized crack length for the 2-D notched plate. The normalized crack length was calculated by dividing the crack length (a) by notch radius (r). The effect of different crack lengths on the magnitude of normalized SIF in 2-D plate with semi-circular notch has been investigated by using finite element simulation. Five different crack lengths, which are 0.25, 0.5, 1, 1.5 and 2cm, semi-circular notch radius 0.5cm and plate width 4cm have been studied. The results obtained have been compared with data from the literature Teh [160] and an excellent agreement has been found. It can be observed that there is a direct effect between crack length and normalized SIF due to a decrease in the area of the cross section area of the part and an increase in the magnitude of the stress distribution at the crack tip. Figure 3-15 shows an example of a plate with crack modelling, where, S11 represents the crack opening stresses.

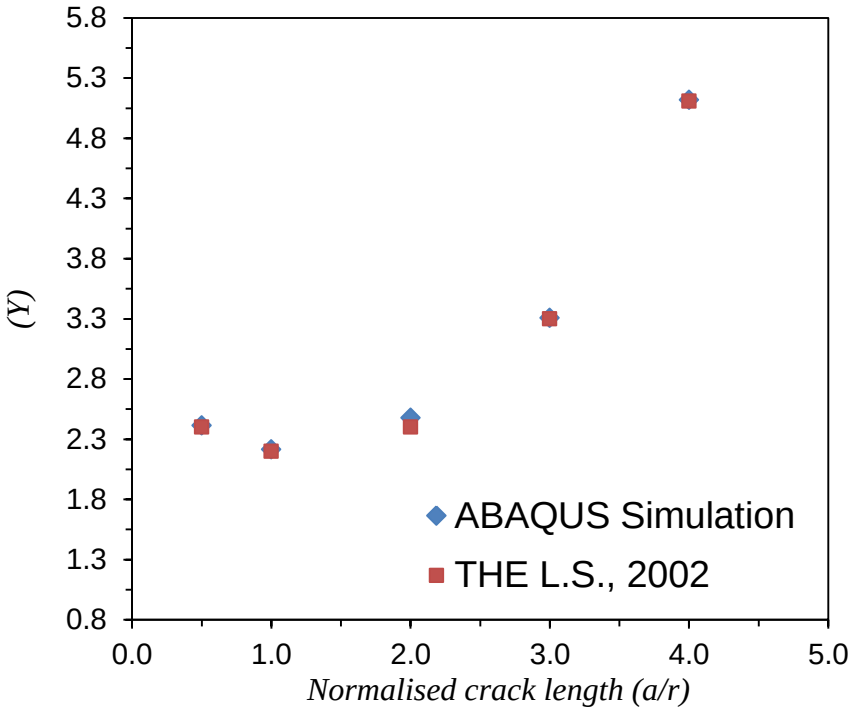

Figure 3-14: Normalized Stress Intensity Factor for a crack from a semi-circular notch in a plate under uniform tension

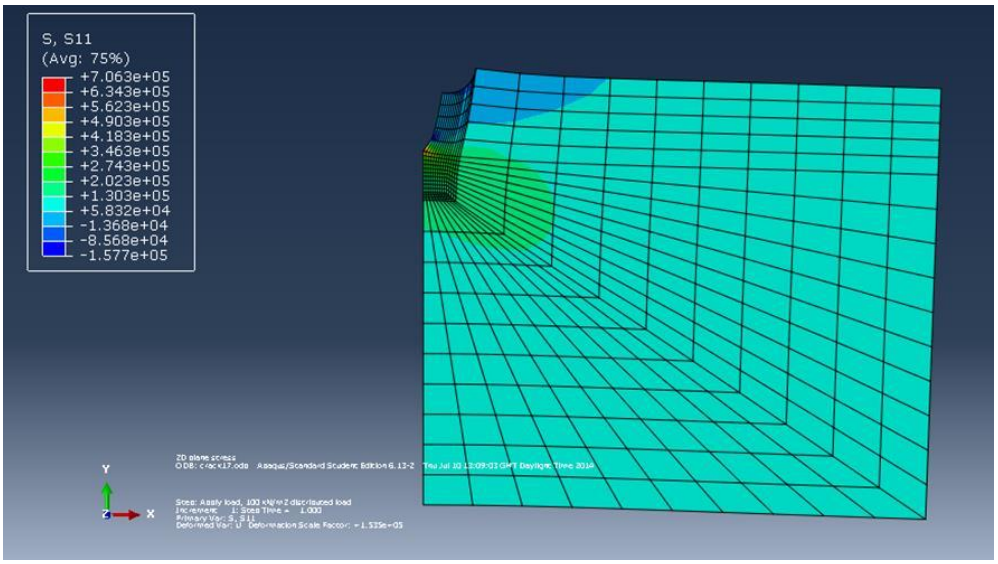

Figure 3-15: Example of finite element model for a plate containing a semi-circular notch and crack

3.4.4 Semi-Elliptical crack in 3-Dimensional SCT specimen

Figure 3-16 shows the relationship between normalized SIF and normalized crack length for the 3-D plate with a semi-elliptical crack. The normalized crack length was calculated by dividing the crack depth (a) by the thickness of the plate (t). The effect of different crack length (a) on the magnitude of normalized SIF in a 3-D plate with semi-elliptical crack has been investigated. Six different crack lengths, which are 0.1, 0.2, 0.25, 0.3, 0.4 and 0.5cm, plate thickness 0.1cm and plate width 4cm, have been studied. The results obtained have been compared with data from the literature [166] and a good agreement has been found. It can be observed that there is a direct effect between crack length and normalized SIF due to a decrease in the area of the cross section area of the part and an increased magnitude of stress distribution at the crack tip. Figure 3-17 shows an example of a finite element model for a 3-D plate containing a semi-elliptical surface crack.

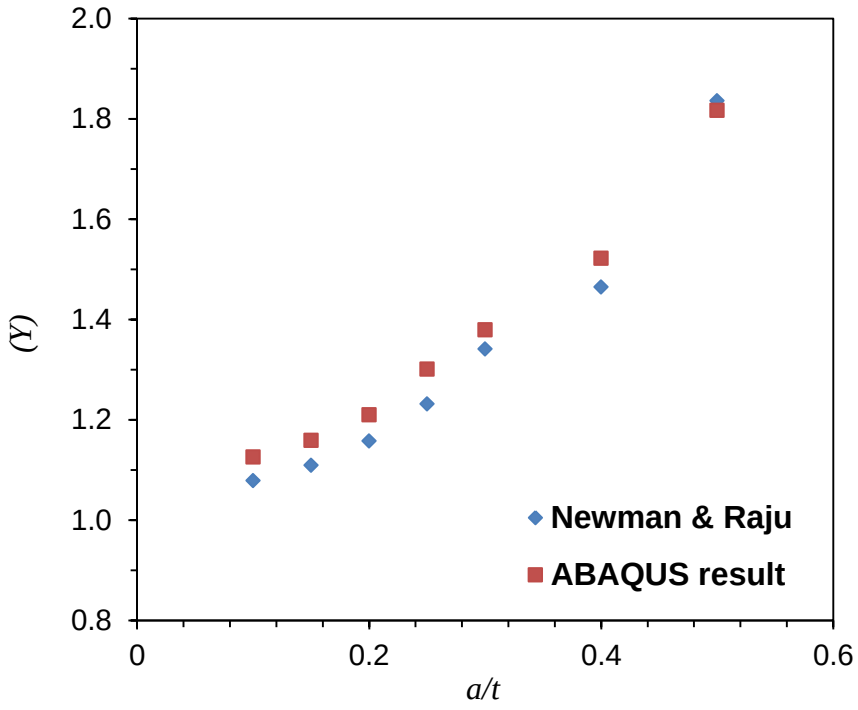

Figure 3-16: Normalized stress intensity factor for a plate with a semi-elliptical surface crack

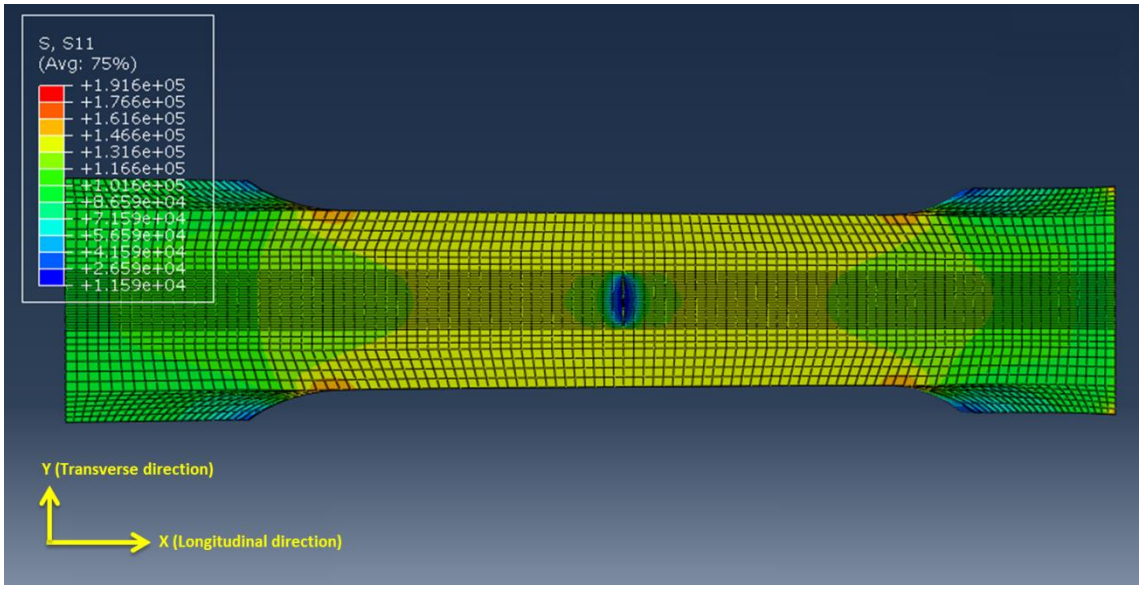

Figure 3-17: Example of a finite element model for a 3-D plate containing a semi-elliptical surface crack

3.4.5 Numerical prediction of the stress concentration factor for a dog-bone specimen

The SCF solutions for the geometry used in this study are not available in the literature. Therefore a finite element model was developed to work out the SCF solutions for the specimen design employed in the experimental study of this project. The SCF solutions are important to calculate the applied load and avoid the plasticity at the crack tip in the experimental investigation of this study. A full-scale model of the dog-bone shaped specimen geometry was constructed in the finite element simulation (see Figure 3-18) with the notch on the middle length of the specimen to calculate the SCF. The geometry was partitioned to obtain a finer mesh at the crack zone, as shown in Figure 3-18. A structured mesh was used in simulations and the mesh was coarsened away from the notch tip region to reduce the computational power in finite element simulations [169]. The mesh structure employed in finite element simulations is shown in Figure 3-19. A standard element type has been used with a 3-D 8-node brick solid element, C3D8. The boundary conditions were applied similarly to the boundary conditions of the validated result from the SCT specimen, as shown in Figure 3-6. Eight different central hole diameter sizes, D, were examined in simulations to investigate the effect of hole

diameter on dog-bone specimen SCF values. The local and global stresses for each hole diameter case were predicted using finite element simulations. The SCF was subsequently calculated using Equation 3-3.

$$SCF = \frac{\sigma_{local}}{\sigma_{global}} \qquad \textbf{Equation 3-3}$$

where, σ_(local) is the maximum stress around the hole, σ_global is the global stress applied on the geometry. The SCF values obtained from finite element simulations are plotted against D the hole diameter normalized by W, and the specimen width, D/W, and the results are shown in Figure 3-13. A second degree polynomial fit was made to develop a general solution for SCF as a function of D/W. The equation of the line of best fit made according to the numerical data points is described in Equation 3-3. As seen in this equation, the SCF for the specimen geometry used in this study with a D/W of 0.083 (see Figure 3-20) is 3.8.

$$SCF = 0.1423(\frac{D}{W})^2 + 2.6346(\frac{D}{W}) + 3.5702 \qquad \textbf{Equation 3-4}$$

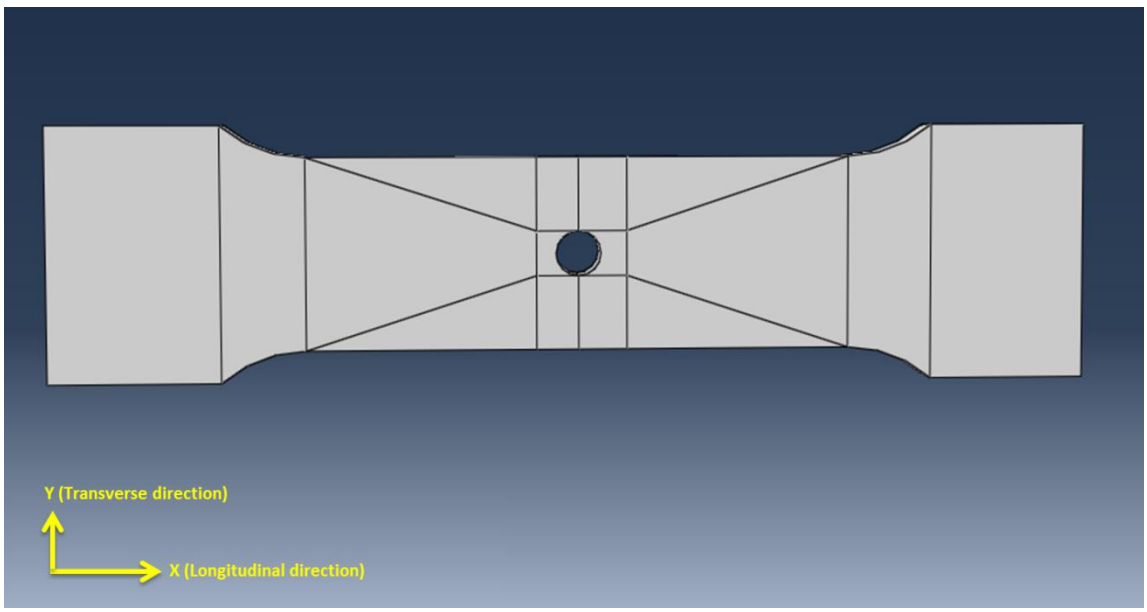

Figure 3-18: Dog-bone specimen partitions

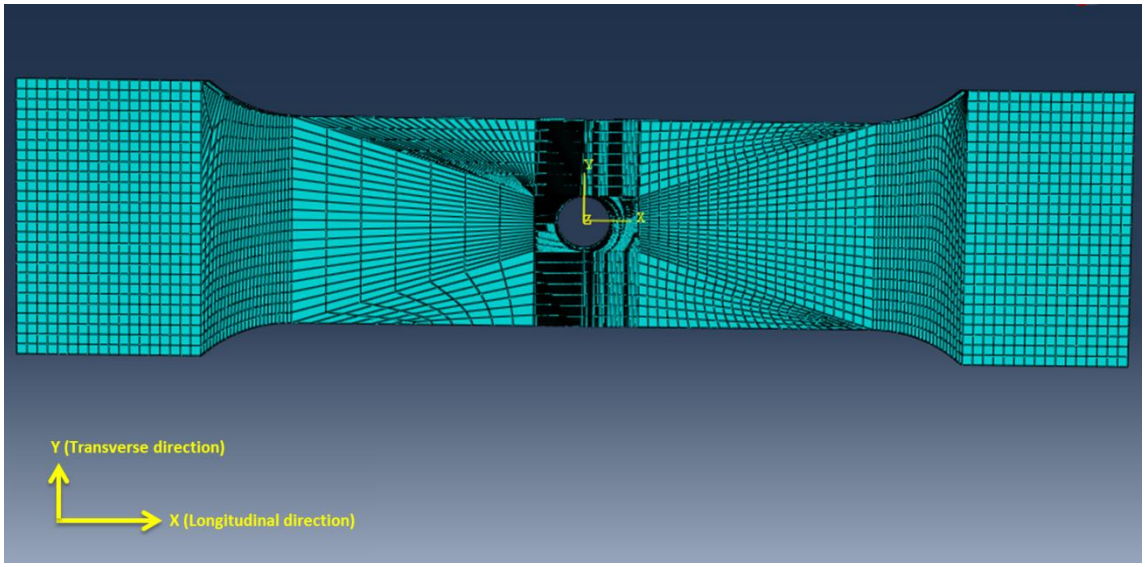

Figure 3-19: The mesh in the finite element simulations for the dog-bone specimen

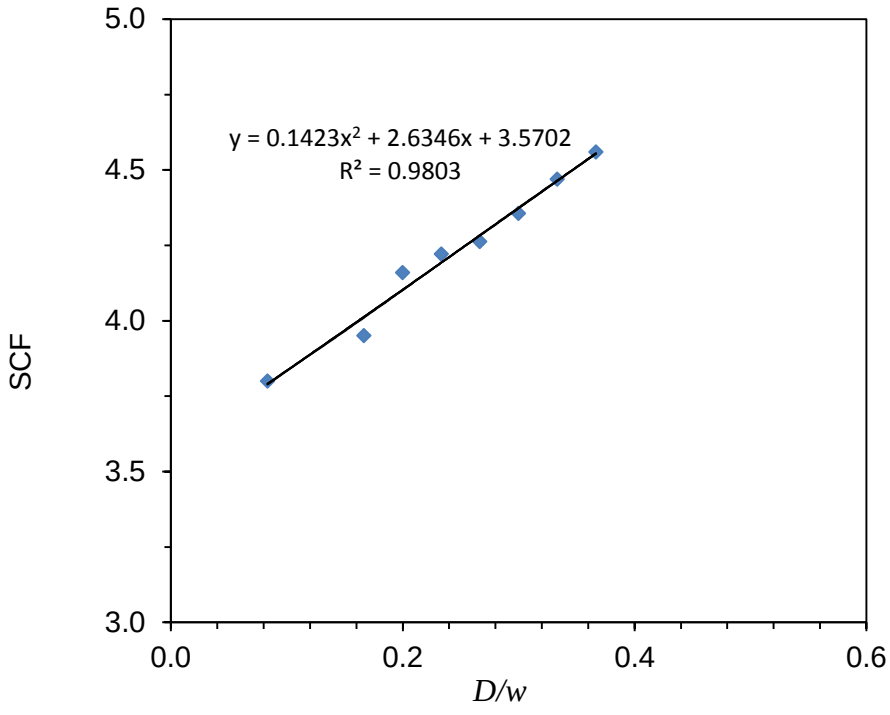

Figure 3-20: Stress concentration factor variation against the normalized hole diameter for the dog-bone specimen

3.4.6 Four-point bending load for the specimen

Figure 3-21 shows the relationship between normalized SIF and normalized crack length for a plate with a semi-circular notch and a plate without a notch under a Four-point bending test. A finite element model of a cracked geometry was used to study the effect of different semi-elliptical crack depths (a) on the magnitude of normalized SIF in a plate with and without a notch. For different crack lengths, which are 1, 2, 3, 4, 5 and 6mm, semi-circular notch radius and semi-elliptical crack length ratio $(a/2c)$ are 5mm and 0.1 , respectively, have been studied. The semi-circular notch radius was added to SIF results obtained from finite element simulations, and the results compared with Newman & Raju [166] and a good agreement has been found. It can be observed that the normalized SIF depends on an equivalent depth of crack. The equivalent depth of crack equals the total depth of the crack from the surface to the crack tip. In the present study, the radius of the semi-circular notch to the crack depth has been added. Also, it can be observed that a normalized SIF trend decreases with increased normalized crack depth (a/t) due to the contact of the crack faces. The contact of crack faces will generate additional loads along the crack line, which leads to a change in the displacement and stress field at the crack tip and reduces SIF [170].

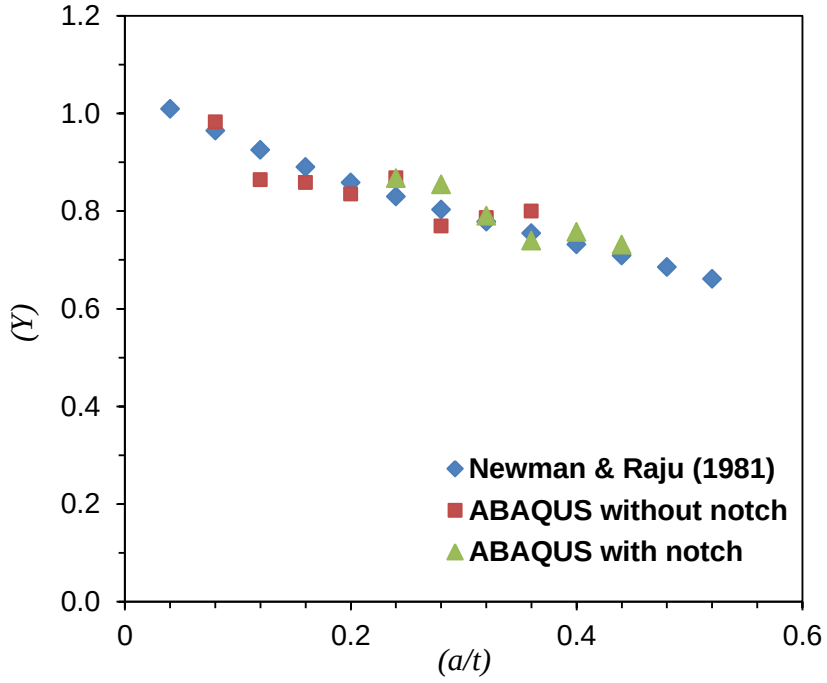

Figure 3-21: Non-dimensional stress intensity factor for plates under 4-Point bending test

3.5 Summary

The SCF solutions for dog-bone specimens and SIF solutions for plate containing a semi-circular notch with semi-elliptical crack are not available in the literature. The available solution for SIF is an empirical equation generated by Newman & Raju [166] obtained from a 3-D, finite element analysis of semi-elliptical surface cracks in finite elastic plate subjected to pure bending or tension loads. The finite element analysis software (ABAQUS) has been used to predict SCF solutions for dog-bone specimens and to shape function (Y) solutions for plate with semi-circular notch which contains semi-elliptical cracks such as those that were used in the experimental work. The mesh convergence and width study to calculate the SCF has been done to reduce the simulation time and improve the accuracy of finite element simulation. It has been found from the mesh convergence results that the optimum mesh size is 8 elements per mm. In order to ensure the finite element simulation results are reliable and validated, different engineering components were modelled and validated with available data from the literature. The findings from the simulation results are summarized as follows:

1. The general equation of an SCF solution for dog-bone specimens was obtained. The SCFs are important to calculate the experimental applied load and avoid the plasticity at the crack tip.
2. The shape function (Y) of plate with a semi-circular notch containing semi-elliptical cracks was calculated to develop Newman & Raju model and calculate the SIF for the specimen of experimental study. The shape function was calculated by using effective crack length. The effective crack lengths have been found by adding the semi-circular notch to the crack depth.

4 RESIDUAL STRESS MEASUREMENT IN PEENED SPECIMENS

4.1 Introduction

To study the effect of partial surface treatment on FCG, the residual stress map must be known. In order to gain a better understanding of the residual stresses present in partially peened specimens made of HSS, residual stress investigations were carried out. Originally, one of main objectives was to evaluate residual stress variation in the peened area. The investigation involved the measurement of the induced stresses and sought to visualize the stress field pattern and behaviour through-thickness across the specimen surface. This chapter presents a study carried out by the ICHD method to evaluate residual stress variation on partially peened specimens. For the incremental centre hole drilling (ICHD), residual stress evaluation was performed using an inverse solution known as the integral method. ICHD is suitable for near surface measurements of in-plane stress profiles, compared to other measurement techniques, but has limitations with sensitivity to noisy data and a maximum stress measurement equal to 70% of the yield stress of material, as shown in Chapter 2. ICHD gives rapid and reliable results with different type of specimens, and introduces often tolerable and localized damage. The measurement method can identify the through-depth profile of the in-plane residual stress to a depth approximately equal to 1mm [45]. In this chapter, the residual stresses distributions in partially peened specimens by i) cavitation shotless peening and ii) shot peening are measured. The specimens were designed to study the influence of partial peening area on FCGR, as it is important to identify the nature of residual stress distribution in and around the peening area, such as compressive or tensile. It is also important to identify the depth of compressive residual stress induced by cavitation shotless peening and shot peening in high strength material that has a yield stress higher than conventional steel and then compare their residual stress profiles.

4.2 The Residual Stress Measurement

In general, stress measurement typically is done by interpreting the strain or displacement measurement. The measurement depends on the evaluation of stress differences in the presence and absence of external loads. There are many challenges from residual stress measurement due to the built-in characteristics of these stresses, despite the measurement technique, because they cannot easily be applied or removed. The residual stress measurement is less precise than load induced stress measurement due to built-in and self-equilibrating characteristics. Some measurements required to remove or cut some stressed material can be inaccurate residual stress measurement. There are many other methods that depend on using another technique to measure residual stress without removing or cutting stressed material, such as acoustic wave, magnetic field, thermal energy, etc. These methods have many challenges when interpreting the proxy measurement as stress data due to the interpreting data requiring some of material details and extensive calibration [45] [171]. In this study, the ICHD technique has been chosen to measure the residual stress distribution, the latter having been investigated in four-point bending and dog-bone tension specimens.

4.3 Hole Drilling Technique

The ICHD method is a semi-destructive technique which involves some damage to the part but can be repairable or tolerable. The method involves drilling a small hole in the required area to calculate residual stress. The drilled hole causes a redistribution of built-in stresses in the remaining material, which creates localized displacement. The strain gauges have the ability to measure the surface deformations due to HD. A commercial ICHD strain gauge has been manufactured to ensure accurate orientation on the workpiece for reducing error and enhancing the quality of the measured data. The ICHD test has been standardized for a clear procedure for stress calculation. ASTM E837 contains the procedure to conduct residual stress measurement as well as three different strain types covering a range of measurement needs [172].

There are two different methods employed to calculate residual stresses in specimens, depending on the thickness of the specimen as well as the kind of residual stresses. A

through-HD method is used for thin specimens and uniform residual stresses. For thick specimens and non-uniform residual stresses, an incremental (blind) HD is usually used [172, 173].

In this study, the ICHD has been used to investigate the residual stress distribution in the test specimens which have been treated by cavitation shotless peening and shot peening. The investigation is important in order to know the magnitude and direction of residual stresses both in the peening area and the surrounding area for further study of the specimens under fatigue tests.

4.3.1 Methodology

The HD technique has been used to investigate the residual stress distribution in the test specimens. The ICHD method has been employed to calculate residual stresses by following the procedure provided in the ASTM E837 standard. The specimen is considered to be a thick specimen due to the specimen thickness being much bigger than the ICHD depth. The specimen thickness is 25mm and the ICHD depth is 1mm.

4.3.1.1 Surface Preparation

Surface smoothness is important for strain gauge application as confirm by the adhesive manufacturer used for strain gauge bonding. Mechanical abrasion should be avoided in the surface preparation due to the sensitivity of residual stresses to mechanical processes. Chemical etching has been done prior to attaching the strain gauge. In the present study, the following procedure has been followed according to the strain gauge manufacturer [174].

1. Clean the surface by using a degreaser and dry it manually. Sandpaper has been used for surface smoothing. The desirable surface smoothness has been achieved by using 320 and 220 grit sandpaper and by repeating the process horizontally and vertically.
2. Clean the surface by using conditioner and neutralizer which are provided by the strain gauge manufacturer, as shown in Figure 4-1.

Figure 4-1: The sand grit with neutralizer

4.3.1.2 Strain gauge selection

A rosette gauge contains three single or pairs of strain gauge grids to be used. The strain gauge selection depends on the place and application required to investigate the residual stress within it. For simple residual stress calculation, a standardized rosette gauge has been designed. There are three different rosette HD geometries, A, B and C, depending on the arrangement of the strain gauge, as shown in Figure 4-2. In the present study, due to using a flat plate, there is easy access to the required residual surface and enough distance from the specimen edge to give flexibility to the strain gauge choice. A rosette strain gauge type (A) $CEA-XX-062UL-120$ with a gauge diameter of 5.13mm has been chosen, which contains three single strain gauges in three different directions, namely longitudinal, transverse and shear directions. The strain gauges have been attached in the desired location, soldered and connected to a strain recorder.

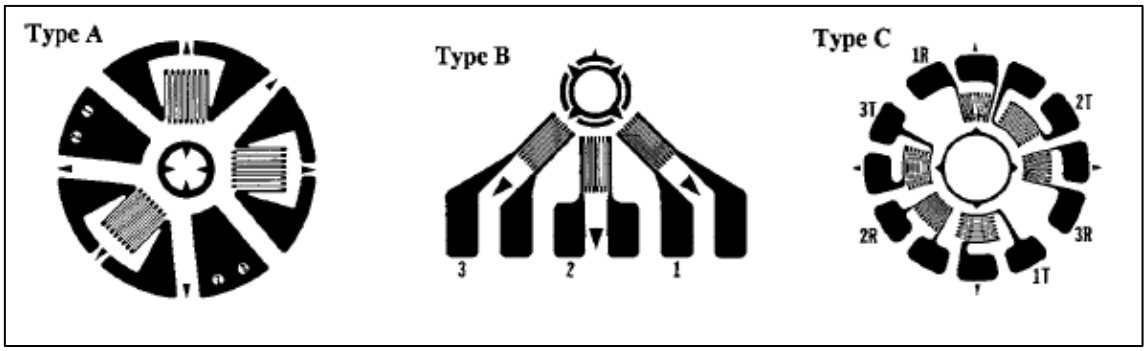

Figure 4-2: Rosette strain gauge types [172]

4.3.1.3 Installation of the strain gauge

The strain gauge installation is important for residual stress measurement. A good installation process ensures a good bonding between the strain gauge and workpiece, which provides a good transfer of surface deformation by shear loading to the resistance grid. In this study, a specific adhesive provided by the strain gauge manufacturer Vishay, [174] is used for the strain gauge bonding.

4.3.1.4 Strain gauge wiring

The wiring process has been straightforward without a protection layer due to the short time of the ICHD process. A three-wire arrangement has been used to reduce the effect of leadwire temperature change. The temperature change affects the stability of the strain readings and the wire length affects the strain gauge measurement due to the wire resistance, as shown in Figure 4-3.

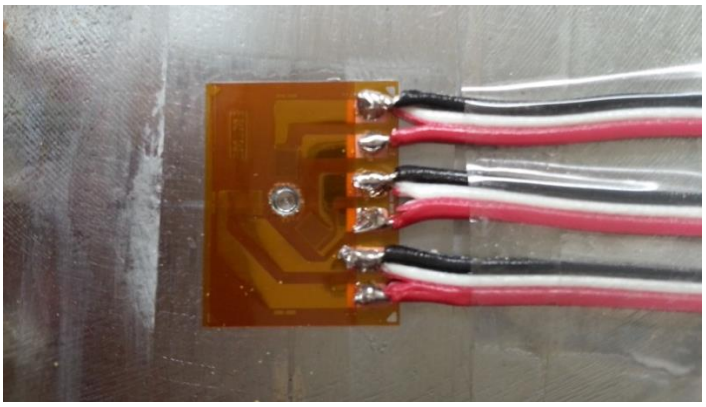

Figure 4-3: Strain gauge wiring

4.3.1.5 Data acquisition or strain recorder

The HD process causes small changes in the strain gauge measurement at every step. The strain recorder has to be stable, accurate and have a high resolution to obtain accurate and smooth results of residual stress. The ICHD instrumentation has to be calibrated by following the guidelines of the strain gauge manufacturer, as shown in Table 4-1. In this study, an electronic recorder strain gauge has been used, as shown in Figure 4-4 .

Table 4-1: Rosette Gauge Factors type (A)

Channel	Strain gauge factor at 24°
1	$2.105 \pm 0.5\%$
2	$2.070 \pm 0.5\%$
3	$2.115 \pm 0.5\%$

4.3.1.6 Drill Cutter Selection

In this study, a tungsten carbide cutter has been used. The cutter diameter has been selected depending on the nominal hole diameter of rosette type (A) which is used in this experiment. The cutter diameter has to be slightly smaller than the required hole diameter because of the clearances required and the vibration. The cutter diameter is 1.6mm. The cutter has an inverted cone shape with a 5^{o} relief on each side for chip removal and to avoid any rubbing between the cutter and workpiece.

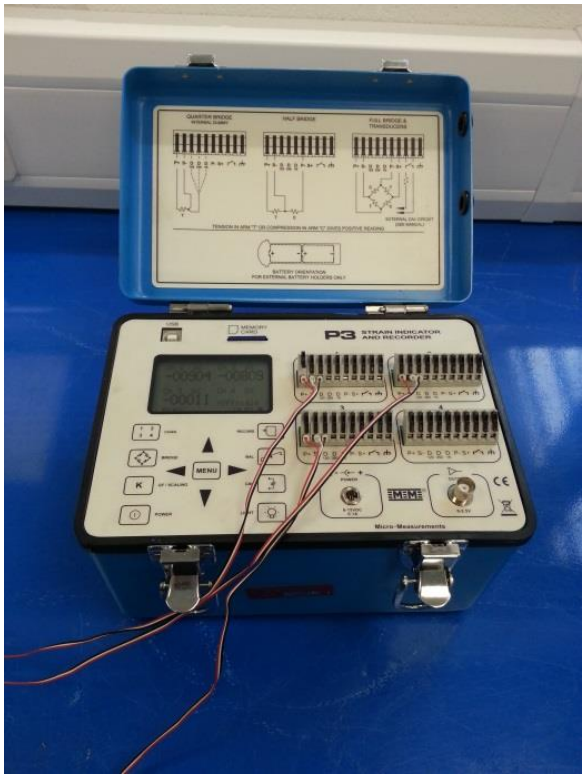

Figure 4-4: Strain gauge recorder

4.3.1.7 Drilling Machines

The HD process is a very sensitive and accurate process which includes drilling a hole in the workpiece through the centre of the strain gauge rosette. The ICHD machine has features involving the cutter holder, position adjustment system for alignment, drill depth and feed control. In this study, a commercial drilling machine has been used which is the Micro – measurements RS – 200 (Vishay Precision Group), as shown in Figure 4-5. The machine has an air turbine drilling motor and micrometer head to control the drill depth manually. The machine uses an optical head for drill alignment and measuring the drilled hole diameter. The machine has three pads for mounting on the workpiece by using cement.

The total depth of ICHD has to be divided into sub-increments in each step. The number of sub-increments depends on the type of strain gauge rosette. In this study, the strain gauge rosette type (A) has been used, so the total depth of ICHD is 1mm divided into 20 steps according to Standard E837-08.

Figure 4-5: The hole drilling machine Micro-measurements RS-200 (Vishay Precision Group)

4.3.1.8 Residual stress calculation

In general, the residual stresses are changing with the depth from the material surface. This characteristic creates a big challenge to the calculation of residual stress due to the deformation of the surface depending on the combination of the stresses through the depth of the material not only having a single uniform stress. For instance, the isotropic stresses and strains:

$$p(h) = \frac{1+\upsilon}{E}\int_0^h \bar{a}(H,h)P(H)dH$$ **Equation 4-1**

Where p(h) is an isotropic strain combination which is relieved when the hole reaches a depth (h), and can be found as follows:

$$p_j = (\varepsilon_3 + \varepsilon_1)_j / 2$$ **Equation 4-2**

$$q_j = (\varepsilon_3 - \varepsilon_1)_j / 2$$ **Equation 4-3**

$$p_j = (\varepsilon_3 + \varepsilon_1 - 2\varepsilon_2)_j / 2$$ **Equation 4-4**

While, p(h), which is the isotropic stress combination that exists at depth h from the measured surface can be calculated as follows:

$$P = \frac{\sigma_y + \sigma_x}{2}$$ **Equation 4-5**

$$Q = \frac{\sigma_y - \sigma_x}{2}$$ **Equation 4-6**

$$T = \tau_{xy}$$ **Equation 4-7**

and the $\bar{a}(H,h)$ is a generalization of the uniform stress calibration constant $\bar{a}(h)$ which can be defined as follows:

$$P = \frac{E}{(1+\upsilon)\bar{a}}p$$ **Equation 4-8**

$$Q = \frac{E}{\bar{b}}q$$ **Equation 4-9**

$$T = \frac{E}{\bar{b}}t$$ **Equation 4-10**

From Equation 4-2 to Equation 4-10, it can be observed that equations are dependent on $\bar{a}, \bar{b}$ and the associated strain quantity.

The form of Equation 4-1 is known mathematically as the Volterra equation of the first kind. It defines an "inverse problem" due to the stress to be determined occurring within the integral on the right side, rather than on the left. The solution can be calculated by using the "inverse method" which is suitable for this equation. The computational method is called the "integral" or "unit pulse" method, which is a generalization of

Equation 4-8, Equation 4-9 and Equation 4-10. The associated measurement method contains HD in a sequence of incremental depth, associated with strain measurements for each increment. According to ASTM E837-08, the total measurement depth is equal to 0.2D and is divided into 20 steps. The inner stresses are supposed to be locally constant at each incremental step and give the stress magnitude at each level of the step as shown in Figure 4-6. In this method, the P, Q and T become vector quantities P_j , Q_j and T_j, where j=1, n which is an index for the n represents the depth in each increment, while the strain values p, q are similar to stresses values and become p, q and t where i= 1, n.

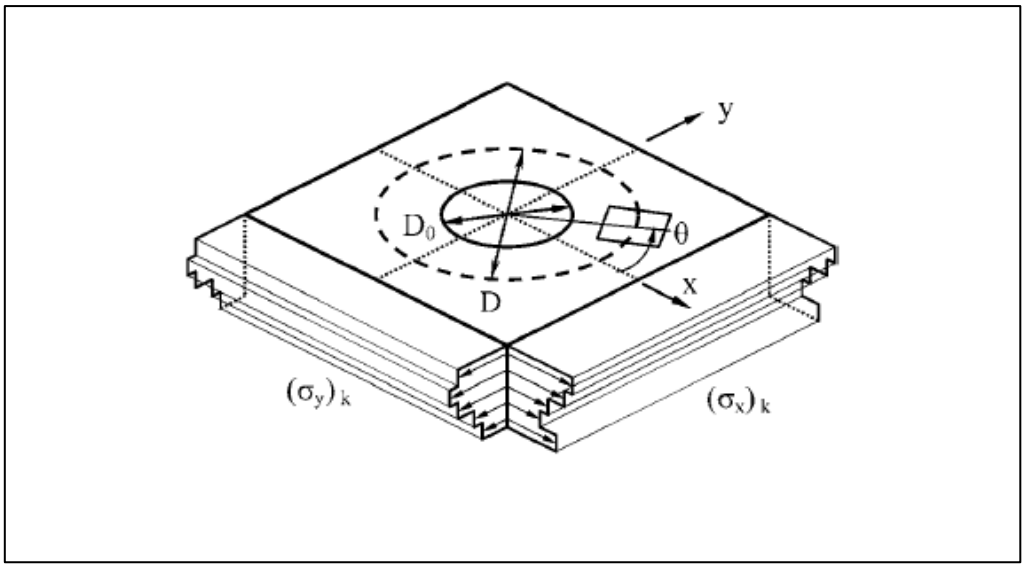

Figure 4-6: Residual stress variation with depth used by the Integral Method [172]

In the analogous method, the calibration constants $\bar{a}$ and $\bar{b}$ become matrix quantities $\bar{a}_{ij}$ and $\bar{b}_{ij}$ whose elements relate the stresses value within depth increment j to the strains measured with a hole i depth of increments

$$\bar{a}_{ij} = \int_{h_{j-1}}^{h_j} \bar{a}(H, h_i) dH$$

$$\bar{b}_{ij} = \int_{h_{j-1}}^{h_j} \bar{b}(H, h_i) dH$$

The physical interpretation of matrix $\bar{a}$ is shown in Figure 4-7. The quantity $\bar{a}_{43}$ represents the strain caused by a unit stress within increment three of a hole four increments deep. The matrix is lower triangular because the stress that exists within the hole contributes constants that can be found using finite element calculations. According to this generalization, Equation 4-5, Equation 4-6 and Equation 4-7 become:

$$\bar{a}P = \frac{E}{1+\upsilon}p \qquad \textbf{Equation 4-11}$$

$$\bar{b}Q = Eq \qquad \textbf{Equation 4-12}$$

$$\bar{b} = Et \qquad \textbf{Equation 4-13}$$

For example $n = 3$, so the equation can be written as

$$\begin{bmatrix} \bar{a}_{11} & & \\ \bar{a}_{12} & \bar{a}_{22} & \\ \bar{a}_{13} & \bar{a}_{23} & \bar{a}_{33} \end{bmatrix} \begin{bmatrix} P_1 \\ P_2 \\ P_3 \end{bmatrix} = \frac{E}{1+\upsilon} \begin{bmatrix} p_1 \\ p_1 \\ p_1 \end{bmatrix}$$

The depth of residual stress in the material is dependent on physical limitations. These physical limitations are described by Saint-Venant's Principle, which are that the stresses away from the measured surface have less effect on the measurement. This influence can be imagined in Figure 4-7 which the matrix elements are expected to be small in size as they represent the strains generated by stresses located next to the bottom of the hole. Due to the material at the bottom of the hole supporting those stresses this leads to minimizing their effect on the surface. When the hole depth increases, this effect becomes greater and gives ever smaller diagonal elements in the matrix. When the diagonal elements reach zero this leads the matrix to become singular and no stress rising is possible. Experimentally, the residual stresses can measured up to 0.2D.

Due to the measurement quality having priority, some mathematical methods can be used to improve the influences of the remaining experimental failure. One of these approaches is to take small measurements with very small hole increments and this leads to increasing the quantity of data for calculations. This approach leads to the creation of a large fluctuation in the stress calculations because stress calculations

depend on the difference in strains measurements. In this case, the strains measurements are very small and lead to large errors; to overcome this problem is to use the best-fit of data by using smoothed approximations of the strains data. The effective method to do best-fit is to use the "Tikhonov regularization". The method includes a little modification to Equation 4-11, Equation 4-12 and Equation 4-13 to reduce the noisy component of the stress calculation:

$$(\bar{a}^{T}\bar{a}+\alpha pC^{T}c)P=\frac{E}{1+\upsilon}\bar{a}^{T}p \qquad \text{Equation 4-14}$$

Where the matrix c contains the second-derivative operator, such as n=4:

$$C=\begin{bmatrix} 0 & 0 & & \\ -1 & 2 & -1 & \\ & -1 & 2 & -1 \\ & & 0 & 0 \end{bmatrix}$$

The matrix contains the sequence of numbers [-1 2 -1] in each row, at the centre of the main diagonal, except the first and the last rows. α represents the regularization parameter which controls the regularization's parameter. A small value of α represents too much noise and insufficient smoothing of the stress values, while a large value of α represents excessive smoothing and removes the local details. An optimal value of α has to be used to remove measurement noise and keeping the spatial details of stress calculation. The optimal regularization occurs then the misfit, such as:

$$p_{misfit}=p-\frac{1+\upsilon}{E}\bar{a}P \qquad \text{Equation 4-15}$$

The Tikhonov regularization and Integral method are working well in practice for large quantitities of measured data. The smoothing trends of strains data can lead to easily identifying the wrong measurement. The MATLAB code was programmed to compute the residual stresses, as shown in Appendix B.

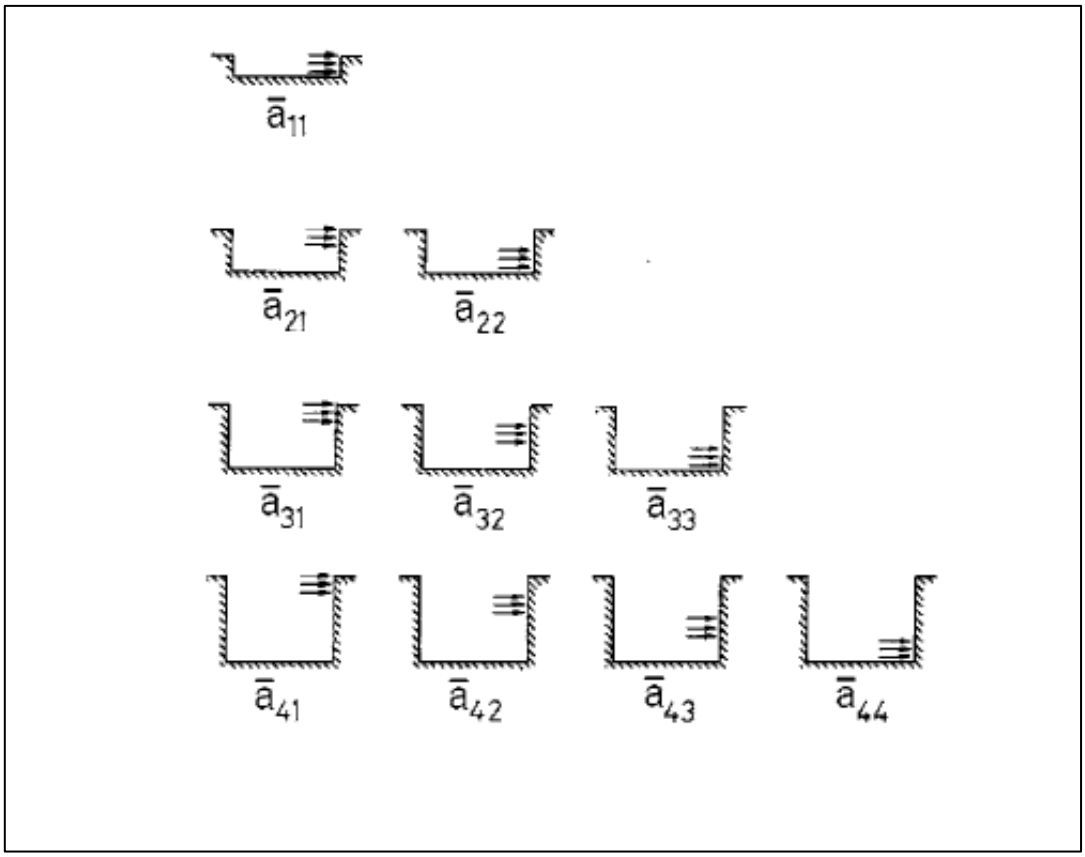

Figure 4-7: Physical interpretation of coefficient $\bar{a}_{ij}$ [172]

The drilling process can be done by a plunging or orbiting technique [172]. In this work, the plunging technique was used, in which the cutter is advanced axially. The advantage of using the plunging technique is both its simplicity and the hole diameter being almost the same as the cutter diameter. The cutter diameter used in this work is 1.6mm and the hole diameter was 2.1mm, experimentally measured. The hole diameter is important to ensure the target range is within that specified in ASTM E-837. The calibration data used in this work were tabulated in Table 5 in ASTM E-837 due using a type (A) rosette strain gauge.

4.4 Results

4.4.1 Results of Residual Stress Distribution on 4-point Bending Specimen

Four-point bending fatigue specimens have been fabricated from Optim700QL high strength ferritic steel. The mechanical and chemical compositions of this material were provided by manufacturer certificate in Appendix E. To conduct this study, 4-point bend specimens were machined from an *Optim*700*QL* plate. As seen in Figure 4-8 the 4-point bend specimens had 330mm length, 100mm width and 25mm thickness. As shown in Figure 4-8, a semi-circular starter notch with a radius of 5mm was machined at the centre of the 4-point bend specimens. The specimens were partially peened using the cavitation shotless peening technique for 120mm along the axial direction of the specimen geometry. Seven test specimens with different extents of cavitation shotless peening areas, with a 10, 20 and 30mm gap in the unpeened region (see the "A" dimension in Figure 4-8), were prepared for this study. The A20 specimen has been chosen in order to study the residual stress distribution. Seven points have been chosen to study the residual stress distribution on the specimen, as shown in Figure 4-8. Incremental HD has been used to measure residual stress distribution at a room temperature of 25C^{o}.

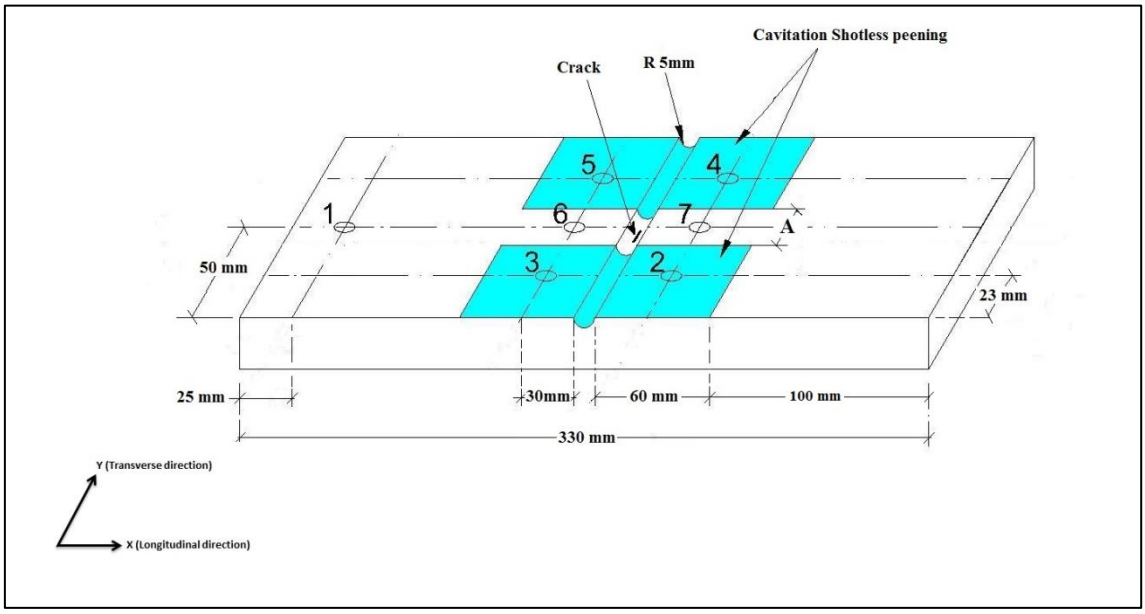

Figure 4-8: Schematic graph of residual stress measurement points on four-point bending specimen geometry

a) Point 1

Figure 4-9 shows the strain reading against each step of ICHD for point 1, as shown in Figure 4-8. It can be observed that the strain trends for ϵ_1, ϵ_2 and ϵ_3 are rough, which represent the strain values created due to the specimen's fabricated process; where, ϵ_1 represents the strain readings in longitudinal direction (x), ϵ_2 represents the strain readings in transverse direction (y), and ϵ_3 represents the strain readings in the (xy) direction. The residual stresses were calculated from the strain values as shown in Figure 4-10. It can be seen that the maximum residual stress near the surface is around 200MPa in the longitudinal direction and around 100MPa in the transverse direction. The shear stress is around 50MPa close to the surface. The residual stresses in longitudinal and transverse directions have anegative sign which indicates that the residual stress is in a compressive state. The compressive residual stresses decrease gradually through the specimen's thickness and are then converted into tensile residual stress at 0.2mm depth from the surface.

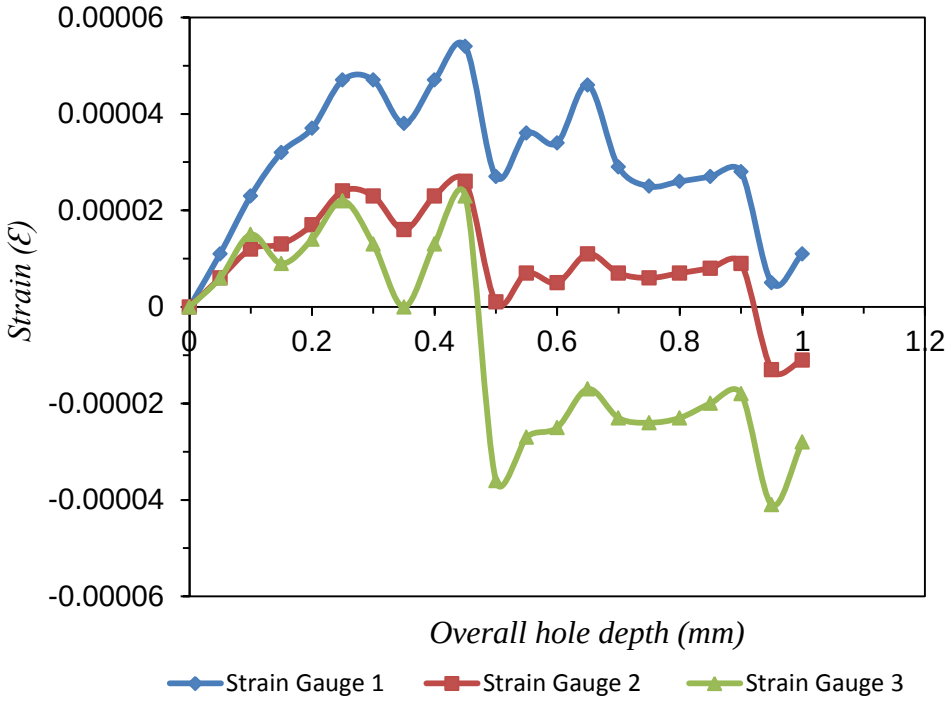

Figure 4-9: Strain gauge reading versus depth at point 1

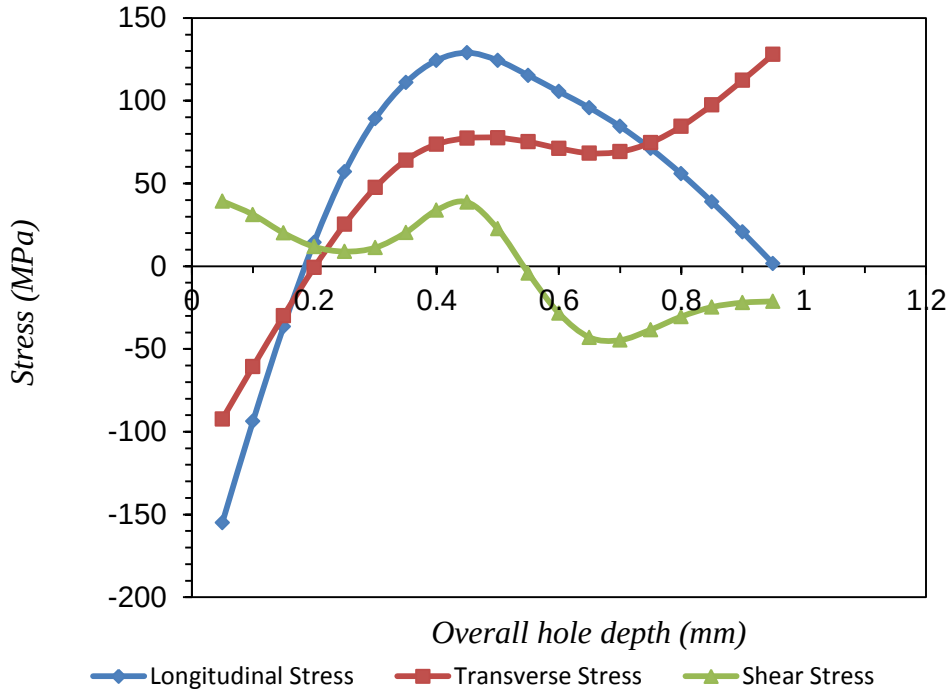

Figure 4-10: Residual stress distribution versus depth at point 1

b) Point 2

Point 2 lies inside the peened region on the specimen, as shown in Figure 4-8. The strain readings were plotted versus hole depth where, ϵ_1 represents the strain readings in longitudinal direction (x), ϵ_2 represents the strain readings in transverse direction (y), and ϵ_3 represent the strain readings in the (xy) direction, as shown in Figure 4-11, from which it can be observed that the strain trends are rough due to the noise effect during the test. The residual stress in longitudinal, transverse and shear were calculated from strains and plotted against hole depth, as shown in Figure 4-12. It can be seen that the maximum residual stresses are around 500MPa and 300MPa in longitudinal and transverse directions, respectively. Although the results are rough due to the de-bonding of the strain gauge from the material surface during the test procedure, the residual stresses magnitude near the surface give an idea of the nature and value of residual stresses which are compressive residual stress around 500MPa and 300MPa in longitudinal and transverse directions respectively.

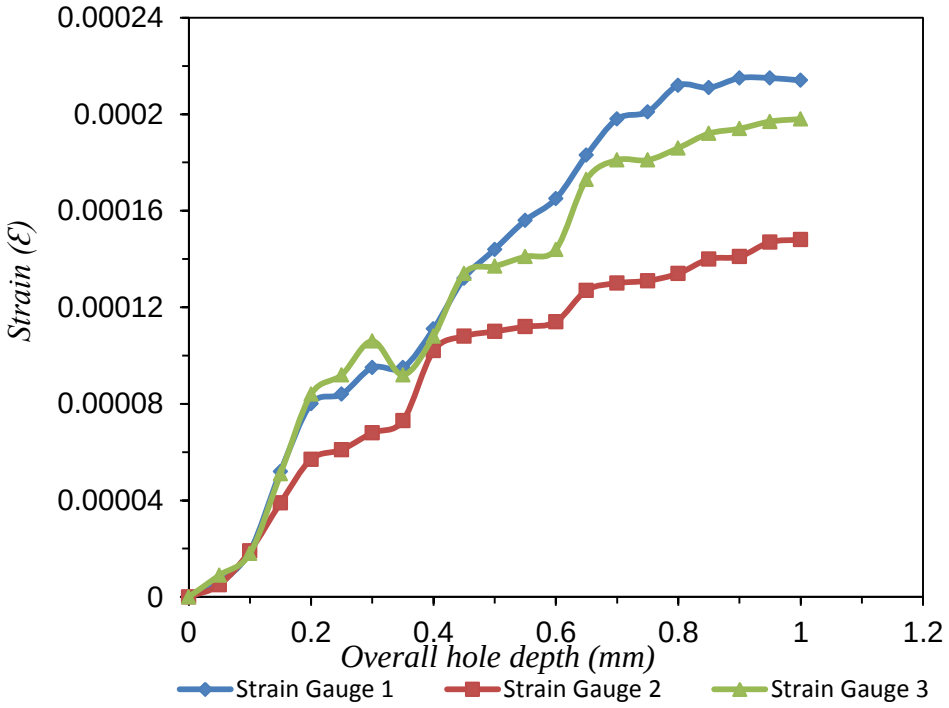

Figure 4-11: Strain reading versus depth at point 2

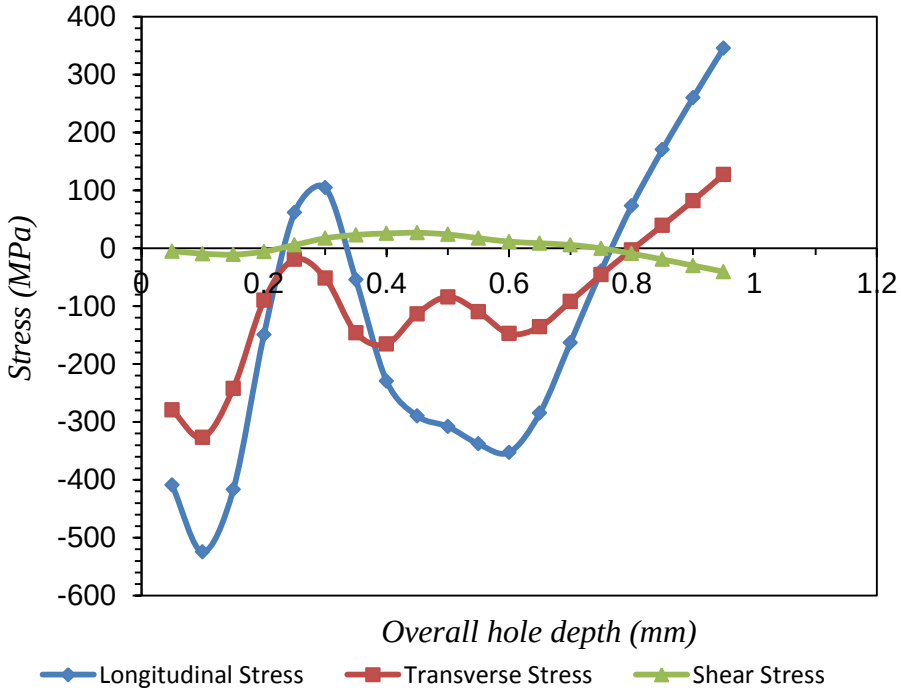

Figure 4-12: Residual stress distribution versus depth at point 2

c) Point 3

The strain readings were plotted versus the hole depth for point 3, as shown in Figure 4-13. It can be observed that the strain reading trends are smoothly increased through the depth due to the good bonding between the strain gauge and the workpiece and existence of residual stress according to the ASTM-837 test procedure. The residual stresses were calculated from the strain readings and plotted against the hole depth, as shown in Figure 4-14. It can be observed that the maximum residual stresses are around 300MPa and 200MPa in longitudinal and transverse directions, respectively. The residual stress values are within the measurement range of the ICHD technique i.e. between 50-70% of yield strength of the workpiece's material. The residual stresses are decreased gradually through the thickness and converted into tensile residual stress due to the self-equilibrating characteristics of residual stress in the material. The depth of compressive residual stress is around 0.4mm before being converted into tensile residual stress.

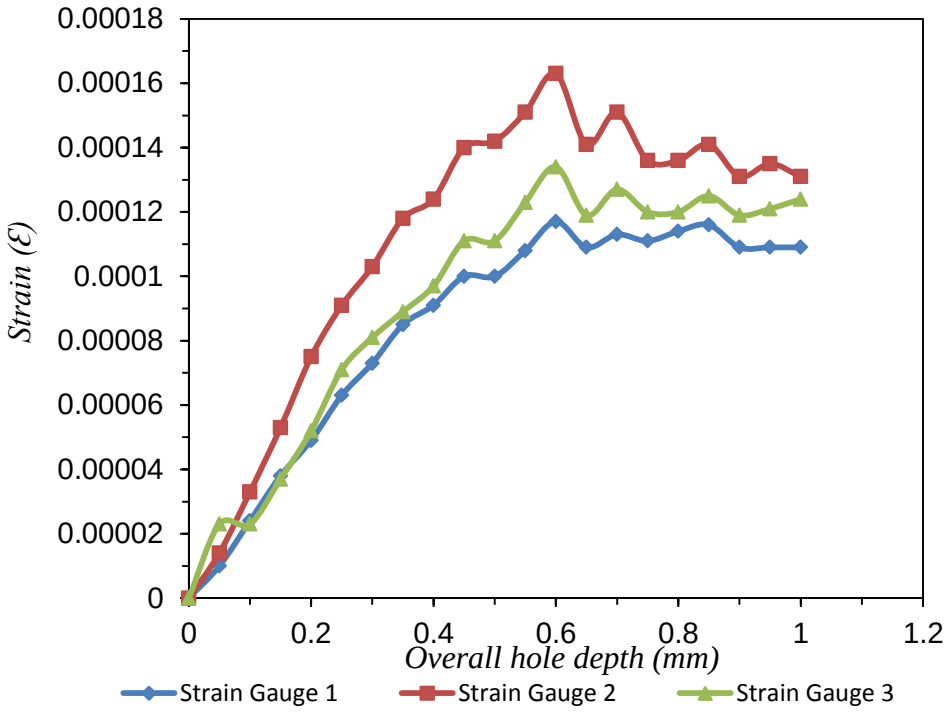

Figure 4-13: Strain reading versus depth at point 3

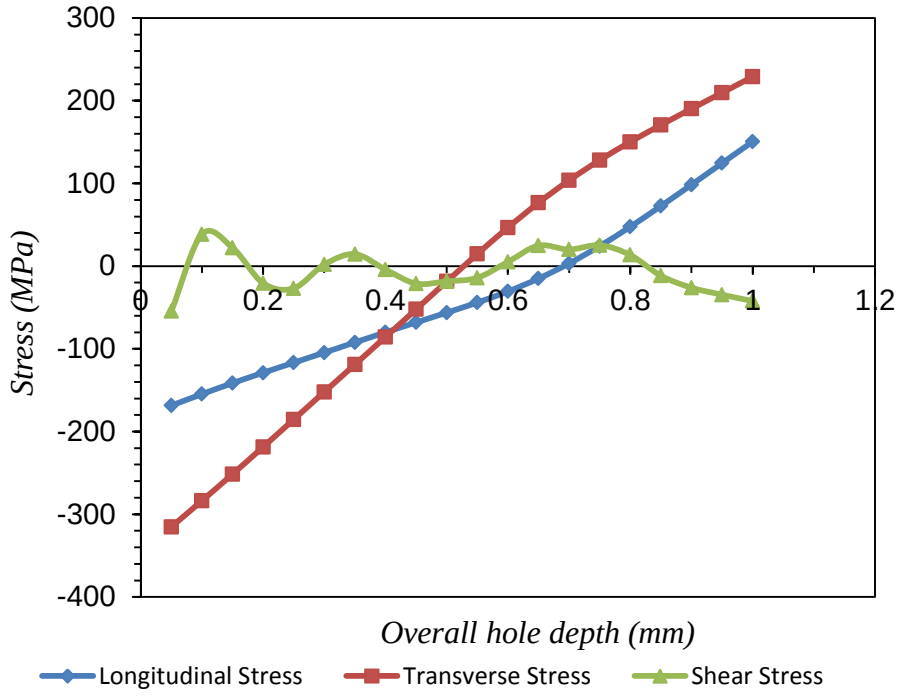

Figure 4-14: Residual stress distribution versus depth at point 3

d) Point 4

The residual stress distribution was measured at point 4 which lies in the peened region, as shown in Figure 4-8. It can be seen in Figure 4-15 that the trend of strain reading against the hole depth increases smoothly as the hole depth increases due to minimizing the external effects during the fatigue test, such as strain gauge bonding and external noise effect. The residual stress was calculated for each increment of ICHD and plotted against hole depth, as shown in Figure 4-16. It can be seen that the maximum compressive residual stresses are around 400MPa and 250MPa in longitudinal and transverse directions, respectively, which confirms the residual stress results from points 2 and 3. The compressive residual stress is reduced gradually through the thickness and starts being converted into tensile residual stress at 0.4mm from the surface, as shown in Figure 4-16.

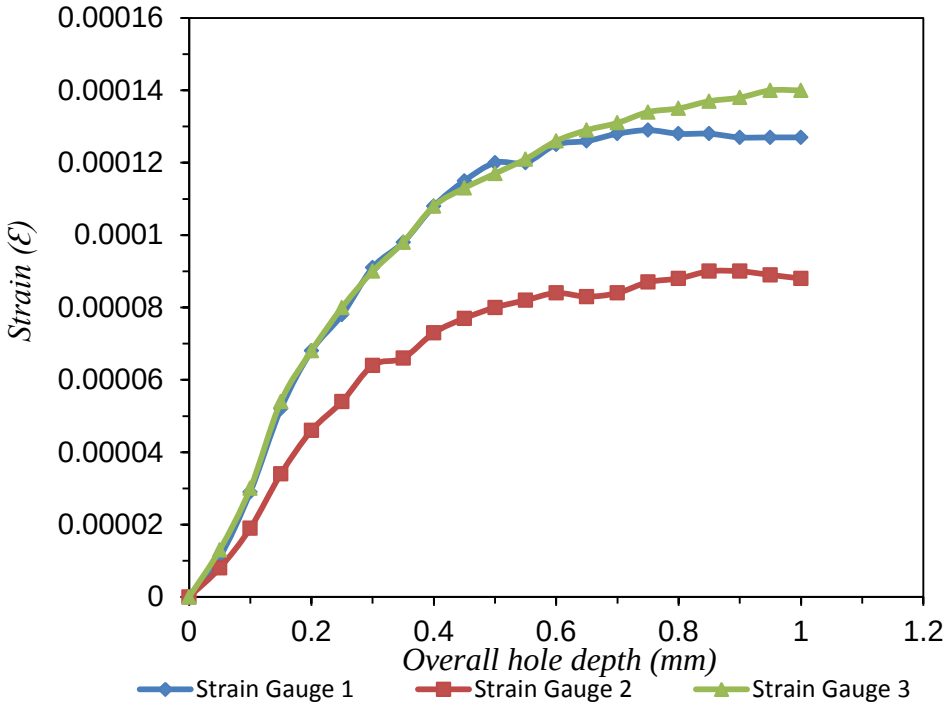

Figure 4-15: Strain reading versus depth at point 4

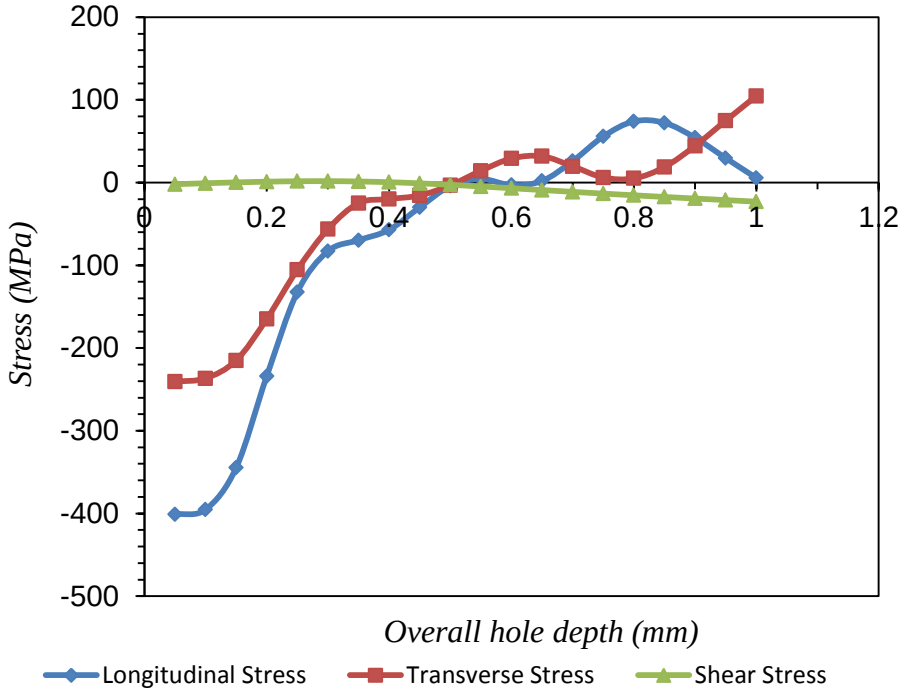

Figure 4-16: Residual stress distribution versus depth at point 4

e) Point 5

Figure 4-17 shows the strain recorder reading versus hole depth for point 5 which lies in the peened region, as shown in Figure 4-8. It can be observed that the strain recorder readings increase smoothly with the increasing hole depth. The residual stress for point 5 was plotted versus the hole depth, as shown in Figure 4-18. The maximum compressive residual stresses are around 400MPa and 300MPa in longitudinal and transverse directions, respectively. The residual stress magnitude is within the range of measurement of the ICHD technique which is 50-70% of yield strength of the workpiece's material. The compressive residual stress depth is around 0.4mm before starting to be converted into tensile residual stress and the depth result matches those at the peened areas of points 3 and 4.

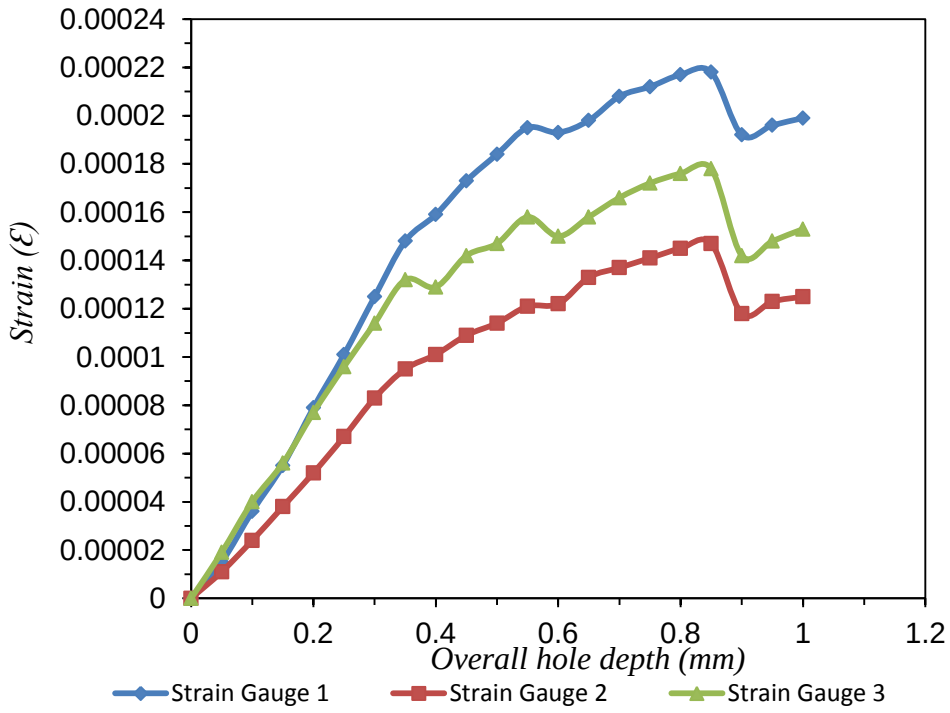

Figure 4-17: Strain reading versus depth at point 5

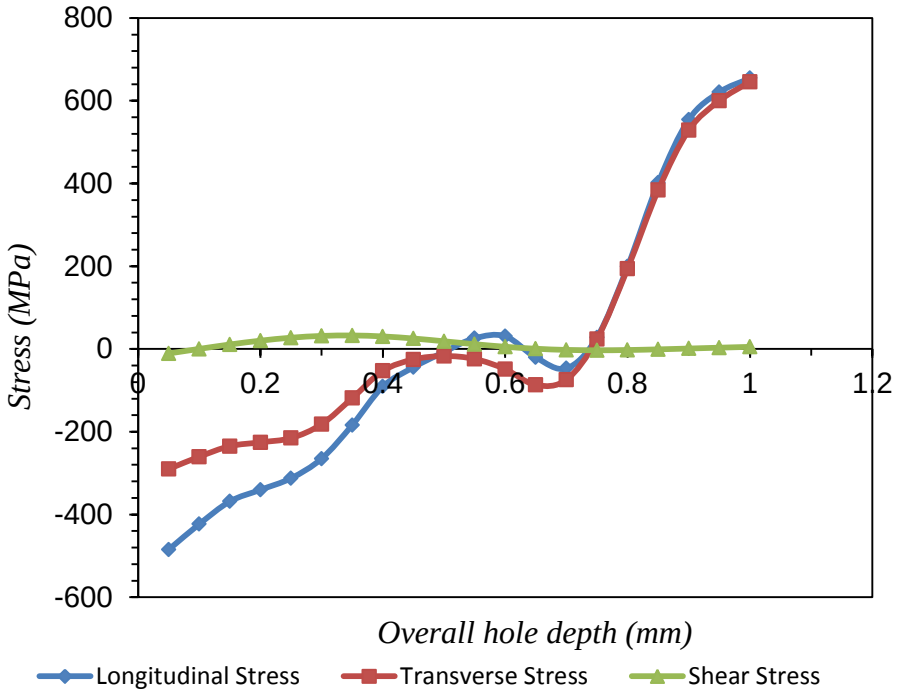

Figure 4-18: Residual stress distribution versus depth at point 5

f) Point 6

The residual stresses in between two peened regions were measured and presented in points 6 and 7, as shown in Figure 4-8. The strain readings were plotted against the hole depth, as shown in Figure 4-19 and Figure 4-21 for points 6 and 7, respectively. It can be observed that the strain reading trend is rough through the hole depth. The residual stresses were computed and plotted against the hole depth for points 6 and 7, as shown in Figure 4-20 and Figure 4-22, respectively. For the residual stress for points 6 and 7, it can be seen that the residual stresses are in a tensile state and converted gradually through the thickness into compressive residual stress due to the self-balancing characteristic of residual stress in the material. The maximum tensile residual stress is around 300MPa and 100MPa in longitudinal and transverse directions, respectively for points 6 and 7. The tensile residual stress converts into compressive residual stress at 0.4mm depth from the specimen surface.

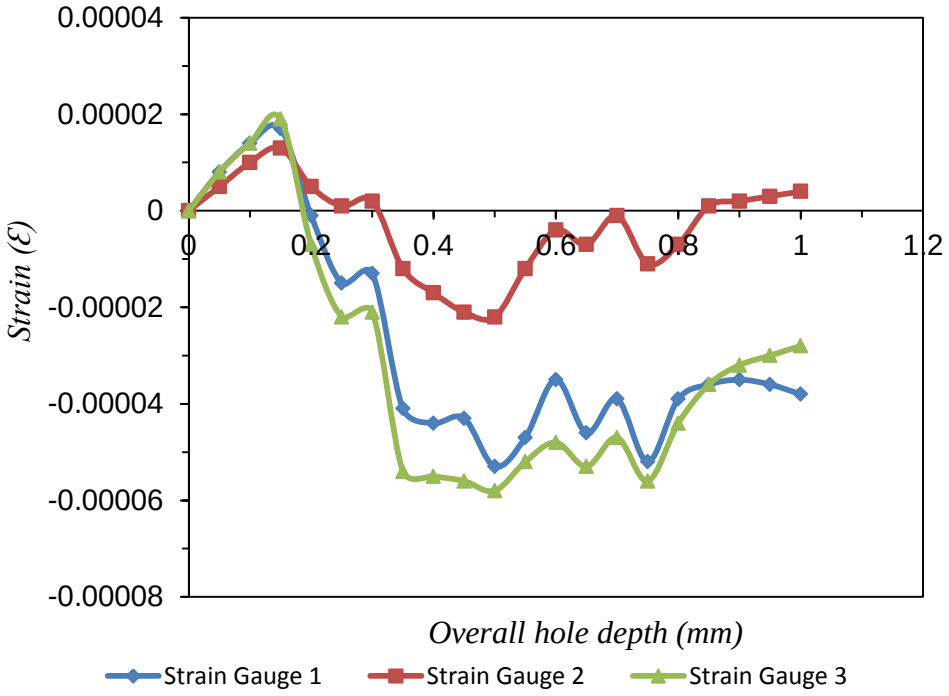

Figure 4-19: Strain reading versus depth at point 6

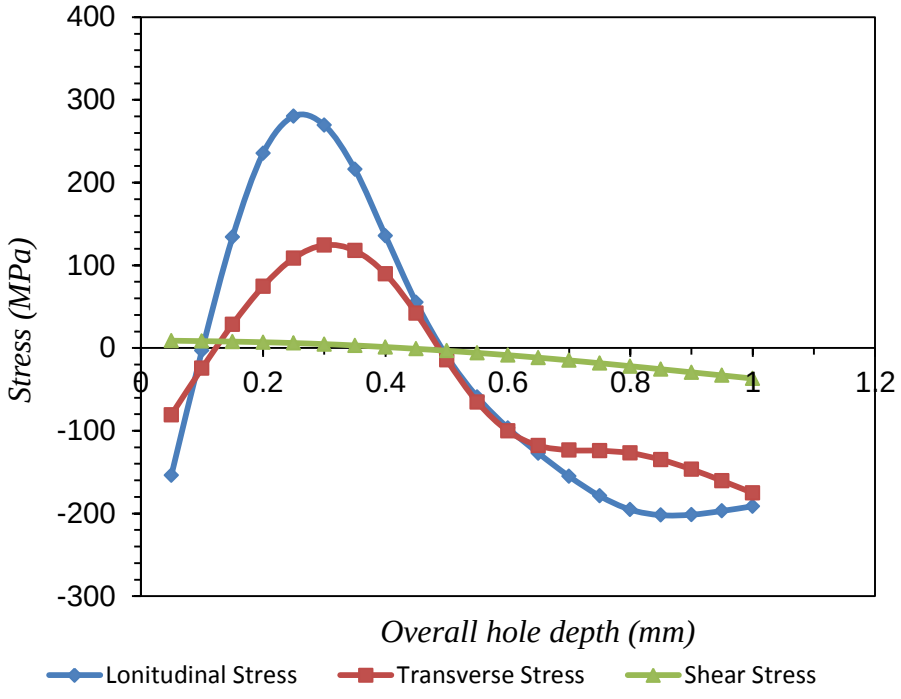

Figure 4-20: Residual stress distribution versus depth at point 6

g) Point 7

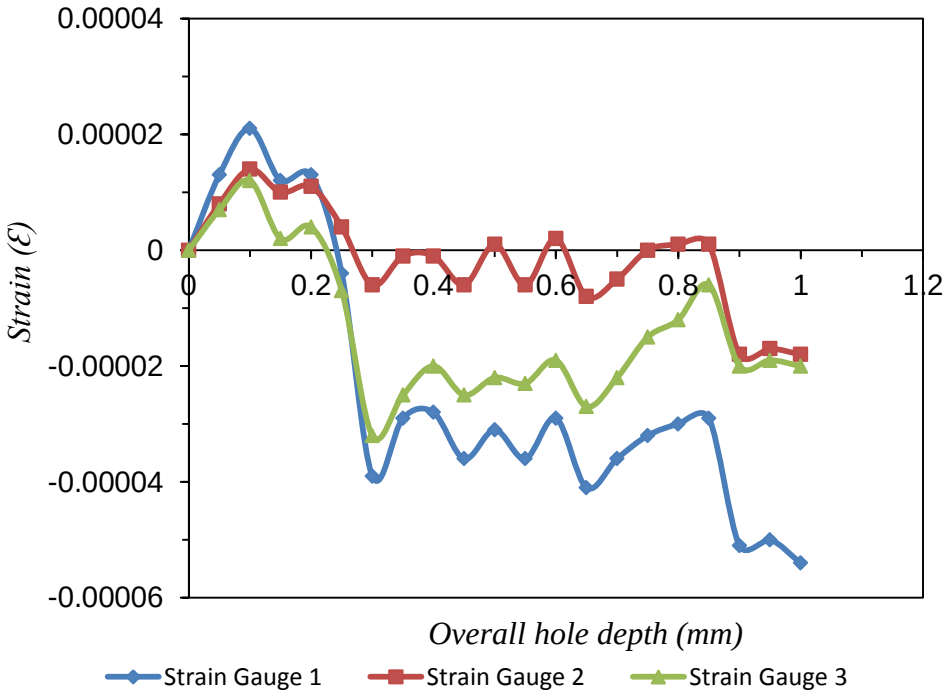

Figure 4-21: Strain reading versus depth at point 7

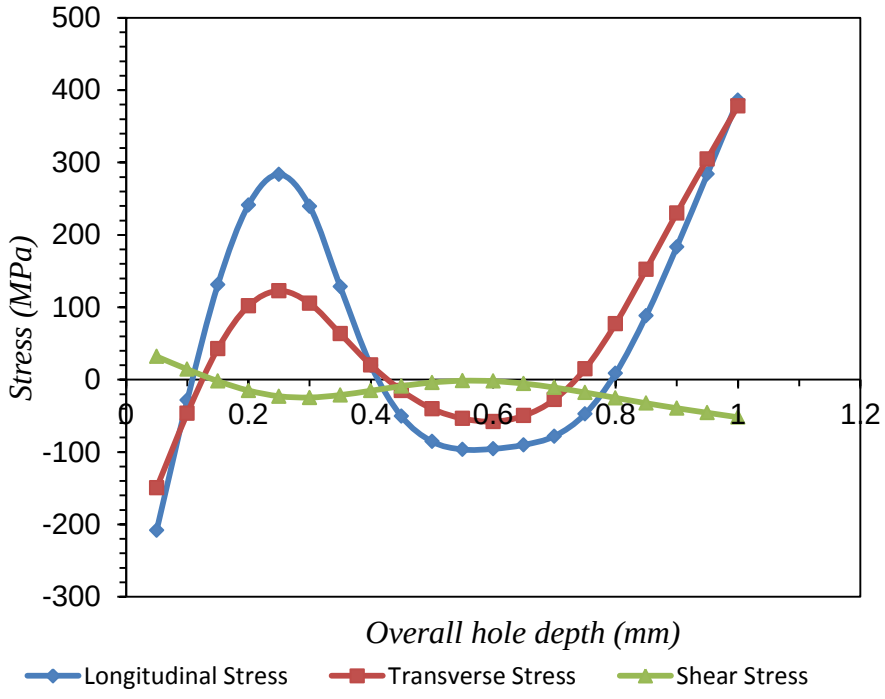

Figure 4-22: Residual stress distribution versus depth at point 7

4.4.2 Result of Residual Stress Distribution on dog-bone M(T) Specimen:

Dog-bone fatigue specimens have been treated by “shot peening”. The specimen has been treated at selected areas, as shown in Figure 4-23. Five test specimens with different extents of shot peening areas, with a 10, 20 and 30mm gap in the unpeened region (see the “A” dimension in Figure 4-23), were prepared for this study. The (A20) specimen has been chosen in order to study the residual stress distribution. Three-point has been chosen to study the residual stress distribution on the specimen, as shown in Figure 4-23. ICHD has been used to measure residual stress distribution at a room temperature of $25^{o}C$.

The residual stress measurements in the peened area are represented in points 1 and 2. The strain recorder readings were plotted against the hole depth for points 1 and 2, as shown in Figure 4-24 and Figure 4-26, respectively. It can be observed that the strain recorder readings increase smoothly with the increasing hole depth, which represent the strain values created due to the specimen’s fabricated process. Whereas, ϵ_1 represents the strain readings in longitudinal direction (x), ϵ_2 represents the strain readings in transverse direction (y), and ϵ_3 represents the strains readings in the (xy) direction. It can be observed that there is a similar trend in behaviour between points 1 and 2 due to both points lying in the peened region and the strain recorder readings increase smoothly with the increasing hole depth. The residual stress for points 1 and 2 were plotted versus the hole depth, as shown in Figure 4-25 and Figure 4-27, respectively. The magnitude of residual stress at points 1 and 2 is around 500MPa in a longitudinal direction and around 400MPa in a transverse direction, and these values are within the measurement range of ICHD which is around 50-70% of the yield strength of material. The negative sign of residual stress indicates that the residual stress is in a compressive state. The self-balancing feature of residual stress in material that causes the residual stress, decreases gradually through the thickness and is then converted into tensile residual stress. The compressive residual stress starts converting into tensile residual stress around 1mm from the surface. The residual stress results indicate that the cavitation shotless peening causes compression up to 1mm depth through the specimen.

The residual stresses between two peened areas were measured, which are represented by point 3. The strain readings were plotted against the hole depth, as shown in Figure

4-28. It can be observed that the strain reading trend is rough through the hole depth due to these strains resulting from compressive residual stress in the peened region. The residual stresses at point 3 were calculated from strain recorder readings and plotted against the hole depth, as shown in Figure 4-29. It can be observed that maximum value of residual stresses around 150MPa and 50MPa in longitudinal and transverse directions, respectively, with a positive sign. The positive sign indicates that the nature of the residual stress is a tensile residual stress. The tensile residual stress is generated due to the self-balancing features of residual stress in the transverse directions, as shown in Figure 4-23.

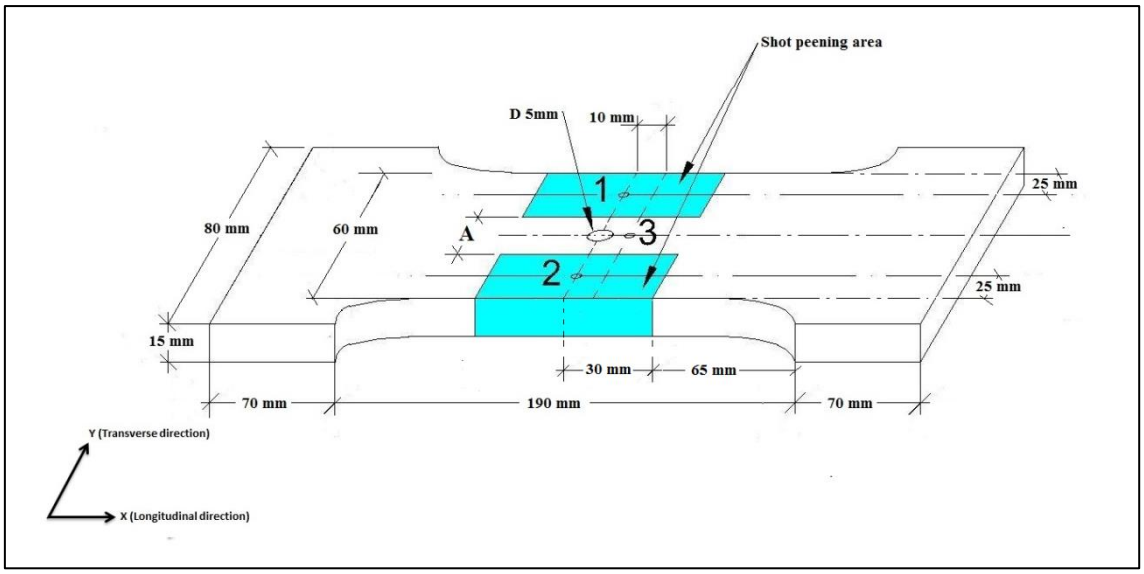

Figure 4-23 Schematic diagram of Surface Crack Tension Specimen

a) Point 1

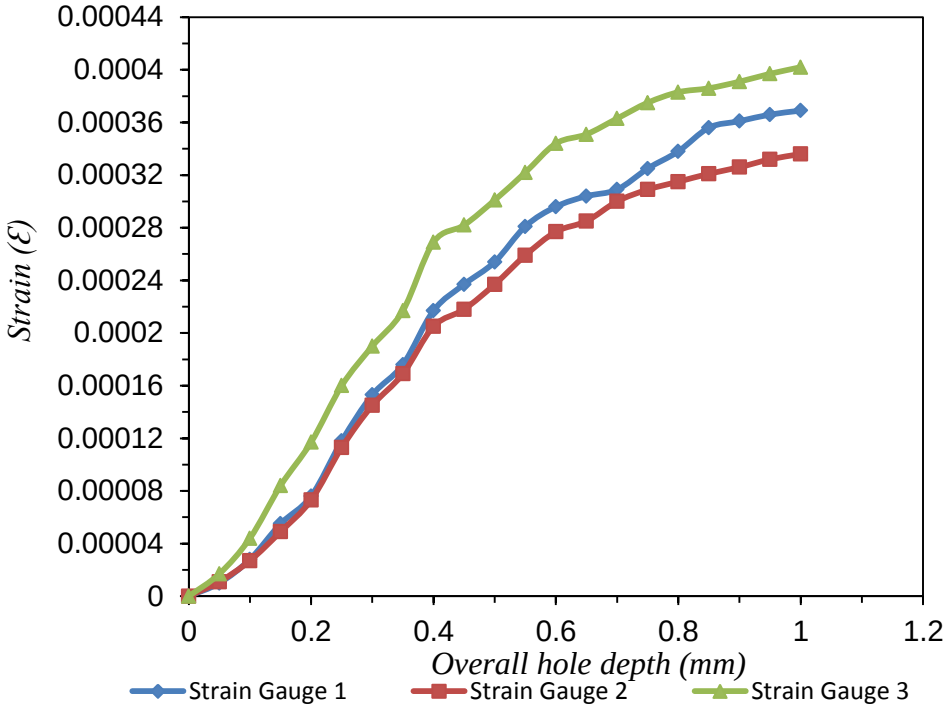

Figure 4-24 Strain reading versus depth at point 1

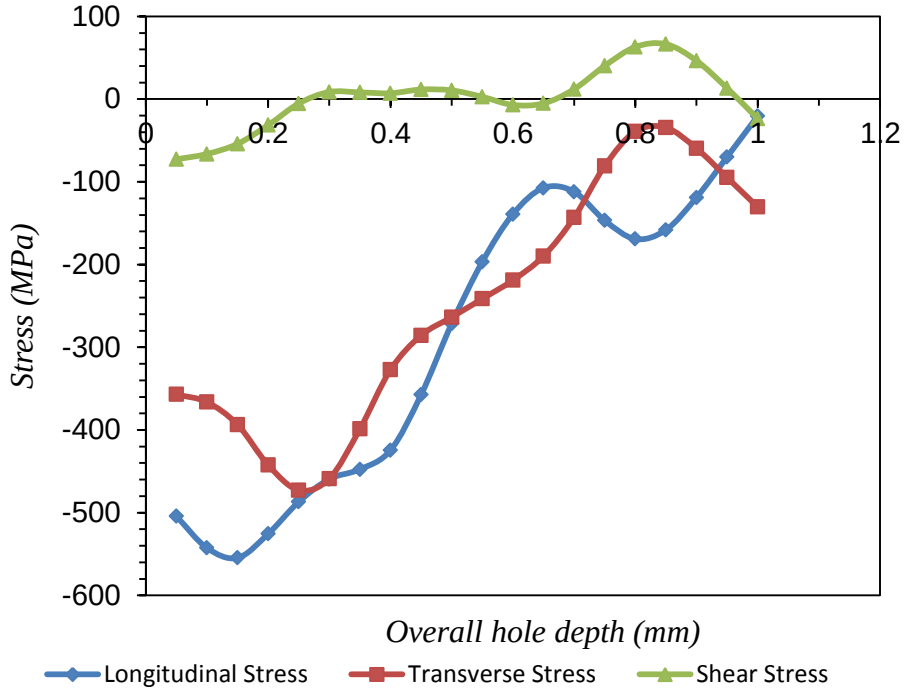

Figure 4-25 Residual stress distribution versus depth at point 1

a) Point 2

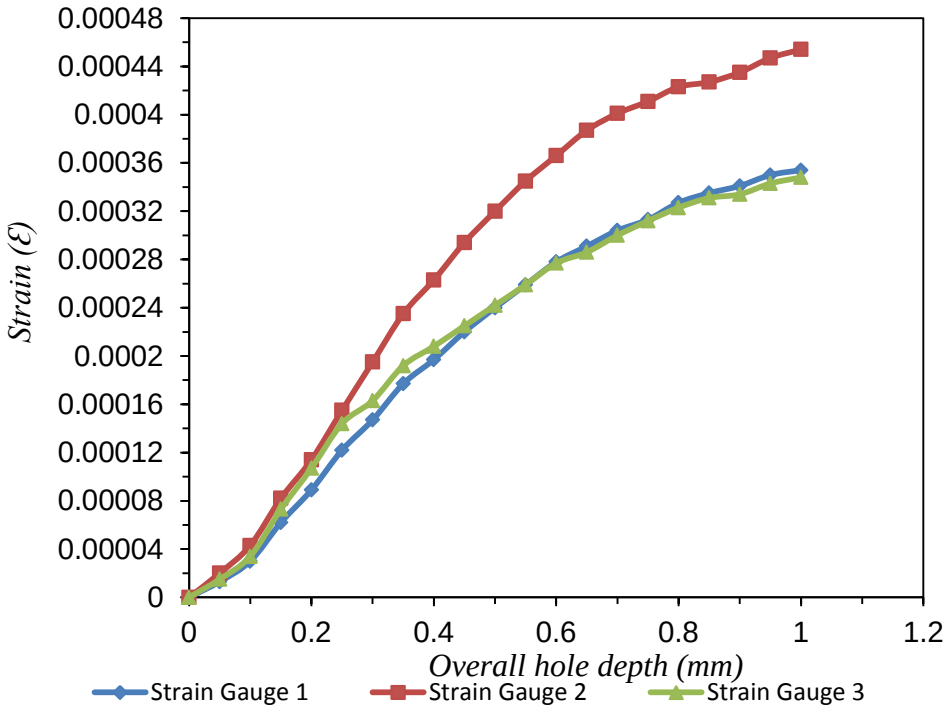

Figure 4-26 Strain reading versus depth at point 2

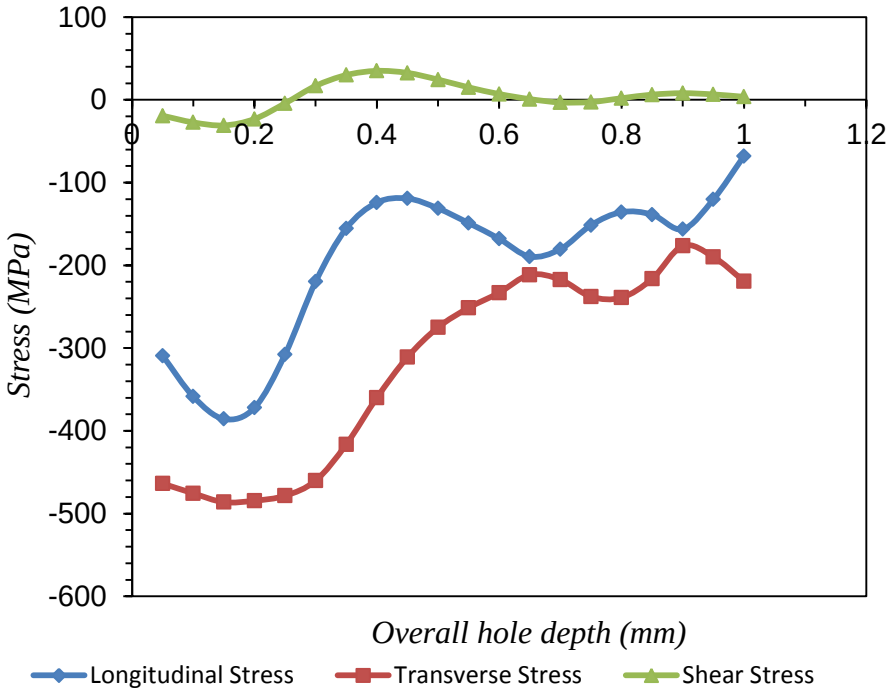

Figure 4-27 Residual stress distribution versus depth at point 2

Point 3

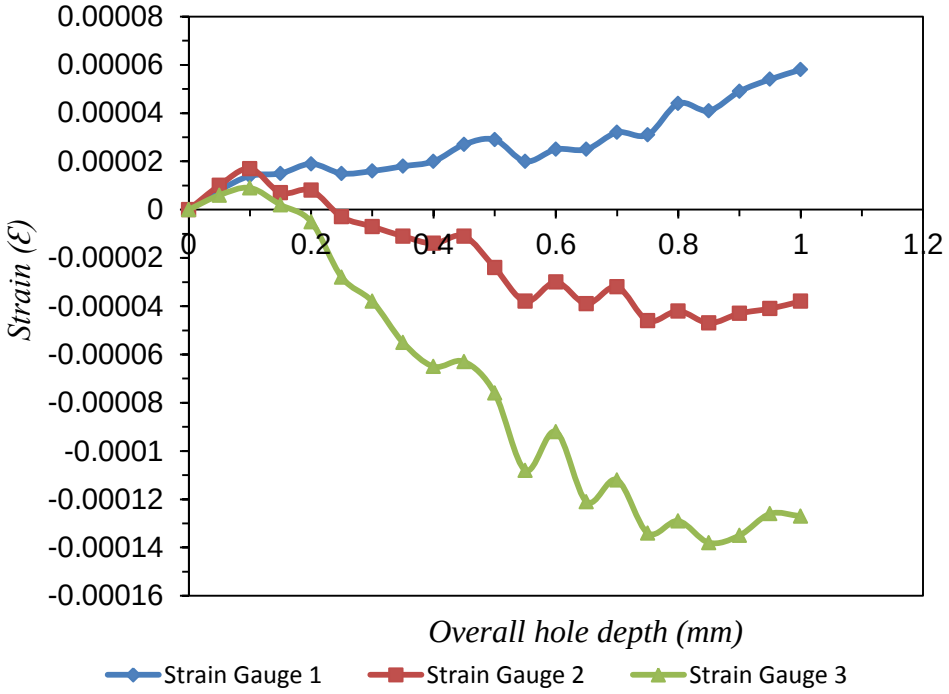

Figure 4-28 Strain reading versus depth at point 3

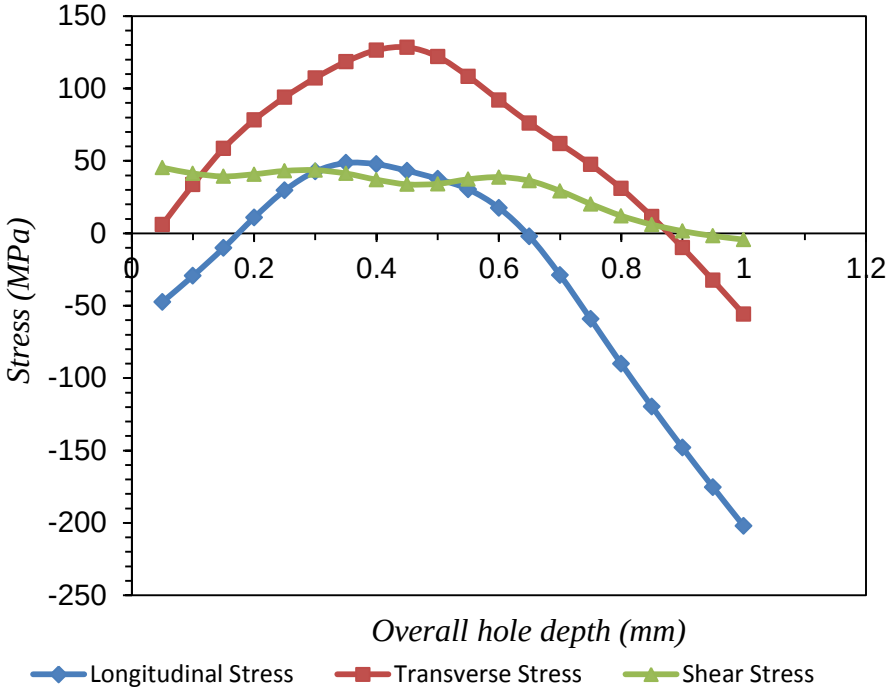

Figure 4-29 Residual stress distribution versus depth at point 3

4.5 Comparison of residual stresses

The comparisons of residual stress measurements in the peened and unpeened regions of the specimens used in this study were plotted together collectively, as shown in Figure 4-30. It can be observed that the maximum compressive residual stress measured by ICHD is around 500MPa for both peened regions induced by cavitation shotless peening and by shot peening. The maximum depth of compressive residual stress induced by cavitation shotless peening was around 0.5mm, while the maximum compressive residual stress induced by shot peening was around 1mm before converting into tensile residual stress, as can be seen in Figure 4-30. The results from this study are compared with the data from the open literature of residual stress induced by LSP on carbon-manganese ship structural steel grade DH275 with a yield strength of 436MPa [175] as shown in Figure 4-30. The data from the literature were measured by using different methods such as ICHD, neutron diffraction and contour method. It can be observed that the maximum compressive residual stress induced by LSP measured ICHD was around 350MPa, which is around 60-70% of the material's yield strength and by using different measurement technique to measure the depth of compressive residual stress is around 2.7mm, which is ICHD measured up to 1mm and ND start to be measured from around 0.7mm beneath the surface.

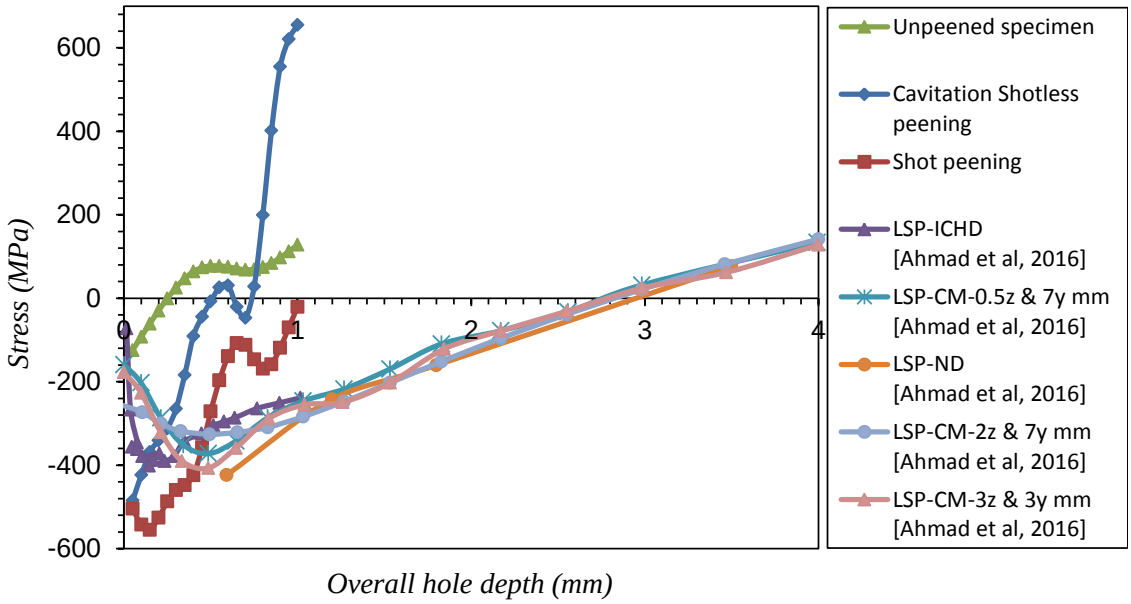

Figure 4-30: Comparison of residual stresses

4.6 Summary

In order to identify the nature and depth of residual stress generated by cavitation shotless peening and shot peening in HSS, the residual stresses measurements have been taken in this chapter. The residual stress distributions on a partially peened 4-point bend and dog-bone tension specimen have been measured. ICHD has been used to measure residual stress distribution and the residual stress has been calculated by using a non-uniform stress integral method. The 4-point bending specimen was treated by cavitation shotless peening and the middle tension M(T) dog-bone specimen by shot peening.

The residual stress results of the 4-point bending fatigue test specimen show that the cavitation shotless peening causes a compressive residual stress at the peening area in both longitudinal and transverse directions. The magnitude of the compressive residual stress in the peening region is around 400MPa in a longitudinal direction and around 300MPa in a transverse direction. The residual stress results indicate that the cavitation shotless peening causes compression until 0.4mm depth through the specimen. The residual stress generated due to the manufacturing process of the specimen is compressive residual around 200MPa in a longitudinal direction and around 100MPa in a transverse direction. The residual stress at the region between the two peened regions indicates that there is a tensile residual stress around 300MPa and 100MPa in longitudinal and transverse directions, respectively. Figure 4-31 and Figure 4-32 show a 3-D residual stress distribution in longitudinal and transverse directions respectively based on sparse measurement points for the 4-point bending specimen.

The residual stress results from the tension specimen show that the shot peening causes a compressive residual stress at the peening area in both longitudinal and transverse directions. The magnitude of residual stress at the peened region point is around 500MPa in a longitudinal direction and around 400MPa in a transverse direction. The compressive residual stress depth created by shot peening is around 1mm from the surface. The tensile residual stress between the two shot peened regions is around 150MPa and 50MPa in longitudinal and transverse directions, respectively. Figure 4-33 and Figure 4-34 show 3-D residual stress distribution in the tension fatigue test based on extrapolated measurement points. The results are important to justify the FCGR result of partially peened specimens as one of the main objectives of this thesis.

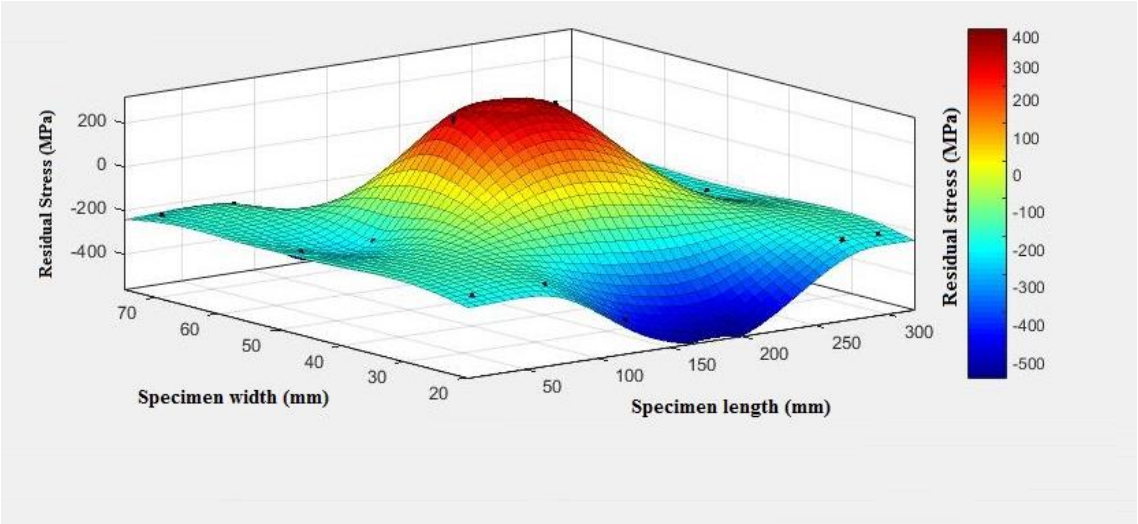

Figure 4-31: 3-D illustration of longitudinal residual stress distribution in 4-point bending specimen

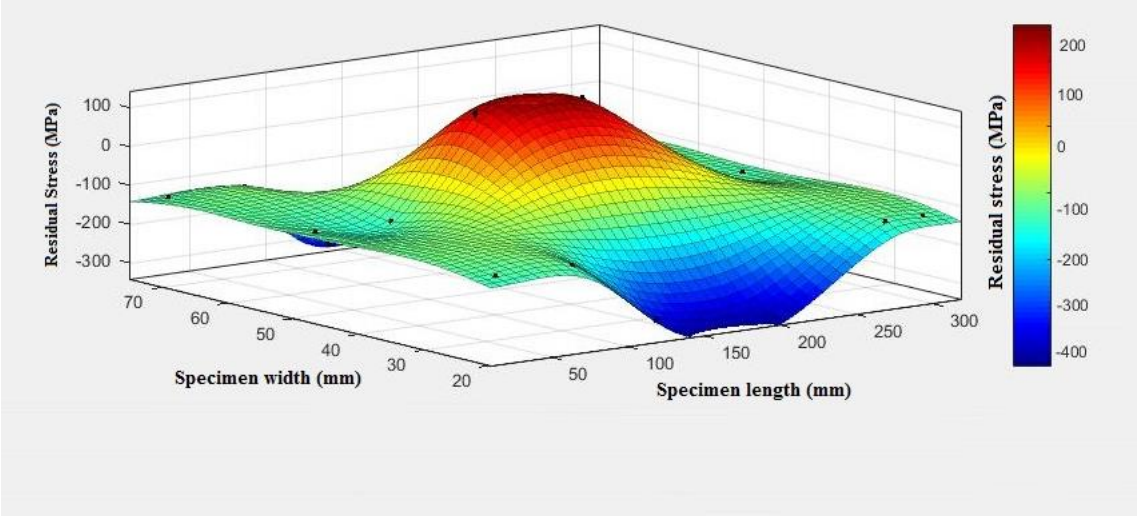

Figure 4-32: 3-D illustration of transverse residual stress distribution in 4-point bending specimen

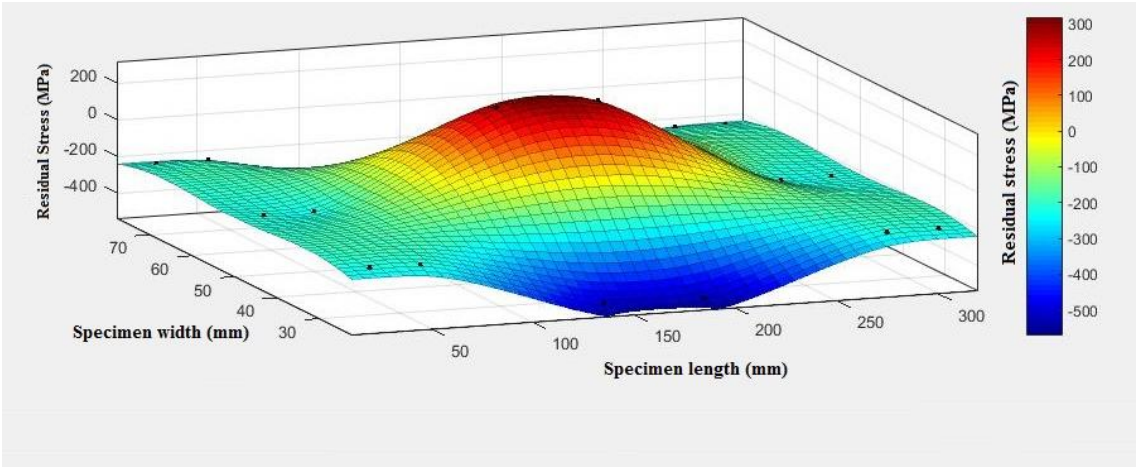

Figure 4-33: 3-D illustration of longitudinal residual stress distribution in tension specimen

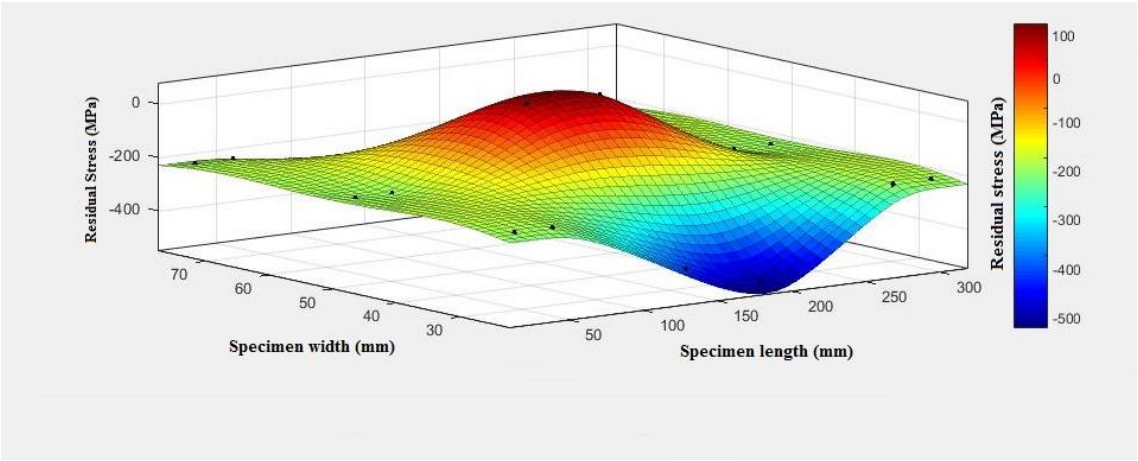

Figure 4-34: 3-D illustration of transverse residual stress distribution in tension specimen

5 The Influence of Partial Surface Shot Peening On Fatigue Crack Growth

5.1 Introduction

Surface treatment is known to be an efficient technique to improve the fatigue life of engineering components and structures [176]. Shot peening is one of the mechanical surface treatment techniques used to create compressive residual stresses underneath the surface to reduce the effective local stresses and improve structural integrity and fatigue resistance in structures. Shot peening is performed by projecting small particles at high speed onto the surface of the material, leading to a local plastic deformation on the surface. By using this technique a compressive residual stress field appears in the surrounding elastically deformed material [177, 178].

A review of the past studies has revealed that shot peening influences the fatigue crack initiation and growth behaviour of engineering materials. However, the influence of partial peening on subsequent FCG behaviour is yet to be investigated and compared with similar specimens with no peening. Applying partial surface peening has advantages over conventional full peening, such as being cost-effective, less time-consuming and it minimizes the area of peened surface that is subjected to erosion. In the present study, partial shot peening areas were introduced in *Optim*700*QL* HSS specimens. The HSSs provide advantages over conventional steels where the strength to weight ratio is important. HSSs with yield strength ranging from 500 to 700MPa are being increasingly used in a wide range of applications, from offshore and aerospace to the power generation industry, involving production jack-ups with demanding requirements [155].

In this chapter, partial shot peening was implemented at three different distances from the initial notch tip in dog-bone specimens to study the subsequent effects on the FCG and crack retardation behaviour of the material. The results from these tests are presented below and compared with the FCG behaviour of the material in unpeened specimens.

5.2 Experimental details

5.2.1 Material and specimen design

The material used in this study is *Optim700QL* HSS. The mechanical properties and chemical composition of this material are summarised in Table 5-1 and in Appendix E. This material is used for offshore structures such as jack-ups and moorings due to its advantages over conventional steel where the strength to weight ratio is high**.**

Table 5-1: Chemical composition and Mechanical properties of Optim700QL [179]

Chemical composition of *Optim700QL*	
Element	WT%
C	0.156
SI	0.32
MN	0.99
P	0.009
AL	0.047
NB	0.002
V	0.01
TI	0.023
CU	0.023
CR	0.59
NI	0.2
MO	0.198
B	0.0016
ZR	0.002
Mechanical properties of *Optim700QL*	
Ultimate Tensile Strength (MPa)	833
Yield Strength (MPa)	690

Dog-bone shaped test specimens were extracted from a 25mm thick plate in such a way that the loading axis was parallel to the rolling direction of the steel plate. Figure 5-1

illustrates the specimen geometry details as well as the initial notch details, which were introduced into the specimen using the EDM method. The dog-bone specimen has been designed based on the ASTM E740 standard. As shown in Figure 5-1, the maximum width and length are 80mm and 330mm respectively, while the thickness and radius of curvature are 15mm and 40mm respectively. Three nominally identical specimens were machined and then subsequently subjected to partial shot peening to different extents, with respect to the initial notch tip. The partial shot peening was applied on both top and bottom faces as well as on the side of specimens, as shown in Figure 5-1. Note that in this figure A is the size of the unpeened region at the mid-width of the sample. Table 5-2 shows the details and number of specimens used in this study. As seen in this table, samples with 10, 20 and 30mm unpeened region at the mid-width are denoted A10, A20 and A30, respectively whereas the specimen with no peening is called A60.

Table 5-2: Test matrix

Specimen name	Extent of the unpeened area A	Number of specimens
A60	Without peening	1
A10	10mm	1
A20	20mm	1
A30	30mm	2

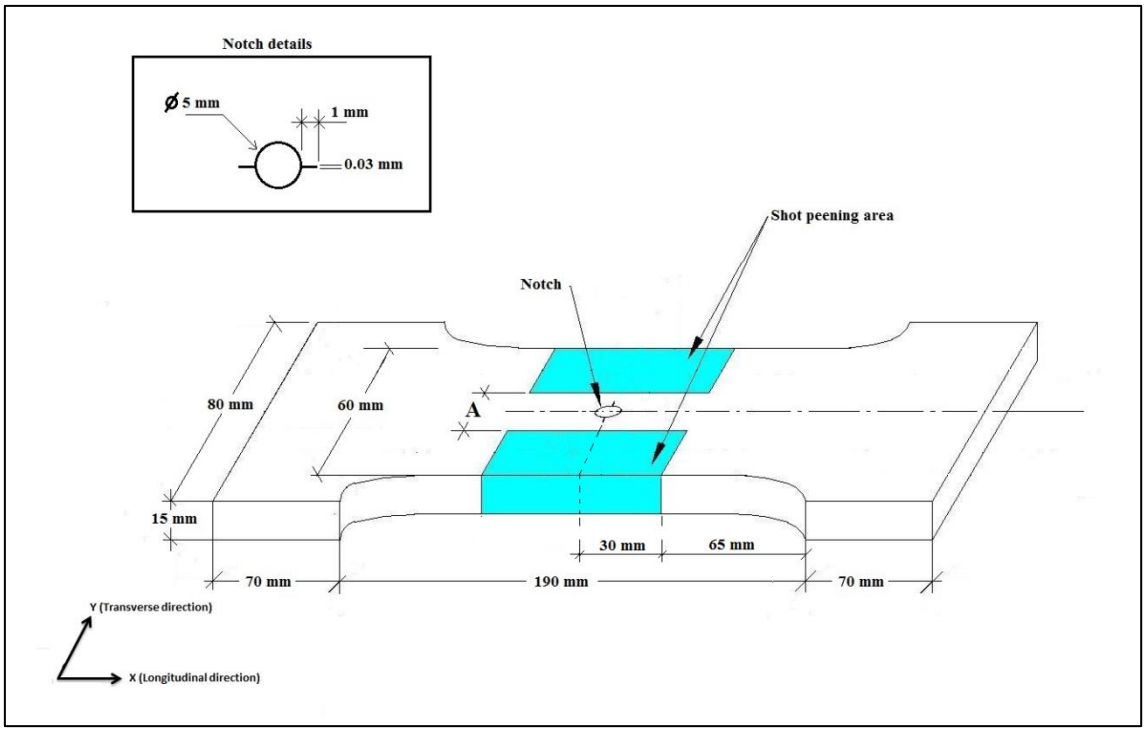

Figure 5-1: Test specimen and notch details

5.2.2 Partial surface shot peening details

A shot peening technique, in which the surface is blasted with millions of small metallic or ceramic spheres, was used to introduce compressive residual stresses on the outer surface of the specimens. There are various factors which influence the level of residual stresses due to shot peening, such as shot hardness, shot size and peening intensity [180, 181, 182, 183]. In this study, a dual peening process was used to introduce partial peening areas on specimens. The dual peening process provides uniform compressive residual stresses on the peened surface by using smaller shot and lower intensity to drive the peaks into the valleys that are left from the first peening process. The dual peening enhances the fatigue strength of the material [184]. Table 5-3 shows details of the dual peening process used in this study. The shots used were made of cast steel shot in both processes, with the media diameters being 1.9812mm and 0.5842mm for the first and second operations, respectively. The media flow rates were 8kg/min and 6kg/min for the first and second operations, respectively. The nozzle stood at a distance of 150mm from the test specimens at a 90^{o} angle.

Table 5-3: Shot peening process details

Operation details	S780H Shot Peening (1st Operation)	S780H Shot Peening (2nd Operation)
Media Type	Cast Steel Shot	Cast Steel Shot
Media Diameter	1.9812mm	0.5842mm
Media Mass	32.00414mg	0.82055mg
Media Particles per 100g	3,125	121,869
Media Flow Rate	8kg/min	6kg/min
Nozzle Stand off	150mm	150mm
Peening Angle	90°	90°

5.2.3 Fatigue crack growth testing

Tension-tension fatigue tests were carried out in ambient temperature of 25^oC, 3Hz frequency, maximum load of 90kN and load ratio of R = 0.1. An Instron machine equipped with a 250kN load cell was used to perform these tests. The pre-cracking has been done for tension fatigue specimens to reduce the machining effects at the initial notch tip. The pre-cracking started with the maximum load of 120kN which was gradually reduced to 90kN towards the end of pre-cracking. A constant *R*-ratio of 0.1 was maintained during the pre-fatigue cracking process. The sinusoidal wave loads were implemented in the wave matrix software provided by Instron and applied to the samples. The implemented test method in the software contains three steps for continuous fatigue crack propagation. These three-steps, as shown in Figure 5-2, are described as follows:

a) Step 1: The specimen was ramped up to the minimum load (within 2 seconds).

b) Step 2: Sinusoidal load was applied between the maximum and minimum loads.

c) Step 3: The test was ramped down to zero load at the end of the test.

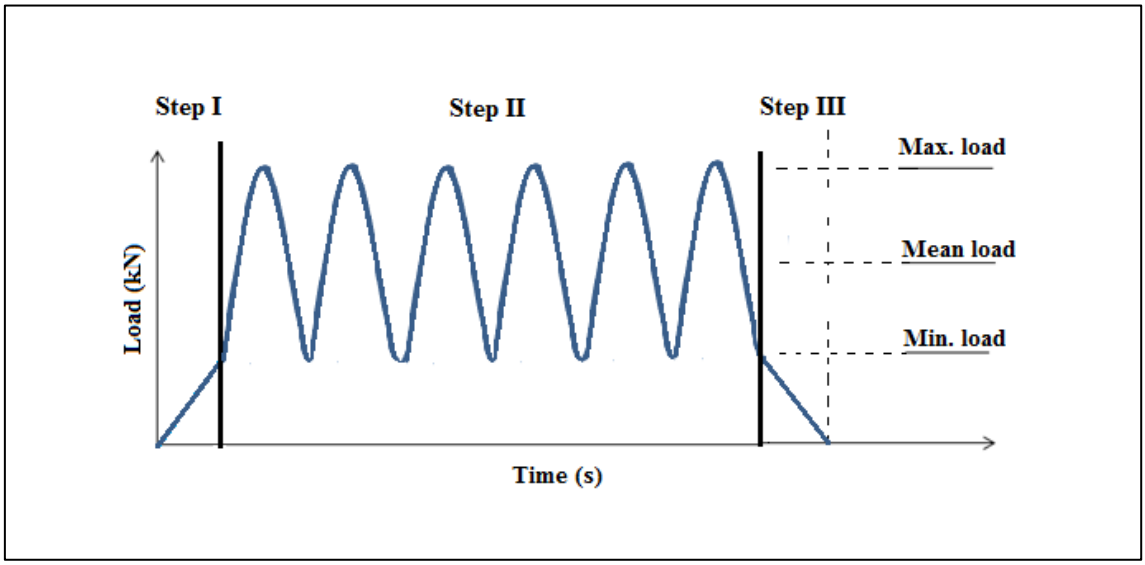

Figure 5-2: Demonstration of the test method implemented in the wave matrix

5.2.4 Crack growth monitoring and fatigue crack growth rate calculations

The crack length was monitored during fatigue tests using a StreamPix5 digital camera. The crack length data were recorded and collected manually in conjunction with the cycle numbers, as shown in Figure 5-5 to Figure 5-9. The data were presented as total fatigue crack length against the number of cycles where the total crack lengths were calculated by Equation 5-6 and are shown in Figure 5-3. An example of the crack growth monitoring process is shown in Figure 5-4. The SIF range ΔK for this specimen geometry was calculated according to $ASTM\ E647$ by using the following equations:

$$\alpha = \frac{2a}{W} \qquad \textbf{Equation 5-1}$$

$$\Delta K = \frac{\Delta P}{B}\sqrt{\frac{\pi\alpha}{2W}}\sec\frac{\pi\alpha}{2} \qquad \textbf{Equation 5-2}$$

In Equation 5-1 and Equation 5-2, a is the total crack length, W is the total width of the specimen, B is the specimen thickness and ΔP is the difference between the maximum load P_{max} and minimum load P_{min}.

The FCGR, which is the crack extension rate due to fatigue loading, can be represented by the average crack extension per cycle. The seven-point incremental polynomial technique, which is suitable for a test performed continuously and smoothly, has been used to calculate the FCGR in accordance with *ASTM E*647 [185].

$$a_i = b_o + b_1\left(\frac{N_i - C_1}{C_2}\right) + b_2\left(\frac{N_i - C_1}{C_2}\right)^2 \qquad \textbf{Equation 5-3}$$

where

$$-1 \le \left(\frac{N_i - C_1}{C_2}\right) \le +1 \qquad \textbf{Equation 5-4}$$

$$\left(\frac{da}{dN}\right)_{ai} = (b_1)/(C_2) + 2b_2(N_i - C_1)/C_2^2 \qquad \textbf{Equation 5-5}$$

where: b_0, b_1, and b_2 are the regression parameters that can be determined by the least squares method.

$$\text{Total crack length} = D_n + a_s + d \qquad \textbf{Equation 5-6}$$

Where: D_n represents the notch diameter (Dn=5mm), a_s represents the crack starter (a_s=2mm) and d represents the distance to peening area.

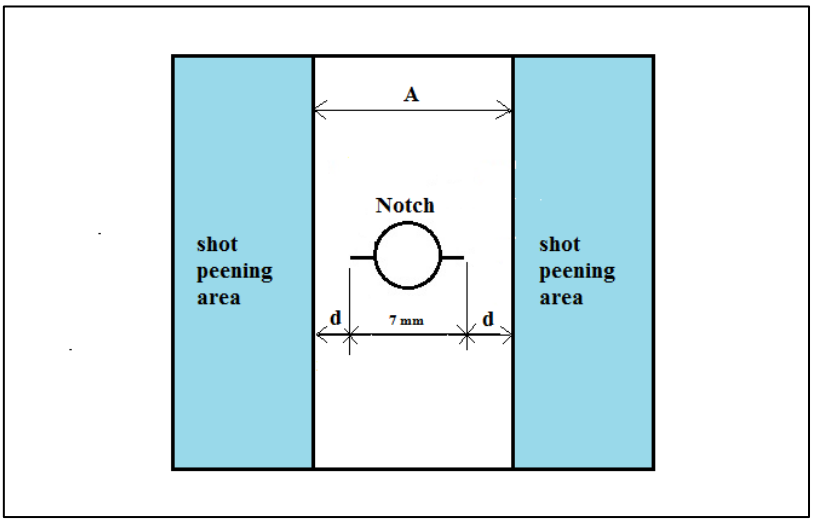

Figure 5-3: Illustration of initial notch regarding peening area

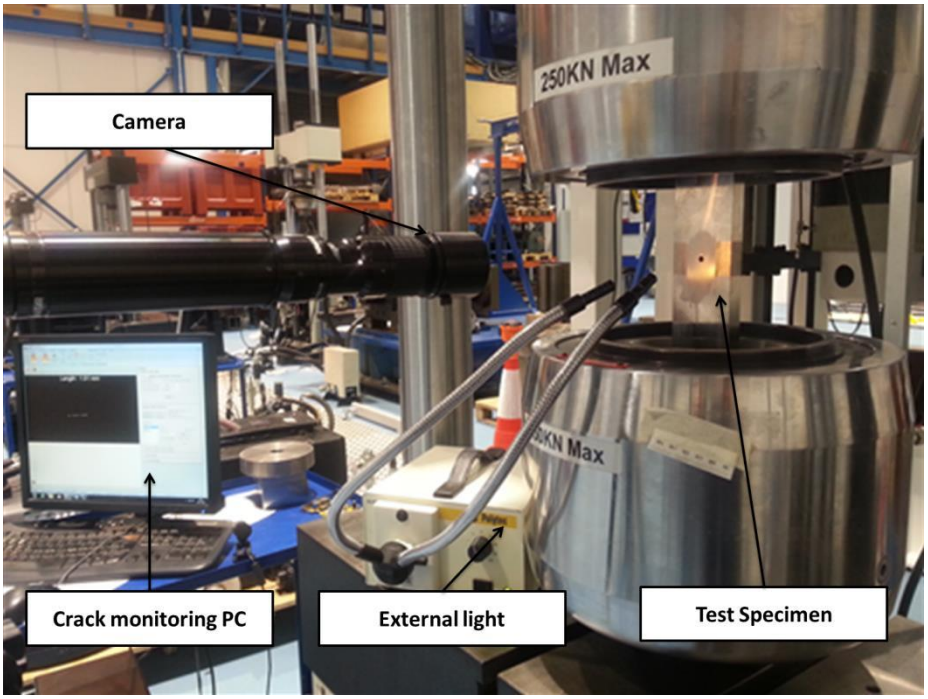

Figure 5-4: Crack growth monitoring during fatigue tests

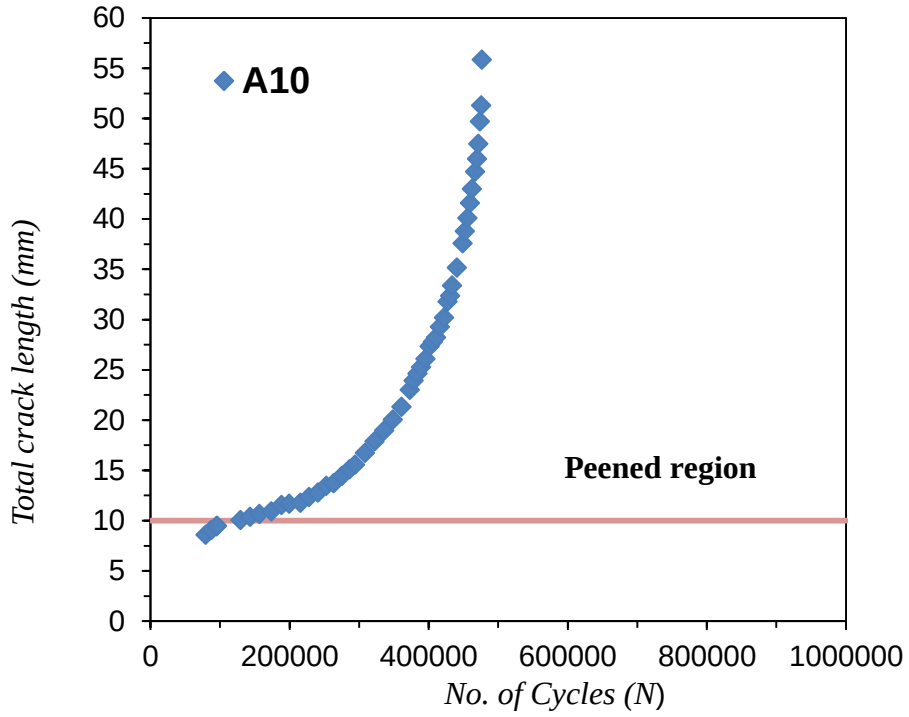

Figure 5-5: Fatigue crack growth data for A10

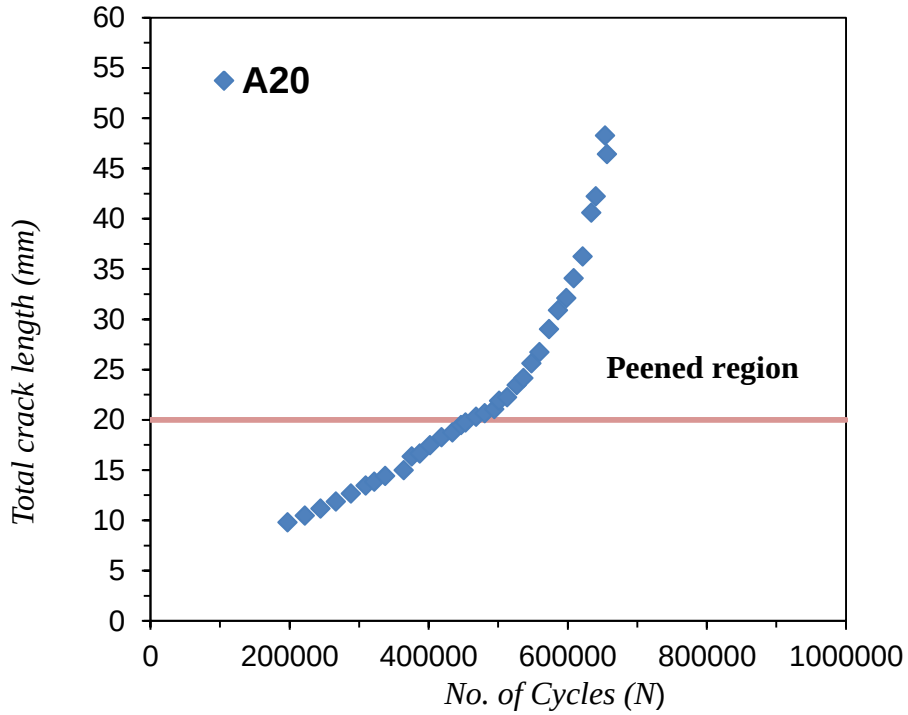

Figure 5-6: Fatigue crack growth data for A20

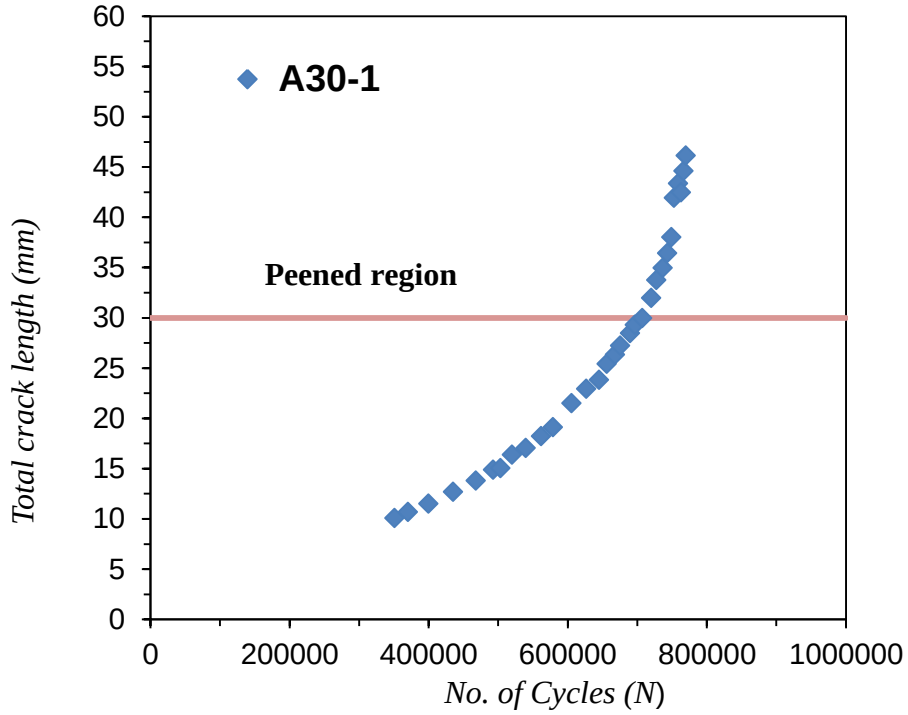

Figure 5-7: Fatigue crack growth data for A30-1

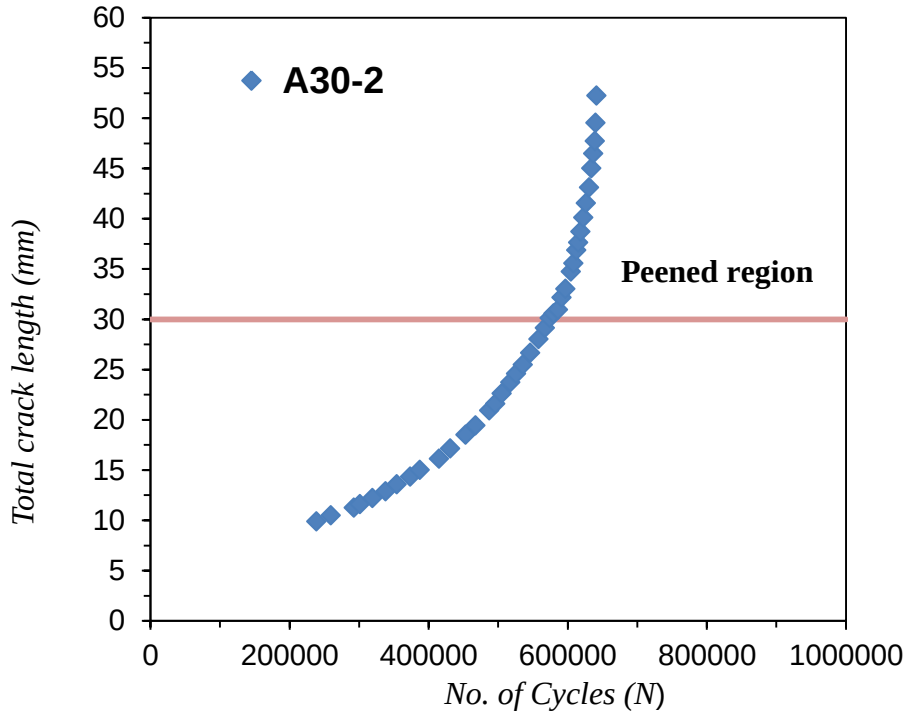

Figure 5-8: Fatigue crack growth data for A30-2

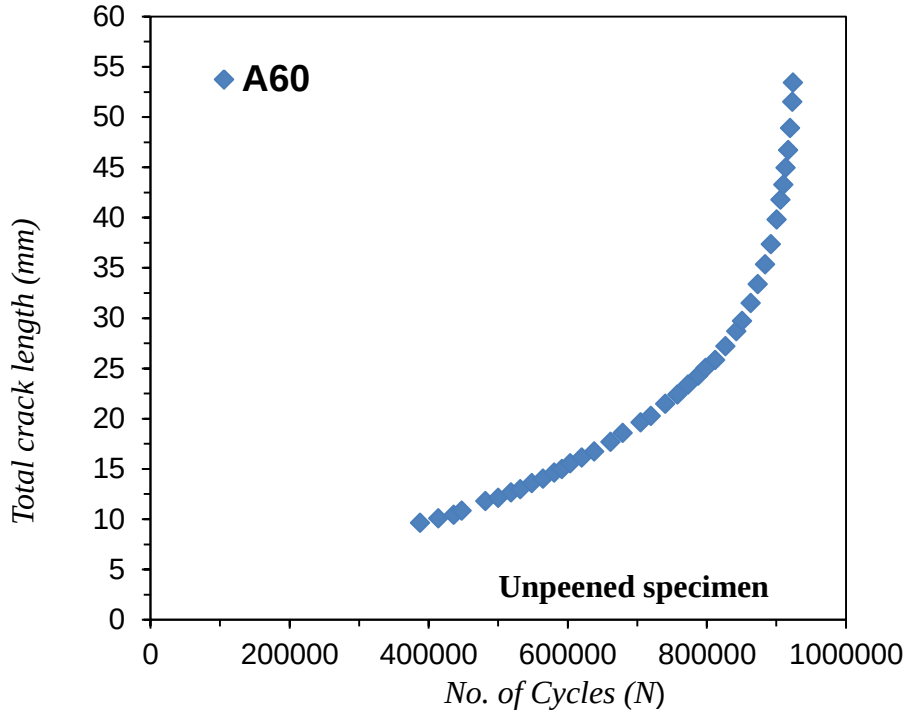

Figure 5-9: Fatigue crack growth data for A60

5.3 Experimental results from fatigue crack growth tests

The FCG data from each test were analysed using the equations and procedure detailed in section 5.2.4. The FCGRs, *da/dN*, for each test are correlated with the SIF range ΔK and the results are shown in Figure 5-11, Figure 5-12, Figure 5-13 and Figure 5-14 for the A10, A20, A30 and A60 specimens, respectively and the collected data from various tests are compared with each other in Figure 5-17. Note that the loading conditions and cyclic frequency were kept the same in all FCG tests performed in this study.

5.3.1 Fatigue test results for the A10 specimen

Specimen A10, contains a peening area 1.75mm from the head of the crack tip from each side. The total distance ahead of crack tip before reaching the peening area was 3.5mm. The A10 specimen was tested under tension-tension fatigue loading conditions. It was observed during the test that the FCG became retarded when the fatigue crack reached the peened region in the sample, as shown in Figure 5-10. The FCGR versus SIF range in the log-log scale for the A10 specimen in Figure 5-11 shows that there is deceleration in the early stage of the test and this is interpreted as fatigue crack retardation. Except for the retardation in the early stage in the FCG test, it can be seen that there is a relatively linear relationship between FCGR *da/dN* and SIF range ΔK for the rest of the test. As shown in Figure 5-11, the retardation due to the beneficial compressive residual stress in the peened area occurred in this specimen at the beginning of the test.

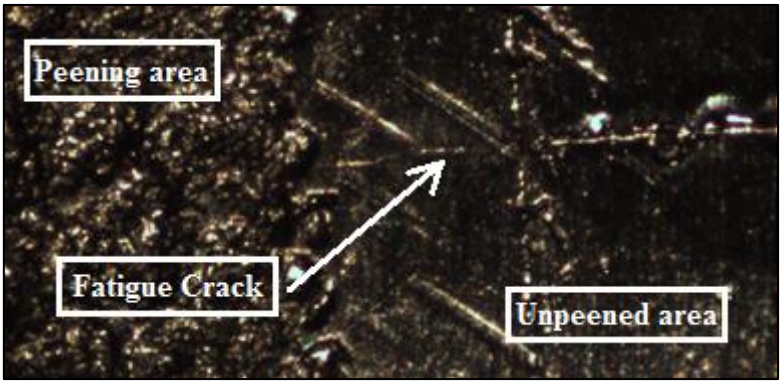

Figure 5-10: Fatigue crack growth retarded in the peened area

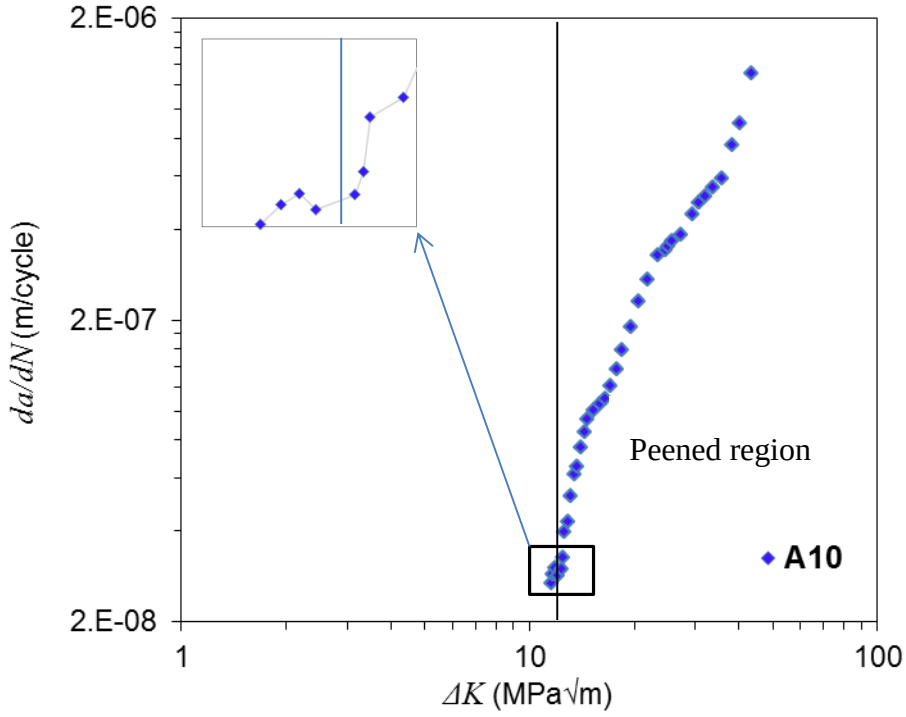

Figure 5-11: Fatigue crack growth results for A10

5.3.2 Fatigue test results for the A20 specimen

Specimen A20 which has a peened area 6.5mm from the head of the notch tip was tested under fatigue loading conditions and the results are shown in Figure 5-12. It can be observed in this figure that compressive residual stresses induced as a result of shot peening have decelerated the crack growth once the crack reached the peened region. Further seen in Figure 5-12 is that the FCGR shows an increasing trend with an increase in ΔK after the crack has entered the peened area.

5.3.3 Fatigue test results for A30 specimen

The FCG results obtained from the A30-1 and A30-2 specimens are presented in Figure 5-13. It can be seen in this figure that the FCGR decreases gradually when the fatigue crack reaches the peened area, which is a behaviour consistent with what was observed in the A20 and A10 specimens. Similarly, this reduction in the FCG trend is thought to be due to compressive residual stresses in the loading direction. Also, it can be observed that the starting points of the FCGR of A30-1 and A30-3 are different due to the uncertainty in machining of the starter notch by EDM.

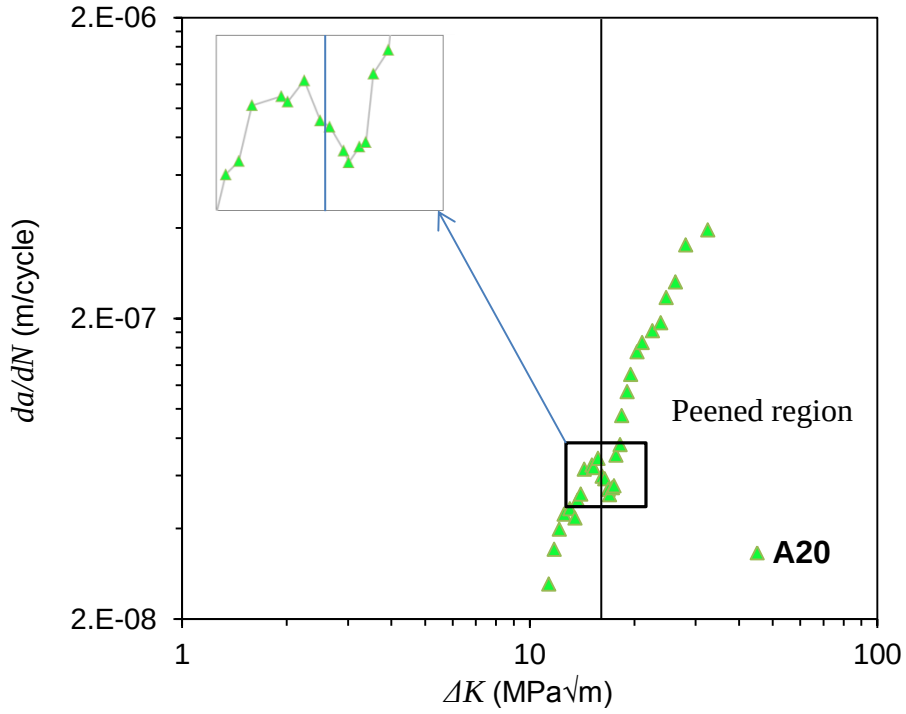

Figure 5-12: Fatigue crack growth results for A20

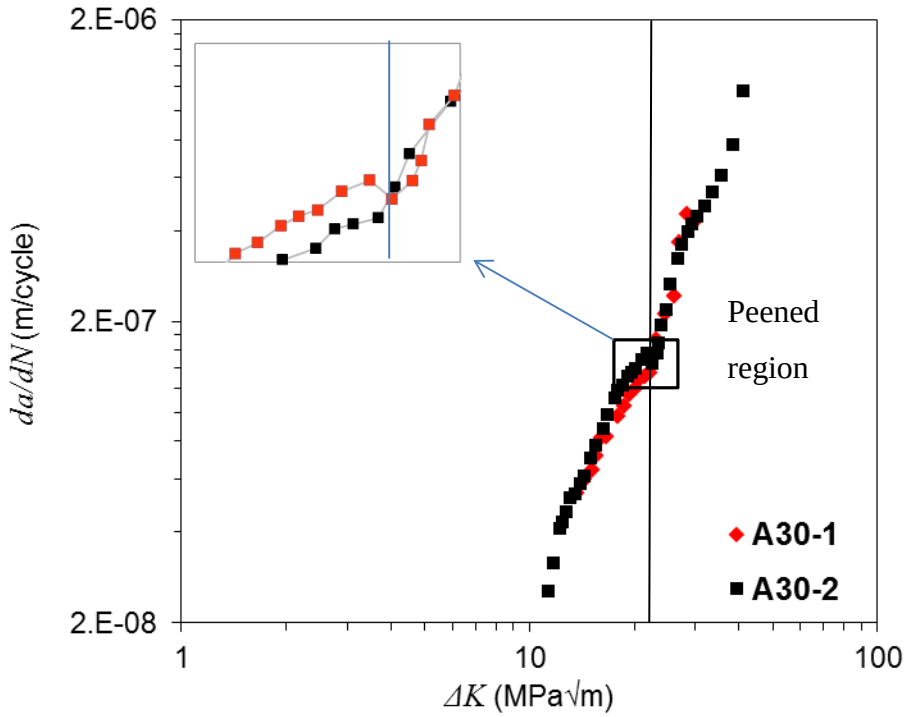

Figure 5-13: Fatigue crack growth results for A30

5.3.4 Fatigue test results for the A60 specimen

FCG test results from the tests performed on the A60 unpeened specimen are shown in Figure 5-14. The fatigue test results obtained from the unpeened specimen show that there is a smooth increase in FCGRs with an increase in the SIF range when the data are plotted in log-log axes, with no evidence of crack retardation (reduction in FCGR) in this sample. The results from the A60 unpeened specimen are compared with the data from the open literature on other grades of steel such as 50D with a yield strength of 370MPa (in unpeened condition), tested under load ratio 0.1 [186] and SE702 with a yield strength of 780MPa (in unpeened condition) [187] tested under load ratio 0.7 in Figure 5-14. It can be seen in this figure that the FCG versus stress intensity range data for all materials exhibit similar trends. The Optim700QL steel appears to have better resistance to FCG compared to SE702 steel and is less fatigue resistant compared to 50D steel.

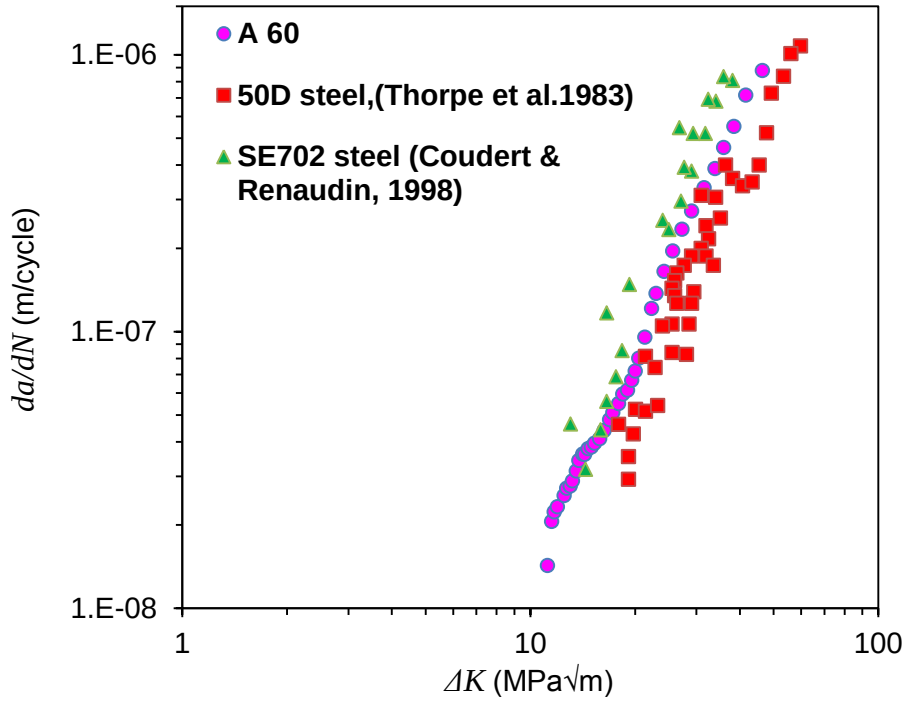

Figure 5-14: Fatigue crack growth rate for A60

5.4 Fractography

All FCG specimens were soaked in liquid nitrogen for 30 minutes post-testing and then broken open by loading them under tension on an Instron machine. The fracture surface of all FCG specimens were examined after being broken open and those for the A10 and A30-1 specimens are shown in Figure 5-15 and Figure 5-16, respectively, as examples. These pictures show that distinctive regions can be clearly observed on the fracture surface of the broken open specimens. First of all, the pre-cracking area, where the fatigue load was reduced from 120kN to 90kN, leads to the generation of beachmarks on the fracture surfaces, which can be observed and identified on the fracture surface. The next region observed on the fracture surface is the fatigue propagation region which is clearly demarcated on the fracture surface. Also, it can be clearly seen that a transition area from fatigue to fast fracture is observed towards the end of the tests where the SIF approaches its critical K_{IC} value in the accelerating FCG region. Crack tunnelling is also apparent at the end of the transition region which demonstrates a faster crack growth at the mid-thickness of the specimen, compared to the outer sides of the specimen. This transition region is followed by a fast fracture region at the end of the fracture surface which appears to be shinier than the rest of the fracture surface. Also observed in Figure 5-15 and Figure 5-16 is that there are shiny edges in both the A10 and A30-1 specimens which happened to be in the shot peened area. Knowing that shot peening induces compressive residual stresses on the outer surface of the specimens, which subsequently retard the FCG, the force-balance characteristic of residual stress leads to a tensile residual stress field in the mid-thickness of the test specimens. The tensile residual stress forces the fatigue crack to grow faster at the mid-thickness of the specimen and it is retarded at the outer surface of the specimen, which leads to a more severe crack tunnelling in these partially surface shot peened specimens, as seen in Figure 5-15 and Figure 5-16. This implies that when an optical technique is used to monitor the crack growth on the outer surface of partially peened specimens, some inaccuracies might be encountered in FCG measurements. This is due to crack tunnelling, and hence a greater difference between the crack growth at the mid-thickness of the sample and the extent of the crack extension is measured using a camera at the outer surface of the specimen.

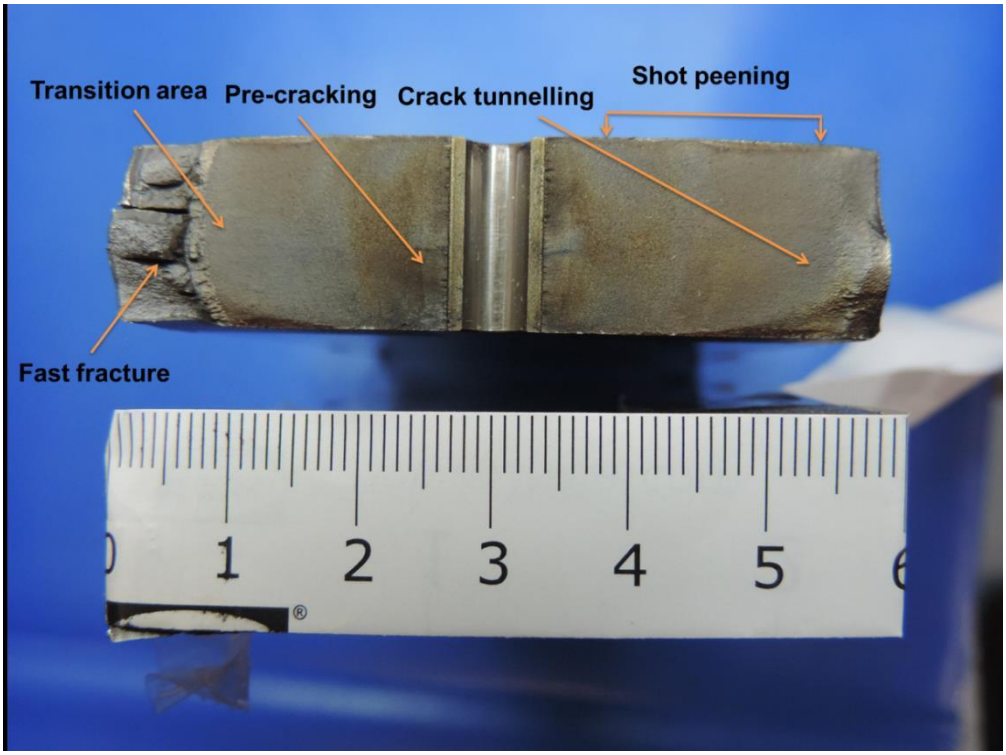

Figure 5-15: Fracture surface for A10 specimen

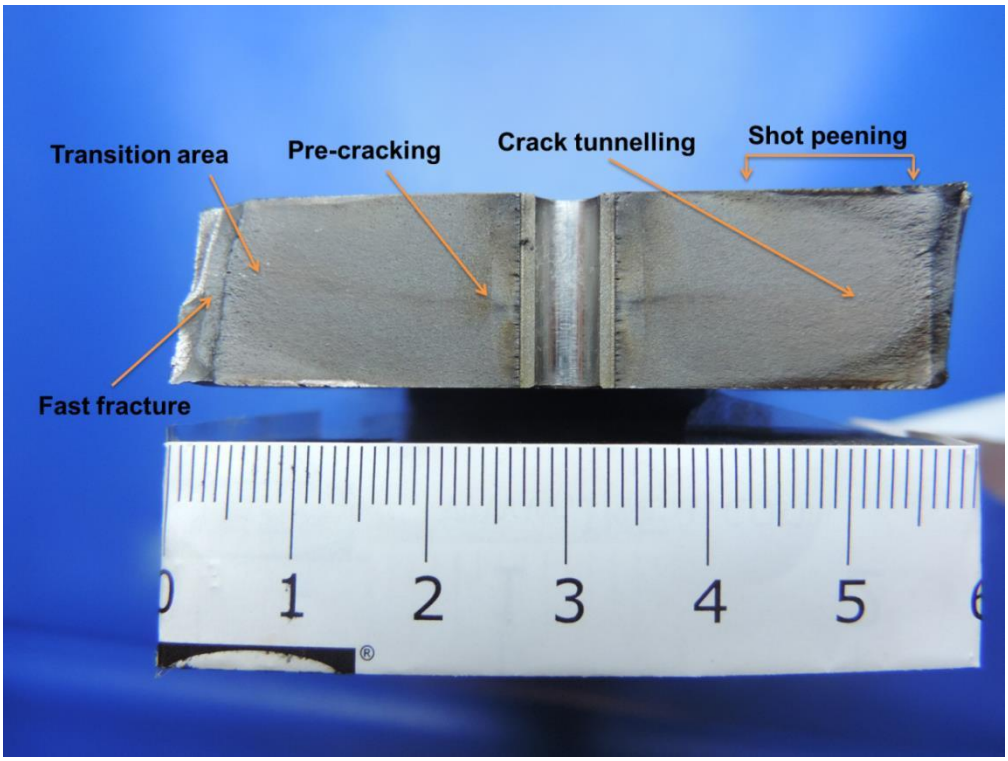

Figure 5-16: Fracture surface for A30 specimen

5.5 Discussion

The FCG results from the tests performed in this study are collectively shown and compared in Figure 5-17. This figure clearly demonstrates that partial surface shot peening significantly influences the FCG behaviour of the material. The results of the A60 test data show that the FCGR linearly increased with an increase in the SIF range when the data were plotted in log-log axes. This behaviour is known as the Paris law and is typically observed in all FCG tests [4]. It can be seen in Figure 5-17 that a reduction in FCGRs was observed in all specimens, which were partially peened, with the A10, A20 and A30 specimens showing a retardation at lower, intermediate and higher ΔK values at the entrance of peened region, respectively. This shows that the SIF range at which the fatigue crack retardation occurs increases as the area of the unpeened region increases on the surface of the examined specimens. The presented test results have been divided into three regions in Figure 5-17 for clarity. At lower range of SIF (region I), it can be observed in Figure 5-17 that there is no noticeable difference in the FCG results, though the fatigue crack in A10 specimen has already entered the peened region and shows a slight drop in FCG rate. The most interesting region is the intermediate SIF range of 15-30MPa$\sqrt{m}$, which is referred to as region II in Figure 5-17, in which the partial peening area has significantly affected the FCGRs in all of the partially peened specimens, as demonstrated in Figure 5-18. The comparison of the test results from A10, A20 and A30 specimens in region II shows that the highest and lowest FCG trends were observed in A10 and A60 (i.e. unpeened) specimens, respectively, with the test data from A20 and A30 samples falling in between and close to each other. It can be seen that within region II the SIF range for a given value of ΔK, the FCGR in the A10 partially peened specimen is around twice faster than the unpeened sample. This indicates that although the FCG is retarded as a result of partial surface shot peening, the FCG trend shifts up simultaneously due to the formation of tensile residual stresses at the mid-thickness of the specimen. Further observed in Figure 5-17 is that the extent of FCG rate reduction in the A20 specimen is greater than those seen in the A10, A30-1 and A30-2 specimens. The fatigue test results confirm that the extent of tensile residual stresses increases as the size of the unpeened region decreases in the partially shot peened specimens. In other words, if surface shot peening is used to introduce compressive residual stresses in a component, and subsequently reduce

FCGRs, a partially unpeened region can lead to a significant increase in the overall FCG trends. Finally seen in Figure 5-17 is that in the highest SIF range of larger than 30MPa√m (region III) similar FCG trends can be observed in the unpeened and partially peened specimens.

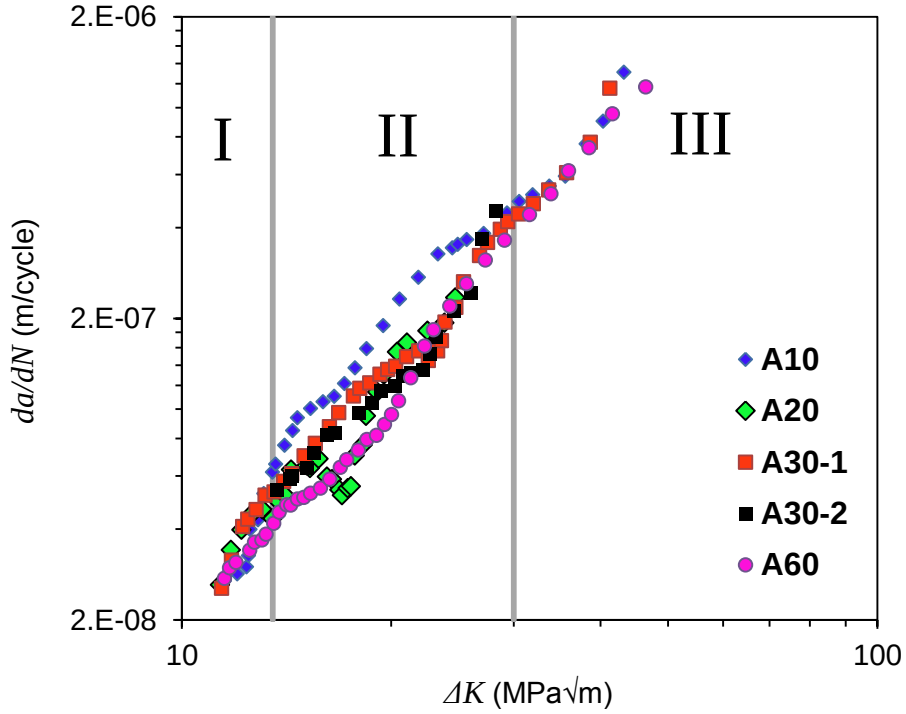

Figure 5-17: Comparison between different fatigue crack growth trends

Knowing the shot peening induces compressive residual stresses on the outer surface of the specimens, which subsequently retard the FCG, the force-balance characteristic of residual stress leads to a tensile residual stress field in the mid-thickness of the test specimens. In the present study, the crack introduced through the thickness implies that the crack front is subjected to compressive residual stress and tensile residual stress. The crack front is subjected to compressive residual stress at the outer surface due to the peening process while the crack front is subjected to tensile residual stress at the mid-thickness of the specimen, as shown in Figure 5-19. Under tension-tension fatigue load, the tensile residual stress forces the fatigue crack to grow faster at the mid-thickness of the specimen and it is retarded at the outer surface of the specimen, which leads to a more severe crack tunnelling in these partially surface shot peened specimens, as seen in the fractography investigation. However, despite the fact that the full surface peening

improves the fatigue crack initiation (S-N curves) according to the data in the literature, the observed trends in this work suggest that fatigue crack propagation will be the fastest in fully peened specimens.

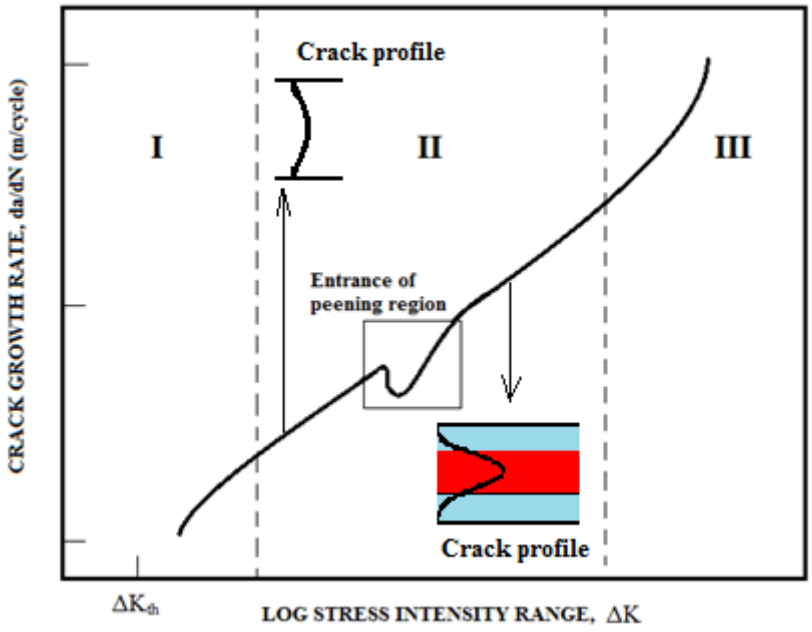

Figure 5-18: Illustrative diagram demonstrating the effect of partial peening on FCGR

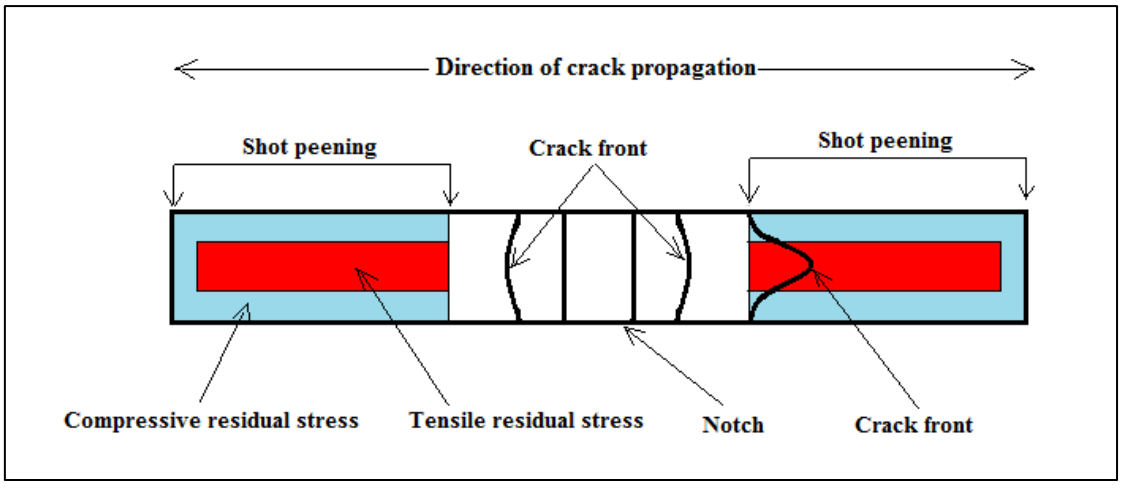

Figure 5-19: Schematic diagram for a cross section of the dog-bone specimen

5.6 Summary

This chapter presented the experimental investigation into the effect of a partial shot peening on FCGR under tension-tension fatigue loads. Dog-bone specimens were fabricated from high strength ferritic steel with a yield strength of 690MPa. A total of five fatigue tests were carried out under different, partial shot peening regions with respect to crack tip and specimen symmetry line. The loading conditions were kept the same during all the FCG tests performed in this study with a maximum fatigue load of 90kN and load ratio of 0.1. The FCG results of peened specimens were compared with those obtained from the specimen geometry but with no peening. The results show the partial shot peened region ahead of the initial notch tip plays a significant role in the fatigue crack behaviour of the material. The FCGs were retarded when the fatigue crack reached the peened region due to beneficial residual stress existence. Although partial peening resulted in crack retardation as the crack entered the peened region, the overall fatigue crack growth rate for the majority of region II was higher for the peened samples compared to the unpeened sample. The tensile residual stress generated in the mid-width of the specimens due to the partial shot peening region led to the acceleration of the fatigue crack propagation. The tensile residual stress generated in the mid-thickness of the specimen caused crack tunnelling. The fatigue test results show that the partial shot peened region led to a crack growth rate around twice as fast as that of the unpeened specimen. The partial peening is harmful for specimens under tension-tension fatigue load due to the fatigue crack front facing tensile residual stress region in the mid-thickness of the specimen which can lead to accelerate of the FCGR. In the case of fatigue crack or defect/flaw existence under tension-tension fatigue load, applying shot peening on the entire surface can affect the fatigue crack initiation and growth due to the fatigue crack front lying within the compressive residual stress.

6 The Influence of Partial Surface Cavitation Shotless Peening on Crack Shape Evolution and Fatigue Crack Growth

6.1 Introduction

The lifetime of structural components subjected to cyclic loading conditions is influenced by different factors, such as pre-existing defects/flaws, operation environment, effective stresses and the number of fatigue cycles. The effective stresses in components and structures may consist of applied stresses and residual stresses induced during fabrication processes such as welding, surface treatment, bending, etc. The residual stresses can be beneficial (i.e. compressive) or harmful (i.e. tensile) depending on their pattern and magnitude. The introduction of compressive residual stresses in components and structures is known to be an efficient tool to improve the fatigue life and enhance the mechanical properties of the engineering components and structures.

Most fatigue failures in engineering components occur due to surface cracks/defects and the remaining lifetime strongly depends on the material's resistance to surface crack growth [188]. Therefore, surface treatment prior to operation can potentially play a significant role in the life extension and fatigue resistance of structural components. Various studies have been carried out in the past to investigate the effects of residual stresses, induced into structural components due to surface treatment, on the subsequent fatigue behaviour of engineering materials.

Although some limited studies have been performed in the past to examine the influence of cavitation shotless peening on the structural integrity of metallic materials, the influence of cavitation shotless peening on the FCG behaviour of HSSs has received little attention so far to expand the application of this surface treatment technique to wider industries such as offshore oil & gas and offshore wind. Cavitation shotless peening has advantages over conventional peening methods, such as better surface finish and penetration depth of residual stress up to 0.5mm. In this chapter, an experimental investigation has been conducted to examine the influence of a peened area on surface crack evolution and propagation in a high strength ferritic steel. The

results obtained from the experiments are presented and discussed in terms of the effectiveness of the partial surface shotless peening technique in crack retardation and fatigue life extension of engineering components and structures.

6.2 Experimental details

6.2.1 Material and specimen design

The material used in this project is *Optim700QL* high strength ferritic steel. The mechanical properties and chemical composition of this material have been summarised in Table 5-1. To conduct this study, 4-point bend specimens were machined from an *Optim700QL* plate. As seen in Figure 6-1 the 4-point bend specimens had 330mm length, 100mm width and 25mm thickness. As shown in Figure 6-1, a semi-circular starter notch with a radius of 5mm was machined at the centre of the 4-point bend specimens. The specimens were partially peened using the cavitation shotless peening technique for 120mm along the axial direction of the specimen geometry.

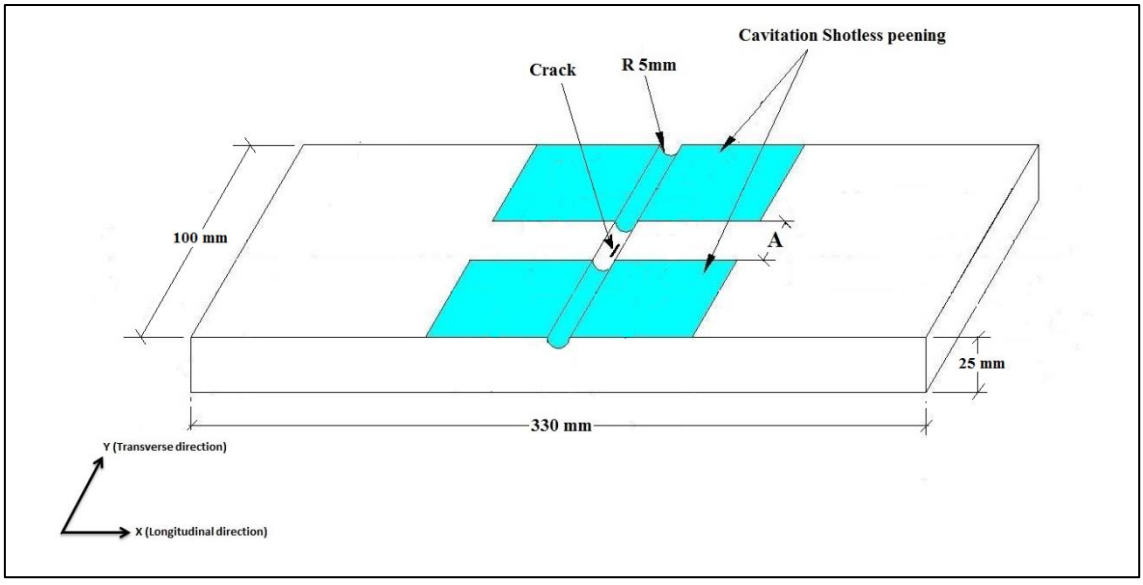

Figure 6-1: Geometry of 4-point bend test specimen

Seven test specimens with different extents of cavitation shotless peening areas, with a 10, 20 and 30mm gap in the unpeened region (see the "A" dimension in Figure 6-1), were prepared and tested in total. Visual inspection shows that cavitation shotless peening leads to a good surface finish on which it is hard to distinguish between peened and unpeened regions. Figure 6-2 shows the surface finish of *Optim700QL* high strength ferritic steel treated by cavitation shotless peening and shot peening. The number of tests performed on specimens with different extents of partially peened area and the corresponding loading conditions in each test are summarised in Table 6-1. The applied loads for each test were chosen by considering the SCF and yield strength of the material to avoid any significant plasticity at the crack tip. The SCF solutions for this geometry were found in Peterson's Handbook [189] in which the SCF value for the specimen dimensions employed in this project was found to be 2.9.

Table 6-1: Fatigue crack growth test matrix for 4-point bend specimens

Specimen ID	Extent of the unpeened area, A	Number of specimens	Operation load
A10-1	10mm	1	Max. load = 70kN
A20-1	20mm	1	Min Load = 7kN
A30-1	30mm	1	Load ratio = 0.1
A60-1	Without peening	1	Loop wave matrix
A10-2	10mm	1	Max. load = 60kN
A20-2	20mm	1	Min Load = 6kN
A30-2	30mm	1	Load ratio = 0.1 Loop wave matrix

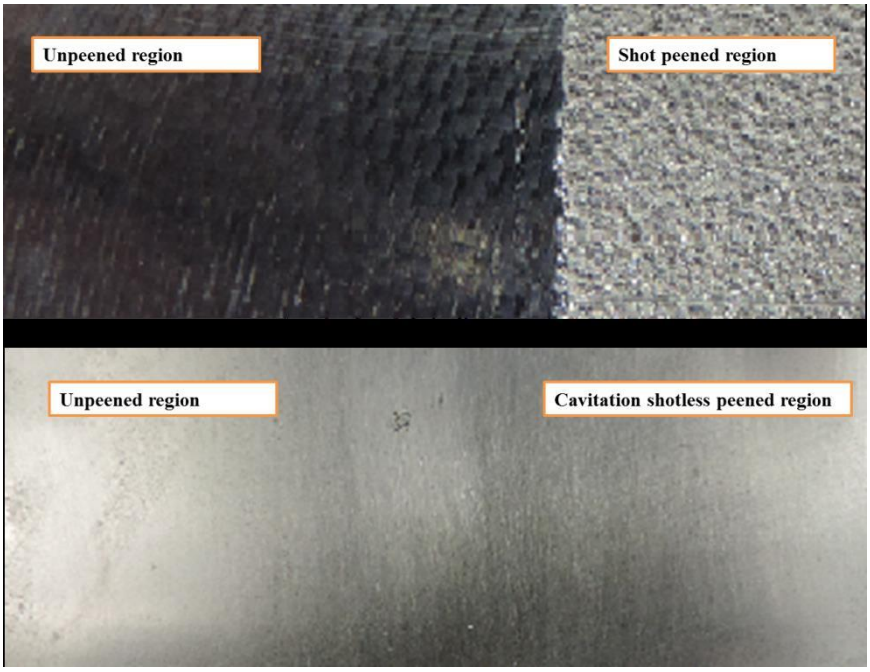

Figure 6-2: Surface finish of cavitation shotless peening and shot peening

6.2.2 Fatigue test set-up

FCG tests were set up and conducted on four-point bend specimens using a servo-hydraulic Instron machine with maximum load carrying capacity of 100kN, as shown in Figure 6-3. The schematic force and moment diagrams for a 4-point bend test are schematically shown in Figure 6-4. The applied load was calculated by considering the SCF to avoid the plasticity at the notch tip. In order to examine the influence of different stress levels on the FCG behaviour of the material, two maximum load cases of 70kN and 60kN were considered. The load R-ratio of 0.1 and frequency of 3Hz were applied in all tests. A summary of the loading conditions applied in all tests is given in Table 6-1.

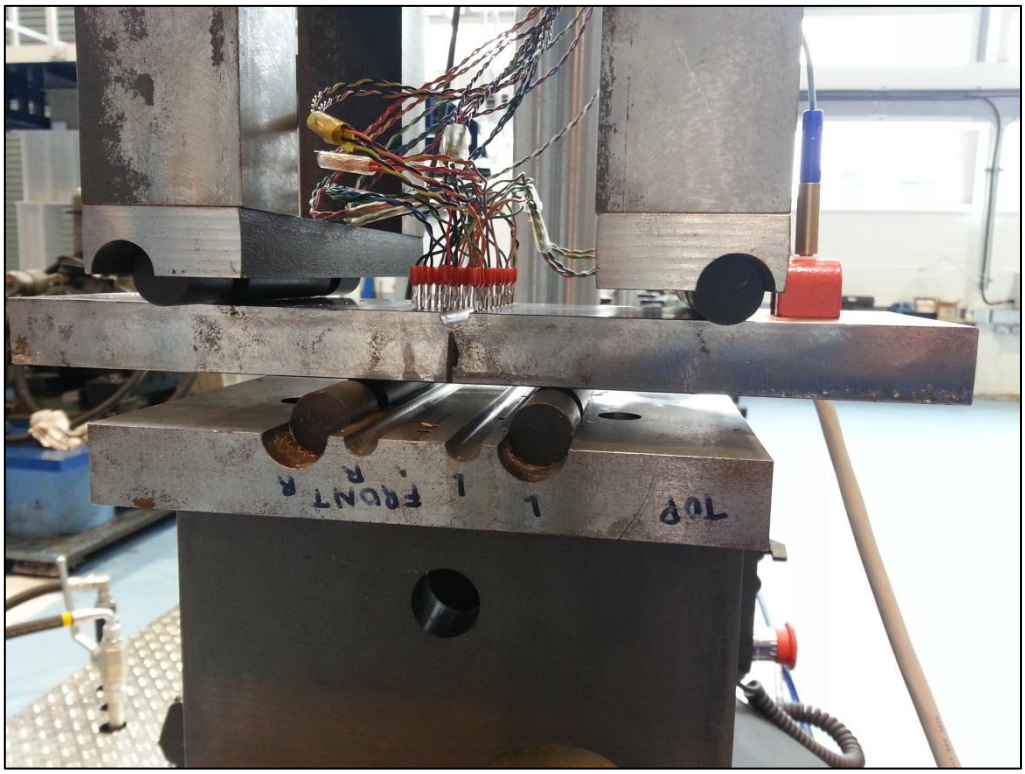

Figure 6-3: Experimental set-up of four-point bend fatigue test

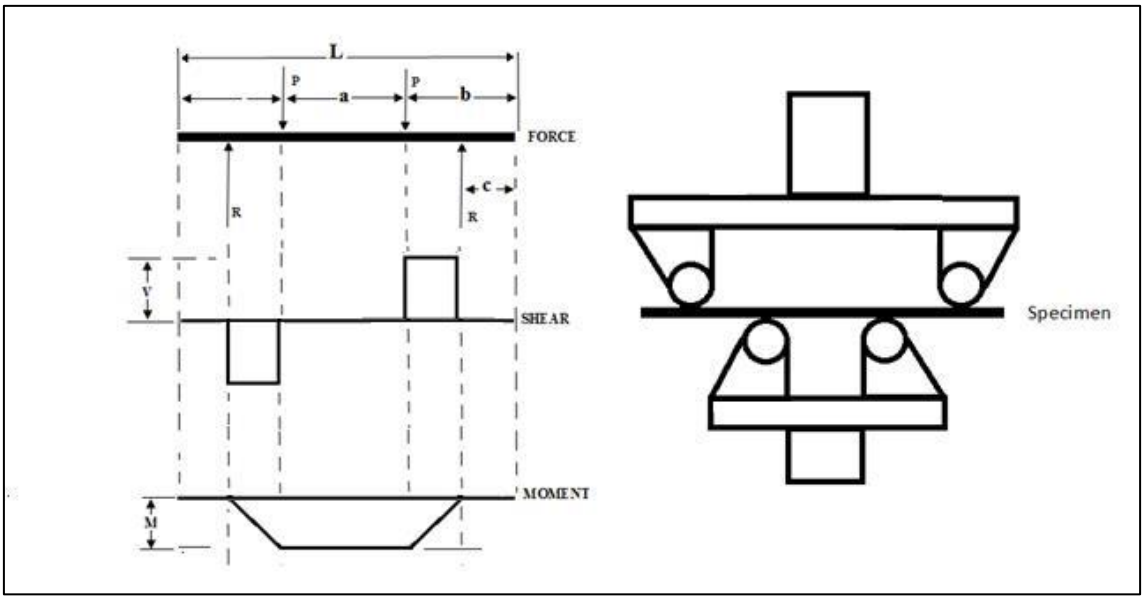

Figure 6-4: Schematic diagram for 4-point bend test set-up

6.2.3 Crack inspection and monitoring

The Alternating Current Potential Difference (ACPD) technique was used to measure and monitor the crack depth during FCG tests. The ACPD is a non-destructive technique in which the current is injected through a conductor and this causes the current to flow in a thin layer on the outer surface, which is often referred to as the skin effect. High surface voltage is generated as a result of the current passing through the small section area of the material [190]. The ACPD requires two connections between the specimen and the instrument, which are the field connection, or current output, and the voltage input. The voltage input can be from a single probe or from a multi-number of probes to monitor crack growth during the test [191, 192]. In this technique, the alternating current (AC) is injected at one side of the crack (P1) and flows along the specimen surface, down and up the crack, and out through the another side of the crack (P2) as shown in Figure 6-5. The current passes through the thin skin of the specimen's thickness (δ) and encompasses the crack of depth (d). The dropping in the voltage is measured by a probe with a fixed distance between its electrodes (Δ). [193]

$$d = \frac{\Delta}{2}\left(\frac{V_2}{V_1} - 1\right) \qquad \textbf{Equation 6-1}$$

where: V_1 represent the reference voltage which is measured away from the crack, and V_2 represent the voltage measured across the crack sides. The voltage ratio represents the crack depth by means of a calibration procedure.

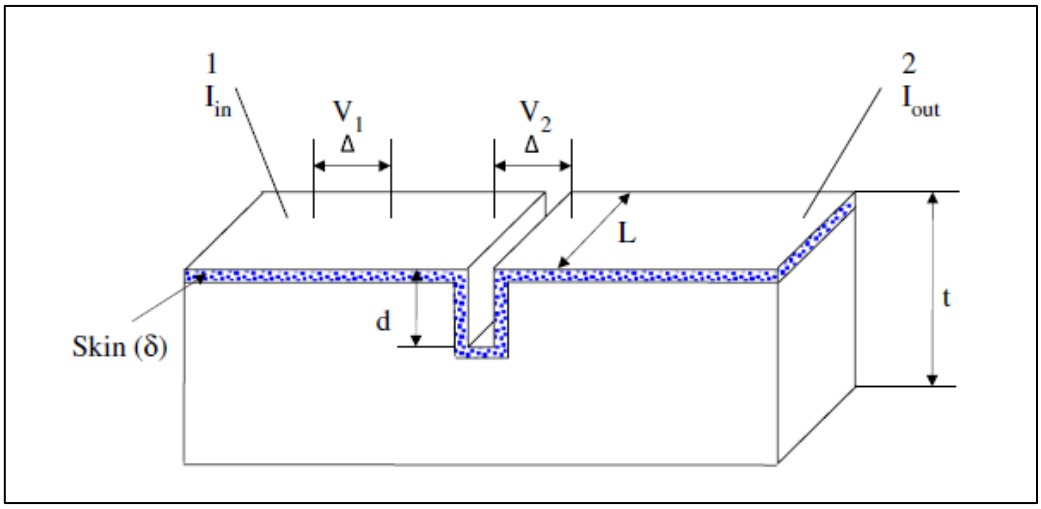

Figure 6-5: Schematic diagram of the ACPD technique-surface crack [193]

In this work, in order to monitor the crack growth, the voltage connections were held in fixed positions on the specimen. This was done by using spot welded pins as shown in Figure 6-6. An eight-set of spot welded pins was used to monitor the crack evolution and growth in the test specimens and a pin was used to eliminate common-mode voltages, as seen in Figure 6-7. The crack depths were auto-recorded in (mm) by using an ACPD Crack Microgauge-TSC [194].

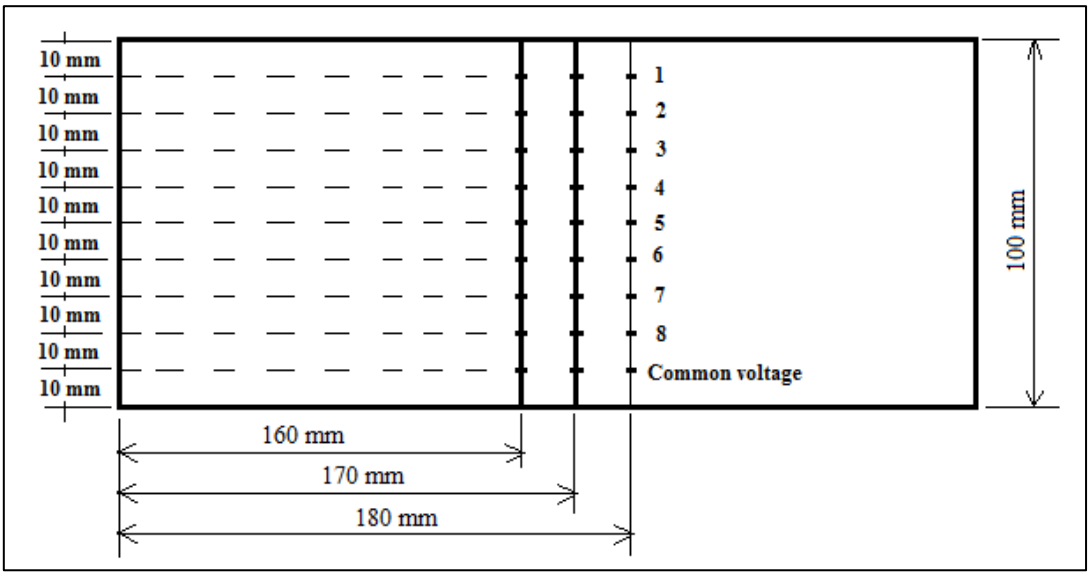

Figure 6-6: Map of spot welded pins distribution along the width of the specimen

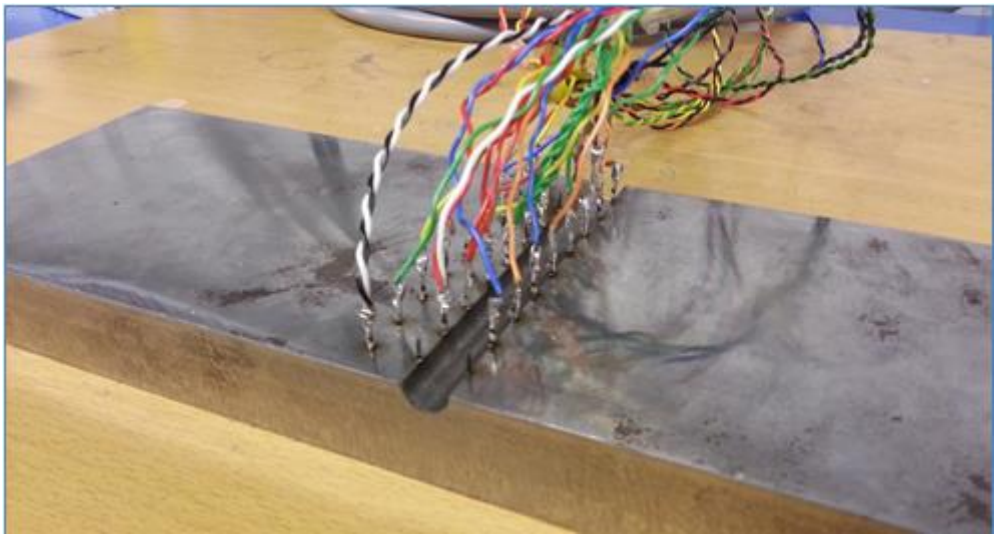

Figure 6-7: ACPD wires connected to spot welded pins on the specimen

6.2.4 Fatigue crack growth test method

FCG tests were carried out on 4-point bend specimens at the ambient temperature of 25°C. The sinusoidal wave loads were implemented in the wave matrix software provided by Instron and applied to the samples. A loop wave matrix was employed in the fatigue tests to account for an extra step to hold the specimen under mean load while the crack mouth was open for accurate ACPD measurements to be made, as schematically shown in Figure 6-8. A sequence of loops was designed in the wave matrix to apply fatigue loading to the test specimens. Each loop was divided into three steps with a total time of 14.5 minutes. These three steps are described as follows:

Step 1 : The specimen is ramped up to the minimum load (within 2 seconds).

Step 2 : The sinusoidal load is applied between the maximum and minimum loads.

Step 3 : Holding for 26 seconds at the mean load to allow ACPD measurement to be made while the crack mouth is open.

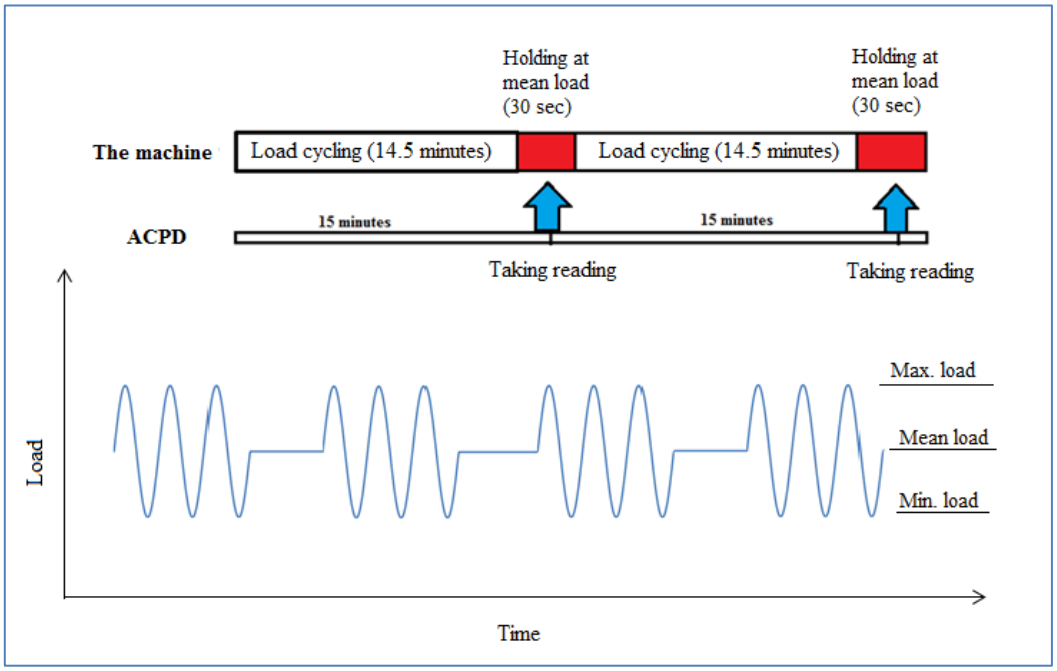

Figure 6-8: Schematic diagram of the loop wave matrix

6.2.5 Fatigue crack growth analysis

The SIF range ΔK for the specimen geometry considered in this study was calculated according to the Newman & Raju model [166]. This model involve equations to calculate the SIF for the semi-elliptical surface crack, which depends on crack length, crack depth, plate width, plate thickness and parametric angle for bending and tension load. The model was originally derived based on a 3-D finite element analysis for an elastic plate subjected to pure bending or tension loading conditions.

According to the Newman & Raju [166] model, the SIF for combined bending and tension load can be calculated using:

$$K_I = (S_t + HS_b)\sqrt{\pi \frac{a}{Q}} F(\frac{a}{t}, \frac{a}{c}, \frac{c}{b}, \phi) \qquad \textbf{Equation 6-2}$$

where K_I is the SIF for Mode I. The full procedure is detailed in Appendix F.

The FCGR, which is the crack extension rate due to fatigue loading, can be represented by the average crack extension per cycle. A seven-point incremental polynomial technique, which is suitable for a test performed continuously and smoothly, has been used to calculate the FCGR in accordance with ASTM E647 [185] as explained in section 5.2.4.

6.3 Experimental results from fatigue crack growth tests

6.3.1 Crack length measurements

The fatigue tests were conducted on 4-point bend specimens. Seven specimens were tested to investigate the effect of partial peening on the FCG behaviour under bending loads. The FCG was monitored throughout the width and thickness of the specimens using ACPD. The ACPD probes were allocated to A10, A20 and A30 on fixed distances, as shown in Figure 6-9, Figure 6-11 and Figure 6-13, respectively. As explained earlier and seen in Table 6-1, the first four specimens, denoted A10-1, A20-1, A30-1 and A60-1, were tested under 70kN maximum load and load ratio of R = 0.1, whereas the last three specimens, denoted A10-2, A20-2 and A30-2, were tested under 60kN maximum load and R = 0.1. The fatigue crack length measurements, obtained from ACPD measurements, plotted against the number of fatigue cycles, are as shown

in Figure 6-10 to Figure 6-15 for A10-1, A20-1, A30-1 and A60-1, respectively. The datasets presented in this figure are given for 10-80mm distances from the outer edge of the specimen (i.e. which has been taken as the reference point) along the width of the specimen. Comparing the crack growth trends at 20mm and 80mm distances from the outer edge it can be observed that similar trends are evident due to symmetrical peening with respect to the specimen symmetry line. The FCG results show that the reading of the probe lies at mid-width of the specimens (50mm away from the outer edge and along the specimen symmetry line) and is around 0.5mm, which is the depth of the machined crack as the starter crack. Figure 6-12 shows that the fatigue crack was initiated at the mid-width of the specimen (50mm away from the outer edge and along the specimen symmetry line) where the started crack was machined into the specimen. Also seen in this figure and the results obtained from other tests performed under 70kN maximum load, is that no evidence of crack retardation due to cavitation shotless peening was observed in the FCG behaviour of this specimen, which was tested at 70kN maximum load, and smooth crack growth trends were measured throughout the entire duration of the fatigue tests. However, in the remaining three tests under 60kN maximum load, the crack retardation is evident in the crack growth data, as shown in Figure 6-16 to Figure 6-18 for A10-2, A20-2 and A30-2, respectively.

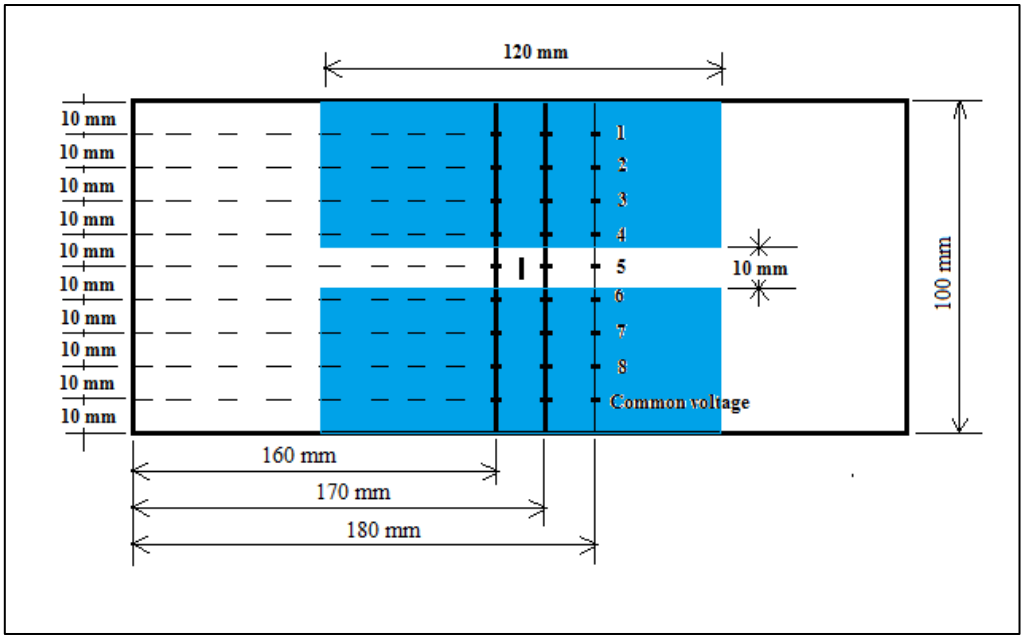

Figure 6-9: Map of spot welded pins distribution along the width of the A10 specimen

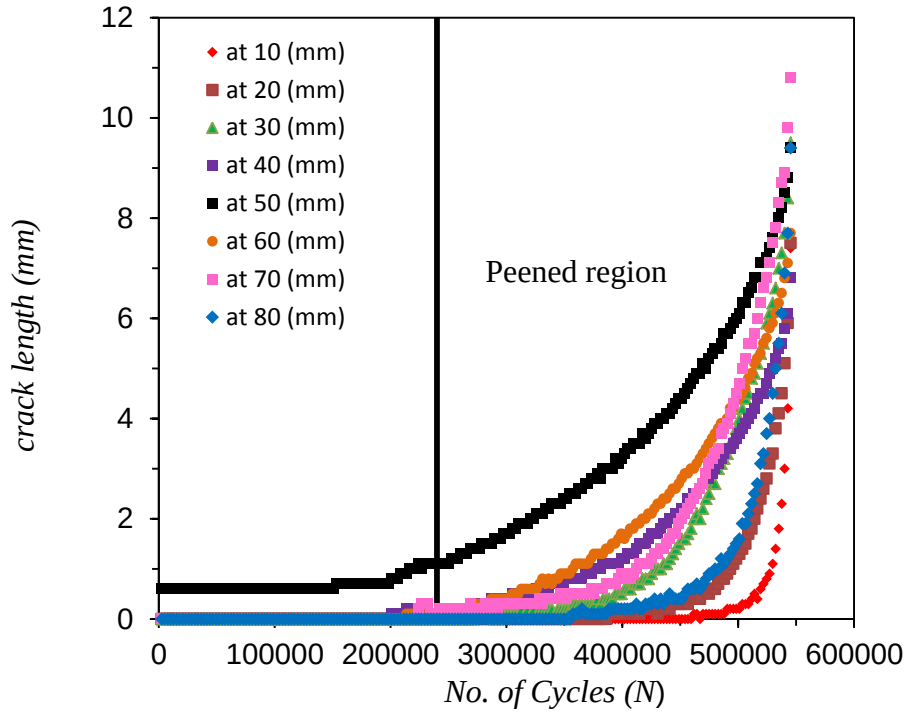

Figure 6-10: Fatigue crack growth data versus number of cycles for A10-1 specimen

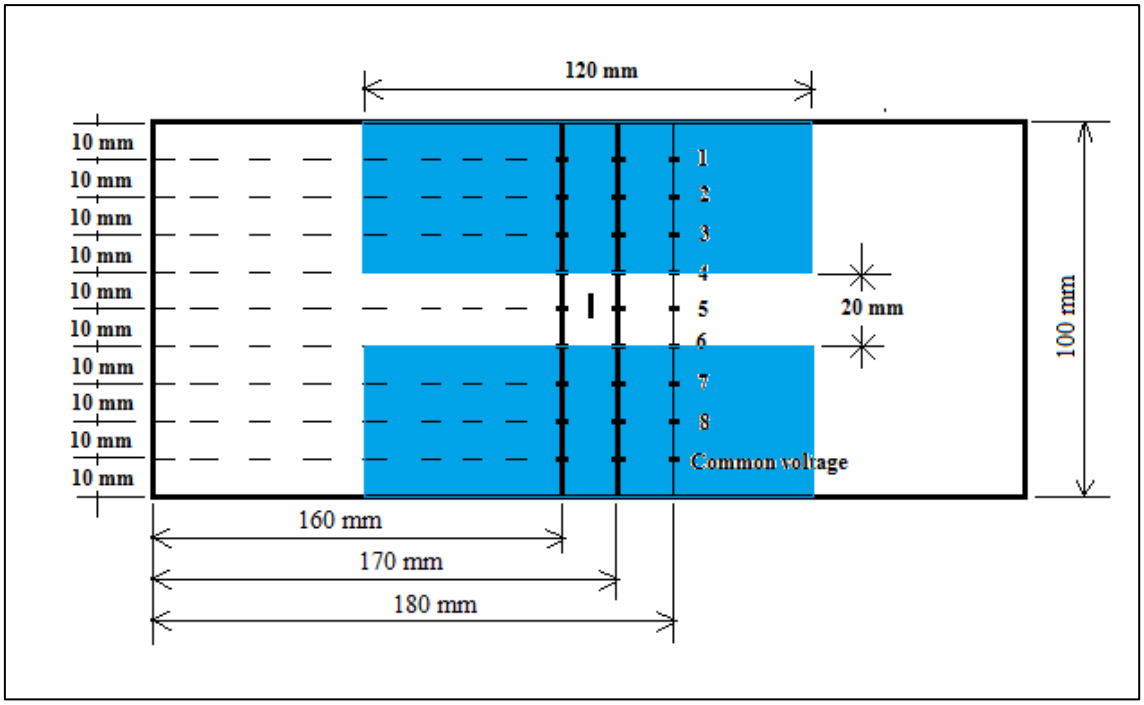

Figure 6-11: Map of spot welded pins distribution along the width of the A20 specimen

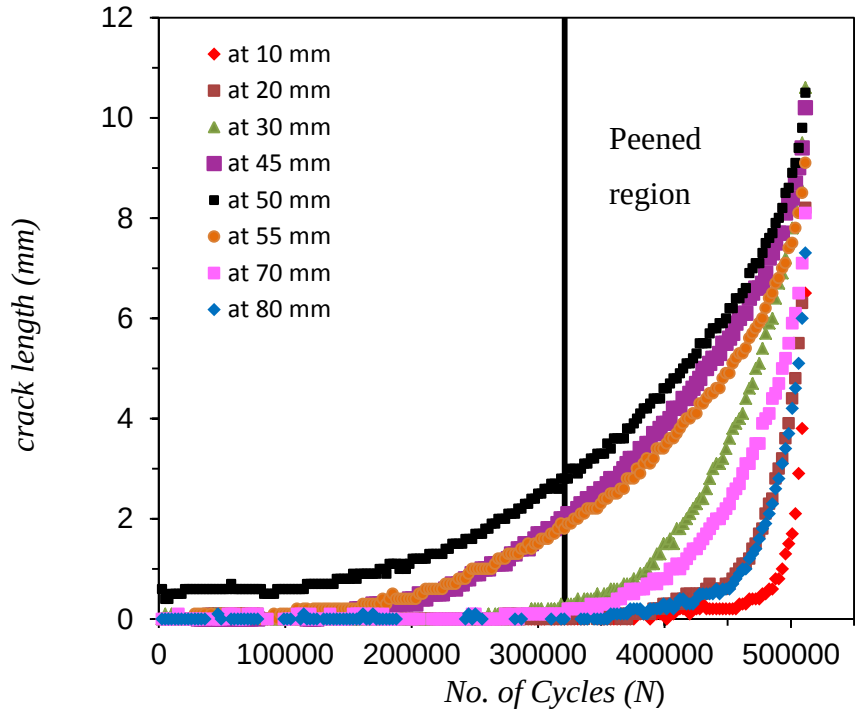

Figure 6-12: Fatigue crack growth data versus number of cycles for A20-1 specimen

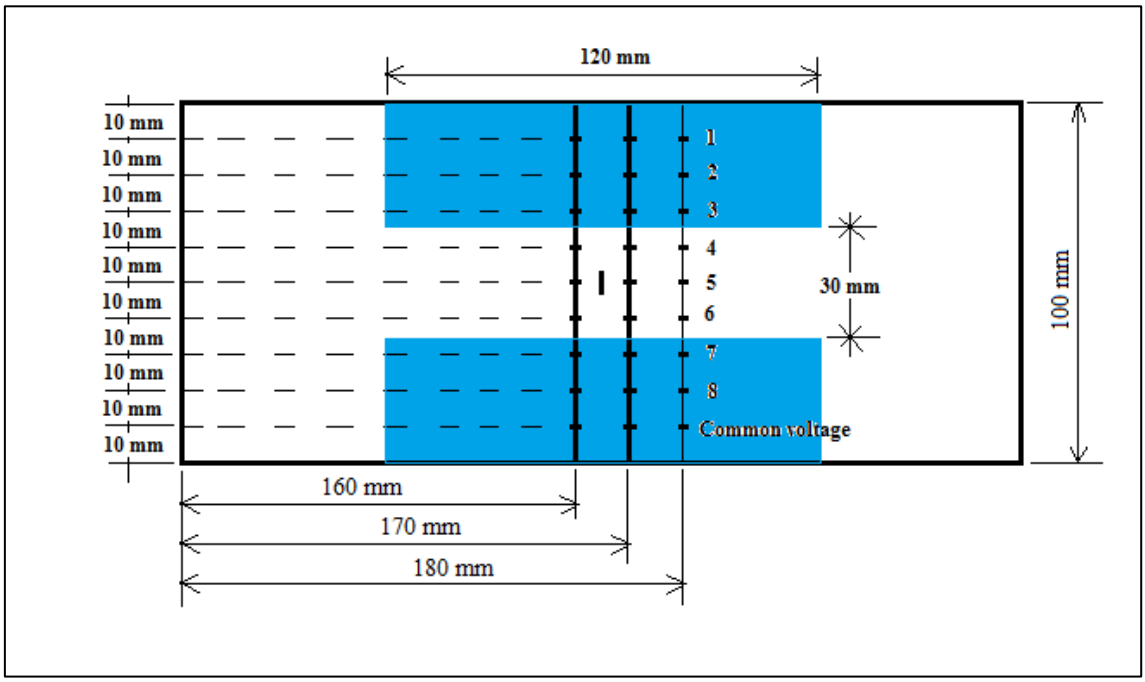

Figure 6-13: Map of spot welded pins distribution along the width of the A30 specimen

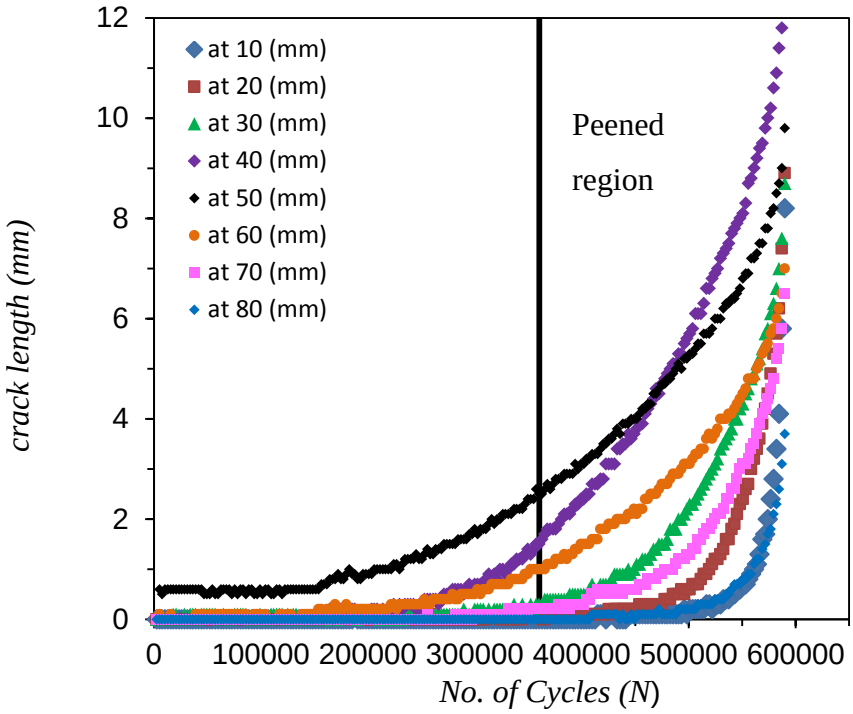

Figure 6-14: Fatigue crack growth data versus number of cycles for A30-1 specimen

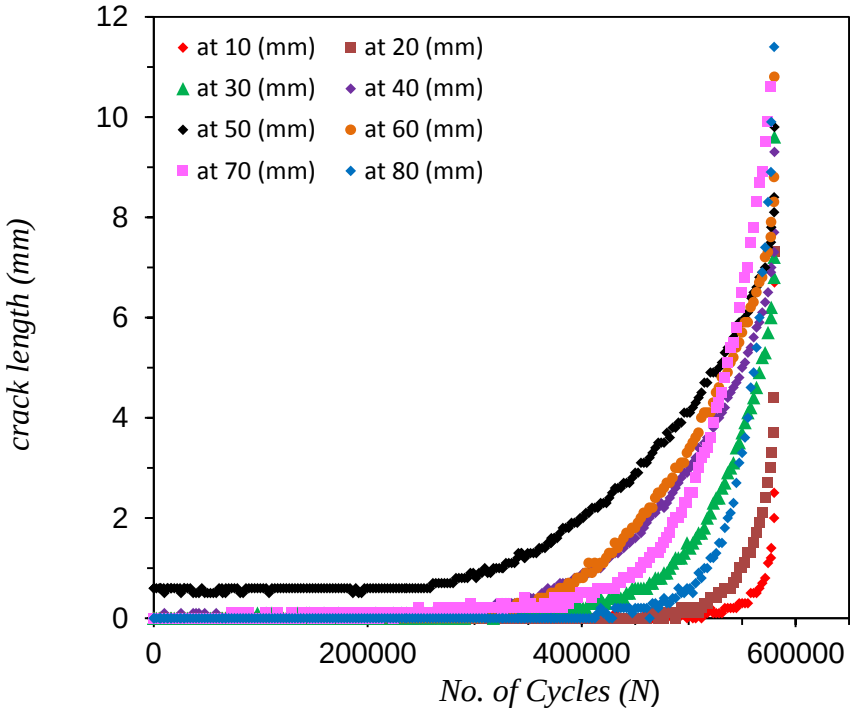

Figure 6-15: Fatigue crack growth data versus number of cycles for A60-1 specimen

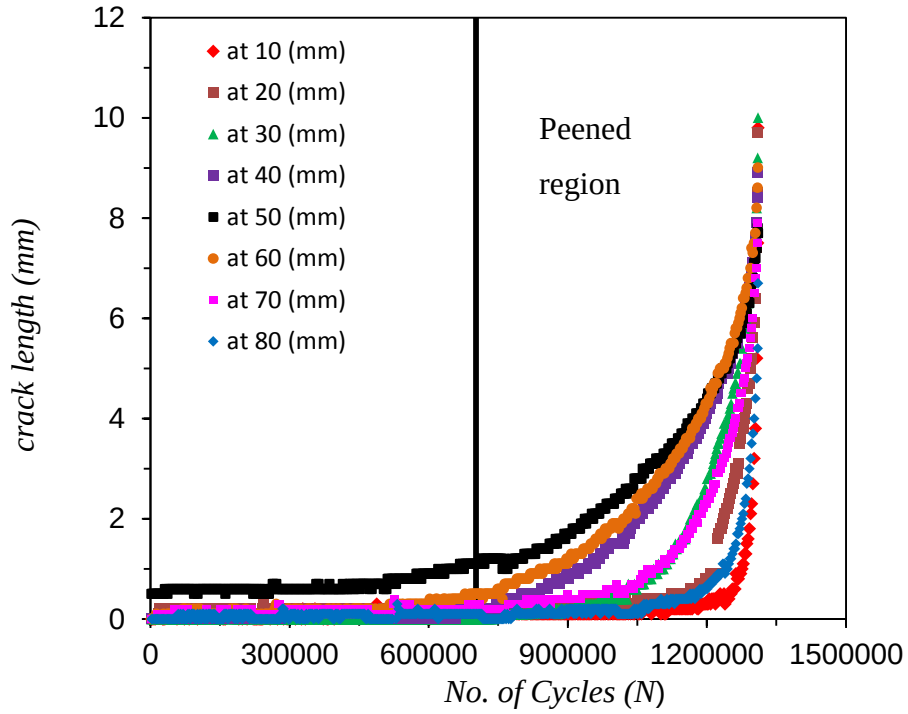

Figure 6-16: Fatigue crack growth data versus number of cycles for A10-2 specimen

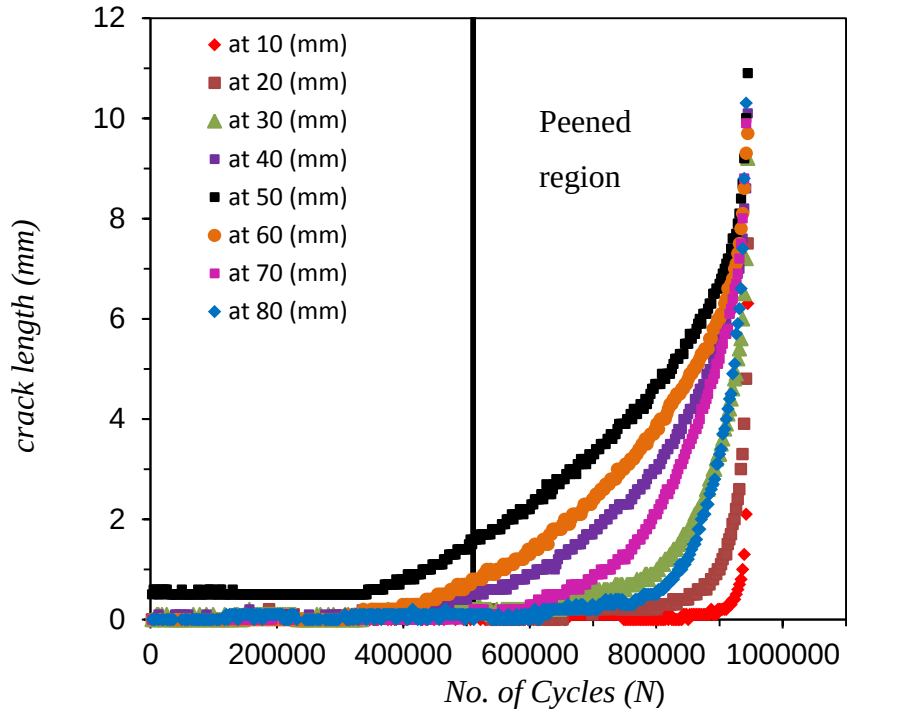

Figure 6-17: Fatigue crack growth data versus number of cycles for A20-2 specimen

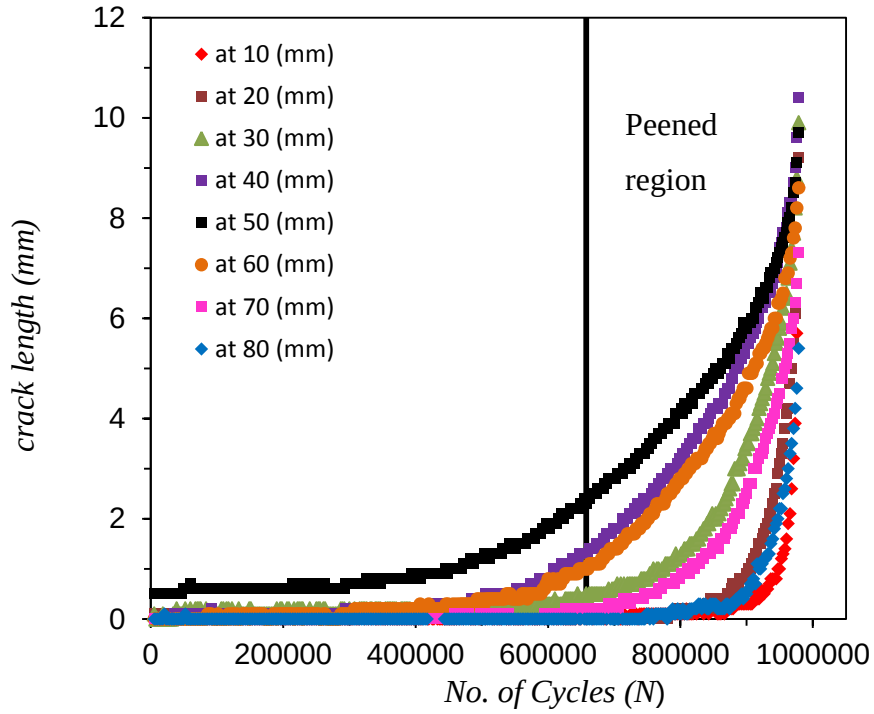

Figure 6-18: Fatigue crack growth data versus number of cycles for A30-2 specimen

6.3.2 Crack shape evolution results

The fatigue crack shape evolution was monitored during the fatigue test using ACPD probes attached along the width of the specimens. The fatigue crack length readings from each probe are plotted against the distance of the probe from the outer edge in Figure 6-20, Figure 6-21, Figure 6-22 and Figure 6-23 for A10-1, A20-1, A30-1 and A60-1 respectively and, as shown in Figure 6-24, Figure 6-25 and Figure 6-26 for A10-2, A20-2 and A30-2, respectively. For each of the test specimens, these measurements were repeated at different cycle numbers to capture the crack shape evolution throughout the fatigue tests. Comparing Figure 6-20, Figure 6-21, Figure 6-22 and Figure 6-23, it can be seen that for a given loading condition (maximum load of 70kN with R = 0.1) the extent of partial surface peening significantly influences the crack shape evolution in various specimens. It can be clearly seen in these figures that the deepest crack in all specimens has been measured at the mid-width of the samples, as expected, and shorter cracks were found in the peened areas where the compressive residual stresses existed. Comparison of Figure 6-20, Figure 6-21 and Figure 6-22, also

shows that the FCG at the mid-width of the A10-1 specimen was faster than A20-1 and A30-1. This is thought to be due to higher tensile residual stresses in the unpeened region in this specimen. These figures confirm that the partial surface peening controls the fatigue crack evolution shape and rate in the bend specimens.

Figure 6-27 shows the evolution of crack aspect ratio for the specimens tested under pure bending in this project. The crack aspect ratio is here defined as the ratio of fatigue crack depth "a" to fatigue crack length "c", which has been plotted against the ratio of fatigue crack depth "a" to specimen depth "t", as shown in Figure 6-19. Brennan et al. have previously shown that under pure bending loads, the fatigue crack tends to grow to an optimum ratio regardless of the initial crack shape [195]. Further observed and reported in their study is that the crack shape evolution is dependent on material anisotropy and loading modes, and is independent of the applied stress magnitude [195]. It can be seen in Figure 6-27 that due to partial cavitation shotless peening, which has led to material anisotropy, the crack aspect ratio has been altered and deviates from the favourable trend which is a straight line.

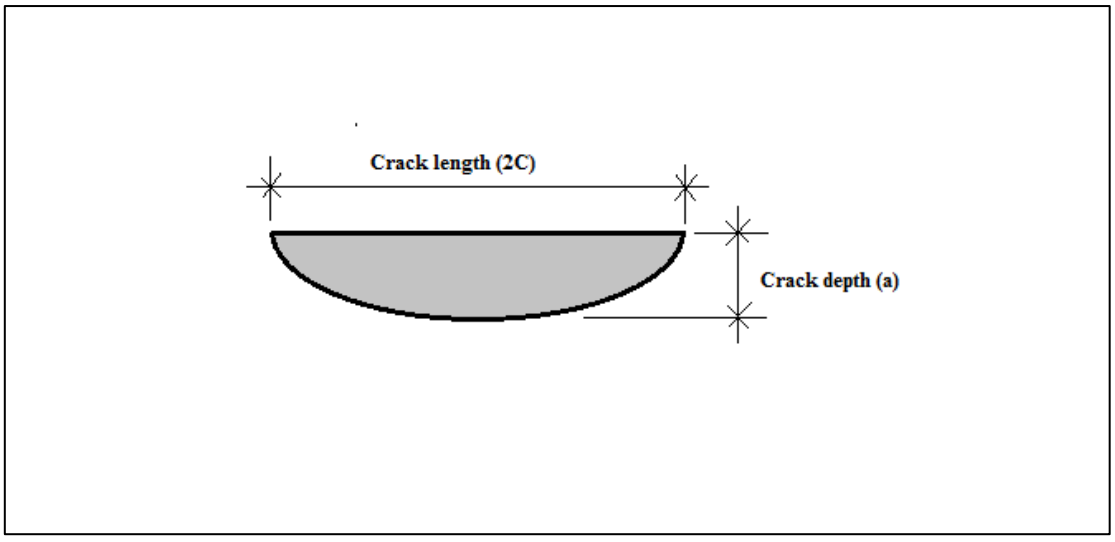

Figure 6-19: Geometry of semi-elliptical crack

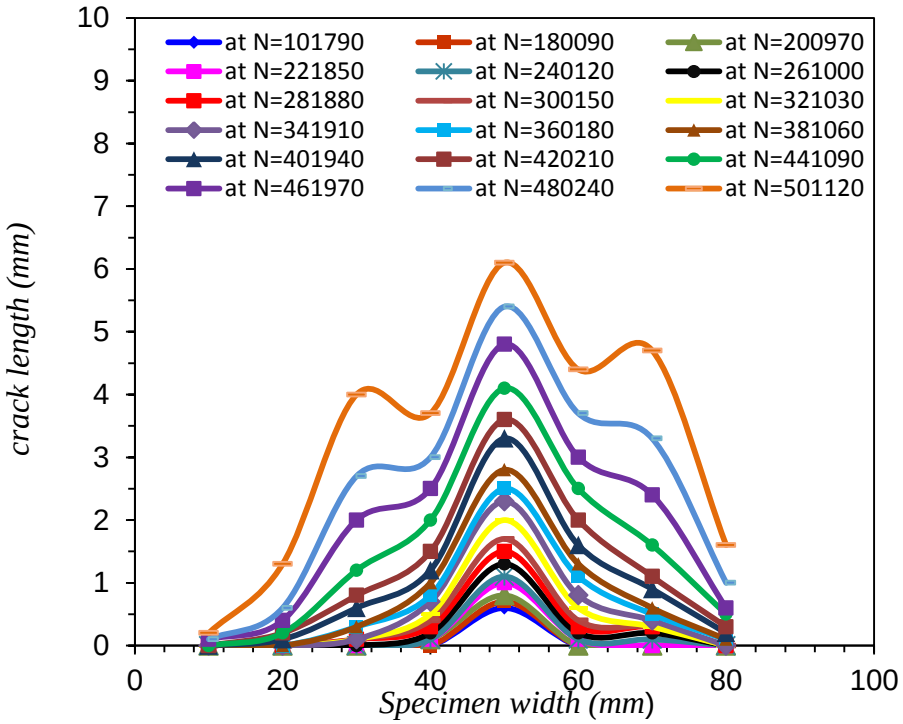

Figure 6-20: Crack Shape evolution for A10-1 specimen

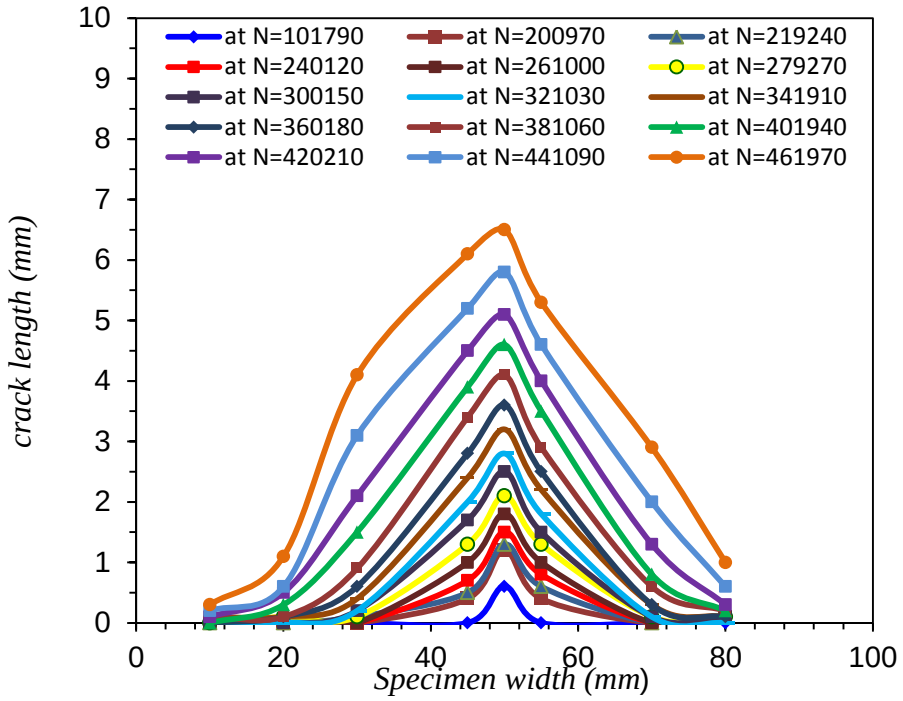

Figure 6-21: Crack Shape evolution for A20-1 specimen

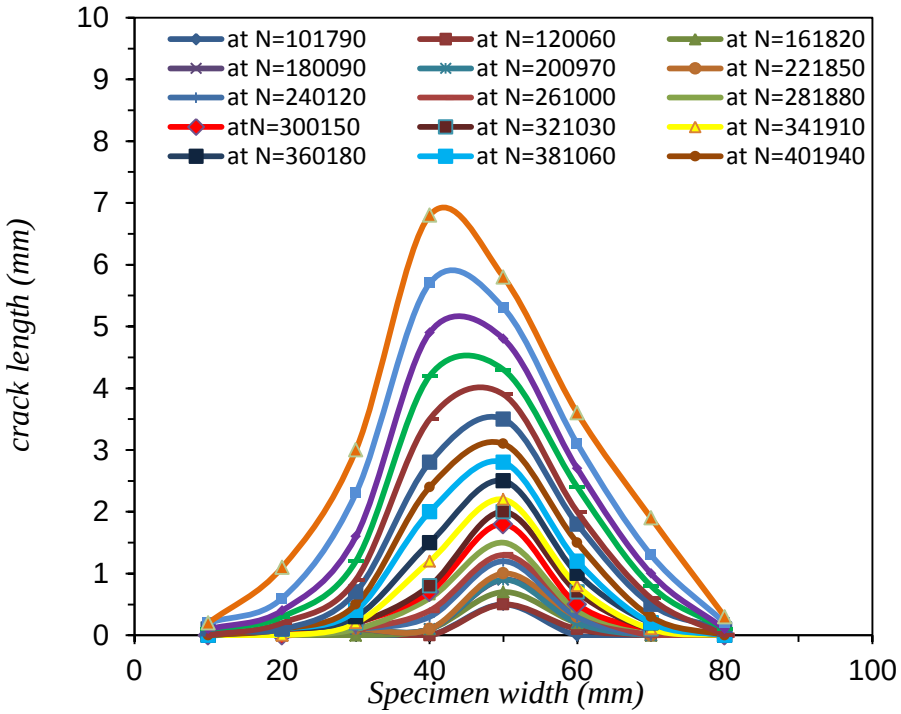

Figure 6-22 : Crack Shape evolution for A30-1 specimen

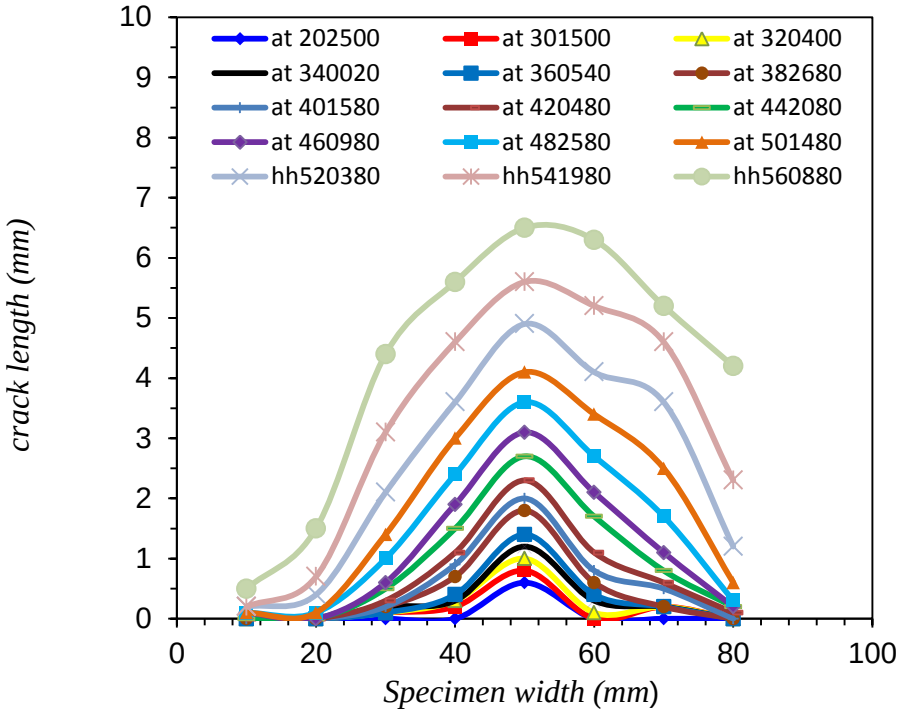

Figure 6-23: Crack Shape evolution for A60-1 specimen

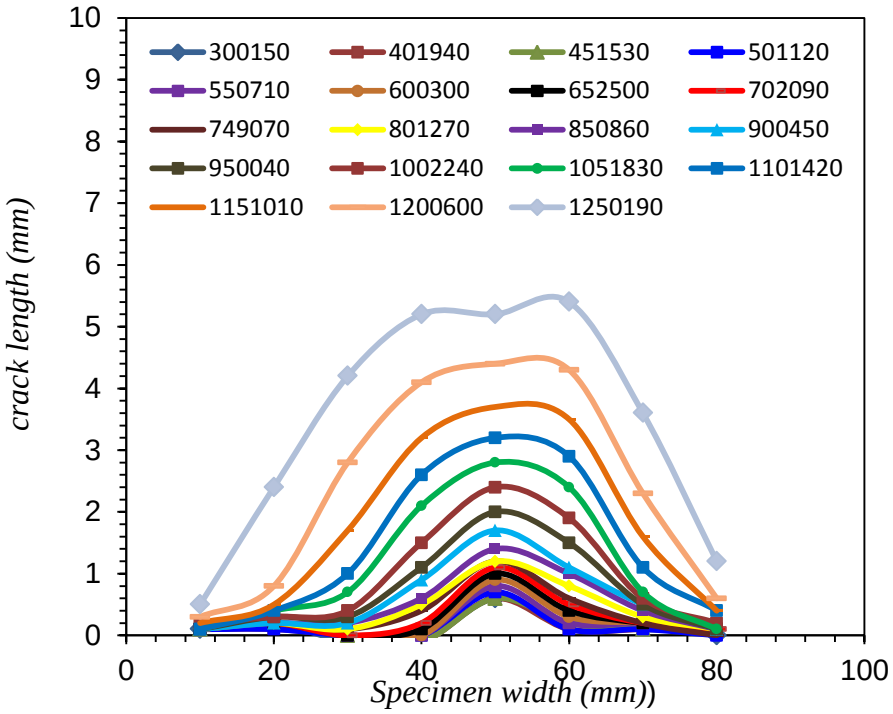

Figure 6-24: Crack Shape evolution for A10-1 specimen

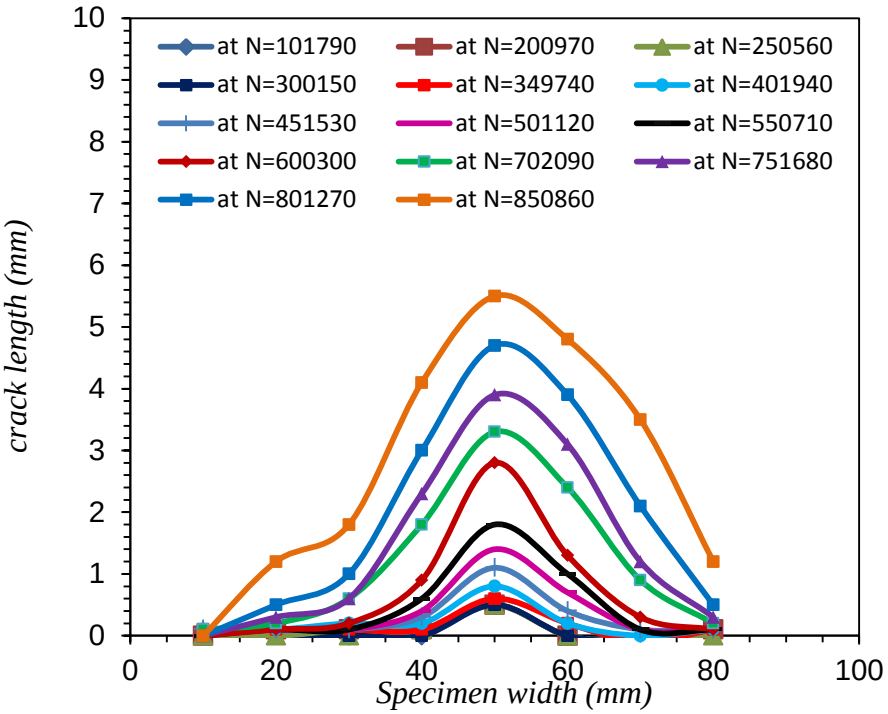

Figure 6-25: Crack Shape evolution for A20-2 specimen

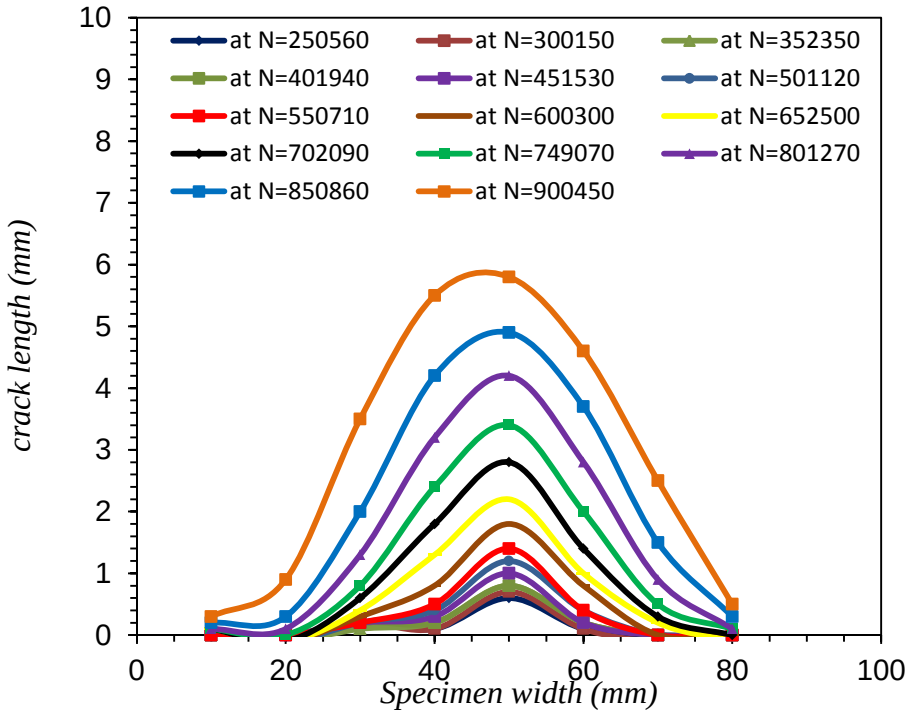

Figure 6-26: Crack Shape evolution for A30-2 specimen

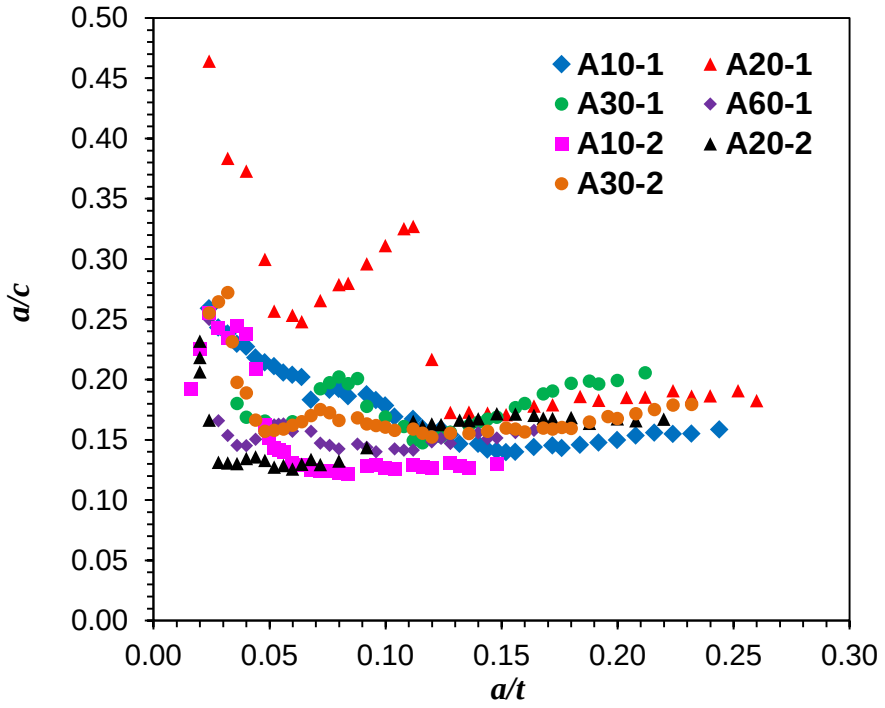

Figure 6-27: Aspect ratio of fatigue crack shape evolution for test specimens

6.3.3 Fatigue crack growth rate results

The FCG data from each test were analysed using the equations and procedure detailed in section 6.2.5. The FCGRs, *da/dN*, were calculated using a 7-point polynomial technique for each test and correlated with the SIF range, ΔK. It must be noted that for the FCG analysis, the deepest crack lengths are measured at the mid-width of the specimens when employed in calculations.

The FCGRs from the tests on A10-1, A20-1, A30-1, A60-1, are shown in Figure 6-28 to Figure 6-31, respectively under 70kN pure bend fatigue load; the FCGR results for A10-2, A20-2 and A30-2 at 60kN maximum pure bend fatigue load are shown in Figure 6-32 to Figure 6-34, respectively. For the first test on the A10-1 specimen it can be observed in Figure 6-28 that the FCG results plotted against ΔK show a linear trend in the log-log scale and there is a drop in the FCGR in the early stages of the test which corresponds to the time when the crack tip reached the partially peened area. For the A20-1 and A30-1 results, it can be observed that there is a linear trend between the FCGR and ΔK in the log-log scale similar to A10-1, with a similar reduction in FCGR when the crack tip enters the peened region. FCG test results from the tests performed on the A60 unpeened specimen is shown in Figure 6-31. The fatigue test results obtained from the unpeened specimen show that although some minor reductions in FCGR have been observed in this sample presumably due to the inherent scatter in the data,the overall trend is showing a continuous increase in FCG trend as the stress intensity factor range increases. Figure 6-31 shows that within the inherent experimental scatter, no noticeable drop in FCGRs is observed in the unpeened specimen, as expected. This is due to the lack of residual stress distribution fields in the unpeened specimen. It can be seen in Figure 6-32, Figure 6-33 and Figure 6-34 that a more pronounced reduction in the FCGRs is observed in the specimens tested under a lower load level, which is a consistent observation with those performed at the 70kN maximum load.

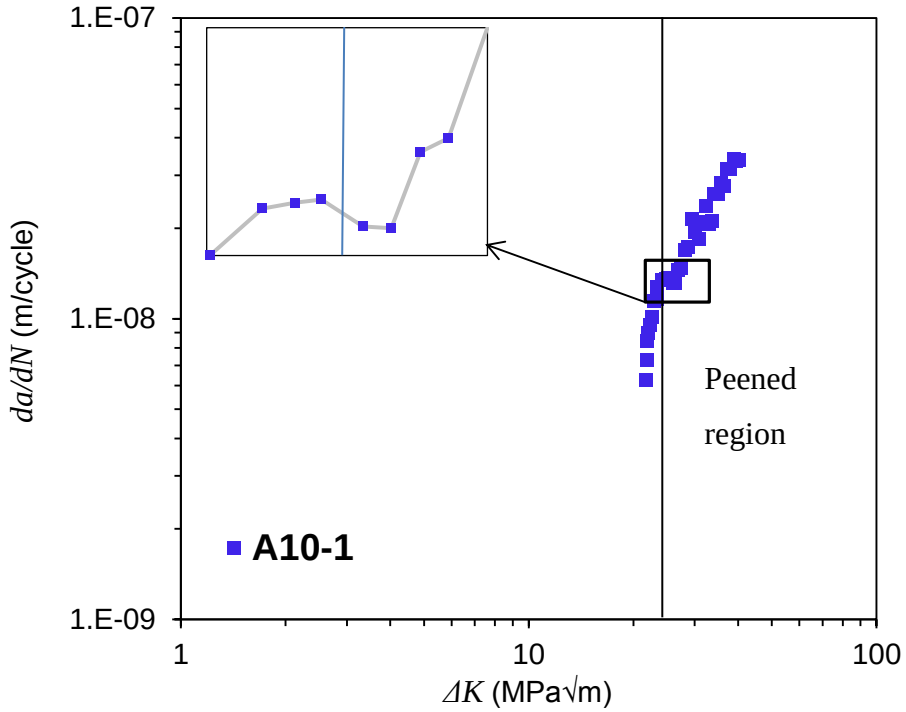

Figure 6-28: Fatigue crack growth results for A10-1 specimen

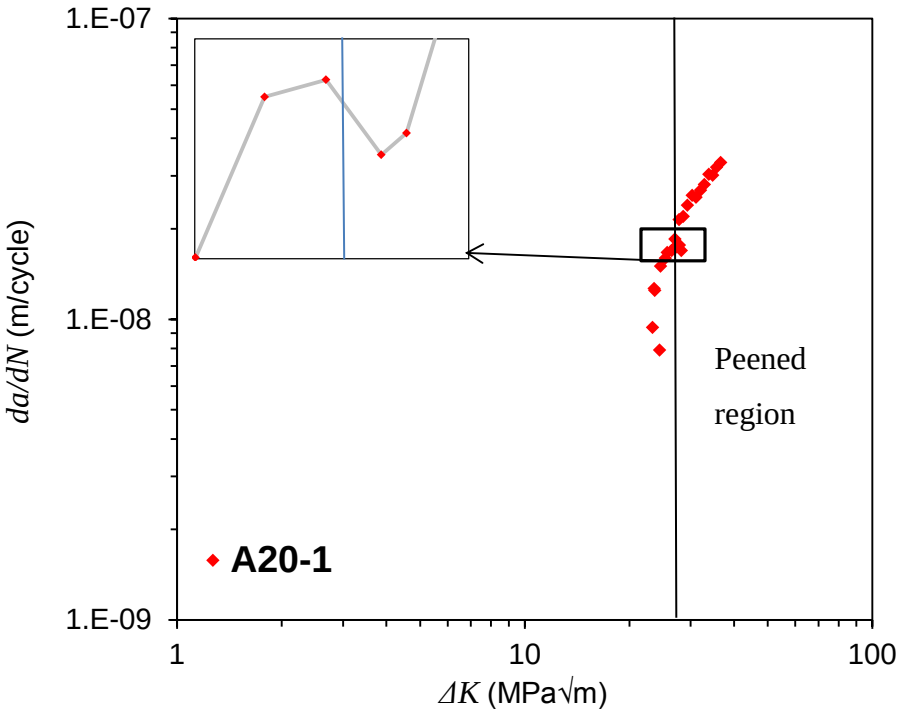

Figure 6-29: Fatigue crack growth results for A20-1 specimen

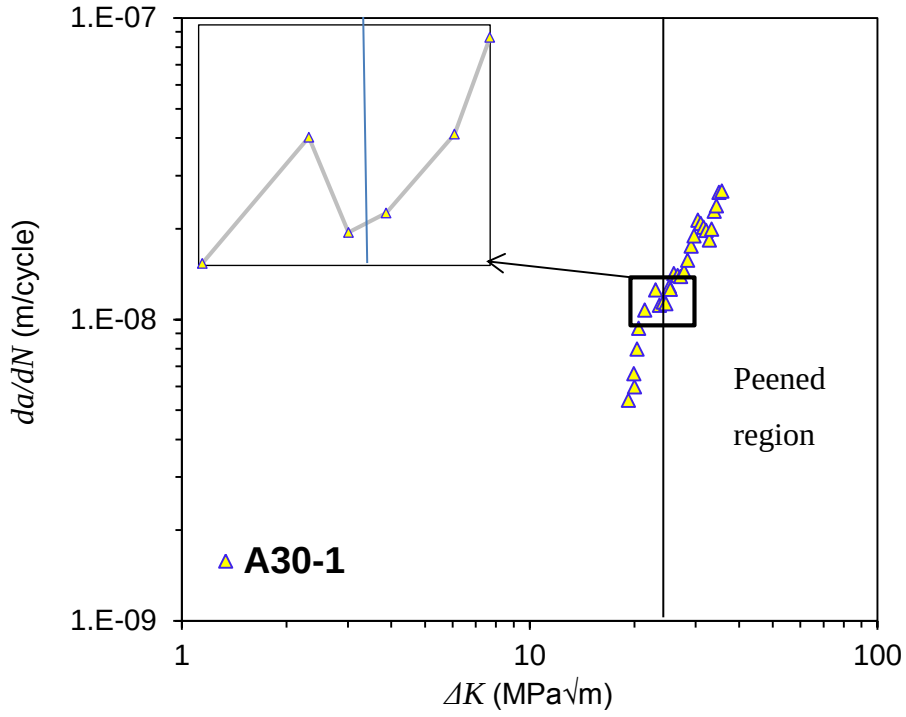

Figure 6-30: Fatigue crack growth results for A30-1 specimen

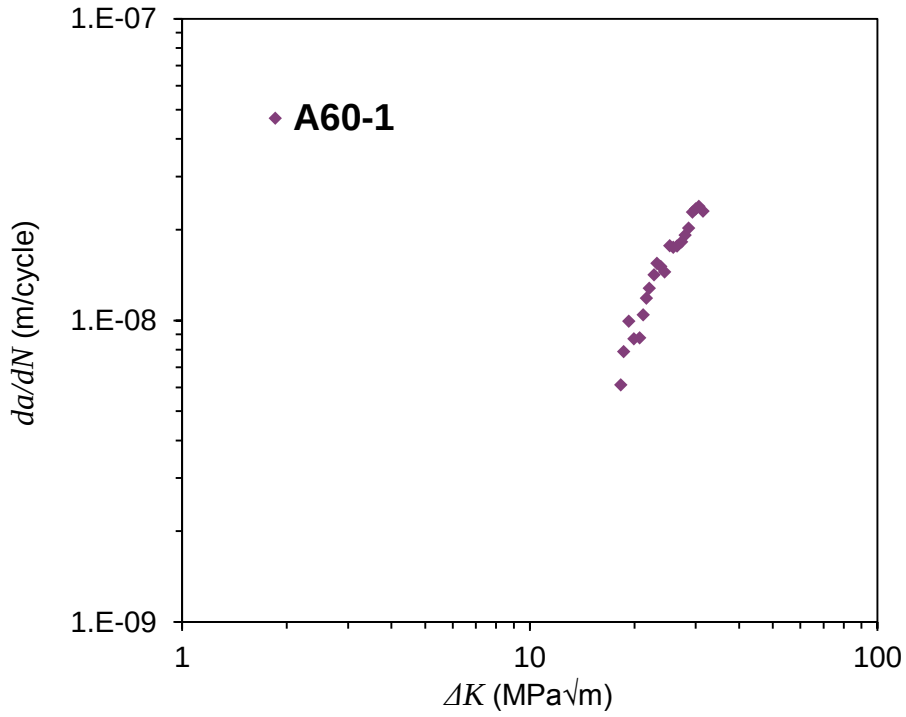

Figure 6-31: Fatigue crack growth results for A60-1 specimen

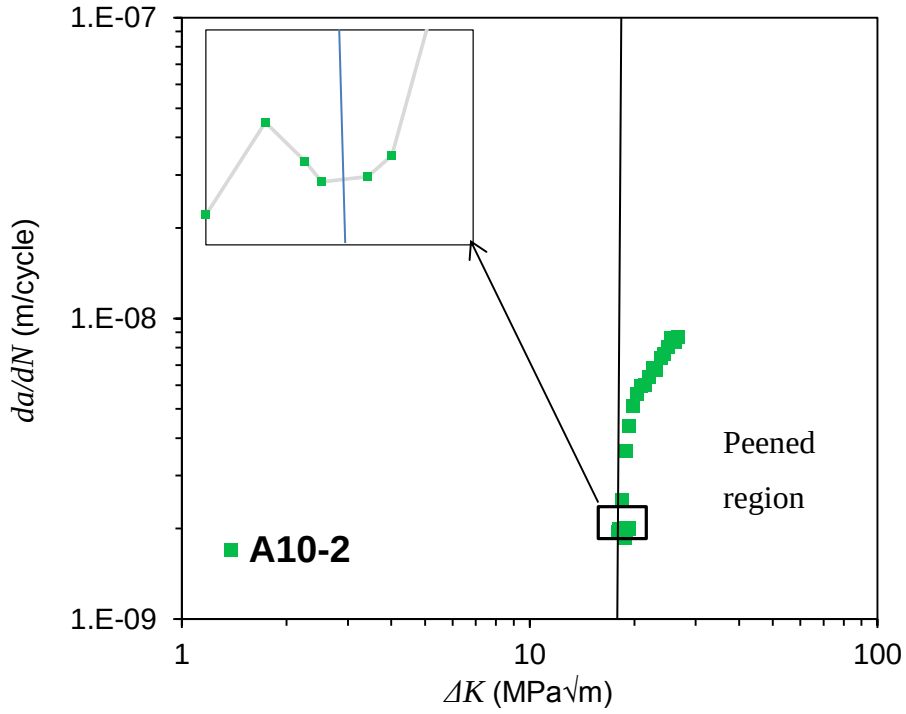

Figure 6-32: Fatigue crack growth results for A10-2

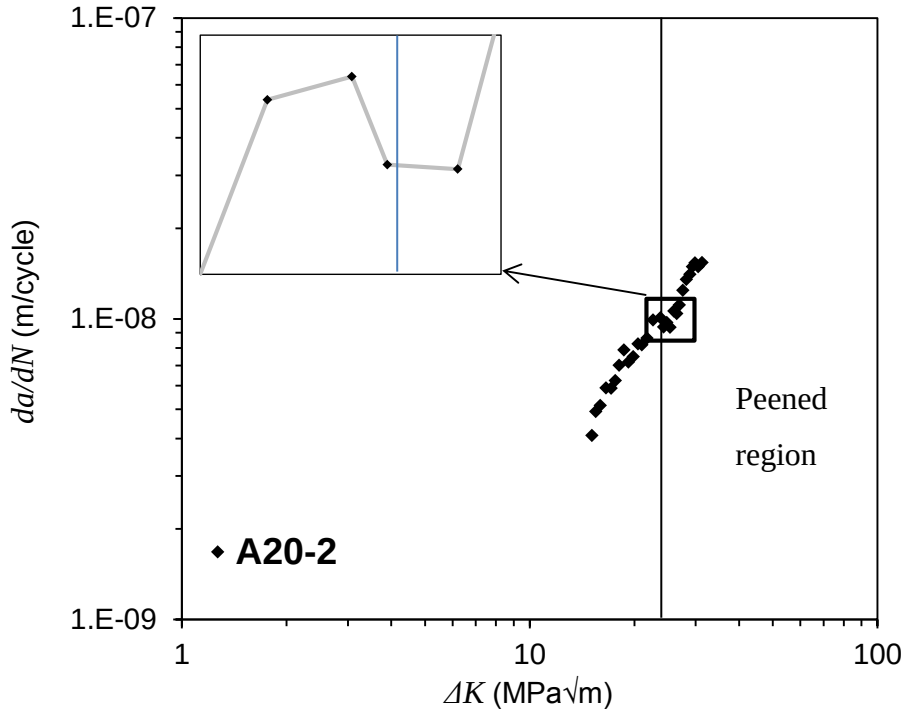

Figure 6-33: Fatigue crack growth results for A20-2

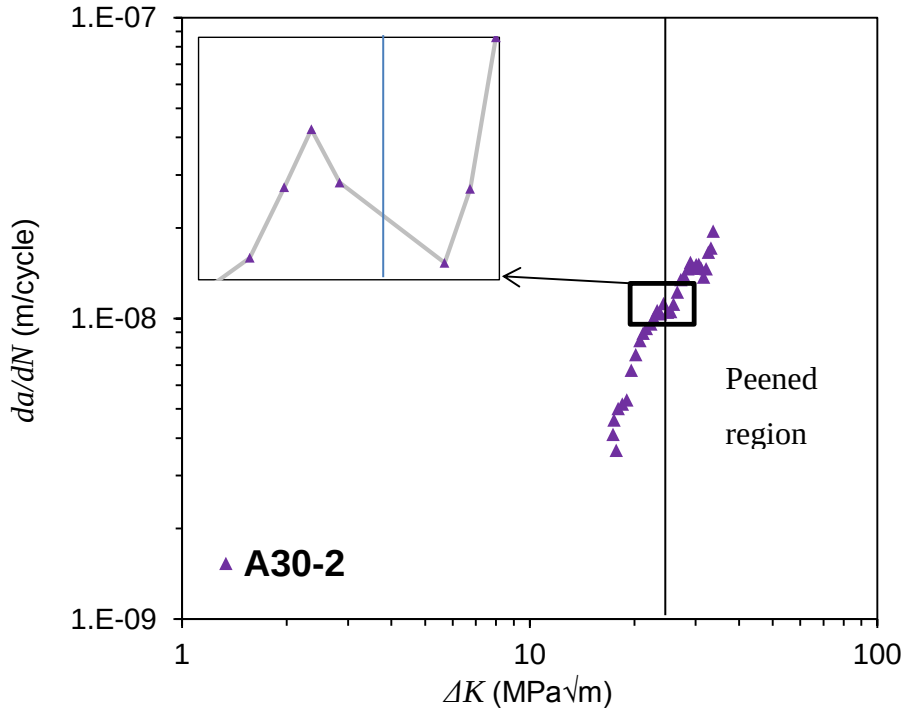

Figure 6-34: Fatigue crack growth results for A30-2

6.4 Fractography

The ACPD measurements have been validated by comparing the final crack length measurement at the end of the test with that measured on the fracture surface after the specimen was broken open. The percentage of error in ACPD measurements at the deepest point was found to be as small as $\pm$3%, which confirms that ACPD is a reliable technique to estimate the crack length throughout the width of the samples. The FCG specimens were soaked in liquid nitrogen for 30 minutes post-testing and then broken open on an Instron machine. The fracture surface of all FCG specimens were examined after being broken open and those for the A10-1 and A30-1 specimens are shown in Figure 6-35 and Figure 6-36, respectively, as examples. These pictures show that distinctive regions can be clearly observed on the fracture surface of the broken open specimens, which have been identified and marked in Figure 6-35 and Figure 6-36. First of all, the crack initiation region, where the fatigue crack initiated from the machined notch with the typical semi-elliptical fatigue crack evolution shape, can be observed on the fracture surface. It can be clearly seen that a transition area from fatigue to fast

fracture is observed towards the end of the tests where the SIF approaches its critical KIC value in the accelerating FCG region. Finally, the fast fracture region, due to the specimen being broken open, can be observed on the fracture surface of the specimens. Also noted in fractography studies is that the slower FCG behaviour in the peened regions cannot be identified in the high resolution pictures; however, these regions have been marked in Figure 6-35 and Figure 6-36 for the reader's attention.

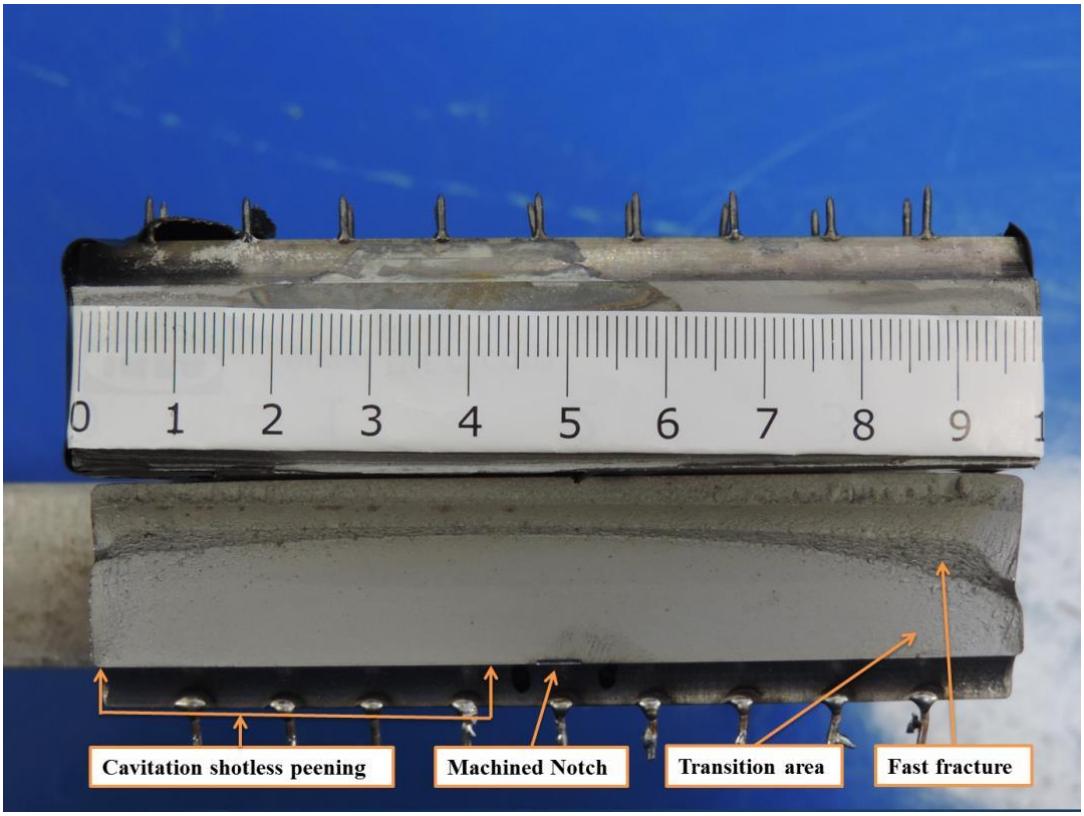

Figure 6-35: Fracture surface for A10-1 specimen

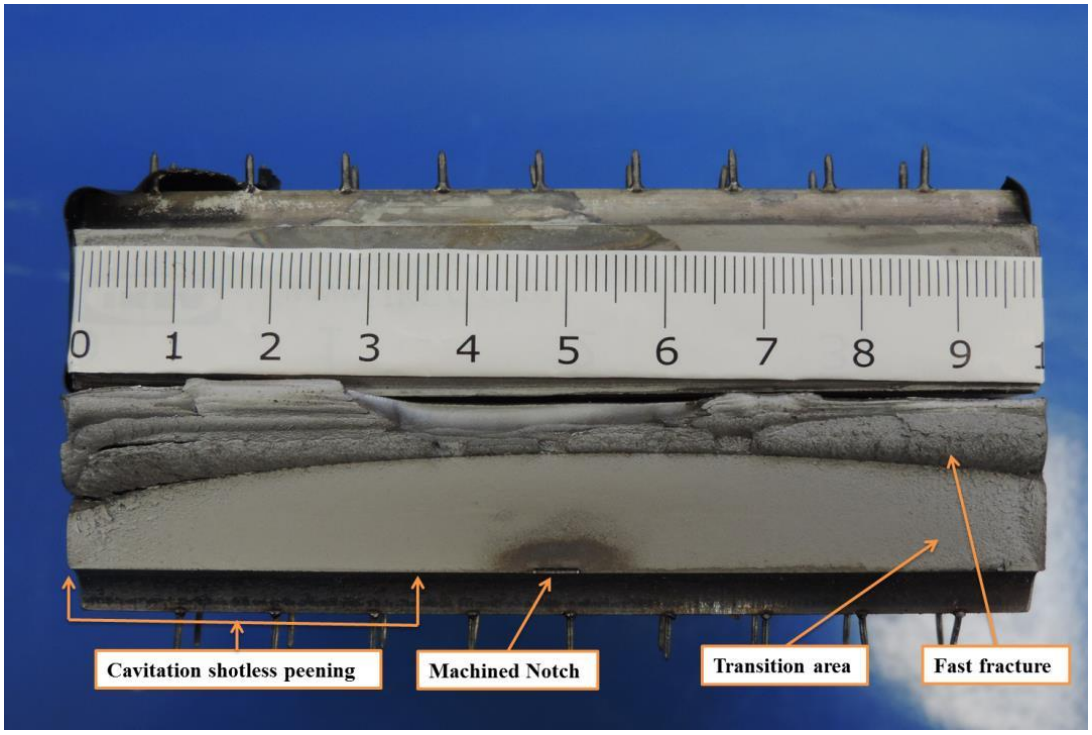

Figure 6-36: Fracture surface for A30-1 specimen

6.5 Discussion

The FCG results from the tests performed in this study are collectively shown and compared in Figure 6-39. This figure clearly demonstrates that partial surface cavitation shotless peening significantly influences the FCG behaviour of the material. The results from the A60-1 test data show that the FCGR linearly increased with an increase in the SIF range when the data were plotted in log-log axes. This behaviour is known as the Paris law and is typically observed in all FCG tests [4]. It can be seen in Figure 6-39 that a reduction in FCGRs was observed in all specimens, which were partially peened, with the A10, A20 and A30 specimens showing a retardation at lower, intermediate and higher ΔK values, respectively, for both applied load levels of 60kN and 70kN. This shows that the SIF range, at which the fatigue crack retardation occurs, increases as the area of the unpeened region increases on the surface of the examined specimens.

Firstly, the comparison of the tests results from A10-1, A20-1, A30-1 and A60-1 specimens in Figure 6-37 at 70kN pure bending fatigue load have been divided into two distinct regions for clarity. At the lower range of SIF (region I), it can be observed that the highest and lowest FCG trends were observed A60-1 (i.e. unpeened) and A10-1

specimens, respectively, with the test data from A20-1 and A30 falling in between and close to each other. In Figure 6-37 (region I), the fatigue crack has already entered the peened region. It can be seen that within region I SIF range for a given value of ΔK, the FCGR in the A10-1 partially peened specimen is around three times slower than the unpeened sample. This indicates that the partial peening area causes a reduction in FCGR due to the fatigue crack in A10-1 having already entered the peened area. In other words, if surface cavitation shotless peening is used to introduce compressive residual stresses in a component and subsequently reduce FCGRs, a partially unpeened region can lead to a significant decrease in the overall FCG trends under pure bending fatigue load. However, in Figure 6-37 the highest SIF range of larger than 25MPa√m (region II) can be seen; it can also be observed that the highest and lowest FCG trends were observed for the A30-1 and A20-1 specimens, respectively, with the test data from A60-1 and A10-1 falling in between and close to each other. It can also be seen that within region I SIF range for a given value of ΔK, the FCGR in the A30-1 partially peened specimen is around twice slower than the A20-1 sample. This indicates that at higher SIF range, the FCGR changed due to high estimated applied fatigue load leading to the applied load dominating the effect of the residual stress of the FCG. So it has been decided to reduce the fatigue load for the rest of the test specimens (i.e. A10-2, A20-2 and A30-2).

Secondly, the comparison of the tests results from A10-2, A20-2 and A30-2 specimens in Figure 6-38, at 60kN pure bending fatigue load, have been divided into two distinct regions for clarity. At the lower range of SIF (region I), it can be observed that the highest and lowest FCG trends were observed for the A20-2 and A10-2 specimens, respectively, with the test data from A30-2 falling in between. In Figure 6-38 (region I), the fatigue crack in the A10-2 specimen has already entered the peened region. It can be seen that within the region I SIF range for a given value of ΔK, the FCGR in the A20-2 partially peened specimen is around twice faster than the A10-2 sample. This indicates that the partial peening area causes a reduction in FCGR due to the fatigue crack in A10-2 having already entered the peened area. In other words, if surface cavitation shotless peening is used to introduce compressive residual stresses in a component and subsequently reduce FCGRs, a partially unpeened region can lead to a significant decrease in the overall FCG trends under pure bending fatigue load. However, it can be

seen in Figure 6-38 that in the highest SIF range of larger than 20MPa√m (region II), the highest and lowest FCG trends were observed for the A30-2 and A10-2 specimens, respectively, with the test data from A20-2 falling in between. It can also be seen that within region I SIF range for a given value of ΔK, the FCGR in the A30-1 partially peened specimen is around 1.5 times faster than the A20-1 sample. This indicates that the partial peening area causes a reduction in FCGR due to the fatigue crack in A10-1 having already entered the peened area. In other words, if surface cavitation shotless peening is used to introduce compressive residual stresses in a component and subsequently reduces FCGRs, a partially unpeened region can lead to a significant decrease in the overall FCG trends under pure bending fatigue load.

The FCG results from the tests performed in this study are collectively shown and compared in Figure 6-39. Comparisons of the test results obtained from this study show that for A10-1, A20-1 and A30-1 specimens have faster FCG trends, which are obtained from the higher load tests (70kN maximum load) compared to those tested at a lower load (i.e. 60kN maximum load), at around 1.5 for a given value of the SIF range. From the results discussion, it can be observed that the partial cavitation shotless peening effect is positive for FCGR, the FCGR dropped at the entrance of the partial shotless peening and the general trend of FCG decreases with increases in the partial peening area under pure bend load. This is due to the fatigue crack front being affected by compressive residual stress induced by the peening region more than the tensile residual stress, which leads to decreasing the FCG and improving the fatigue life, as shown in Figure 6-40.

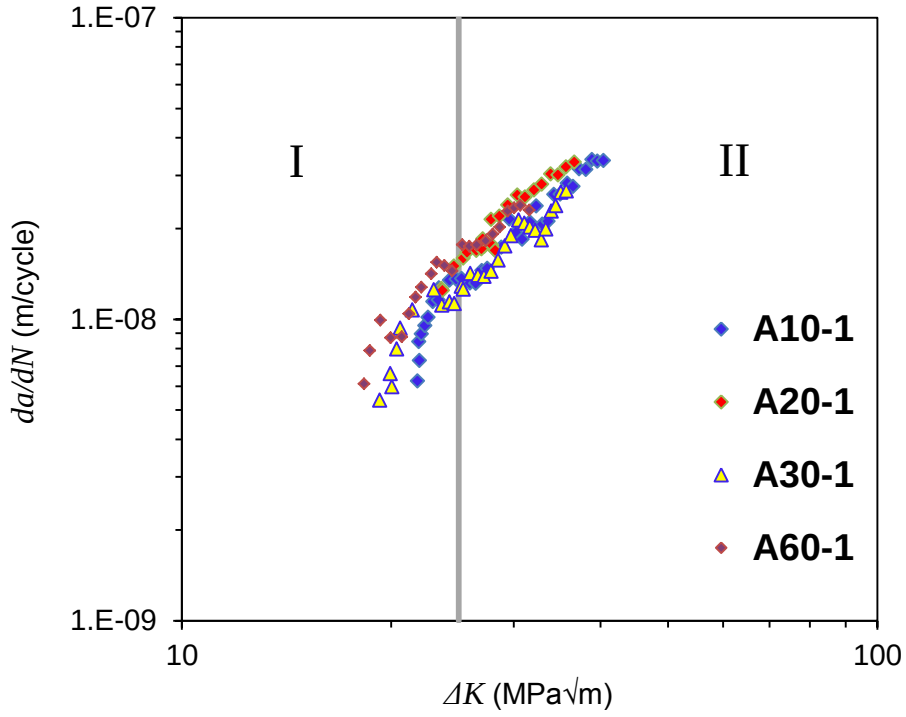

Figure 6-37: Comparison of fatigue crack growth trends in different specimens under 70kN pure bend fatigue load

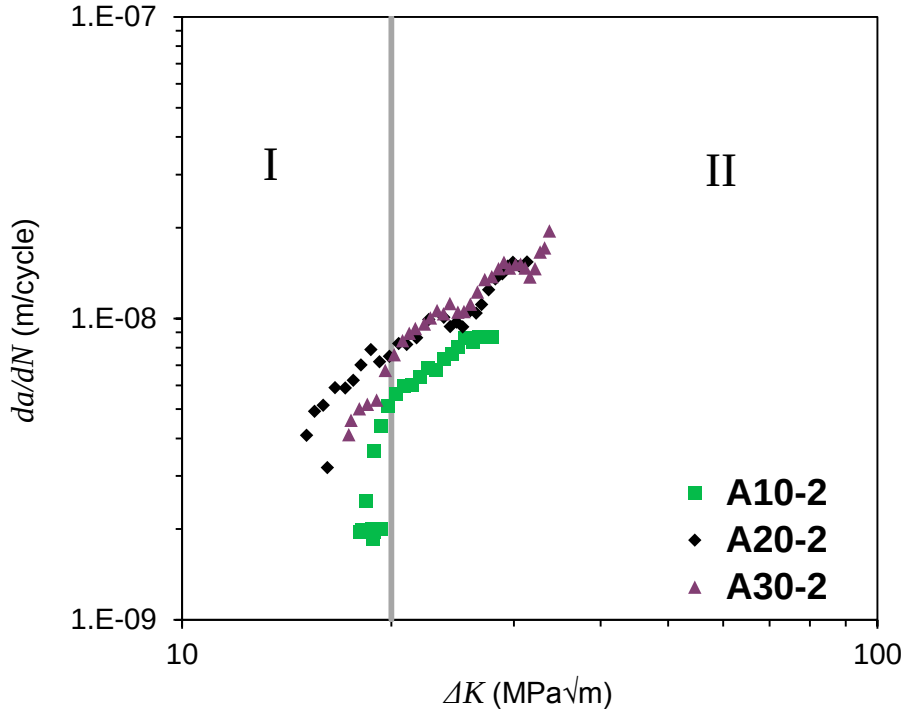

Figure 6-38: Comparison of fatigue crack growth trends in different specimens under 60kN pure bend fatigue load

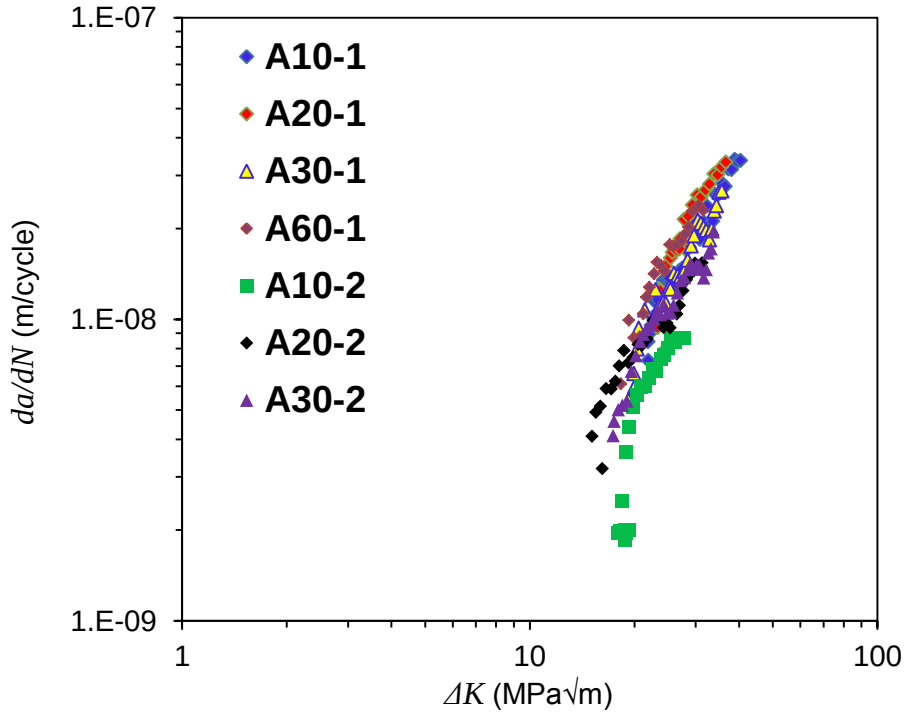

Figure 6-39: Comparison of fatigue crack growth trends in different specimens

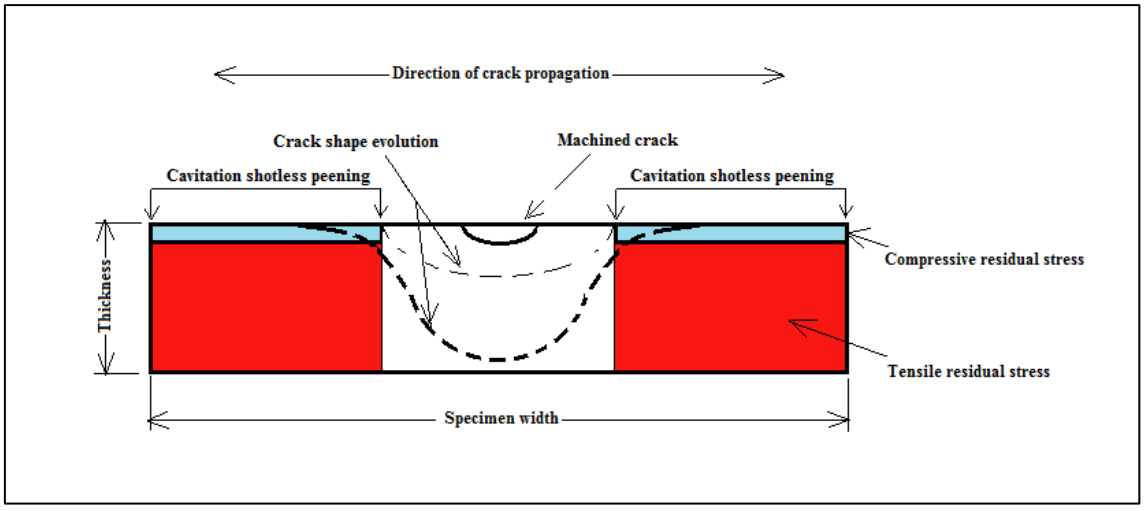

Figure 6-40: Schematic diagram for a cross section of the dog-bone specimen

6.6 Summary

This chapter presented the experimental investigation into the effects of partial surface cavitation shotless peening on the FCG behaviour of HSS grade Optim700QL. Seven specimens were tested under a 4-point bend fatigue load. Three distinct extents of partial cavitation shotless peening, with respect to the crack tip and specimen symmetry line, were applied to the specimen geometry. The specimens contained a circular machined notch in the centre, with a radius of 5mm, to create a starter crack. The experiment tests were conducted in air under two different values of maximum fatigue load, which are 70kN and 60kN, with a load ratio and frequency of 0.1 and 3Hz, respectively. ACPD with multi-probes were used to measure and monitor the crack depth along the specimens' width. The SIFs were calculated by using the Newman & Raju model [166] for surface cracks and by adding the notch radius to crack depth as proven by numerical simulation. The FCGRs results from these experiments have been compared with those obtained from similar specimen geometry but with no peening. The results show that the residual stress fields formed ahead of the initial notch tip due to the peening process play a significant role in the fatigue crack evolution and effectively result in decelerating the crack propagation of the material. The FCG retardation was observed at lower, intermediate and higher ΔK values when the fatigue crack entered the peened region due to compressive residual stress. The SIF range in which the fatigue crack retardation occurs increases as the area of the unpeened region increases on the surface of the examined specimens. Also, the results show that the partial peening causes decreasing in FCGR due to the compressive residual stress. The partial surface peening is effective under pure bend fatigue load due to the fatigue crack front facing only to compressive residual stress, which can be translated into a decrease in FCGR. The partial cavitation shotless peened region ahead of the initial notch plays a significant role in the fatigue crack behaviour of the material, in which the FCG was retarded when the fatigue crack reached the peened region due to the existence of beneficial residual stress.

7 Conclusions and Future Work

7.1 Summary of thesis

The residual stress origins and their measurements are detailed in Chapter 2. Also, LEFM and FCGR principles are highlighted. The tensile residual stress can accelerate the FCGR while compressive residual stress can decelerate the fatigue crack initiation and growth effect of the mean residual stress. The material properties play an important role in the fatigue life of non-metallic inclusion, grain size and environment. The non-metallic inclusion has little effect on ΔK_{th} in the case of medium-strength pearlitic steels but a significant influence on FCGR due to inducing small amounts of ductile fracture. The finer grain size causes higher FCGR in the intermediate stage of FCG due to less distance between grain boundaries needing a fatigue crack to follow. A corrosive environment leads to accelerating the fatigue crack rates. To sum up, the compressive residual stresses are beneficial and lead to a reduction in the FCGR, while the tensile residual stresses are damaging and lead to an increase in the FCGR. The peening process induces compressive residual stress on the material surface and, due to the self-equilibrating feature, leads to tensile residual stress through the thickness as a reaction to the compressive residual stress on the surface. The HSS has a higher FCGR than medium strength steel due to the grain size effect. However, the HSS has a better strength to weight ratio as its advantage.

The numerical investigations were conducted to study the effect of notch radius and crack length on the magnitude of SCF and normalized SIF in different engineering structures. The numerical investigation has been carried out by using the finite element commercial software package ABAQUS/6.13 and the results were validated through comparison with the data available in the literature. The numerical analyses conducted in this study included a 2-D notched plate containing a crack, a 3-D SCT specimen containing a semi-elliptical surface crack, and a 3-D plate with notch and without notch under a 4-point bending load. It has been found that there is a direct correlation between the circular notch radius and the SCF due to decreases in the remaining area leading to increases in the local stress in the root of the notch. Also, it has been found that the normalized SIF increases with crack length increase due to increases in the stress

distribution at the crack tip. The numerical investigation shows that the normalized SIF results from FEM/ABAQUS match the results found in the semi-analytical solution of Newman & Raju [166] for surface cracks. Furthermore, the notched plate and plate without notch with a semi-elliptical crack have been validated with the Newman & Raju model by adding the radius of the semi-circular notch to the crack length in order to calculate the normalized SIF.

The experimental investigation of residual stress distribution has been performed by using an ICHD technique. The non-uniform stress integral has been used to calculate residual stress through the specimen thickness. The investigation involved two specimens as an example to measure the residual stress profile through the specimen thickness and the residual stress distribution on the specimens. The specimens are 4-point bend specimen geometry partially peened by the cavitation shotless peening technique and a dog-bone specimen with a central notch peened partially by shot peening. The specimens were fabricated from HSS grade Optim700QL with a yield strength of 690MPa. The compressive residual stresses were generated by cavitation shotless peening around 400MPa in a longitudinal direction and around 300MPa in the transverse direction of the specimen. The residual stresses created by cavitation shotless peening were uniform in all partially peened areas. The compressive residual stress decreased gradually through the specimen thickness and is converted into tensile residual stress at 0.4mm depth due to the self-balancing features of residual stress; due to the latter features, the partial compressive residual stress area causes the generation of residual stress in the surrounding area around the machined notch. The tensile residual stresses were around 300MPa and 110MPa in longitudinal and transverse directions, respectively. The residual stresses distribution in the dog-bone specimen peened partially by shot peening have been investigated. The compressive residual stresses created by shot peening were around 550MPa in a longitudinal direction and around 450MPa in a transverse direction. The compressive residual stress created by shot peening decreased gradually through the specimen thickness and reached zero magnitude of residual stress at a depth of around 1mm below the peened surface. The tensile residual stresses generated by compressive residual stress were around 150 and 50MPa in longitudinal and transverse directions, respectively.

The effects of partial surface shot peening on the FCG behaviour of HSS grade Optim700QL have been experimentally investigated. Dog-bone specimens were tested under a tension-tension fatigue load. Three distinct extents of partial shot peening, with respect to the crack tip and specimen symmetry line, were applied to the specimen geometry. An initial notch was machined in the middle-width of all specimens to create a starter crack for fracture mechanics studies. The FCG results from these experiments have been compared with those obtained from similar specimen geometry but with no peening. The results show that the residual stress fields formed ahead of the initial notch tip due to the peening process play a significant role in the FCG behaviour of the material. The tensile residual stress created in the mid-thickness of the specimen, due to compressive residual stress below the surface, dominates the compressive residual stress and affects the results in the accelerated crack propagation at the mid-width of the plate within the unpeened region.

The effects of partial surface shotless peening on the FCG behaviour of a ferritic steel have been experimentally investigated in this study. Seven fatigue tests were performed on 4-point bend specimens fabricated from Optim700QL HSS. Three distinct extents of partial cavitation shotless peening, with respect to the crack tip and specimen symmetry line, were applied to the specimen geometry. An initial notch was machined at the mid-width of all specimens to create a starter crack for fracture mechanics studies. ACPD was used to measure and monitor the crack depth during fatigue tests. The tests on partially surface-peened specimens were conducted under two different load levels. The FCG results from these experiments on partially peened specimens have been presented and compared with the results from an additional test on an unpeened specimen. The results show that the residual stress distribution fields formed due to the peening process play a significant role in the fatigue crack shape evolution, crack retardation and crack propagation behaviour of the material.

7.2 Achievement and conclusions

In this thesis, a fracture mechanics approach has been used to study the influence of different extents of partial peening on FCGRs in HSS. The main focus of this study was

to provide a better understanding of the residual stress distribution generated by the peening area and its subsequent effects on the FCGRs and also the effect of the partial peening area on FCGRs under tension-tension fatigue and pure bending fatigue loads. The study involved the fatigue crack shape evolution in complex stress fields. The following conclusions can be drawn from this research:

1. By using the effective crack length to determine the SIF when the crack is initiated in a plate containing a semi-circular notch, the effective crack length in the root of the notch is equal to the summation of the crack length and the radius of the notch.
2. The residual stress is a self-balancing stress that exists in the material without applying an external load. The self-balancing characteristic of residual stresses is not only through the specimen thickness but in the transverse direction of residual stress. It has been found that the area between two peening regions is subjected to tensile residual stress.
3. A reduction in FCGRs is observed when the crack tip enters the shot peened region under tension-tension fatigue load.
4. The SIF range at which the crack retardation occurs in partially shot peened specimens increases by increasing the extent of the unpeened region size from 10mm to 20mm and 30mm under tension-tension fatigue load.
5. Although partial surface peening leads to crack retardation as a result of compressive residual stresses, due to the induced global tensile residual stresses in the material, higher FCG trends are observed in the partially shot peened specimens compared to the unpeened sample under tension-tension fatigue load.
6. The highest FCG trend in partially shot peened specimens is observed in the specimen with the smallest unpeened region size (A10) for the intermediate SIF range of 15-30MPa$\sqrt{m}$.
7. For a given value of ΔK under tension-tension fatigue load, the FCGR in the A10 partially shot peened specimen is around twice as fast as in the unpeened sample for the intermediate SIF range of 15-30MPa$\sqrt{m}$.
8. The fatigue crack retards when reaching the peening area but continues in the mid-thickness of the specimen, causing severe crack tunnelling under tension-tension fatigue load.

9. The partial peening has a negative effect on FCGR under tension-tension fatigue load due to the fatigue crack front facing the compressive residual stress on the outer surface and the tensile residual stress in the mid-thickness of the material which can lead to causing severe crack tunnelling and acceleration of the FCGR.
10. The partial surface cavitation shotless peening introduced beneficial compressive residual stresses of up to 400MPa, in a longitudinal direction, with the penetration depth of around 0.4mm under the outer surface of the test specimens.
11. Tensile residual stresses were formed in the unpeened region of the partially cavitation shotless peened specimens due to the force equilibrium.
12. The cavitation shotless peening influences the fatigue crack shape evolution due to the compressive residual stress under pure bend fatigue load.
13. The cavitation shotless peening results in a good surface finish compared to shot peening.
14. A reduction in FCGRs under pure bend fatigue load is observed when the fatigue crack tip enters the cavitation shotless peened region in partially peened test specimens under pure bend fatigue load.
15. The SIF range, at which the fatigue crack retardation was observed in partially cavitation shotless peened specimens, increased by increasing the area of the unpeened region (i.e. decreasing the area of the peened region) under pure bend fatigue load.
16. Higher FCG trends were observed in partially peened specimens tested under higher load levels of pure bend fatigue load due to the applied load dominating the effect of compressive residual stress induced by cavitation shotless peening.
17. The influence of partial cavitation shotless peening on fatigue crack retardation was more pronounced in the tests performed at the lower load of the pure bend fatigue load.
18. For the tests performed under the lower pure bend fatigue load, the lowest FCG trend was observed in the specimen with the largest peened region size (i.e. A10).

19. The partial surface peening is more effective under pure bend fatigue load due to the fatigue crack front subjected only to compressive residual stress, which can be translated into a decrease in FCGR.

7.3 Limitations of this work

1. Residual stress measurements were done by using an ICHD technique due to availability in the lab and time frame limitations.
2. The residual stresses were measured at one point in the peening area and assumed to be uniform in all peening areas due to using the ICHD technique for measuring residual stress and its characteristic of residual stress relaxation during measurement.
3. Maximum depths of residual stress measured were 1mm due to the ICHD technique.
4. Residual stress investigations were measured in two specimens as an example due to the number of samples and time frame limitations.
5. Probe spacing in ACPD for crack measurement was 10mm due to the ACPD unit available in the lab.
6. Surface cracks were measured during tension fatigue tests due to using a camera for crack length measurement. This has appeared to introduce a level of uncertainty in the crack length measurements because the cracks were growing faster in mid-thickness of the specimen tests due to tensile residual stress.

7.4 Recommendations for Future Work

1. Investigate and accurately measure the residual stress arising due to partial peening area being in a lateral direction and through the thickness by using a non-destructive residual measurement technique, such as neutron diffraction.
2. Develop the numerical model in Chapter 3 to implement the partial peening area and compare the results with the experimental data. This would help to have a better understanding of the stress gradient ahead of the crack tip.

3. Conduct experimental tests with fully peened specimens, calculate FCGR and SIF range, then compare the results with partially peened specimens. This would help to have a better understanding of the effect of peening on FCGR.
4. Conduct experimental tests for partially and fully peened specimens under different load ratio (R). This would make it possible to observe the effect of peening on FCGR.
5. Conduct experimental tests on specimens with various thicknesses to study the thickness on the dissipated tensile residual resulting from the peening area, on FCG under tension fatigue load.
6. Develop an analytical technique to take into account the compressive residual stress and tensile residual stress resultant in mid-thickness and in the surrounding partial peening area, to have a better understanding of local stress on fatigue crack propagation.
7. Continuous measurement of residual stress relaxation during fatigue crack propagation to understand the change in FCG trends as a result of residual stress relaxation.
8. Repeat the tests in a seawater environment to examine the effectiveness of partial peening for offshore environments.

REFERENCES

[1] L. Xianghuai, "Recent advance in surface treatment and its applications in China," *Surf. Coatings Technol.*, vol. 131, no. 1–3, pp. 261–266, 2000.

[2] D. Ulutan and T. Ozel, "Machining induced surface integrity in titanium and nickel alloys: A review," *Int. J. Mach. Tools Manuf.*, vol. 51, no. 3, pp. 250–280, 2011.

[3] V. Schulze, *Modern Mechanical Surface Treatment*. Weinheim: Wiley-Vch, 2006.

[4] T. L. Anderson, *FRACTURE MECHANICS Fundamentals and Applications*, vol. ISBN:97808, no. 1. 2004.

[5] N. Perez, *Fracture mechanics*, 1st-4020th–786th ed. New York, Boston, Dordrecht, London, Moscow: KLUWER ACADEMIC PUBLISHERS, 2004.

[6] G. E. Dieter and D. Bacon, "Mechanical Metallurgy (Materials Science & Engineering)." McGraw-Hill Publishing Co., 1990.

[7] P. P. Milella, *Fatigue and Corrosion in Metals*. Milano: Springer Milan, 2013.

[8] N. Pugno, M. Ciavarella, P. Cornetti, and A. Carpinteri, "A generalized Paris' law for fatigue crack growth," *J. Mech. Phys. Solids*, vol. 54, no. 7, pp. 1333–1349, 2006.

[9] R. O. RITCHIE and J. F. KNOTT, "MECHANISMS OF FATIGUE CRACK GROWTH IN LOW ALLOY STEEL," *Acta Metall.*, vol. 21, pp. 639–650, 1973.

[10] M. B. Shah, J. L. Ferracane, and J. J. Kruzic, "Mechanistic aspects of fatigue crack growth behavior in resin based dental restorative composites," *Dent. Mater.*, vol. 25, no. 7, pp. 909–916, 2009.

[11] K. J. Nix and H. M. Flower, "The metallography of fatigue in the high strength aluminium alloy 7010," *ICF 5, Cannes, Fr.*, pp. 915–922, 1981.

[12] T. O. Smith, "The metallography of impact fatigue," *Int. Compress. Eng. Conf.*, paper 253, 1978.

[13] T. F. Murphy, B. A. Lindsley, and C. T. Schade, “A metallographic examination into fatigue-crack initiation and growth in ferrous PM materials,” *Int. J. Powder Metall.*, vol. 49, no. 4, pp. 23–34, 2013.

[14] H. Rutz, T. Murphy, and T. Cimino, “The Effect of Microstructure on Fatigue Properties of High Density Ferrous P/M Materials Howard,” *PM~EC ’96 World Congr. June 16-21, 1996- Washingt. D.C.*, pp. 1–20, 1996.

[15] T. M. Cimino, H. G. Rutz, A. H. Graham, T. F. Murphy, H. Corporation, and J. July, “the Effect of Microstructure on Fatigue Properties of Ferrous P / M Materials,” *PM2 TEC ’97 Intentional Conf. Powder Metall. Part. Mater. June 29 - July 2, 1997 Chicago, USA Abstr.*, pp. 1–11, 1997.

[16] M. O. Speidel, “The Resistance to Fatigue Crack Growth of the Platinum Metals,” *Platin. Met. Rev.*, vol. 25, no. 1, pp. 24–31, 1981.

[17] A. Trudel, M. Levesque, and M. Brochu, “Microstructural effects on the fatigue crack growth resistance of a stainless steel CA6NM weld,” *Eng. Fract. Mech.*, vol. 115, pp. 60–72, 2014.

[18] D. F. Laurito, C. A. R. P. Baptista, M. A. S. Torres, and A. J. Abdalla, “Microstructural effects on fatigue crack growth behavior of a microalloyed steel,” *Procedia Eng.*, vol. 2, no. 1, pp. 1915–1925, 2010.

[19] R. O. Ritchie, “Mechanisms of fatigue crack propagation in metals, ceramics and composites: Role of crack tip shielding,” *Mater. Sci. Eng.*, vol. 103, no. 1, pp. 15–28, 1988.

[20] A. Ray, S. Tangirala, and S. Phoha, “Stochastic modeling of fatigue crack propagation,” *Appl. Math. Model.*, vol. 22, no. 3, pp. 197–204, 1998.

[21] D. Broek, “The effect of intermetallic particles on fatigue crack propagation in aluminium alloys,” Proc: *2nd Int. Conf. on Fracture*, Brighton,1969, pp. 754–764, 1969.

[22] A. D. Wilson, “FATIGUE CRACK PROPAGATION IN A533B STEELS,” *J. Press. Vessel Technol.*, vol. 99, pp. 459–469, 1977.

[23] J. Lindigkeit, G. Terlinde, A. Gysler, and G. Lütjering, “The effect of grain size on the fatigue crack propagation behavior of age-hardened alloys in inert and corrosive environment,” *Acta Metall.*, vol. 27, no. 11, pp. 1717–1726, 1979.

[24] F. R. Stonesifer, “Effect of grain size and temperature on fatigue crack propagation in A533 B steel,” *Eng. Fract. Mech.*, vol. 10, no. 2, pp. 305–314, 1978.

[25] L. A. James, “The effect of grain size upon the fatigue-crack propagation behavior of alloy 718 under hold-time cycling at elevated temperature,” *Eng. Fract. Mech.*, vol. 25, no. 3, pp. 305–314, 1986.

[26] L. Li, Z. Zhang, and G. Shen, “The Effect of Grain Size on Fatigue Crack Propagation in Commercial Pure Titanium Investigated by Acoustic Emission,” *J. Mater. Eng. Perform.*, vol. 24, no. 7, pp. 2720–2729, 2015.

[27] A.W. Thompson and W.A. Backofen, “The effect of grain size on fatigue,” *Acta Metall.*, vol. 19, no. 7, pp. 597–606, 1971.

[28] Y. Hong, Y. Qiao, N. Liu, and X. Zheng," Effect of grain size on Collective Damage of Short Cracks and Fatigue Life Estimation For A Stainless Steel", *FFEMS,*, vol. 21, pp. 1317-1325, 1998.

[29] Y. Kitsunai, “Effect of Microstructure on Fatigue Crack Growth Mechanisms in High Strength Steel (Relationship between Crack Growth Rate and Prior by KITSUNAI Austenite Grain Size),” *J. Soc. Mater. Sci. Japan*, vol. 29, no. 323, pp. 795–800, 1980.

[30] A. Hartman and J. Schijve, “The effects of environment and load frequency on the crack propagation law for macro fatigue crack growth in aluminium alloys,” *Eng. Fract. Mech.*, vol. 1, no. 4, pp. 615–631, 1970.

[31] Yasuo Kobayashi, Toshinori Shibusawa and Keisuke Ishikawa “Environmental effect of fatigue crack propagation of magnesium alloy,” *Materials Science and Engineering*, A234-236, pp. 220-222, 1997.

[32] D. Rhodes and J. C. Radon “Environmental effects on crack propagation in

aluminium alloys," *FFEMS*, vol. 1, pp. 383–393, 1979.

[33] L. Weng, J. Zhang, S. Kalnaus, M. Feng, and Y. Jiang, "Corrosion fatigue crack growth of AISI 4340 steel," *Int. J. Fatigue*, vol. 48, pp. 156–164, 2013.

[34] D. H. Kang, J. K. Lee, and T. W. Kim, "Corrosion fatigue crack propagation of high-strength steel HSB800 in a seawater environment," *Procedia Eng.*, vol. 10, pp. 1170–1175, 2011.

[35] P. M. Scott, T. W. Thorpe, and D. R. V Silvester, "Rate-determining processes for corrosion fatigue crack growth in ferritic steels in seawater," *Corros. Sci.*, vol. 23, no. 6, pp. 559–575, 1983.

[36] R. P. Wei and C. Song, "Corrosion fatigue crack growth and electrochemical reactions for an X-70 linepipe steel in carbonate-bicarbonate solution," *Eng. Fract. Mech.*, vol. 41, no. 4, pp. 463–473, 1992.

[37] S. Sivaprasad, S. Tarafder, V. R. Ranganath, M. Tarafder, and K. K. Ray, "Corrosion fatigue crack growth behaviour of naval steels," *Corros. Sci.*, vol. 48, no. 8, pp. 1996–2013, 2006.

[38] S. A. SHIPILOV, "Mechanisms for corrosion fatigue crack propagation," *Fatigue Fract. Eng. Mater. Struct.*, vol. 25, no. 3, pp. 243–259, 2002.

[39] W. Cheng and I. Finnie, *Residual stress measurement and the slitting method*. Springer, 2007.

[40] P. J. Withers, "Residual stress and its role in failure," *Reports Prog. Phys.*, vol. 70, no. 12, pp. 2211–2264, 2007.

[41] Z. T. Zhang and S. J. Hu, "Stress and residual stress distributions in plane strain bending," *Int. J. Mech. Sci.*, vol. 40, no. 6, pp. 533–543, 1998.

[42] S. K. Bate, D. Green, and D. Buttle, "A review of residual stress distribution in welded joints for the deffect assessment of offshore structures," HSE Report no. OTH 482 , 1997.

[43] K. Amouzouvi, R. Styles, L. Clegg, D. McCooeye, L. Zhao, and A. Koul, "Effect of heat treatments on the relief of residual stresses and recrystallisation behaviour

of shot peened Zr-2.5Nb Pressure Tube Material," *ICSP* 1996.

[44] F. O. Neves, T. Luis, L. Oliviera, D. U. Braga, and A. Sander, "Influence of Heat Treatment on Residual Stress in Cold-Forged Parts," *Advances in Materials Science & Engineering*, vol. 2014, 2014.

[45] G. S. Schajer, *Practical Residual Stress Measurement Methods*. John Wiley & Sons Ltd, 2013.

[46] P. Prevey and N. Jayaraman, "Introduction of Residual Stresses to Enhance Fatigue Performance in the Initial Design," *Most*, vol. 2004, no. 513, pp. 7–9, 2004.

[47] M. N. James, "Residual Stress Influences in Mechanical Engineering," *XVIII Congr. Nac. Ing. Mec.*, 2010.

[48] N. S. Rossini, M. Dassisti, K. Y. Benyounis, and A. Olabi,, "Methods of Measuring Residual Stresses in Components ," *Materials & Design* pp. 1–50, 2012

[49] Guo B.L and L. T-X, "Experimental research of the effect of autofrettage on fatigue lives of cracked pressurized thick walled cylinders," in *proceedings of High Pressure Technology:Material, Design, Stress Analysis*, , pp. 579–589, 1988.

[50] Y. Fu, E. Ge, H. Su, J. Xu, and R. Li, "Cold expansion technology of connection holes in aircraft structures: A review and prospect," *Chinese J. Aeronaut.*, vol. 28, no. 4, pp. 961–973, 2015.

[51] Y. Zhang, M. E. Fitzpatrick, and L. Edwards, "Analysis of the residual stress around a cold-expanded fastener hole in a finite plate," *Strain*, vol. 41, no. 2, pp. 59–70, 2005.

[52] D. Stefanescu, A. Steuwer, R. A. Owen, B. Nadri, L. Edwards, M. E. Fitzpatrick, and P. J. Withers, "Elastic strains around cracked cold-expanded fastener holes measured using the synchrotron X-ray diffraction technique," *J. Strain Anal. Eng. Des.*, vol. 39, no. 5, pp. 459–469, 2004.

[53] K. Amjad, W.-C. Wang, and E. Patterson, “A comparison of split sleeve cold expansion in thick and thin plates,” *J. Strain Anal. Eng. Des.*, vol. 51, no. 5, pp. 375–386, 2016.

[54] B. K. N. Shanmukh, “Cold Hole Expansion Process for Stress Analysis and Evaluation of Fatigue Properties,” *IOSR J. Mech. Civ. Eng.*, vol. 2, no. 2278–1684, pp. 21–27, 2003.

[55] R. Cook and P. Holdway, “Residual stresses induced by hole cold expansion,” *Trans. Eng. Sci.*, vol. 2, pp. 91–100, 1993.

[56] P. Sanjurjo, C. Rodrguez, I. F. Pariente, F. J. Belzunce, and A. F. Canteli, “The influence of shot peening on the fatigue behaviour of duplex stainless steels,” *Procedia Eng.*, vol. 2, no. 1, pp. 1539–1546, 2010.

[57] D. J. Child, G. D. West, and R. C. Thomson, “Assessment of surface hardening effects from shot peening on a Ni-based alloy using electron backscatter diffraction techniques,” *Acta Mater.*, vol. 59, no. 12, pp. 4825–4834, 2011.

[58] H. Y. Miao, D. Demers, S. Larose, C. Perron, and M. Levesque, “Experimental study of shot peening and stress peen forming,” *J. Mater. Process. Technol.*, vol. 210, no. 15, pp. 2089–2102, 2010.

[59] G. Donzella, R. Gerosa, C. Petrogalli, B. Rivolta, G. Silva, and M. Beretta, “Evaluation of the residual stresses induced by shot peening on some sintered steels,” *Procedia Eng.*, vol. 10, pp. 3399–3404, 2011.

[60] H. Yang, X. Wu, G. Cao, and Z. Yang, “Enhanced boronizing kinetics and high temperature wear resistance of H13 steel with boriding treatment assisted by air blast shot peening,” *Surf. Coatings Technol.*, vol. 307, pp. 506–516, 2016.

[61] J. Gan, D. Sun, Z. Wang, P. Luo, and W. Wu, “The effect of shot peening on fatigue life of Q345D T-welded joint,” *J. Constr. Steel Res.*, vol. 126, pp. 74–82, 2016.

[62] B. Pyttel, I. Varfolomeyev, M. Luke, C. Berger, and D. Siegele, “FKM Guideline ‘Fracture Mechanics Proof of Strength for Engineering Components’ —

Overview and Extension Topics," *Weld. World*, vol. 51, no. 5–6, pp. 85–93, 2013.

[63] E. Giannakis and G. Savaidis, "Fatigue assessment of high strength leaf springs based on the FKM guideline," *Materwiss. Werksttech.*, vol. 47, no. 10, pp. 897–903, 2016.

[64] A. H. Mahmoudi, A. Ghasemi, G. H. Farrahi, and K. Sherafatnia, "A comprehensive experimental and numerical study on redistribution of residual stresses by shot peening," *Mater. Des.*, vol. 90, pp. 478–487, 2016.

[65] F. Yang, Z. Chen, and S. A. Meguid, "Effect of initial surface finish on effectiveness of shot peening treatment using enhanced periodic cell model," *Int. J. Mech. Mater. Des.*, vol. 11, no. 4, pp. 463–478, 2014.

[66] K. Takahashi, H. Okada, and K. Ando, "Effects of shot peening on the torsional fatigue limit of high-strength steel containing an artificial surface defect," *Int. J. Struct. Integr.*, vol. 3, no. 3, pp. 274–284, 2012.

[67] F. Klocke, J. Gomes, C. Löpenhaus, and R. R. Rego, "Assessing the heterogeneity of residual stress for complementing the fatigue performance comprehension," *J. Strain Anal.*, vol. 51, no. 5, pp. 1–11, 2016.

[68] M. A. Torres and H. J. Voorwald, "An evaluation of shot peening, residual stress and stress relaxation on the fatigue life of AISI 4340 steel," *Int. J. Fatigue*, vol. 24, no. 8, pp. 877–886, 2002.

[69] H. Lee, D. Kim, J. Jung, Y. Pyoun, and K. Shin, "Influence of peening on the corrosion properties of AISI 304 stainless steel," *Corros. Sci.*, vol. 51, no. 12, pp. 2826–2830, 2009.

[70] D. Závodská, M. Guagliano, O. Bokůvka, and L. Trško, "Fatigue Resistance of Low Alloy Steel after Shot Peening," *Mater. Today Proc.*, vol. 3, no. 4, pp. 1220–1225, 2016.

[71] P. Zhang, J. Lindemann, and C. Leyens, "Shot peening on the high-strength wrought magnesium alloy AZ80-Effect of peening media," *J. Mater. Process.*

Technol., vol. 210, no. 3, pp. 445–450, 2010.

[72] B. N. Mordyuk and G. I. Prokopenko, "Ultrasonic impact peening for the surface properties ' management," *J. Sound Vib.*, vol. 308, pp. 855–866, 2007.

[73] A. Gujba and M. Medraj, Laser Peening Process and Its Impact on Materials Properties in Comparison with Shot Peening and Ultrasonic Impact Peening, *Materials*, vol. 7, no. 12. 2014.

[74] H. Kumar, S. Singh, and P. Kumar, "Modified Shot Peening Processes – A review," *International Journal of Engineering Sciences & Emerging Technologies*, vol. 5, no. 1, pp. 12–19, 2013.

[75] T. Zhang, D. Wang, Y. Wang, C. Deng, and B. Gong, "Applied Surface Science Surface alloying method of ultrasonic shot peening on iron surface," *Appl. Surf. Sci.*, vol. 265, pp. 671–676, 2013.

[76] J. Tricoire, "Process Review: Ultrasonic Shot Peening," Springer, 2016.

[77] C. a. Rodopoulos, A. T. Kermanidis, E. Statnikov, V. Vityazev, and O. Korolkov, "The Effect of Surface Engineering Treatments on the Fatigue Behavior of 2024-T351 Aluminum Alloy," *J. Mater. Eng. Perform.*, vol. 16, no. 1, pp. 30–34, Jan. 2007.

[78] C. Pilé, D. Retraint, M. François, and J. Lu, "Effect of very high stress levels on the fatigue life of a TiAl based alloy," in *7th International Conference on Residual Stresses*, 2004, pp. 418–423.

[79] N. R. Tao, M. L. Sui, J. Lu, and K. Lua, "Surface nanocrystallization of iron induced by ultrasonic shot peening," *Nanostructured Mater.*, vol. 11, no. 4, pp. 433–440, 1999.

[80] G. Liu, J. Lu, and K. Lu, "Surface nanocrystallization of 316L stainless steel induced by ultrasonic shot peening," *Mater. Sci. Eng. A*, vol. 286, no. 1, pp. 91–95, 2000.

[81] A. H. Clauer, "LASER SHOCK PEENING FOR FATIGUE RESISTANCE," *Met. Soc. AIME*, no. 1996, pp. 217–230, 1996.

[82] O. Hatamleh, “A comprehensive investigation on the effects of laser and shot peening on fatigue crack growth in friction stir welded AA 2195 joints,” *Int. J. Fatigue*, vol. 31, no. 5, pp. 974–988, May 2009.

[83] S. Sathyajith and S. Kalainathan, “Effect of laser shot peening on precipitation hardened aluminum alloy 6061-T6 using low energy laser,” *Opt. Lasers Eng.*, vol. 50, no. 3, pp. 345–348, 2012.

[84] C. S. Montross, T. Wei, L. Ye, G. Clark, and Y. W. Mai, “Laser shock processing and its effects on microstructure and properties of metal alloys: A review,” *Int. J. Fatigue*, vol. 24, no. 10, pp. 1021–1036, 2002.

[85] O. HATAMLEH, J. LYONS, and R. FORMAN, “Laser and shot peening effects on fatigue crack growth in friction stir welded 7075-T7351 aluminum alloy joints,” *Int. J. Fatigue*, vol. 29, no. 3, pp. 421–434, Mar. 2007.

[86] A. Kadhim, E. T. Salim, S. M. Fayadh, A. A. Al-Amiery, A. A. H. Kadhum, and A. B. Mohamad, “Effect of multipath laser shock processing on microhardness, surface roughness, and wear resistance of 2024-T3 Al alloy,” *Sci. World J.*, vol. 2014, 2014.

[87] E. Maawad, H. G. Brokmeier, L. Wagner, Y. Sano, and C. Genzel, “Investigation on the surface and near-surface characteristics of Ti-2.5Cu after various mechanical surface treatments,” *Surf. Coatings Technol.*, vol. 205, no. 12, pp. 3644–3650, 2011.

[88] S. Spanrad and J. Tong, “Characterisation of foreign object damage (FOD) and early fatigue crack growth in laser shock peened Ti-6Al-4V aerofoil specimens,” *Mater. Sci. Eng. A*, vol. 528, no. 4–5, pp. 2128–2136, 2011.

[89] D. W. See, J. L. Dulaney, A. H. Clauer, and and R. D. Tenaglia, “The air force manufacturing technology laser peening initiative,” *Surf. Eng.*, vol. 18, pp. 32–36, 2002.

[90] Z. Zhou, S. Bhamare, G. Ramakrishnan, S. R. Mannava, K. Langer, Y. Wen, D. Qian, and V. K. Vasudevan, “Thermal relaxation of residual stress in laser shock peened Ti-6Al-4V alloy,” *Surf. Coatings Technol.*, vol. 206, no. 22, pp. 4619–

4627, 2012.

[91] C. Dane, L. Hackel, J. M. Halpin, J. Daly, J. Harrisson, and F. Harris, “High-throughput laser peening of metals using a high-average-power Nd: glass laser system,” *Proc. Soc. Photo-Optical Instrum. Eng.*, vol. 3887, November, pp. 211–221, 2000.

[92] J. Ocatia, M. Morales, C. Molpeceres, J. Porro, J. Grum, and M. Zupancic, “Laser Shock Processing As A Method For Surface Properties Modification Of Metallic Materials,” *Conf. Proc. ICSP-9*, pp. 466–471, 2005.

[93] P. Peyre, R. Fabbro, P. Merrien, and H. P. Lieurade, “Laser shock processing of aluminium alloys. Application to high cycle fatigue behaviour,” *Mater. Sci. Eng. A*, vol. 210, no. 1–2, pp. 102–113, Jun. 1996.

[94] C. Rubio-González, J. L. Ocaña, G. Gomez-Rosas, C. Molpeceres, M. Paredes, A. Banderas, J. Porro, and M. Morales, “Effect of laser shock processing on fatigue crack growth and fracture toughness of 6061-T6 aluminum alloy,” *Mater. Sci. Eng. A*, vol. 386, no. 1–2, pp. 291–295, Nov. 2004.

[95] R. Voothaluru, C. R. Liu, and G. J. Cheng, “Finite Element Analysis of the Variation in Residual Stress Distribution in Laser Shock Peening of Steels,” *J. Manuf. Sci. Eng.*, vol. 134, no. 6, p. 61010, Nov. 2012.

[96] P. Ganesh, R. Sundar, H. Kumar, R. Kaul, K. Ranganathan, P. Hedaoo, G. Raghavendra, S. Anand Kumar, P. Tiwari, D. C. Nagpure, K. S. Bindra, L. M. Kukreja, and S. M. Oak, “Studies on fatigue life enhancement of pre-fatigued spring steel specimens using laser shock peening,” *Mater. Des.*, vol. 54, pp. 734–741, Feb. 2014.

[97] C. Correa, L. Ruiz de Lara, M. Díaz, A. Gil-Santos, J. A. Porro, and J. L. Ocaña, “Effect of advancing direction on fatigue life of 316L stainless steel specimens treated by double-sided laser shock peening,” *Int. J. Fatigue*, vol. 79, pp. 1–9, 2015.

[98] I. Černý and J. Sís, “Fatigue Strength of Laser Hardened 42CrMo4 Steel Considering Effects of Compressive Residual Stresses on Short Crack Growth,”

Procedia Eng., vol. 74, pp. 417–420, 2014.

[99] A. Chahardehi, F. P. Brennan, and A. Steuwer, "The effect of residual stresses arising from laser shock peening on fatigue crack growth," *Eng. Fract. Mech.*, vol. 77, no. 11, pp. 2033–2039, 2010.

[100] D. Odhiambo and H. Soyama, "Cavitation shotless peening for improvement of fatigue strength of carbonized steel," *Int. J. Fatigue*, vol. 25, no. 9–11, pp. 1217–1222, 2003.

[101] H. Soyama, D. O. Macodiyo, and S. Mall, "Compressive residual stress into titanium alloy using cavitation shotless peening method," *Tribol. Lett.*, vol. 17, no. 3, pp. 501–504, 2004.

[102] H. Soyama, "Cavitation S Peening ® Cavitation S Peening ® ― Improvement of Fatigue Strength ―," vol. 127, no. 4, pp. 1095–1101, 2005.

[103] H. Soyama, Y. Sekine, and Y. Oyama, "Improvement of the Fatigue Strength of Stainless Steel SUS316L by a Cavitating Jet with an Associated Water Jet in Water," *ISIJ Int.*, vol. 48, no. 11, pp. 1577–1581, 2008.

[104] H. Soyama, K. Saito, and M. Saka, "Improvement of fatigue strength of aluminum alloy by cavitation shotless peening," *J. Eng. Mater. Technol. Asme*, vol. 124, no. 2, pp. 135–139, 2002.

[105] H. Soyama, M. Shimizu, Y. Hattori, and Y. Nagasawa, "Improving the fatigue strength of the elements of a steel belt for CVT by cavitation shotless peening," *J. Mater. Sci.*, vol. 43, no. 14, pp. 5028–5030, 2008.

[106] H. Soyama and N. Yamada, "Relieving micro-strain by introducing macro-strain in a polycrystalline metal surface by cavitation shotless peening," *Mater. Lett.*, vol. 62, no. 20, pp. 3564–3566, 2008.

[107] A. Kai and H. Soyama, "Visualization of the plastic deformation area beneath the surface of carbon steel induced by cavitation impact," *Scr. Mater.*, vol. 59, no. 3, pp. 272–275, 2008.

[108] V. J. Papazoglou and K. Masubuchi, "Analysis and control of distortion in

welded aluminum structures," *Weld. Journal, Res. Suppl.*, vol. 86, no. September, p. 251s–262s, 1978.

[109] Heat Treatment of Friction-Stir-Welded 7050 Aluminum Plates," *Lyndon B. Johnson Space Center, Houston, Texas* , March, pp. 19–20, 2006.

[110] M. McClinton and J. B. Cohen, "Changes in Residual Stress during the Tension Fatigue of Normalized and Peened SAE 1040 Steel," vol. 56, pp. 259–263, 1982.

[111] D. Tchoffo Ngoula, H. T. Beier, and M. Vormwald, "Fatigue crack growth in cruciform welded joints: Influence of residual stresses and of the weld toe geometry," *Int. J. Fatigue*, 2016.

[112] F. C. Smith, R. A. Smith, and T. Street, "Fatigue crack growth in a fillet welded joint," *Stress Int. J. Biol. Stress*, vol. 18, no. 4, pp. 861–869, 1983.

[113] R. Manna, "Heat Treatment," *Dep. Metall. Eng. Inst. Technol. Banaras Hindu Univ.*, vol. 1, pp. 2–38, 2012.

[114] SECO Warwick, *Heat Treating Data Book*, vol. 1. 2011.

[115] L. Mordfin, American Society for Testing and Materials. Committee E-328 on Mechanical Testing., ASTM International., and O. International Symposium on Mechanical Relaxation of Residual Stresses (1987 : Cincinnati, *Mechanical relaxation of residual stresses*. ASTM, 1988.

[116] M. Fitzpatrick, A. Fry, P. Holdway, F. Kandil, J. Shackleton, and L. Suominen, "Determination of Residual Stresses by X-ray Diffraction - Issue 2," *Meas. Good Pract. Guid.*, no. 52, p. 74, 2005.

[117] G. S. Schajer, *Practical residual stress measurement methods, A John Wiley & Sons, Ltd., Publication, 2013*.

[118] M. B. Prime, "Cross-Sectional Mapping of Residual Stresses by Measuring the Surface Contour After a Cut," *J. Eng. Mater. Technol.*, vol. 123: 162-6, 2001.

[119] P. Pagliaro, M. B. Prime, H. Swenson, and B. Zuccarello, "Measuring multiple residual-stress components using the Contour method and multiple cuts," *Exp. Mech.*, vol. 50, no. 2, pp. 187–194, 2010.

[120] M. Prime and R. Martineau, “Mapping Residual Stresses After Foreign Object Damage Using The Contour Method,” *Mater. Sci. Forum* 404-407 521-26, 2002.

[121] Y. Zhang, S. Ganguly, L. Edwards, and M. E. Fitzpatrick, “Cross-sectional mapping of residual stresses in a VPPA weld using the contour method,” *Acta Mater.*, vol. 52, no. 17, pp. 5225–5232, 2004.

[122] H. Kaplan, “Laser Gauging Enters a Submicron World,” *Photonics Spectra*, vol. 31, no. 6, pp. 67–68, 1997.

[123] Z. B. Zhao, J. Hershberger, S. M. Yalisove, and J. C. Bilello, “Determination of residual stress in thin films: a comparative study of X-ray topography versus laser curvature method,” *Thin Solid Films*, vol. 415, pp. 21–31, 2002.

[124] P. J. Withers, M. Preuss, A. Steuwer, and J. W. L. Pang, “Methods for obtaining the strain-free lattice parameter when using diffraction to determine residual stress,” *J. Appl. Cryst.*, no. 40, pp. 891–904, 2007.

[125] B. D. Cullity and S. R. Stock, *Elements of X-ray diffraction*, 3rd edition. 2001.

[126] I. C. Noyen and J. B. Cohen, *Residual Stress Measurement by Diffraction and Interpretation*. Berlin: Springer-Verlag, 1987.

[127] H. H. Lester and R. H. Aborn, “Behaviour of iron crystals under load,” *Army Ordnance*, vol. 6, pp. 120–364, 1925-1926.

[128] V. Hauk, (Ed), “Structural and residual stress analysis by nondestructive methods,” *Elsevier*, 1997.

[129] P. J. Withers and H. K. D. H. Bhadeshia, “Residual stress. Part 1–measurement techniques,” *Mater. Sci. Technol.*, vol. 17, April, pp. 355–365, 2001.

[130] Y. Zhan, C. Liu, X. Kong, and Z. Lin, “Experiment and numerical simulation for laser ultrasonic measurement of residual stress,” *Ultrasonics*, vol. 73, pp. 271–276, 2017.

[131] Y. Javadi, S. Sadeghi, and M. A. Najafabadi, “Taguchi optimization and ultrasonic measurement of residual stresses in the friction stir welding,” *Mater. Des.*, vol. 55, pp. 27–34, 2014.

[132] H. Du and J. A. Turner, “Dependence of diffuse ultrasonic backscatter on residual stress in 1080 steel,” *Ultrasonics*, vol. 67, pp. 65–69, 2016.

[133] C. Xu, W. Song, Q. Pan, H. Li, and S. Liu, “Nondestructive testing residual stress using ultrasonic critical refracted longitudinal wave,” *Phys. Procedia*, vol. 70, pp. 594–598, 2015.

[134] Y. Javadi and M. A. Najafabadi, “Comparison between contact and immersion ultrasonic method to evaluate welding residual stresses of dissimilar joints,” *Mater. Des.*, vol. 47, pp. 473–482, 2013.

[135] Y. Javadi, M. Akhlaghi, and M. A. Najafabadi, “Using finite element and ultrasonic method to evaluate welding longitudinal residual stress through the thickness in austenitic stainless steel plates,” *Mater. Des.*, vol. 45, pp. 628–642, 2013.

[136] Y. Kudryavtsev, J. Kleiman, O. Gushcha, V. Smilenko, and V. Brodovy, “Ultrasonic Technique and Device for Residual Stress Measurement,” *2004 SEM X Int. Congr. Expo. Exp. Appl. Mech.*, pp. 1–7, 2004.

[137] D. I. Crecraft, “The measurement of applied and residual stresses in metals using ultrasonic waves,” *J. Sound Vib.*, vol. 5, no. 1, pp. 173–192, 1967.

[138] Y. Zhan, C. Liu, X. Kong, and Z. Lin, “Experiment and numerical simulation for laser ultrasonic measurement of residual stress,” *Ultrasonics*, vol. 73, pp. 271–276, 2017.

[139] M. R. Viotti and A. Albertazzi, “Approximated Repair Methods for Outlier Strain Data from Hole-Drilling Residual Measurements,” *Exp. Mech.*, vol. 53, no. 3, pp. 393–403, 2013.

[140] T. Rickert, “Residual Stress Measurement by ESPI Hole-Drilling,” *Procedia CIRP*, vol. 45, pp. 203–206, 2016.

[141] C. J. Lammi and D. A. Lados, “Effects of Processing Residual Stresses on Fatigue Crack Growth Behavior of Structural Materials: Experimental Approaches and Microstructural Mechanisms,” *Metall. Mater. Trans. A*, vol. 43,

no. 1, pp. 87–107, 2011.

[142] S. Y. Oakley and D. Nowell, “Prediction of the combined high- and low-cycle fatigue performance of gas turbine blades after foreign object damage,” *Int. J. Fatigue*, vol. 29, no. 1, pp. 69–80, 2007.

[143] D. J. Cartwright and, D. P. Rooke, “Approximate Compounded Stress Intensity Factors From Known Solutions,” *Eng. Fract. Mech.,* vol. 6, no. 3, pp.563-571, 1974.

[144] A. Chahardehi, F. P. Brennan, and S. K. Han, “Surface crack shape evolution modelling using an RMS SIF approach,” *Int. J. Fatigue*, vol. 32, no. 2, pp. 297–301, 2010.

[145] J. H. Kim and I. S. Hwang, “Crack shape evolution of surface flaws under fatigue loading of austenitic pipes,” *Nucl. Eng. Des.*, vol. 174, no. 1, pp. 17–24, 1997.

[146] R. Branco and F. V. Antunes, “Finite element modelling and analysis of crack shape evolution in mode-I fatigue Middle Cracked Tension specimens,” *Eng. Fract. Mech.*, vol. 75, no. 10, pp. 3020–3037, 2008.

[147] S. S. Ngiam and F. P. Brennan, “Crack Shape Control using Cold Rolling,” *Proc. Fatigue Crack Paths (FCP 2003)*, 2003.

[148] F. P. Brennan, S. S. Ngiam, and C. W. Lee, “An experimental and analytical study of fatigue crack shape control by cold working,” *Eng. Fract. Mech.*, vol. 75, no. 3–4, pp. 355–363, 2008.

[149] J. D. Almer, J. B. Cohen, and B. Moran, “The effects of residual macrostresses and microstresses on fatigue crack initiation,” *Mater. Sci. Eng. A*, vol. 284, no. 1–2, pp. 268–279, 2000.

[150] Y. C. Lam and K. S. Lian, “The effect of residual stress and its redistribution on fatigue crack growth,” *Theor. Appl. Fract. Mech.*, vol. 12, pp. 59–66, 1989.

[151] W. Elber, “Equivalent constant amplitude concept for crack growth under spectrum loads,” *ASTM*, vol. STP 595, pp. 236-250, 1976.

[152] N. a. Fleck, C. S. Shin, and R. a. Smith, “Fatigue crack growth under

compressive loading," *Engineering Fracture Mechanics*, vol. 21, no. 1. pp. 173–185, 1985.

[153] S. Suresh, "Crack initiation in cyclic compression and its applications," *Eng. Fract. Mech.*, vol. 21, no. 3, pp. 453–463, 1985.

[154] M. E. Fitzpatrick and L. Edwards, "Fatigue Crack/Residual Stress Field Interactions and Their Implications for Damage-Tolerant Design," *Jmepeg*, vol. 7, no. 2 April, pp. 190–198, 1998.

[155] J. Billingham, J. V. Sharp, J. Spurrier, and P. J. Kilgallon, "Review of the performance of high strength steels used offshore," *HSE Research Report No. 105*, pp. 6–8, 2003.

[156] J. R. Shaw and B. K. Zuidema, "New High Strength Steels Help Automakers Reach Future Goals for Safety, Affordability, Fuel Efficiency and Environmental Responsibility." SAE International , 2001.

[157] E. Gogou, "Use of High strength steel grades for economic bridge design," Masters thesis, TUDelft, 2012.

[158] G. Li, Y. Wang, and S. Chen, "The Art Of Application Of High-Strength Steel Structures For Buildings In Seismic Zones," Advanced Steel Construction, vol. 11, no. 4, pp. 492–506, 2015.

[159] G. F. Abdelal, N. Abuelfoutouh, and A. H. Gad, *Finite Element Analysis for Satellite Structures*. Springer, 2013.

[160] L. S. Teh, "Library of Geometric Influences for Stress Intensity Factor Weight Functions," University College London, 2002.

[161] M. Leitner, P. Pauer, P. Kainzinger, and W. Eichlseder, "Numerical effects on notch fatigue strength assessment of non-welded and welded components," *Comput. Struct.*, vol. 191, pp. 51–61, 2017.

[162] Y. Huang and X. Hu, "Fracture Mechanics Theoretical Modelling and FEM Analysis of 3- Point Bending Specimen Suffering Cyclic Loads," *The Proceedingsof 2001 9th International Conference on Reliability, Maintainability*

and Safety, pp. 308–312, 2011.

[163] Y. Yang and M. Vormwald, "Fatigue crack growth simulation under cyclic non-proportional mixed mode loading," *Int. J. Fatigue*, vol. 102, pp. 37–47, 2017.

[164] W. Liu, X. Yao, and X. Chen, "A local stress approach to predict the fatigue life of the U-notched PMMA plate at different temperatures," *Int. J. Fatigue*, vol. 103, pp. 436–443, 2017.

[165] S. Arun, A. H. Sherry, M. C. Smith, and M. Sheikh, "Simulations of the large-scale four point bending test using Rousselier model," *Eng. Fract. Mech.*, vol. 178, pp. 497–511, 2017.

[166] J. C. Newman and I. S. Raju, "An empirical stress-intensity factor equation for the surface crack," *Eng. Fract. Mech.*, vol. 15, no. 1–2, pp. 185–192, Jan. 1981.

[167] ASTM-E740, "Standard Practice for Fracture Testing with Surface-Crack Tension Specimens," 2010.

[169] "Abaqus 6.13 Keywords Reference Manual" and U. 2013 Providence, RI, "Abaqus/CAE User's Manual: Version 6.5 Documentation." pp. 1–19, 2013.

[170] A. T. Zehnder and M. J. Viz, "Fracture Mechanics of Thin Plates and Shells Under Combined Membrane, Bending, and Twisting Loads," *Appl. Mech. Rev.*, vol. 58, no. 1, p. 37, 2005.

[171] W. Cheng and I. Finnie, *Residual Stress Measurement and the Slittin Method*, Springer. 2007.

[172] ASTM-E 837:2008, "Standard Test Method for Determining Residual Stresses by the Hole-Drilling Strain-Gages," vol. 1, no. C, pp. 1–17, 2008.

[173] Micro-measurement/ Vishay precision group, "RS-200 Milling Guide for Residual Stress Measurements RS-200," pp. 62–64, 2011.

[174] Micro-measurement/ Vishay precision group, "Measurement of Residual Stresses by the Hole-Drilling* Strain Gage Method," 2010.

[175] B. Ahmad, Michael E. and M. E. Fitzpatrick, "Analysis of Residual Stresses in

Laser-Shock-Peened and Shot-Peened Marine Steel Welds," *Metall. Mater. Trans. A*, 2016.

[176] A. Niku-Lari , "An overview of Shot Peening," *Intl Conf Shot Peen. Blast Clean.*, IITT.France, pp. 1–25, 1996.

[177] L. Trško, M. Guagliano, O. Bokůvka, and F. Nový, "Fatigue life of AW 7075 aluminium alloy after severe shot peening treatment with different intensities," *Procedia Eng.*, vol. 74, October, pp. 246–252, 2014.

[178] M. K. Kulekci and U. Esme, "Critical analysis of processes and apparatus for industrial surface peening technologies," *Int. J. Adv. Manuf. Technol.*, vol. 74, no. 9–12, pp. 1551–1565, 2014.

[179] U. Masteel UK Ltd, *Vastaanottotodistus inspection certificate*, vol. EN 10204-3. 2004.

[180] G. T. Robertson, "The effect of shot size on the residual stresses resulting from shot peening," *Shot Peen. Mag.*, vol. 11, no. 3, p. 3, 1997.

[181] K. Toshal, J. Lu, B. Guelorget, and E. Nagashima, "Shot Peening and Grit Blasting - Effects on Surface Integrity-," *Icsp9 Shot Peen.*, pp. 400–405, 2005.

[182] H. Guechichi, L. Castex, and M. Benkhettab, "An Analytical Model to Relate Shot Peening Almen Intensity to Shot Velocity," *Mech. Based Des. Struct. Mach.*, vol. 41, no. 1, pp. 79–99, 2013.

[183] A. T. Vielma, V. Llaneza, and F. J. Belzunce, "Effect of coverage and double peening treatments on the fatigue life of a quenched and tempered structural steel," *Surf. Coatings Technol.*, vol. 249, pp. 75–83, 2014.

[184] L. Wagner, *Shot Peening*. Wiley VCH; 1 edition (6 Jun. 2003), 2003.

[185] "Standard Test Method for Measurement of Fatigue Crack Growth Rates," *E647-11*, vol. i, no. C, pp. 1–45, 2010.

[186] T. W. Thorpe, P. M. Scott, A. Rance, and D. Silvester, "Corrosion fatigue of BS-4360-50d structural-steel in seawater," *Int. J. Fatigue*, vol. 5, no. 3, pp. 123–133, 1983.

[187] E. Coudert and C. Renaudin, “Variable amplitude corrosion fatigue behaviour and hydrogen embrittlement of high strength steels for offshore applications,” *Int. Offshore Polar Eng. Conf.*, vol. IV, pp. 116–122, 1998.

[188] K. Moussaoui, M. Mousseigne, J. Senatore and R. Chieragatti, “The effect of roughness and residual stresses on fatigue life time of an alloy of titanium,” *Int J AdvManuf Technol*, Vol. 78, Issue 1–4, pp 557–563, 2015.

[189] W. D. Pilkey and D. F. Pilkey, *Peterson’s Stress Concentration Factors*. Hoboken, NJ, USA: John Wiley & Sons, Inc., 2007.

[190] M. K. Raja, S. Mahadevan, B. P. C. Rao, S. P. Behera, T. Jayakumar, and B. Raj, “Influence of crack length on crack depth measurement by an alternating current potential drop technique,” *Meas. Sci. Technol.*, vol. 21, no. 10, p. 105702, 2010.

[191] M. C. Lugg, “AN INTRODUCTION TO ACPD,” *Technical Software Consultants Ltd.*, February, 6 Mill Square, Featherstone Road, Wolverton Mill, Milton Keynes, MK12 5RB, UK, p. 1.1 (18), 2002.

[192] Matelect, “The Potential Drop Technique & Its Use In Fatigue Testing.”

[193] H. Saguy and D. Rittle, “Flaw detection in metal by the ACPD technique: Theory and experiments,” *NDT&E Int.*, no. 2, pp. 3–7, 2007.

[194] M. C. Lugg, “TSC INSPECTION SYSTEMS,” Technical Software Consultants Ltd., Milton Keynes, MK12 5RB, UK, 2009.

[195] F. P. Brennan, S. S. Ngiam, and C. W. Lee, “An experimental and analytical study of fatigue crack shape control by cold working,” *Eng. Fract. Mech.*, vol. 75, no. 3–4, pp. 355–363, Feb. 2007.

APPENDICES

Appendix A Four-point Bend rig design

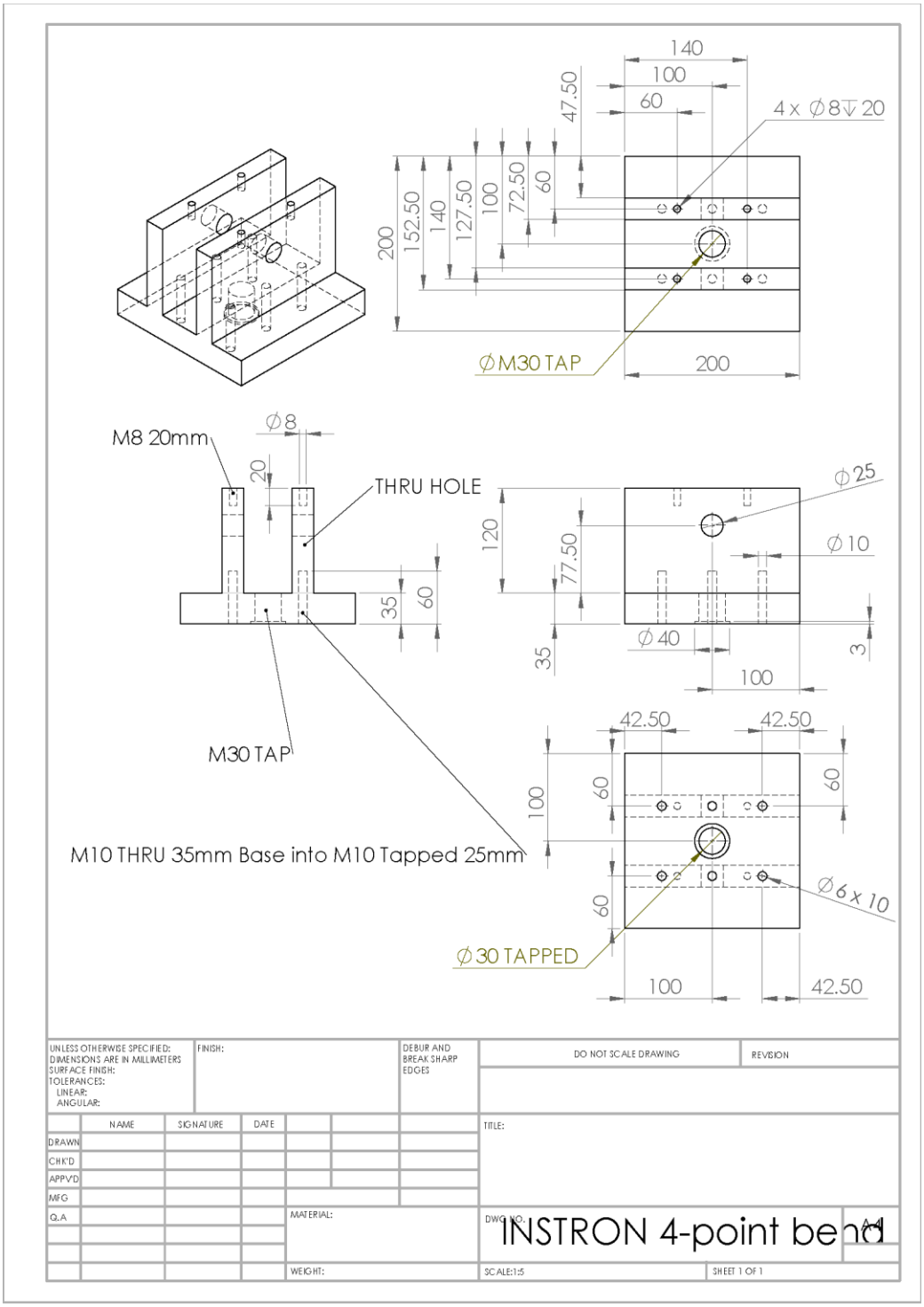

Figure A-1 Four-point bend rig design

Appendix B Matlab Code for calculating residual stress for hole drilling

```
%hd_non_uniform.m

%Harry Coules 2010


%Modified revision:

%hd_non_uniform_simple.m

%Harry Coules 2012


%This program computes residual stresses from blind hole drilling data

%according to ASTM Standard E837-08


%Read data file

    disp('Which file contains the hole drilling data you wish to analyse?');

    disp('File must be tab-separated data in the format:');

    filename = input('Depth S1 S2 S3, without headers    ','s');


    fid = fopen(filename);

    C = textscan(fid,'%f %f %f %f');

    fclose(fid);
```

```
    strain_steps = [C{2},C{3},C{4}];


%User needs to input drilling parameters
    rosette_type = input('Rosette type (A/B/C):   ','s');
    total_depth = input('Overall hole depth (mm):  ');
    hole_dia = input('Overall hole diameter (mm):   ');


    gc_dia = [];
    gc_dia = input('Gauge circle diameter (mm) [5.13]:   ');
    if isempty(gc_dia)
        gc_dia = 5.13;
    end


    d0_over_d = hole_dia/gc_dia;


    E = input('Young modulus (GPa):  ')*10^9;
    nu = input('Poisson ratio:  ');


    disp('If you wish to apply a stress transformation to find');
    disp('the stresses at an angle to the rosette orientation,');
    theta = input('please provide agnle (degrees, anticlockwise +ive [0]:   ');
    if isempty(theta)
        theta = 0;
```

```
    end


%Plot strain vs depth
    plot(depth_steps,strain_steps(:,1),'b');
    hold on
    plot(depth_steps,strain_steps(:,2),'r');
    plot(depth_steps,strain_steps(:,3),'g');
    xlim([depth_steps(1),depth_steps(end)]);
    xlabel('Hole depth (mm)');
    ylabel('Strain');
    legend('Gauge 1','Gauge 2','Gauge 3','Location','SouthOutside')


    disp('Please verify that the strain/hole depth plots ');
    disp('follow generally smooth trends');


%Take the zero depth line off of depth_steps and strain_steps
    depth_steps(1) = [];
    strain_steps(1,:) = [];


%Compute combinational strains (see ASTM standard p742)
    p_j = 0.5*(strain_steps(:,3)+strain_steps(:,1));
    q_j = 0.5*(strain_steps(:,3)-strain_steps(:,1));
    t_j = 0.5*(strain_steps(:,3)+strain_steps(:,1)-2*strain_steps(:,2));
```

```
%Estimate the standard errors

   p_std_sq = sum(((p_j(1:length(p_j)-3)-(3*p_j(2:length(p_j)-2))+(3*p_j(3:length(p_j)-
1)- p_j(4:length(p_j)))).^2)./(20*(length(p_j)-3)));

   q_std_sq = sum(((q_j(1:length(q_j)-3)-(3*q_j(2:length(q_j)-2))+(3*q_j(3:length(q_j)-
1)- q_j(4:length(q_j)))).^2)./(20*(length(q_j)-3)));

   t_std_sq  =  sum(((t_j(1:length(t_j)-3)-(3*t_j(2:length(t_j)-2))+(3*t_j(3:length(t_j)-1)-
t_j(4:length(t_j)))).^2)./(20*(length(t_j)-3)));


%Load calibration matrices:


if rosette_type == 'a'||rosette_type == 'A'

   load non_uniform_calibration_data_a.mat;

elseif  rosette_type == 'b'||rosette_type == 'B'

   load non_uniform_calibration_data_b.mat;

elseif  rosette_type == 'c'||rosette_type == 'C'

   load non_uniform_calibration_data_c.mat;

else

   error('Rosette type not recognised.')

end


   calib_a = calib_a.*(hole_dia/2)^2;  %Adjust calibration matrices for hole dia.

   calib_b = calib_b.*(hole_dia/2)^2;

   %Also loaded: stress_depths, c (second derivitive matrix)
```

```
%Initial guesses at regularisation factors
    alpha_p = 10^-5;
    alpha_q = 10^-5;
    alpha_t = 10^-5;

%Iterate to find good regularisation factors, and hence the stresses
    alpha_p_ok = 0;
    alpha_q_ok = 0;
    alpha_t_ok = 0;
    all_alphas_ok = 0;
    k = 0;

    while all_alphas_ok == 0
        %Apply the regularisation and calculate the stresses
            P = ((calib_a'*calib_a)+(alpha_p*c'*c))\((E/(1+nu))*calib_a'*p_j);
            Q = ((calib_b'*calib_b)+(alpha_q*c'*c))\(E*calib_b'*q_j);
            T = ((calib_b'*calib_b)+(alpha_t*c'*c))\(E*calib_b'*t_j);

            %P = pinv((calib_a'*calib_a)+(alpha_p*c'*c))*((E/(1+nu))*calib_a'*p_j);
            %Q = pinv((calib_b'*calib_b)+(alpha_q*c'*c))*(E*calib_b'*q_j);
            %T = pinv((calib_b'*calib_b)+(alpha_t*c'*c))*(E*calib_b'*t_j);
```

```
%Calculate 'misfit' strains
    p_m = p_j-(((1+nu)/E)*calib_a*P);
    q_m = q_j-((1/E)*calib_b*Q);
    t_m = t_j-((1/E)*calib_b*T);

%Mean squares of misfit vectors
    p_rms_sq = sum(abs(p_m.^2))/length(p_m);
    q_rms_sq = sum(abs(q_m.^2))/length(q_m);
    t_rms_sq = sum(abs(t_m.^2))/length(t_m);

    if isnan(p_rms_sq) == 1 || isnan(q_rms_sq) == 1 || isnan(t_rms_sq) == 1
        error('Mean squares of misfit vector = NaN');
    end

%Check rms of misfit vectors against raw strain errors, and accept the
%regularisation factors if they're similar. If not, make a new guess
%based on the ratio of errors.
    if 0.95*p_std_sq < p_rms_sq && p_rms_sq < 1.05*p_std_sq
        alpha_p_ok = 1;
    else
        alpha_p = alpha_p*(p_std_sq/p_rms_sq);
    end
```

```
        if 0.95*q_std_sq < q_rms_sq && q_rms_sq < 1.05*q_std_sq
            alpha_q_ok = 1;
        else
            alpha_q = alpha_q*(q_std_sq/q_rms_sq);
        end

        if 0.95*t_std_sq < t_rms_sq && t_rms_sq < 1.05*t_std_sq
            alpha_t_ok = 1;
        else
            alpha_t = alpha_t*(t_std_sq/t_rms_sq);
        end

        %Check all factors okay
        if alpha_p_ok == 1 && alpha_q_ok == 1 && alpha_t_ok == 1
            all_alphas_ok = 1;
        end

        %Increment iteration counter
        k = k+1;
    end

%Compute Cartesian stresses:
```

```
s_x = P - Q;      %Note s_x is in the transverse weld dir if gauge 1 was oriented transverse

s_y = P + Q;      %Note s_y is in the longitudinal weld dir if gauge 1 was oriented transverse

tau_xy = T;


%Apply stress transformation

[s_x,s_y,tau_xy] = stress_trans(s_x,s_y,tau_xy,theta);


s_x_av = mean(s_x); %Mean cartesian stresses

s_y_av = mean(s_y);

tau_xy_av = mean(tau_xy);


%Compute Principal stresses

princ_s_1 = P+((Q.^2+T.^2).^0.5);

princ_s_2 = P-((Q.^2+T.^2).^0.5);


princ_s_1_av = mean(princ_s_1); %Mean principal stresses

princ_s_2_av = mean(princ_s_2);


%Display Stress Components

disp(' ');

disp(' ');
```

```
    disp('*** NUMERICAL RESULTS ***');
    disp('Mean stresses over 1mm depth into surface:');
    disp(['Longitudinal: ',num2str(s_y_av*10^-6),' MPa']);
    disp(['Transverse: ',num2str(s_x_av*10^-6),' MPa']);
    disp(['Shear: ',num2str(tau_xy_av*10^-6),' MPa']);
    disp(' ');
    disp(['Principal (1): ',num2str(princ_s_1_av*10^-6),' MPa']);
    disp(['Principal (2): ',num2str(princ_s_2_av*10^-6),' MPa']);

    disp('**************************');



%Plot Cartesian stresses (in MPa) over the depth (in mm)
    figure
    plot(-stress_depths,s_y*10^-6,'or');
    hold on
    plot(-stress_depths,s_x*10^-6,'ob');
    plot(-stress_depths,tau_xy*10^-6,'og');
    line([0,0],[0,-total_depth],'color','k');
```

```
legend('Longitudinal Stress','Transverse Stress','Shear Stress','Location','SouthOutside')  %Assumes that gauge 1 was oriented transverse, and gauge 3 longitudinal.

title('Depth-varying stresses (Cartesian directions)')


xlabel('Depth (mm)');

ylabel('Stress (MPa)');


%Plot Principal stresses (in MPa) over the depth (in mm)

figure

plot(-stress_depths,princ_s_1*10^-6,'or');

hold on

plot(-stress_depths,princ_s_2*10^-6,'ob');

line([0,0],[0,-total_depth],'color','k');

legend('First Principal Stress (s_1)','Second Principal Stress (s_2)','Location','SouthOutside')  %Doesn't sort into max and min principals

title('Depth-varying principal stresses')


xlabel('Depth (mm)');

ylabel('Stress (MPa)');
```

Appendix C Tension-Tension Fatigue test

In this appendix, the results of tension fatigue load at maximum applied loads of 120 kN and 100 kN with a constant load ratio of 0.1. These tests were conducted due to overestimating of the theoretical applied fatigue load.

C.1 Result of A60

A fatigue crack growth test was performed on the A60 specimen (unpeened specimen) and the results are shown in Figure C-1 and Figure C-2. The maximum applied fatigue load was 120 kN and the load ratio 0.1.

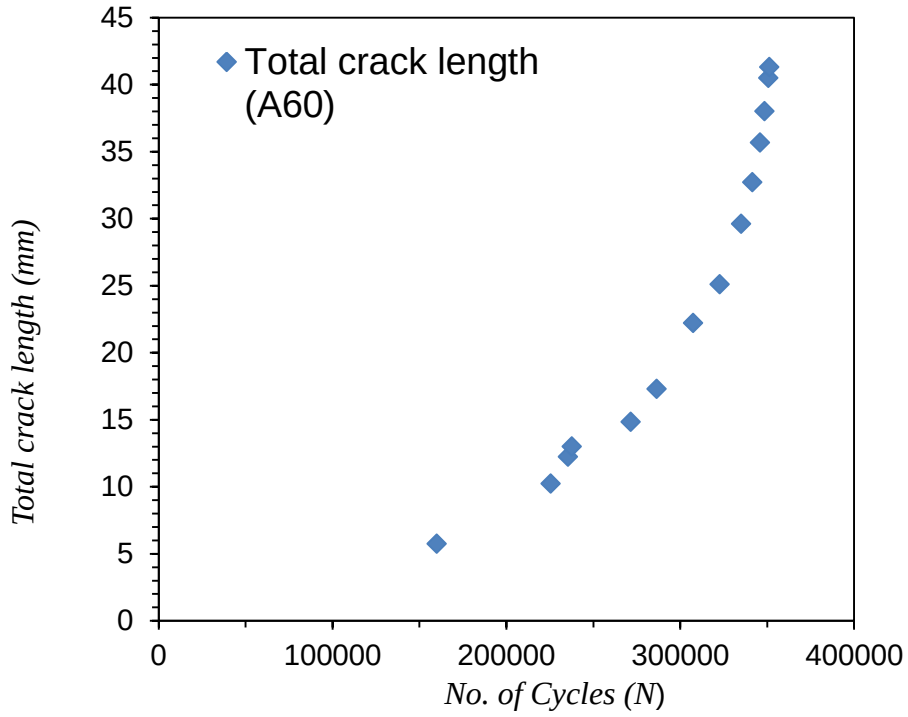

Figure C-1: Fatigue crack growth test A60 specimen

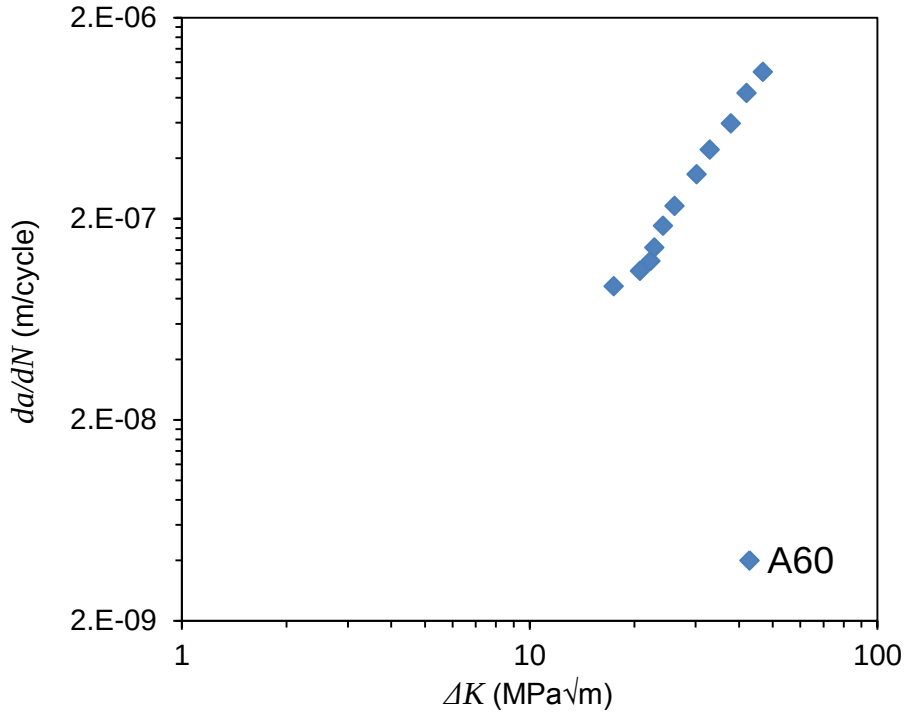

Figure C-2: Fatigue crack growth rate for A60

C.2 Result of A20

The specimen ($A20$) has been examined under a fatigue test which has a peening area ($6.5\ mm$) from the head of the notch tip as shown in Figure C-4 and Figure C-5. The maximum applied fatigue load was 100 kN and the load ratio 0.1.

C.3 Result of A10

The specimen A10 was tested under tension-tension fatigue load which contains a peening area 1.75mm from the head of the crack tip, as shown in Figure C-6. The maximum applied fatigue load was 90 kN and load ratio 0.1. The specimen was used to measure residual stress distribution by using the hole drilling technique. It has been observed during the fatigue test that fatigue crack growth became retarded when the fatigue crack reach the peening area. The retardation happened due to the beneficial compressive residual stress in the partial peening area, as shown Figure C-7. Also, there is a drop in fatigue crack growth rate in the hole drilling place, as shown in Figure C-7, due to first, the residual stress relaxation and second being hard to monitor the fatigue

crack growth inside the drilled hole by using the camera. So, the result is inaccurate near the drilled hole.

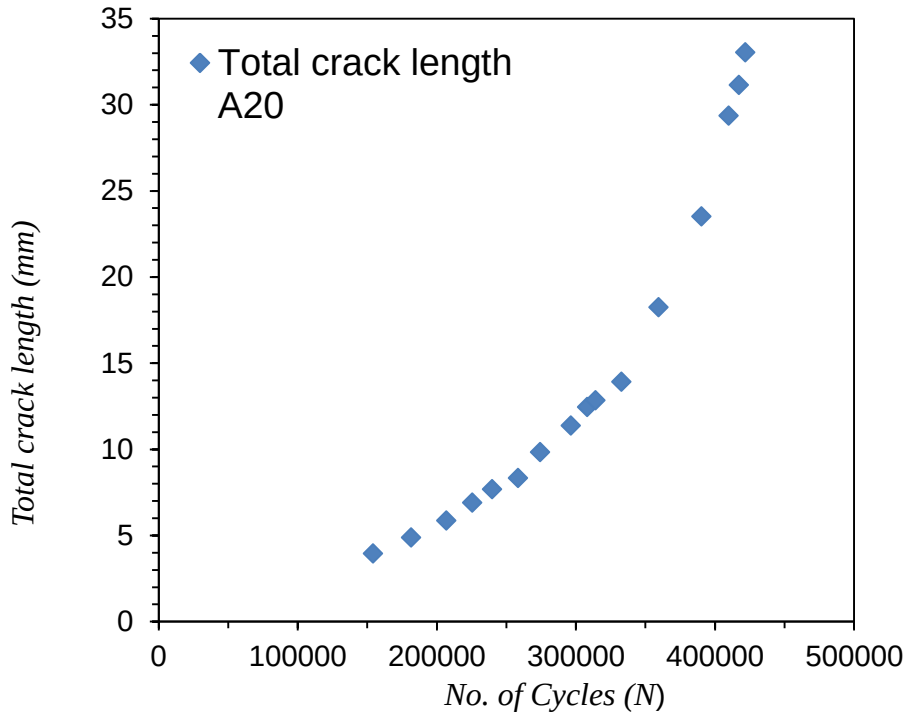

Figure_Apx C-3: Fatigue crack growth for A20 specimen

Figure C-4: Fatigue crack growth for A20 specimen

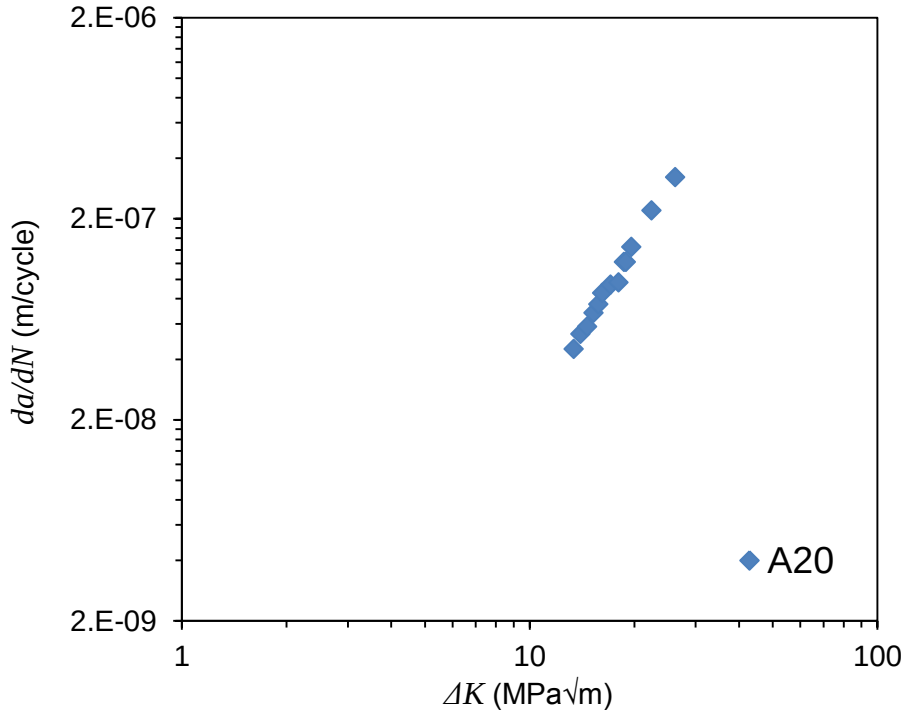

Figure C-5: Fatigue crack growth rate for A60

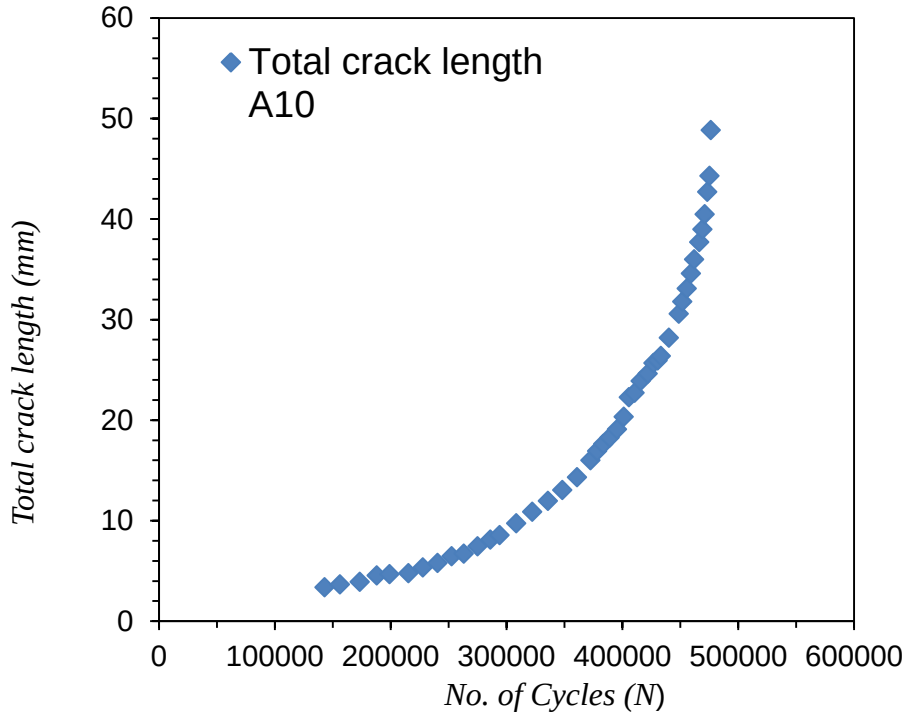

Figure C-6: Fatigue crack growth A10

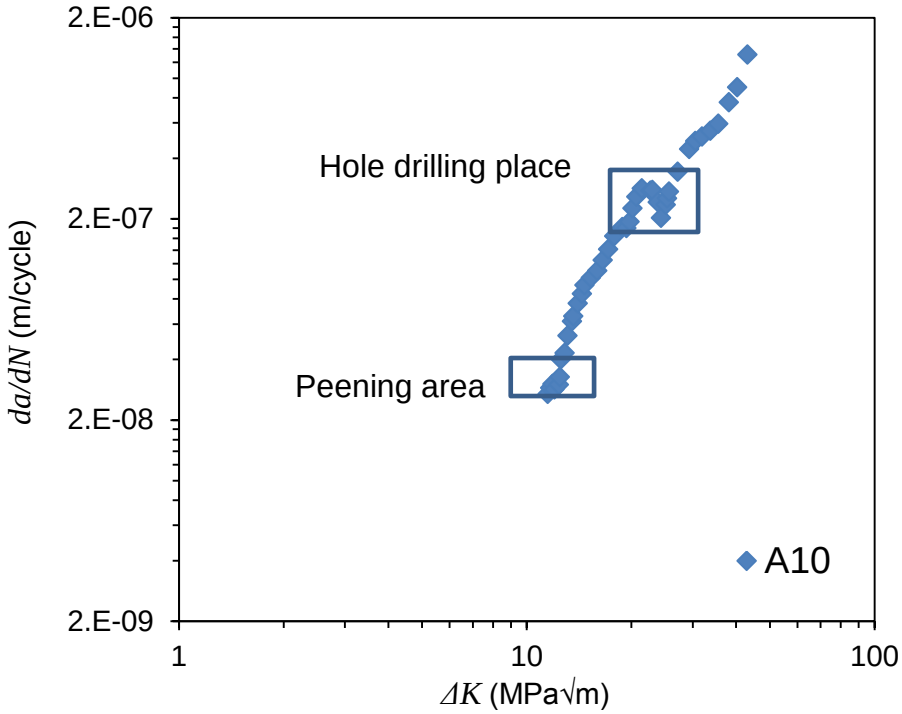

Figure C-7: Fatigue crack growth rate for A10

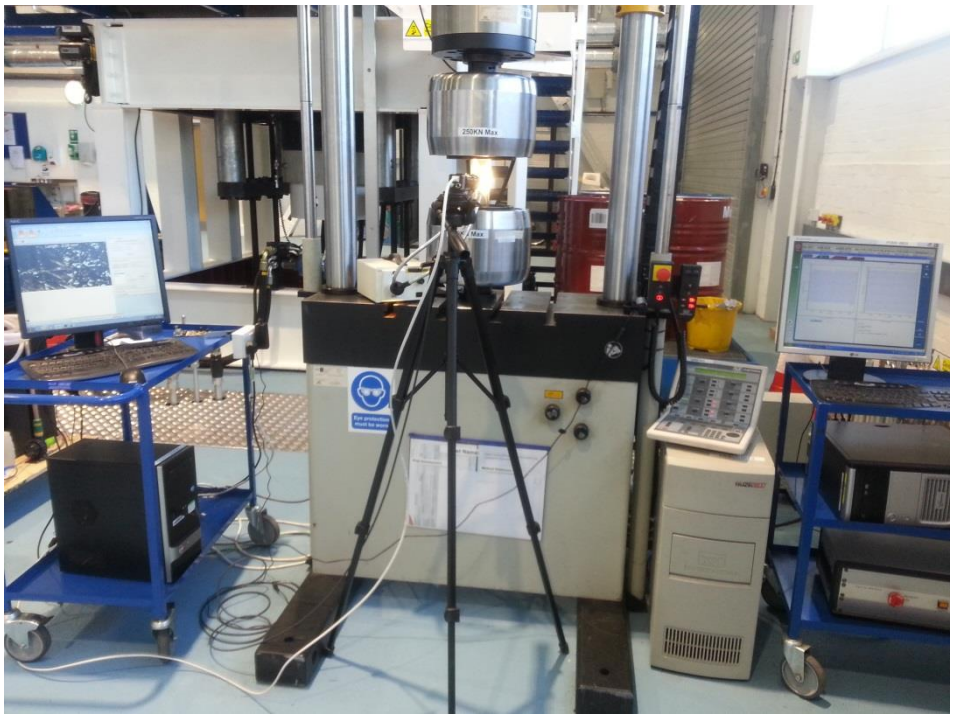

Figure C-8: Experimental set-up

Appendix D Material Microstructure

In this appendix, although the high strength steel used in this investigation is quenched and tempered, a metallographic evolution has been made. The evolution was made following the ASTM E-3 standard. A sample was extracted from the edge of the plate, as shown in Figure D-1, into 40mm x 25mm x thickness specimens for metallographic preparation by using a mechanical method. The sample was cut in two different directions – longitudinal (L) and transverse (T) – as shown in Figure D-2. These are mounted in resin to have better control of the sample as shown in Figure D-2. Successively finer abrasive particles were used until the desired surface quality was achieved, namely, 6 µm, 3 µm, 1 µm and 0.05 µm. The samples were washed and swabbed with Isopropyl Alcohol (ISP) and then dried with hot air. An Optical Microscope (OM) was used to analyse the micro-structure orientation of the material, as shown in Figure D-3 and Figure D-4.

Figure D-1: Sample extracted from the plate

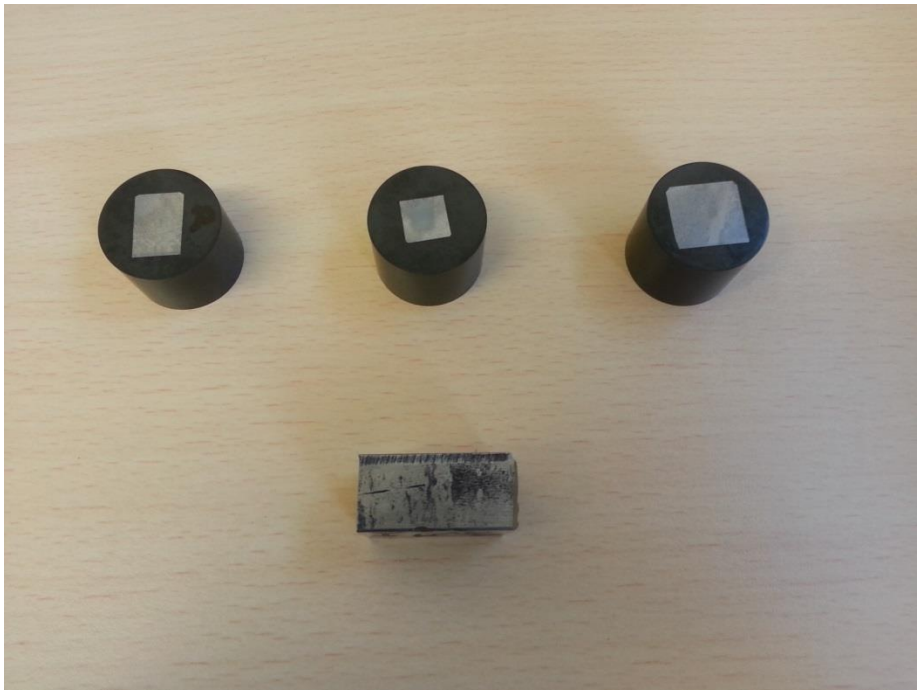

Figure D-2: The sample mounted epoxy

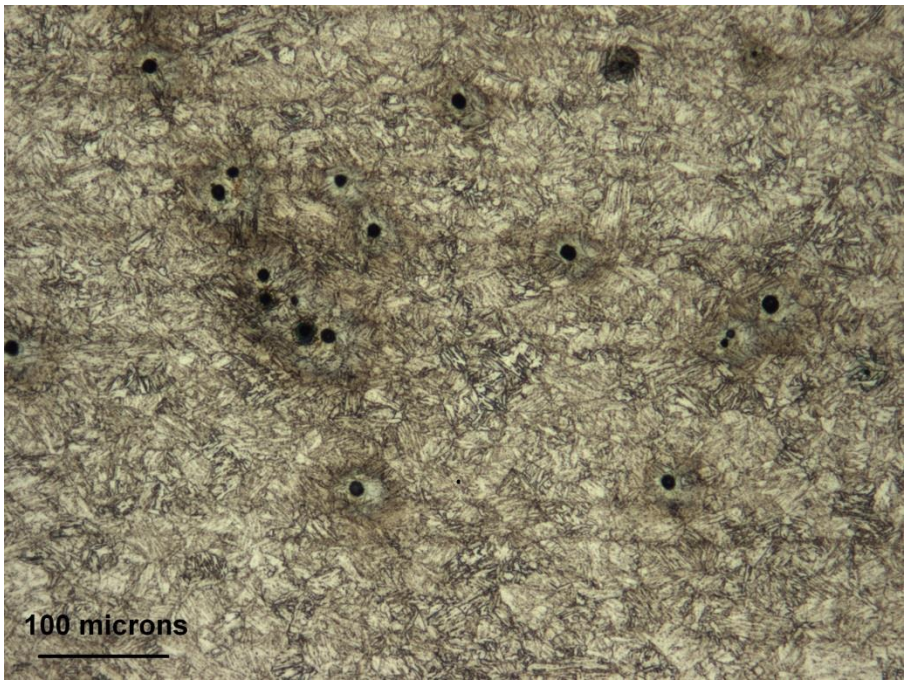

Figure D-3: Micro-structure orientation in longitudinal direction

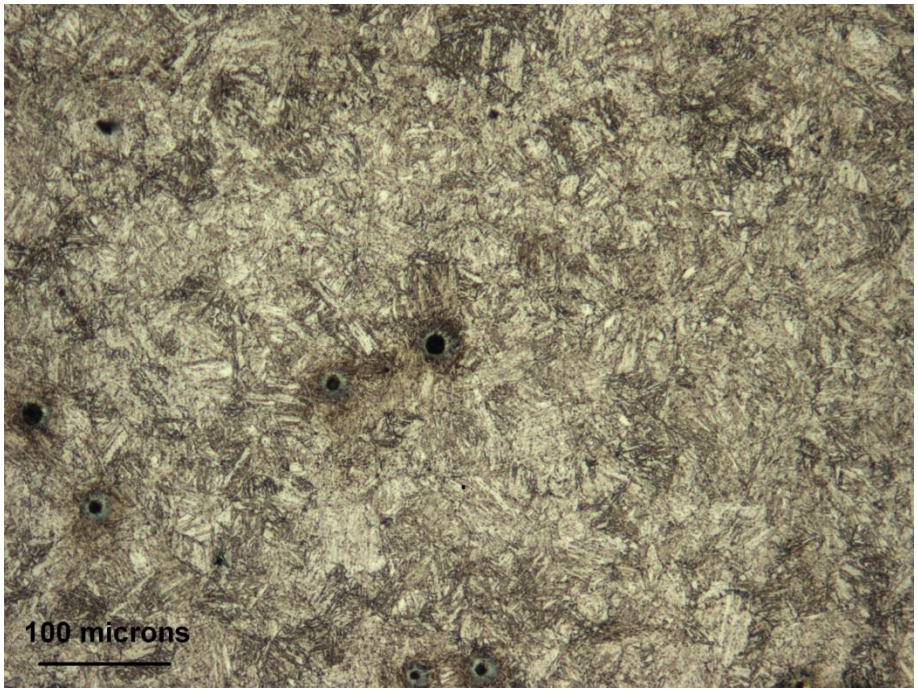

Figure D-4: Micro-structure orientation in transverse direction

Figure D-5: Four-point bend specimen

Appendix E Material Certificate

In this appendix, the chemical and mechanical properties of high strength steel are presented. The tables were provided by the steel manufacturer. The materials used are underlined by the manufacturer.

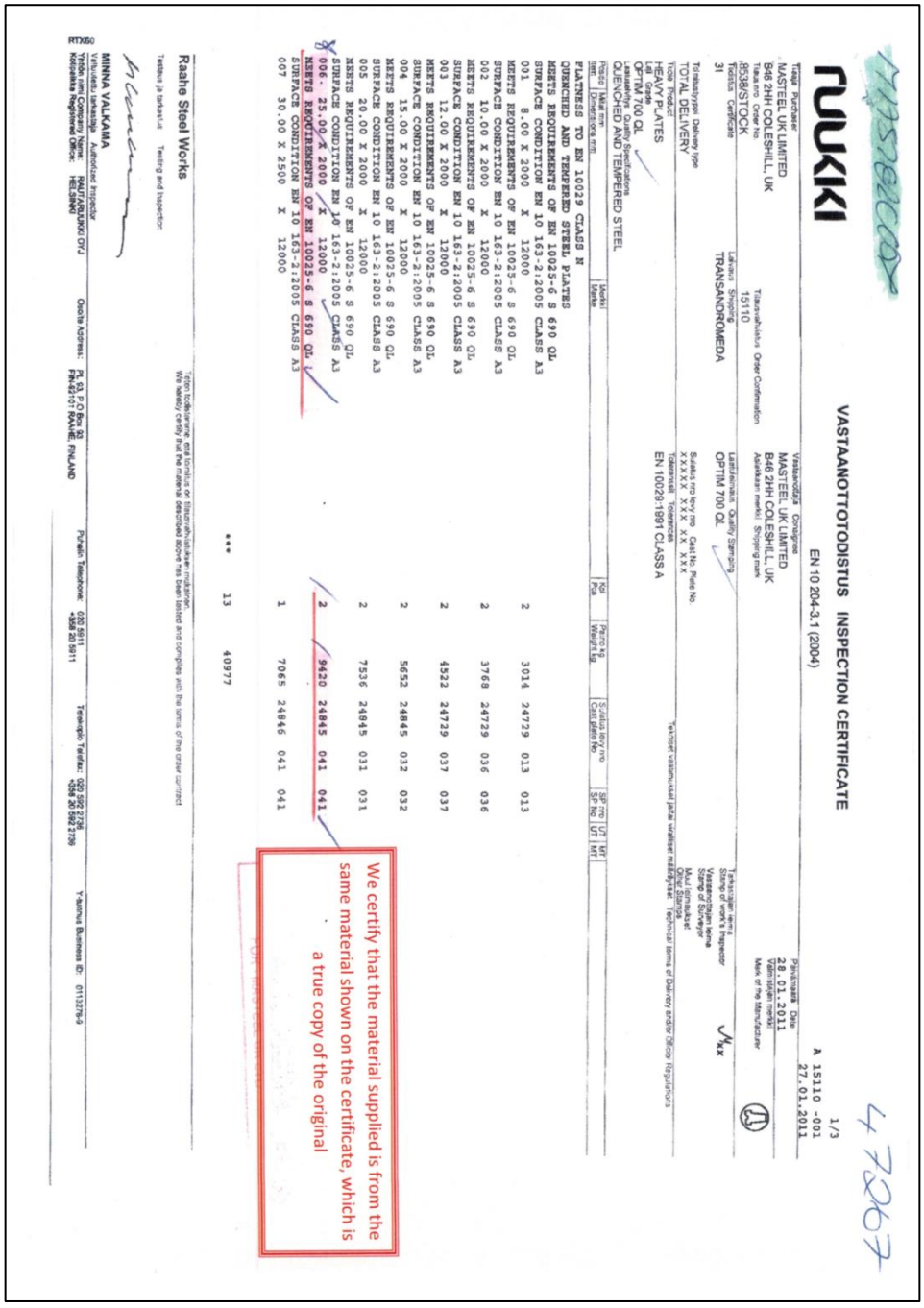

RUUKKI

VASTAANOTTOTODISTUS INSPECTION CERTIFICATE

EN 10 204-3.1 (2004)

A 15110 -001
1/3
27.01.2011

Tilaaja Purchaser
MASTEEL UK LIMITED
B46 2HH COLESHILL, UK
Tilaus nro Order No
15110
Tuotteet Certificate
31
Toimitusehto Delivery type
TOTAL DELIVERY
Tuote Product
HEAVY PLATES
Laji Grade
OPTIM 700 QL
Laatuvaatimus Specification
QUENCHED AND TEMPERED STEEL

Vastaanottaja Consignee
MASTEEL UK LIMITED
B46 2HH COLESHILL, UK
Asiakkaan merkki Shipping mark

Lähetysnro Shipping no
TRANSANDROMEDA

Lähetemerkki Quality Stamping
OPTIM 700 QL

Sulatus nro Cast No Pinoi No
X.X.X.X X.X.X X.X.X.X
Tekemisalt Tolerances
EN 10029:1991 CLASS A

Tarkastajan leima
Inspector's Stamp
Varmennuksen leimaus
Stamp of Surveyor
Muut merkinnät
Other Remarks

Päiväys Date
28.01.2011
Valmistajan merkki
Mark of the Manufacturer

Tarkastustodistus Inspection Certificate

Tekniset vaatimukset ja/tai viralliset määräykset Technical terms of Delivery and/or Official Regulations

Pinoja Item	Mitat mm Dimensions mm	Merkki Marks	Kpl Pcs	Paino kg Weight kg	Sulatus-lämpö no Cast/plate No	SP no SP No	UT	MT
	FLATNESS TO EN 10029 CLASS N							
	MEETS REQUIREMENTS OF EN 10025-6 S 690 QL							
	SURFACE CONDITION EN 10 163-2:2005 CLASS A3							
001	8.00 X 2000 X 12000		2	3014	24729	013	013	
	MEETS REQUIREMENTS OF EN 10025-6 S 690 QL							
	SURFACE CONDITION EN 10 163-2:2005 CLASS A3							
002	10.00 X 2000 X 12000		2	3768	24729	036	036	
	MEETS REQUIREMENTS OF EN 10025-6 S 690 QL							
	SURFACE CONDITION EN 10 163-2:2005 CLASS A3							
003	12.00 X 2000 X 12000		2	4522	24729	037	037	
	MEETS REQUIREMENTS OF EN 10025-6 S 690 QL							
	SURFACE CONDITION EN 10 163-2:2005 CLASS A3							
004	15.00 X 2000 X 12000		2	5652	24845	032	032	
	MEETS REQUIREMENTS OF EN 10025-6 S 690 QL							
	SURFACE CONDITION EN 10 163-2:2005 CLASS A3							
005	20.00 X 2000 X 12000		2	7536	24845	031	031	
	MEETS REQUIREMENTS OF EN 10025-6 S 690 QL							
	SURFACE CONDITION EN 10 163-2:2005 CLASS A3							
006	25.00 X 2000 X 12000		2	9420	24845	041	041	
	MEETS REQUIREMENTS OF EN 10025-6 S 690 QL							
	SURFACE CONDITION EN 10 163-2:2005 CLASS A3							
007	30.00 X 2500 X 12000		1	7065	24845	041	041	
		***	13	40977				

We certify that the material supplied is from the same material shown on the certificate, which is a true copy of the original

Raahe Steel Works

Tarkastaja ja tarkastuksia Testing and Inspection

Tähän todistukseen, sitä koskeviin tai tilaamiinsa tuotteisiin mainitaan:
We hereby certify that the material described above has been tested and complies with the terms of the order contract

MINNA VALKAMA
Virkavastuullinen tarkastaja Authorized Inspector

Yhtiön nimi Company Name: RAUTARUUKKI OYJ
Käyntiosoite Registered Office: HELSINKI

Postiosoite Address: PL 93, P.O.Box 93
FIN-92101 RAAHE, FINLAND

Puhelin Telephone: 020 5511
+358 20 5511

Telekopio Telefax: 020 592 2726
+358 20 592 2726

Y-tunnus Business ID: 0113278-9

RTX60

Figure E-1: Mechanical properties of material 1

RUUKKI

AINESTODISTUS TEST REPORT

EN 10 204-3.1 (2004)

2/3
A 15110 -001
27.01.2011

Tilaaja Purchaser: MASTEEL UK LIMITED
UNIT 8, THE CEDARS

Tilaus no. Order No.: 85381/STOCK

Vaatimustaso Quality Specification: QUENCHED AND TEMPERED STEEL

Vasaanottaja Consignee: MASTEEL UK LIMITED
UNIT 8, THE CEDARS

Asiakkaan merkki Shipping mark:

Lisävaatimukset Additional requirements:

Päivämäärä Date: 28.01.2011

Valmistajan merkki Mark of the Manufacturer: MLK

Valssausmenetelmä Valssaustapa: Oxygen steel, continuous casting
Fully killed, Fine grain predicted

Pos. Item	Sulatuk.& koet.nro Cast. Test No	Tila Cond	Vetokoe Tensile test																		Iskusinnik. Impact test																Taivutuskoe Bend test		Huom. No		Pidätö Tempering °C
			K2	°C	R$_{p0,2}$ MPa	R$_{t0,5}$ MPa	R$_{EL}$ MPa	R$_{EH}$ MPa	R$_M$ MPa 1	R$_M$ MPa 2	R$_M$ MPa 3		A % 50	A % 80	A % 200	R$_{EH}$ / R$_M$	R$_M$ * A5	RAZ % 1	RAZ % 2	RAZ % 3	Keskiarvo Average	Huom. No	K3	°C	1	2	3	Koetinnro Average	Sirrakarkaisu Quenching	Karkaisu Quenching	Karkaisu Quenching	Keskiarvo Average	Erikoiskoe Special test		Huom. No	K4	°C	1	2	Keskiarvo Average	K5	D = X t		
001	24729 013	QT	51		782			825			16																													
002	24729 036	QT	51		834			862			14																													
003	24729 037	QT	51		801			840			15																													
004	24845 032	QT	51		794			852			16																													
005	24845 031	QT	51		788			842			17																													
006	24845 041	QT	51		833			880			16																													
007	24846 041	QT	51		807			856			15																													

K2: 51=BOTTOM,TRANSV.

QT=QUENCHED + TEMPERED

K3: 157=CH-V/ISO-V(J),1X10,BOTTOM,LONGIT,KV600 165=CH-V/ISO-V(J),7.5X10,BOTTOM,LONGIT,KV600 151=CH-V/ISO-V(J),10X10,BOTTOM,LONGIT,KV600

CERTIFIED THAT THIS IS A TRUE COPY OF THE ORIGINAL CERTIFICATE RETAINED IN OUR FILE
3691
24580
FOR - MASTEEL UK LTD

Raahe Steel Works

Tilaus ostoilanmme ehtojen mukaan valmistettu ja tarkastettu materiaali on todettu niiden mukaiseksi.
We hereby certify that the material described above has been tested and complies with the terms of the order contract.

Testaus ja tarkastus Testing and Inspection

MINNA VALKAMA
Valtuutettu tarkastaja Authorized Inspector

Yhtiön nimi Company Name: RAUTARUUKKI OYJ
Kotipaikka Registered Office: HELSINKI

Osoite Address: PL 93, P.O. Box 93
FIN-92101 RAAHE, FINLAND

Puhelin Telephone: 020 5911
+358 20 5911

Telekopio Telefax: 020 592 2736
+358 20 592 2736

Y-tunnus Business ID: 0113274-9

RTX97

4 7267

MA5702C007

47267

RUUKKI

ANALYYSITODISTUS ANALYSIS CERTIFICATE
ANALYSEBESCHEINIGUNG COMPOSITIO CHIMIQUE CERTIFICAT
СЕРТИФИКАТ АНАЛИЗА

A 15110 -001
27.01.2011

Päivämäärä Date Datum Date Дата
28.01.2011 MLK

Analyysi % Chemical composition % Chemisch Zusammensetzung % Composition Chimique % Анализ плавки % (*=ppm)

Sulatus nro Cast No Schmelzen Nr. No de coulée № плавки	Koe nro Test NO Prüf Nr. Essai No. № Пробы	Positio Item Pos. Poste Поз.	Cekv Ceq Ceq Céq Сек.в	C	SI	MN	P	S	AL	NB	V	TI	CU	CR	NI	MO	B	ZR
24729		001	.39	.153	.31	0.81	.008	.001	.042	.001	.006	.021	.014	0.30	0.06	.200	.0015	.001
24729		002	.39	.153	.31	0.81	.008	.001	.042	.001	.006	.021	.014	0.30	0.06	.200	.0015	.001
24729		003	.39	.153	.31	0.81	.008	.001	.042	.001	.006	.021	.014	0.30	0.06	.200	.0015	.001
24845		004	.50	.156	.32	0.99	.009	.000	.047	.002	.010	.023	.023	0.59	0.20	.198	.0016	.002
24845		005	.50	.156	.32	0.99	.009	.000	.047	.002	.010	.023	.023	0.59	0.20	.198	.0016	.002
24845		006	.50	.156	.32	0.99	.009	.000	.047	.002	.010	.023	.023	0.59	0.20	.198	.0016	.002
24846		007	.50	.159	.31	0.99	.009	.001	.042	.002	.010	.020	.024	0.59	0.21	.201	.0016	.003

CERTIFIED THAT THIS IS A TRUE COPY OF ORIGINAL CERTIFICATE RETAINED IN OUR FILE
3691
24450
FOR - MASTEEL UK LTD

CEQ=C+MN/6+(CR+MO+V)/5+(NI+CU)/15

Raahe Steel Works

Testaus ja tarkastus Testing and Inspection Испытание и контроль качества
Prüfung und Kontrolle Essais et Contrôle

Steel manufactured and supplied by Rautaruukki is free from radiation.
Производимая на металлурги-ческом комбинате «Rautaruukki» и поставляемая заказчику сталь не излучают радиации.

MINNA VALKAMA
Valtuutettu tarkastaja Authorized Inspector Уполномоченный инспектор
Bemyndigad inspektör Inspecteur autorisé

Yhtiön nimi Company Name: RAUTARUUKKI OYJ
Kotipaikka Registered Office: HELSINKI
Osoite Address: PL 93, P.O Box 93, FIN-92101 RAAHE, FINLAND
Puhelin Telephone: 020 5911, +358 20 5911
Telekopio Telefax: 020 592 2736, +358 20 592 2736
Y-tunnus Business ID: 0113276-9

E-3

Appendix F Fatigue crack growth rate and Stress Intensity Factor calculation for surface fatigue crack under 4-point bending test

The fatigue crack dimension was monitored during fatigue tests using the ACPD technique. The ACPD probes were deployed along the notch side to measure the depth and length of the fatigue crack during fatigue tests. The SIF range ΔK for this specimen geometry was calculated to correspond to the Newman & Raju model. The model involved empirical equations to calculate the SIF for semi-elliptical surface cracks which depended on many factors, such as crack length, crack depth, plate width, plate thickness and parametric angle for bending and tension loads. The model has been obtained from a 3-D finite element analysis of finite elastic plate subjected to bending or tension load [168]. Figure F-1 shows the flow chart of the Newman & Raju model.

Equation of the SIF for combined bending and tension load:

$$K_I = (S_t + HS_b)\sqrt{\pi \frac{a}{Q}} F(\frac{a}{t}, \frac{a}{c}, \frac{c}{b}, \phi) \qquad \text{Equation F-1}$$

For $0 \langle a/c \le 1.0$, $0 \le a/t \langle 1.0$, $c/b \langle 0.5$ and $0 \le \phi \le \pi$. A useful approximation for Q ,

$$Q = 1 + 1.464(\frac{a}{c})^{1.65} \qquad \text{Equation F-2}$$

F : The tension boundary correction factor, which has been calculated by a systematic curve fitting. Double-series polynomials have been used in terms $(a/c), (a/t)$. The bending-boundary correction factor is equal to H .

$$F = \left[M_1 + M_2(\frac{a}{t})^2 + M_3(\frac{a}{t})^4 \right] f_\phi g f_w$$ Equation F-3

$$M_1 = 1.13 - 0.09(\frac{a}{c})$$ Equation F-4

$$M_2 = -0.54 + \frac{0.89}{0.2 + (a/c)}$$ Equation F-5

$$M_3 = 0.5 - \frac{1.0}{0.65 + (a/c)} + 14(1.0 - \frac{a}{c})^{24}$$ Equation F-6

$$g = 1 + \left[0.1 + 0.35(\frac{a}{t})^2 \right](1 - \sin\phi)^2$$ Equation F-7

$$f\phi = \left[(\frac{a}{c})^2 \cos^2\phi + \sin^2\phi \right]^{\frac{1}{4}}$$ Equation F-8

$$f_w = \left[\sec(\frac{\pi c}{2b}\sqrt{\frac{a}{t}}) \right]^{\frac{1}{2}}$$ Equation F-9

$$H = H_1 + (H_2 - H_1)\sin^P\phi$$ Equation F-10

$$H_1 = 1 - 0.34\frac{a}{t} - 0.11\frac{a}{c}(\frac{a}{t})$$ Equation F-11

$$H_2 = 1 + G_1(\frac{a}{t}) + \mathrm{G}_2(\frac{a}{t})^2$$ Equation F-12

$$G_1 = -1.22 - 0.12(\frac{a}{c})$$ Equation F-13

$$G_2 = 0.55 - 1.05(\frac{a}{c})^{0.75} + 0.47(\frac{a}{c})^{1.5}$$ Equation F-14

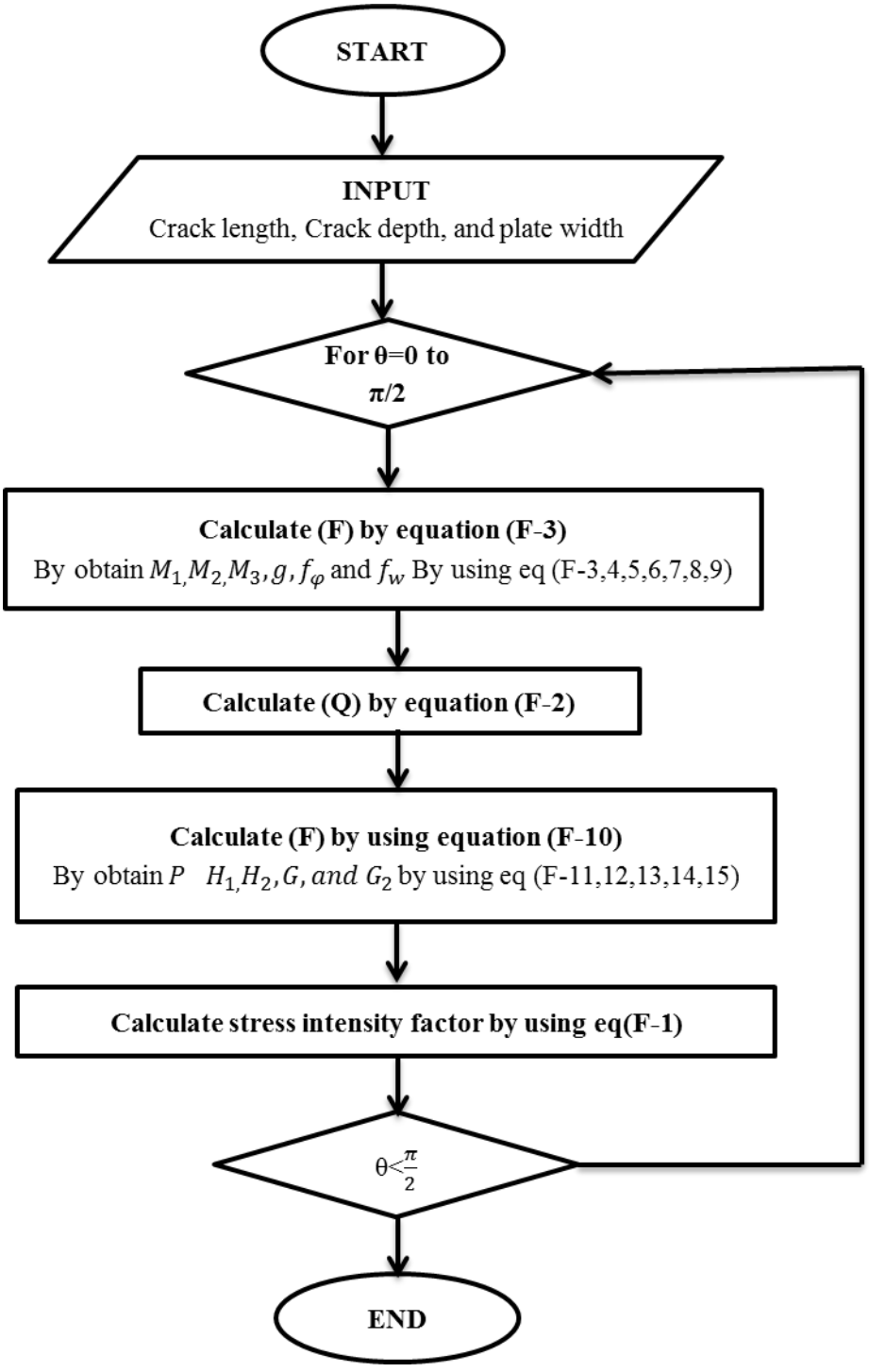

Figure F-1: Flow chart of Newman & Raju model

Appendix G Fatigue crack growth under 4-point bend fatigue load using single wave matrix

The fatigue tests have been conducted by using a 100 kN Instron Machine. The test methods were written by using the wave matrix software provided by Instron. A single wave matrix was used for the test. The single wave matrix means the tests were conducted under a continuous cyclic load between the maximum and minimum load until the test end, as shown in Figure G-1. The single wave matrix contains three steps as shown in Figure G-2 which are:

Step 1: apply minimum load of the test to the specimen.

Step 2: apply sinusoidal load with defined maximum load and load ratio.

Step 3: the test ramp to the zero load and finish the test.

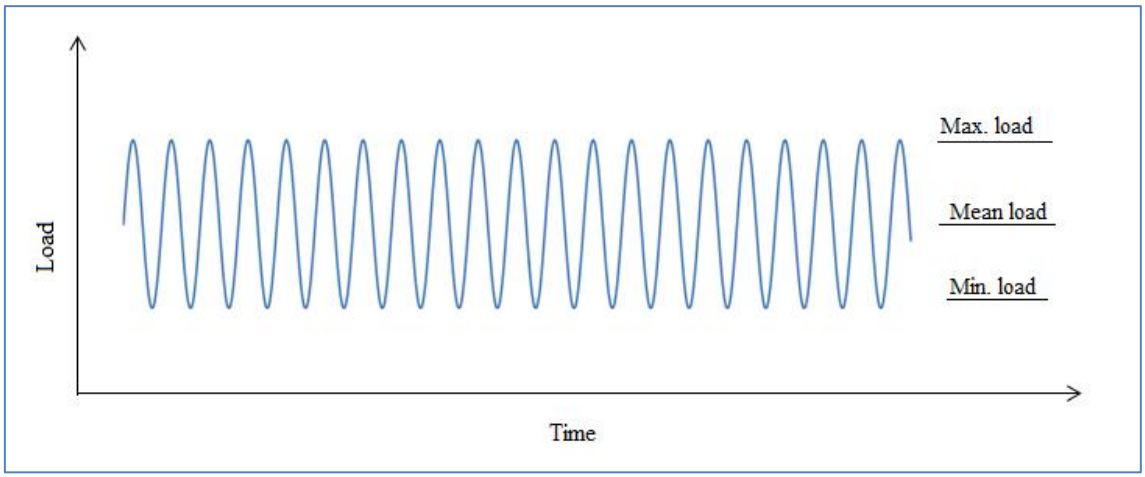

Figure G-1: Schematic diagram of single wave matrix

This test has used the ACPD technique to measures the crack propagation length during the test. The fatigue crack growth data were presented as crack length versus number of cycles as shown in Figure G-3. Figure G-4 represents the fatigue crack evolution for the A60 specimen. The fatigue crack growth rate specimen versus stress intensity factor range of A60 is presented in Figure G-5.

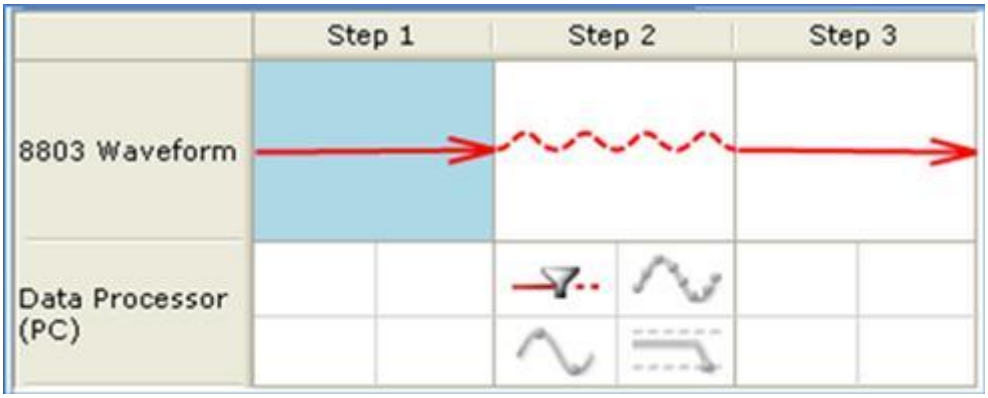

Figure G-2: Demonstration of the test method implemented in the wave matrix

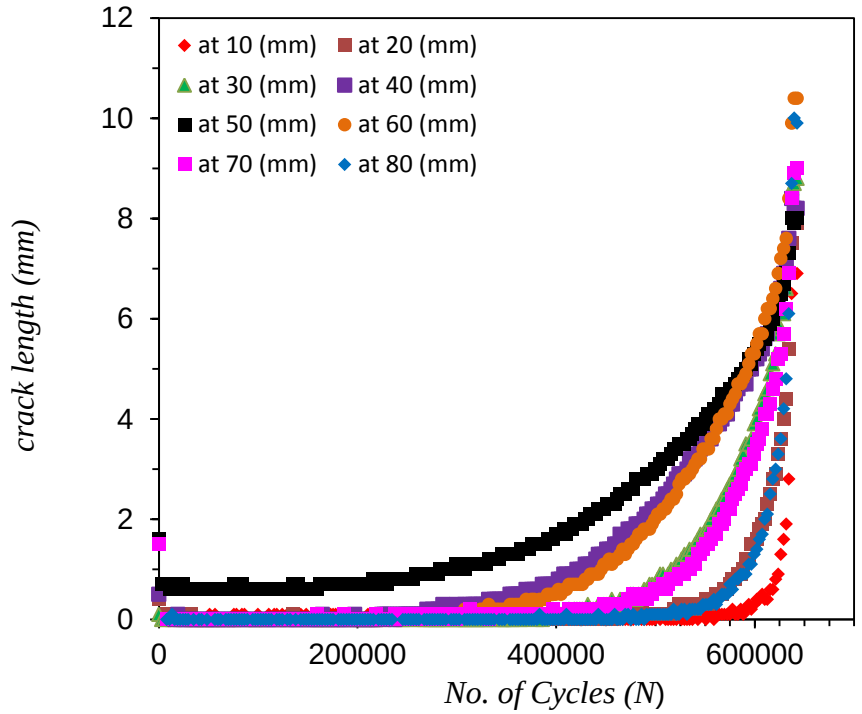

Figure G-3: Fatigue crack growth data versus number of cycles for A60 specimen

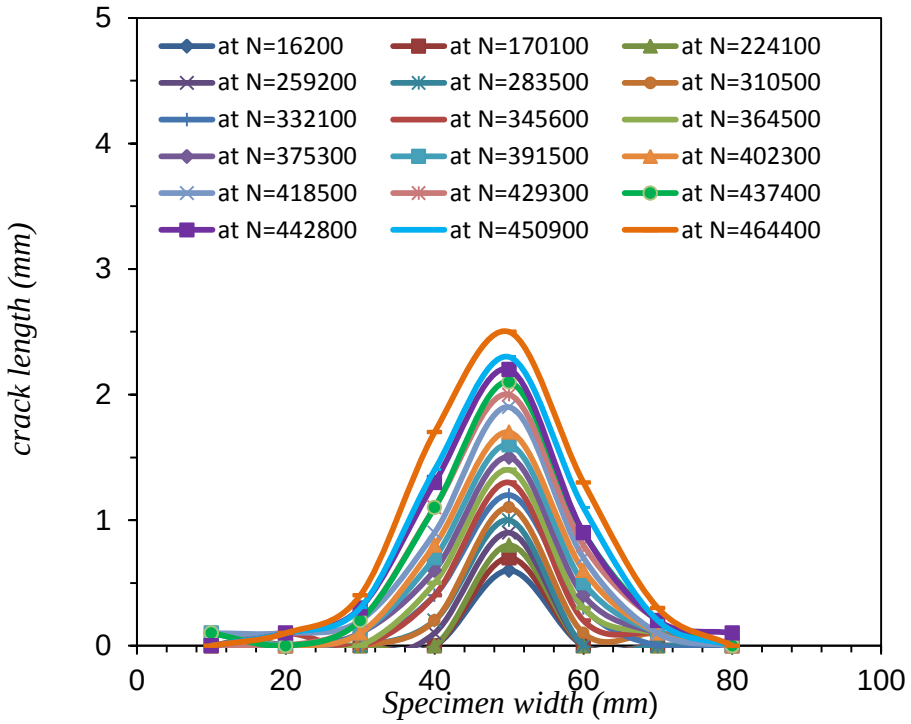

Figure G-4: Crack Shape evolution for A60 specimen

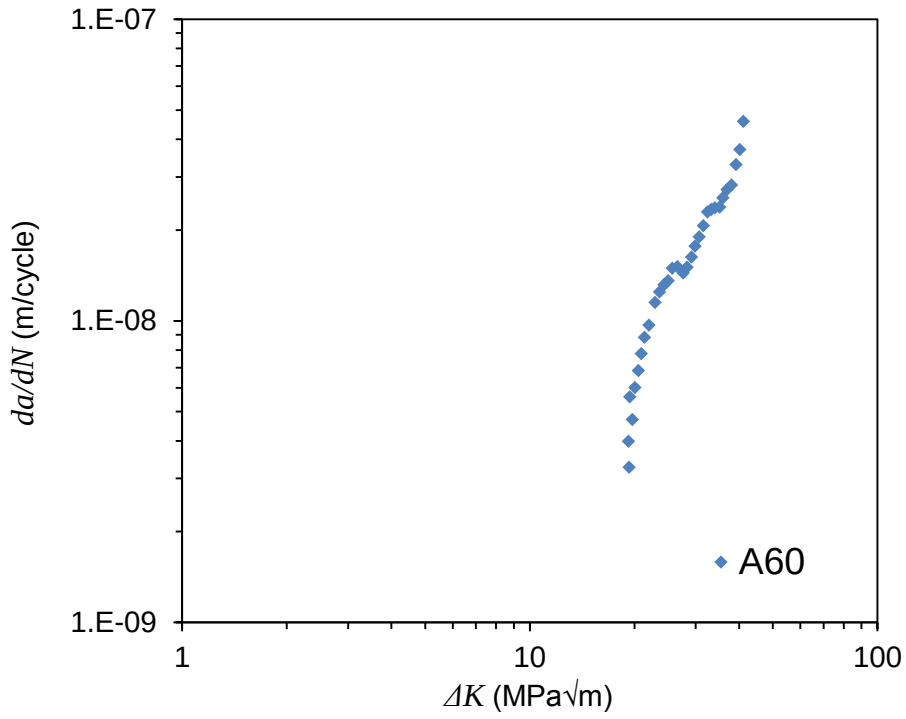

Figure G-5: Fatigue crack growth results for A60

Appendix H Crack modelling in Finite Element Modelling

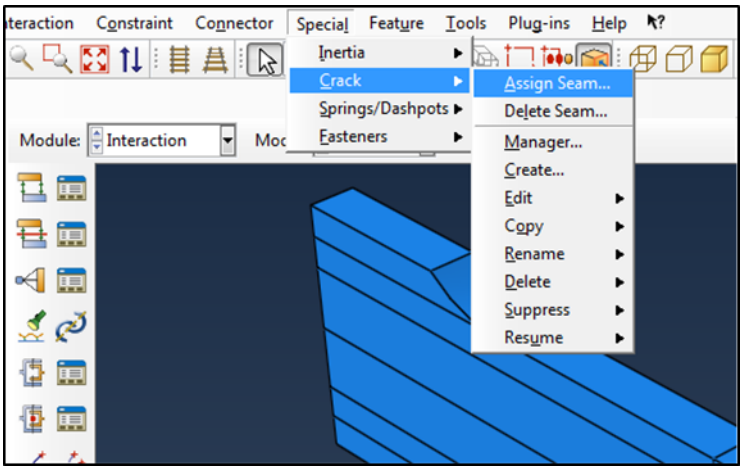

Figure 1-1: create seam procedure

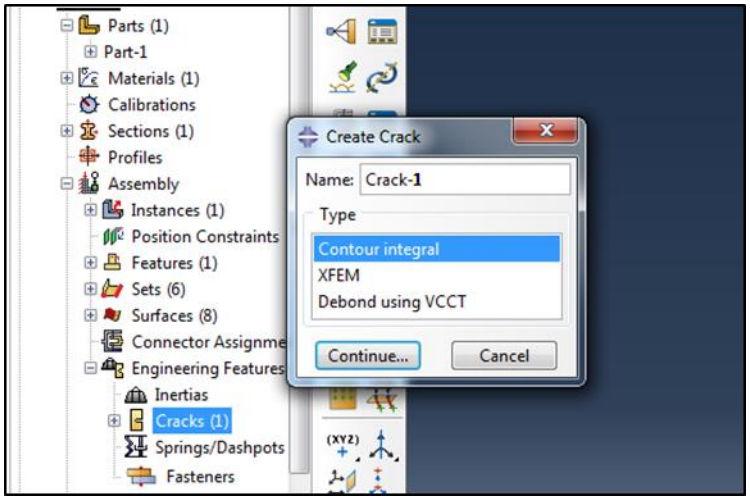

Figure 1-2: crack defines steps

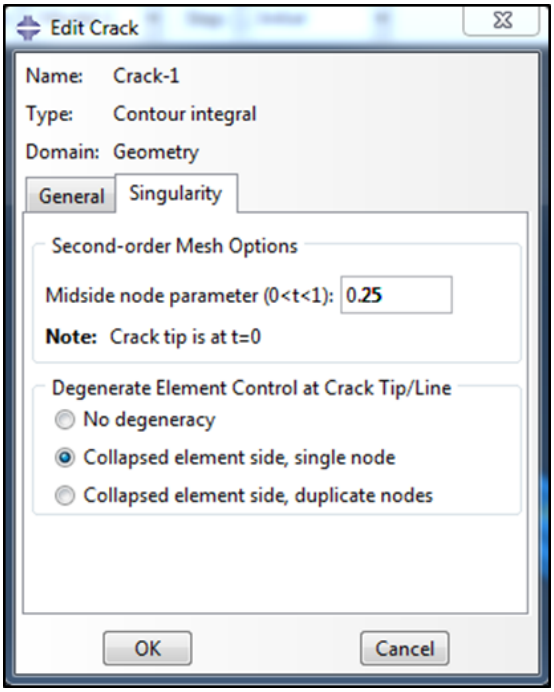

Figure 1-3: crack singularity setup

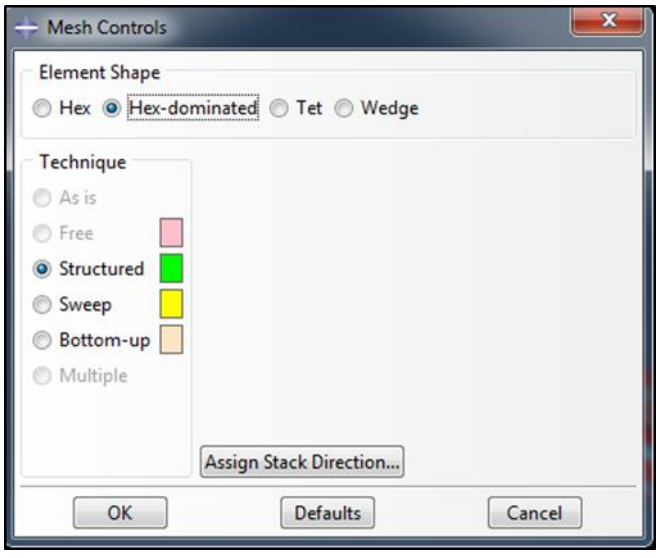

Figure 1-4 Mesh control for the area around the crack tip

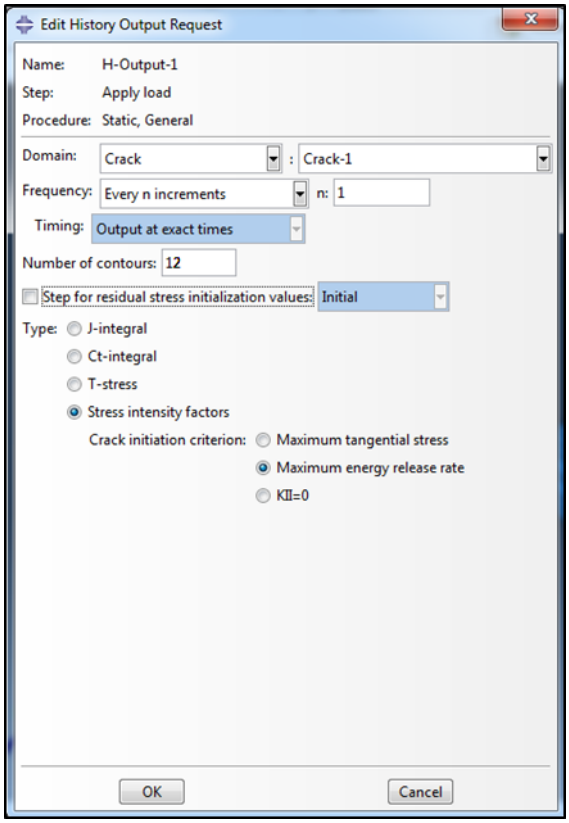

Figure 1-5: SIF calculation by ABAQUS